PEER Arizona Strong-Motion Database and GMPEs Evaluation

Tadahiro Kishida
Pacific Earthquake Engineering Research Center
University of California, Berkeley

Robert E. Kayen
United States Geological Survey
Menlo Park, California

Olga-Joan Ktenidou
Pacific Earthquake Engineering Research Center
University of California, Berkeley
& ISTerre, Université de Grenoble 1, CNRS, Grenoble, France

Walter J. Silva and Robert B. Darragh
Pacific Engineering and Analysis
El Cerrito, California

Jennie Watson-Lamprey
Watson-Lamprey Consulting
Berkeley, California

PEER Arizona Strong-Motion Database and GMPEs Evaluation

Tadahiro Kishida

Pacific Earthquake Engineering Research Center
University of California, Berkeley

Robert E. Kayen

United States Geological Survey
Menlo Park, California

Olga-Joan Ktenidou

Pacific Earthquake Engineering Research Center
University of California, Berkeley
& ISTerre, Université de Grenoble 1, CNRS, Grenoble, France

Walter J. Silva and Robert B. Darragh

Pacific Engineering and Analysis
El Ceritto, California

Jennie Watson-Lamprey

Jennie Watson-Lamprey Consultant
Berkeley. California

ABSTRACT

This report summarizes the products and results of a study on the collection, processing, and analysis of earthquake ground-motions recorded in Arizona at several recording stations within 200 km from the Palo Verde Nuclear Generating Station in central Arizona. The recorded ground motion in Arizona were compiled and processed according to the Pacific Earthquake Engineering Research Center's (PEER) record-processing standards. Shear-wave velocity profiles at ten recording stations were measured through the spectral analysis of surface wave dispersion technique. Additionally, "kappa" a measure of energy dissipation in the top 1 to 2 km of the crust, was estimated by three methodologies. The average κ_0 (kappa at zero-kilometer distance) was estimated from all sites as 0.033 sec. Finally, response spectra of the recorded ground motions in Arizona were compared with those predicted by the NGA-West2 ground motion prediction equations at large distances in Arizona. The comparison showed that overall the recorded 5% damped response spectral ordinates were over predicted by the NGA-West2 models by a range of 0–0.35 natural log units for events occurring in Central California, and by a range of 0.2–0.7 natural log units for events occurring in Southern California and the Gulf of California.

ACKNOWLEDGMENTS

CONTENTS

LIST OF TABLES

x

LIST OF FIGURES

1 Introduction

Recently the NGA-West2 research project developed a comprehensive database of recorded ground motions and a set of ground motion prediction equations (GMPEs) for shallow crustal earthquakes in active tectonic regions [Bozorgnia et al. 2014]. The goals of this study are as follows:

1. Expand the NGA-West2 ground motion database with earthquakes recorded in Arizona;

2. Measure shear-wave velocities at several recording stations in Arizona through the spectral analysis of surface wave (SASW) dispersion technique;

3. Estimate "kappa" at the recording sites in Arizona; and

4. For horizontal components, compare the response spectral ordinates of the recorded motions with those predicted by the NGA-West2 GMPEs at large distances in Arizona.

This study is motivated by the evaluation of the applicability of the NGA-West2 models for Arizona, as there is an important facility, the Palo Verde Nuclear Generating Station (PVNGS), located in central Arizona. A related technical issue to be addressed is to evaluate the effects of attenuation (Q) in Arizona versus California.

Following the interlocutory materials and scope of the study, Chapter 2 of this report addresses Goal (1) of this study as listed above. The chapter describes the data-processing methodology for time series and spectra (both response and Fourier spectra). The metadata for 15 seismographic stations within 200 km from the PVNGS in central Arizona are also discussed. Lastly, recorded ground motions from 26 earthquakes are presented. Fourteen of these earthquakes—with hypocenter locations in California and Mexico—have been previously studied in the NGA-West2 project. Twelve earthquakes with hypocenter locations in Arizona have been added to the database.

Chapter 3 presents one-dimensional shear-wave velocity profiles at 10 recording stations. This study quantified several key site classification parameters, including a detailed site shear-wave velocity profile, average velocity in the upper 30 m of the profile, average velocity for the entire profile, and the NEHRP site classification through the SASW dispersion technique. This work has been a collaborative study with the U.S. Geological Survey (USGS) in Menlo Park, California.

Chapter 4 discusses the estimates of kappa (κ) in the areas of interest in Arizona. The parameter κ models the empirical observation of energy dissipation occurring in the top 1–2 km of

the crust and is important in characterizing strong ground motions for engineering design, especially in the high-frequency range. Three methods are used to estimate κ: employing acceleration spectrum, displacement spectrum, and broadband approaches.

Chapter 5 compares the 5% damped response spectral values from earthquakes recorded at the Arizona stations with the spectral ordinates predicted by the NGA-West2 GMPEs. This comparison allows for determining the effect of the attenuation (Q), which previous studies have found to be higher in Arizona compared to California, thus, leading to lower attenuation in Arizona as compared to California. If the effect of a higher Q is significant, then the ground motion at Arizona stations should be larger than those in California for the same earthquakes and similar distances.

2   Strong-Motion Database

This chapter describes the overview of the development of the Arizona ground motion database and time series processing. The database provides uniformly processed time series for sites within 200 km from the PVNGS in central Arizona (Figure 2.1). The seismographic stations are listed in Table 2.1. Also, a catalog of earthquake hypocenter locations and magnitudes is presented in Table 2.2 [Jeri Young, Arizona Earthquake Information Center, *personal communication*, 2013].

Time series recorded at these stations are corrected for instrument response (Section 2.2), when necessary, to obtain acceleration, velocity, and displacement time series. The data-processing methodology is described in Section 2.3, including definition and selection of various time windows, filtering, conversion from velocity time series to acceleration time series, and calculation of pseudo-spectral acceleration (PSA) at 11 damping values. Section 2.3.5 compares the processed results from two independent analyses to confirm the data-processing methodology; comparisons of 5%`damped response spectra from two co-located recorders at Needles (NEE2) show excellent agreement. Finally, the range of usable frequencies of the processed recordings is presented in Section 2.3.6.

2.1   SEISMOGRAPH STATIONS AND EARTHQUAKE LOCATIONS

There are fifteen seismograph stations in the study area near the PVNGS site. Table 2.1 lists the station coordinates and elevations, which range from 100 to 2000 m. The table also shows Vs_{30} values at nine sites from recent SASW measurements reported in Chapter 3, two sites with measured Vs_{30} values from measured profiles reported in Seyhan et al. [2014], and three sites with an assigned the "Geomatrix 3rd letter" using Vs_{30} correlations documented in Seyhan et al [2014]. Figure 2.1 shows the locations of most of these stations on a bedrock distribution map adopted from Lettis Consultants International, Inc. [2012]. All stations are within 200 km from the PVNGS and the bedrock depth changes depending on the site in the study area.

Twenty-six earthquakes that occurred in Arizona, California, or Mexico after 2007 were selected. These are listed in Table 2.2. The epicenters of the events are shown in Figure 2.2. There are 14 earthquakes with hypocenter locations in California and Mexico. These events, which were previously studied previously in the NGA-West2 project [Ancheta et al. 2013], are all at relatively long distances (greater than about 250 km) from the PVNGS site, with magnitudes exceeding 4.0. There are also 12 earthquakes with hypocenter locations in Arizona [Jeri Young, Arizona Earthquake Information Center, *personal communication*, 2013]. These events have shorter

distances to the PVNGS (generally less than 250 km) and have not been included in earlier NGA projects. For the events and stations shown in Tables 2.1 and 2.2, approximately 230 digital recordings were downloaded from the IRIS Data Management Center [2013] for the transportable array (TA) deployment.

The first step in data processing was to select the ground motions. The time series recordings were plotted without applying any filter in order to visually evaluate record quality. This selection criterion is consistent with the NGA-West1 [Chiou et al. 2008] and the NGA-West2 [Ancheta et al. 2013] projects. Figure 2.3 shows an example recording at Station Z15A (Table 2.1) for the earthquake with EQID 1269 (Table 2.2). Because this recording is very noisy, it is difficult to differentiate the signal (seismic waves) from the noise. Several noisy time series were recorded at Stations Z15A, NEE2, and Y12C, and they were not analyzed further. Most of the visually rejected recordings were from these three stations. After visual selection, 202 three-component records were accepted from 26 events and 14 stations. Figure 2.4 shows the distribution of magnitude versus epicentral distance for these recordings. The magnitude and distance range are from **M** 1.2 to 7.2, and from 9 to 650 km, respectively. Note that the earthquakes that were previously studied in the NGA-West2 project have larger magnitudes with longer distances compared to the Arizona stations, whereas the events located in Arizona have smaller magnitudes with shorter distances to these stations. The figure also shows the recordings measured at Station Z14A, which is 8 km from the PVNGS. The shortest epicentral distance for the recordings measured at this station is 50 km.
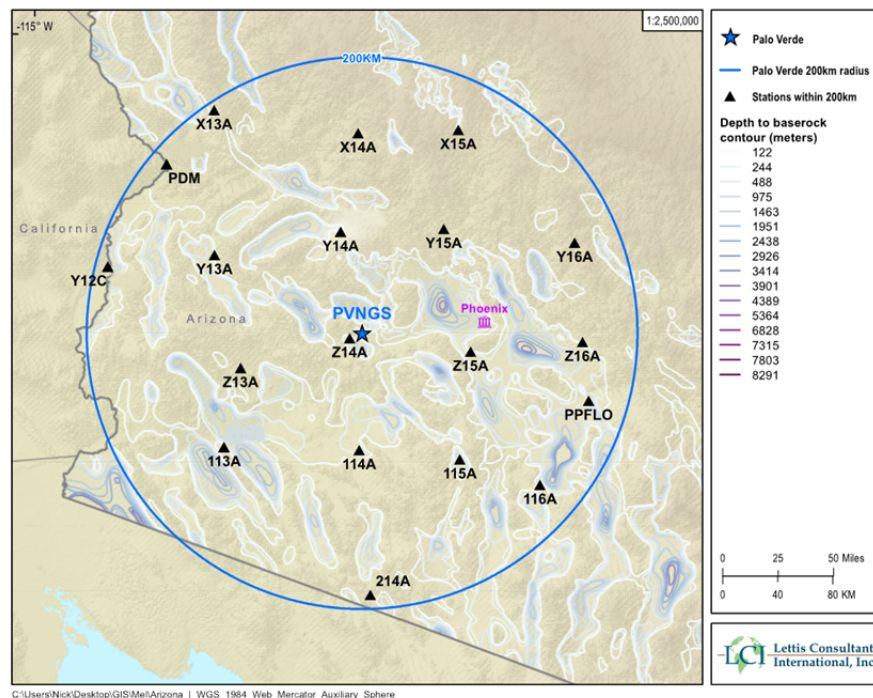
Figure 2.1   **Seismograph locations near the PVNGS site. Base bedrock map is adopted from Lettis Consultants International, Inc. [2012].**

Table 2.1   Seismograph station list.

Station name	SSN	Owner	Latitude (°)	Longitude (°)	Elevation (m)	$Vs_{,30}$ (m\sec)
NEE2	100288	CI, TA	34.7676	-114.6188	271.0	404[*]
PDM	100461	CI, TA	34.3034	-114.1415	144.0	1312[*]
113A	NA	TA	32.7683	-113.7667	118.0	1237
114A	NA	TA	32.7513	-112.8830	279.0	398
115A	NA	TA	32.7006	-112.2279	606.2	460
W13A	NA	TA	35.099	-113.8854	1988.2	660[**]
X13A	NA	TA	34.5935	-113.8302	889.4	425[**]
Y12C	NA	TA	33.7503	-114.5238	196.0	660[**]
Y13A	NA	TA	33.8142	-113.8287	356.9	560
Y14A	NA	TA/AE	33.9383	-113.0048	730.7	520
Y15A	NA	TA	33.9535	-112.3331	572.0	566
Y16A	NA	TA	33.8798	-111.4783	1068.0	1028
Z13A	NA	TA	33.1999	-113.6568	375.0	689
Z14A	NA	TA	33.3627	-112.9458	297.8	524
Z15A	NA	TA	33.2893	-112.1581	318.0	407

CI: California Institute of Technology Network
TA: US Array Transportable Array [US Array 2003]
AE: Arizona Broadband Seismic Network [Arizona Geological Survey 2011]
*: $Vs,30$ from Seyhan et al. [2014]
**: $Vs,30$ from Geomatrix 3rd letter proxy [Seyhan et al. 2014]
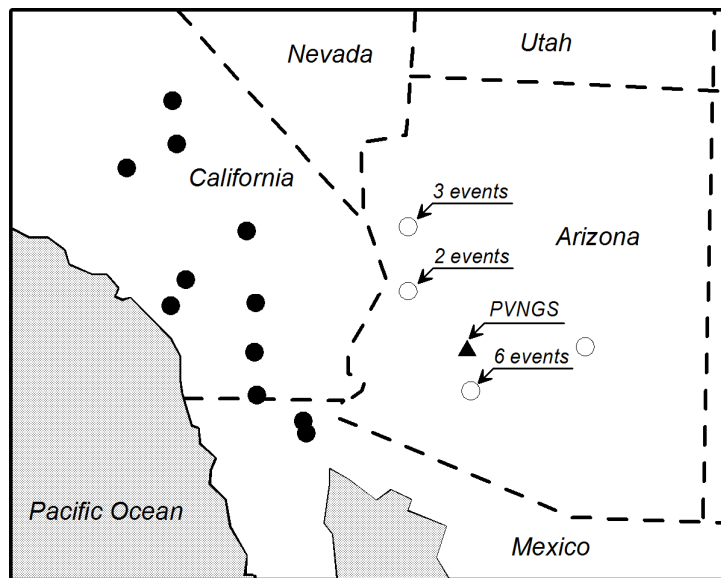
Figure 2.2   Earthquake epicenter locations in the Arizona dataset.

Table 2.2   Earthquake event catalog.

EQID	Earthquake Name	YEAR/MODY/HRMN	Mangitude (*)	Epicenter Latitude	Epicenter Longitude	Depth (km)
1267	NA	2008/0105/2345	3.10 ML	35.0230	-113.9140	1.00
1268	NA	2008/0117/2200	3.40 ML	35.0200	-113.9140	1.00
1269	NA	2008/0120/1728	2.10 ML	35.0260	-113.9290	1.00
1270	NA	2008/0724/1405	2.40 ML	34.1880	-113.8440	6.00
1271	NA	2008/0803/0953	2.00 ML	34.1880	-113.8620	7.00
1272	NA	2008/1129/0148	1.50 ML	32.9520	-112.7740	13.00
1273	NA	2008/1129/0710	1.50 ML	32.9530	-112.7740	13.00
1274	NA	2008/1129/0711	1.50 ML	32.9550	-112.7720	13.00
1275	NA	2008/1129/0722	1.50 ML	32.9550	-112.7710	13.00
1276	NA	2008/1129/1621	1.50 ML	32.9540	-112.7700	13.00
1277	NA	2008/1129/1622	1.20 ML	32.9550	-112.7700	13.00
1278	NA	2012/0203/0242	2.50Md	33.5905	-111.0490	13.87
1028	10275733	2007/0902/1729	4.73 ML	33.7328	-117.4921	10.02
1047	10321585	2008/0501/0811	4.43 ML	35.4744	-118.4262	6.68
1053	14330056	2007/1024/1222	4.34 ML	35.8373	-117.6780	6.86
1058	14285168	2007/0415/2257	4.41 ML	32.7070	-116.0400	10.16
1067	10230869	2007/0209/0333	4.29 ML	33.2262	-116.1472	10.89
1182	14517500	2009/1001/1001	5.00 **M**	36.3864	-117.8583	7.41
1186	14519780	2009/1003/0115	5.19 **M**	36.4034	-117.8499	9.42
280	El Mayor-Cucapah	2010/0404/2240	7.20 **M**	32.3000	-115.2670	0.00
1004	14346868	2008/0209/0712	5.10 **M**	32.4105	-115.3120	18.65
1005	14408052	2008/1206/0418	5.06 **M**	34.8118	-116.4227	9.33
1009	14462064	2009/0523/2258	4.73 ML	36.4011	-117.8397	7.42
1017	10347253	2008/0905/2154	4.63 ML	32.3362	-115.2425	17.16
1018	10370141	2009/0109/0349	4.45 ML	34.1081	-117.3062	14.80
1020	14295640	2007/0602/0511	4.26 ML	33.8776	-116.2019	10.06

Moment magnitude (**M)** and Richter magnitude (ML) for the NGA-West2 earthquakes from Ancheta et al. [2013]. The magnitude for the smaller Arizona events is from Jeri Young [Arizona Earthquake Information Center, *personal communication*, 2013].. Md is duration magnitude.

For the range $3 \leq ML \leq 5$ Richter magnitude (ML) and **M** are identical since they have the same relationship to seismic moment (M_o) given by: $\log M_o = 1.5 * (Mag) + 16.05$ where Mag can be either **M** [Hanks and Kanamori 1979] or ML [Thatcher and Hanks 1973; Bakun 1984; Hanks and Boore 1984]. For smaller (and larger) magnitudes this relationship between these magnitudes does not hold (e.g., see Figure 2, Hanks and Boore [1984]). In later chapters, the data from the smaller magnitudes are not compared to GMPEs based on **M** since only the Fourier amplitude spectra from these small events (magnitude < 3) are used.
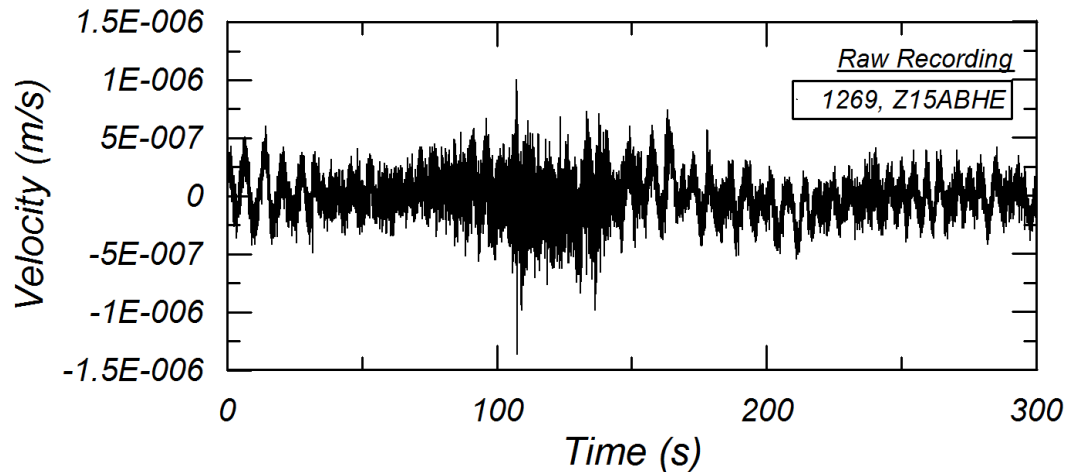
Figure 2.3   Example of rejected recording at Station Z15A.
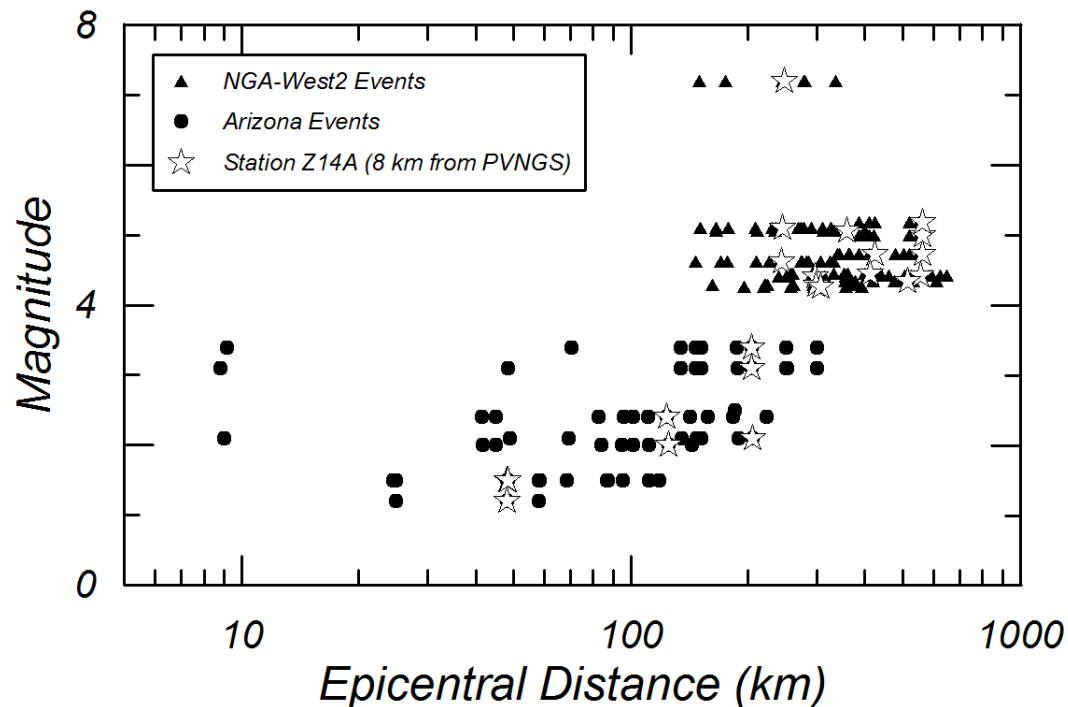
Figure 2.4   Magnitude versus epicentral distance distribution for the Arizona dataset.

2.2   INSTRUMENT RESPONSE

Instrument response parameters collected for each record include gain, natural frequency, damping, sample rate, and anti-alias filter description. For the selected recordings, these parameters were downloaded from the IRIS website [IRIS 2013] with reference to the station name, component, and earthquake origin time. Nearly all the stations listed in Table 2.1 are broadband velocity sensors, and their response is the same as that of the TA instrument shown in Figure 2.5. The two exceptions are the CI stations at NEE2 and PDM. The processing of the CI recordings is the same as in NGA-

West2 [Ancheta et al. 2013]. The Nyquist frequency for all TA recordings is 20 Hz, because the TA has a low sampling rate of 40 Hz. An anti-alias filter was applied to the TA data at about 80% of the Nyquist frequency with a corner frequency near 16 Hz. The figure shows that the instrument response is flat from 0.01 to about 15 Hz, which indicates that instrument-corrected velocity time series can be calculated by multiplying the count value in the downloaded ASCII files with its gain without the application of an instrument correction in this frequency band. For example, if the maximum count and instrument gain were obtained as 9060 in the ASCII file and 6.27192×10^6 (count/cm/sec) from the IRIS Data Management Center website, respectively, then the maximum velocity is calculated as follows:

$$vel_{max} = 9060 \Big/ \left(6.27192 \cdot 10^6\right) = 1.44 \cdot 10^{-3} \left(cm / sec\right) \tag{2.1}$$

Figure 2.6 shows an example plot of the velocity time series obtained using Equation (2.1). There is some long-period noise in the figure with period from about 2 to 10 sec. This long-period noise may be interpreted as microseisms composed of Rayleigh waves generated by ocean waves (e.g., Webb, [2002]). Long-period filtering for noise reduction is described later in Section 2.3.2.
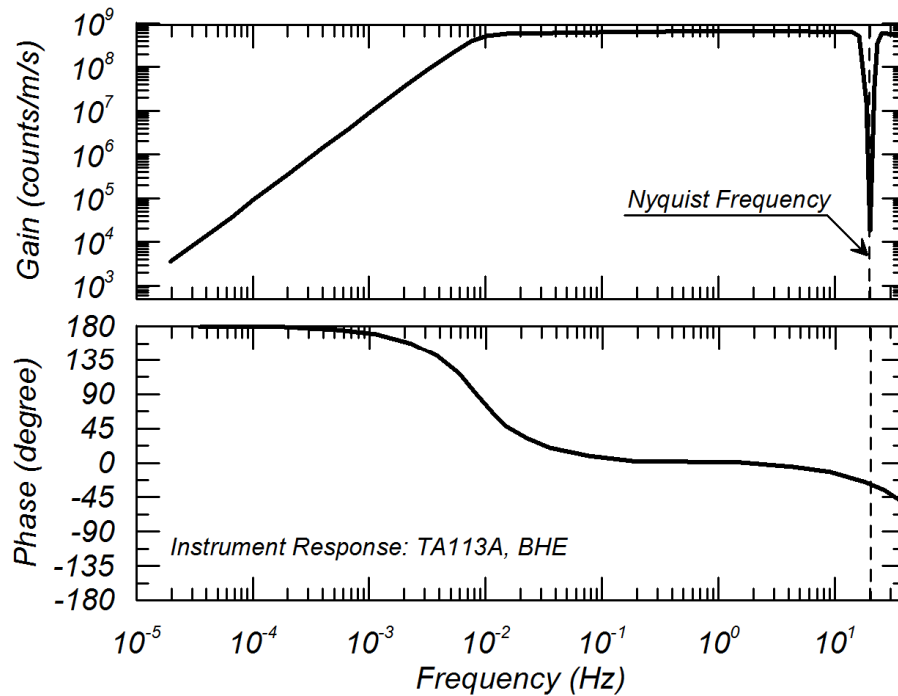
Figure 2.5   **Example of instrument response for TA array stations.**
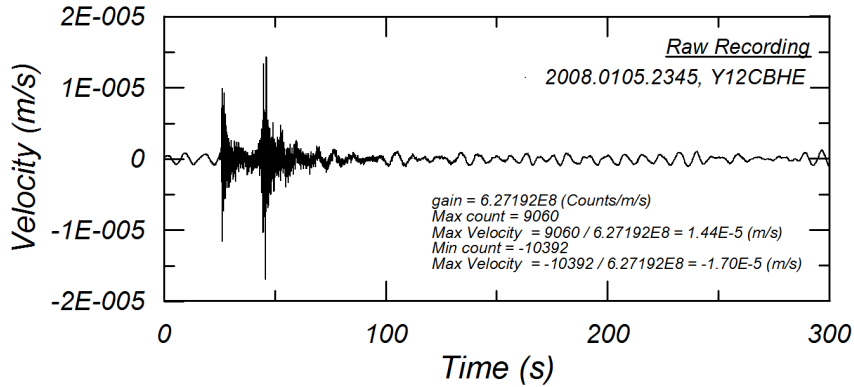
Figure 2.6   Example recording of raw (gain-corrected) velocity time series from Station Y12C.

2.3   DATA PROCESSING

Data processing for the Arizona time series generally followed the NGA-West2 process described in Ancheta et al. [2013]. The main differences are the selection of several windows for the calculation of Fourier amplitude spectra [Kishida et al. 2014] and the conversion of the recorded velocity time series from the TA array to acceleration.

2.3.1 Time Windows for Data Processing

Six different time windows were selected for each time series similar to the NGA-East project as described in Kishida et al.[2014]. Figure 2.7 shows a schematic plot of these windows. The first time window includes the entire record (blue box in the figure). This window includes the pre-event noise (recorded before the P-wave onset), P waves, S waves, and coda waves. The second to fifth windows contain only the pre-event noise (pink box), P waves (yellow box), S waves (green box), and coda waves (gray box), respectively. The sixth window contains both P and S waves. All time windows are selected during data processing in order to calculate the Fourier amplitude spectra (FAS) from the different waves in these windows. Because details of window choice are described in Kishida et al. [2014], this section only briefly outlines the time window selection for the different wave types.
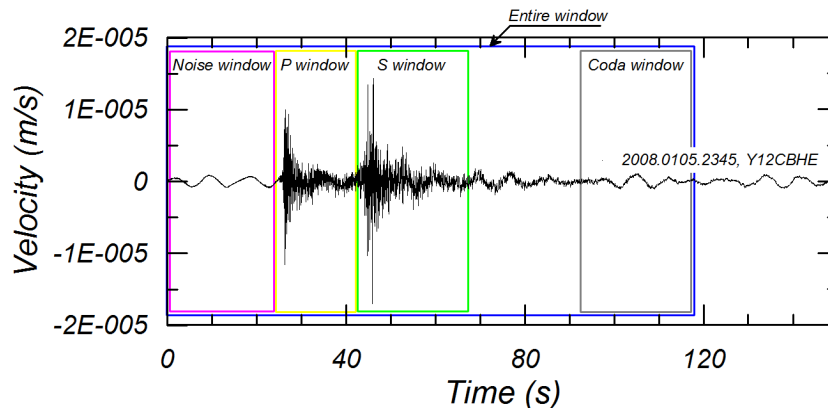
Figure 2.7   Schematic drawing of different time windows.

9

The start time of the P-wave window (t_p), which is the end time of noise window, was first selected visually by inspecting the three components for the first, generally impulsive, large amplitude wave arrival. Then, the end time of the P-wave window, which is the start time of S-wave window, was selected visually by observing the generally longer period and larger amplitude wave arrival in velocity and displacement time series. As a selection guide, the theoretical S arrival time (t_s') is plotted with the time series based on the selected P arrival time and the hypocentral distance as follows:

$$t_s' = t_p + \Delta t_{s-p} \approx t_p + R_h/8 \tag{2.2}$$

where R_h is the hypocentral distance, and P- and S-wave velocities are assumed to be 6.0 and 3.5 km/sec for the crust, respectively. The S arrival time (t_s) was selected visually considering amplitude and frequency content on the three-component acceleration and displacement time series.

The end time of the S-wave window was automatically selected using an assumed S-wave duration, which is a function of magnitude and hypocentral distance, and is expressed as follows:

$$D_S = T_{d-rup} + T_{d-prop} \tag{2.3}$$

where T_{d-rup} is a base duration, which is related to the rupture (source) duration but generally greater, and T_{d-prop} is the duration through the propagation of the S wave to the site and to scattering along the path. Table 2.3 shows the T_{d-rup} used in the data processing, where f_c in the table is calculated by the following formula [Aki 1967; Brune 1970; Boore 1983]:

$$f_c = 4.9 \cdot 10^6 \beta \left(\frac{\Delta_\sigma}{M_0} \right)^{1/3} \tag{2.4}$$

where

$$M_0 = 10^{1.5M + 16.05} \tag{2.5}$$

and β is shear-wave velocity at the source and was assumed to be 3.2 km/sec. The stress drop (Δ_σ) was assumed to be 6 MPa (60 bars), an average value for large earthquakes in California [Atkinson and Silva 1997]. The hypocentral distance effects on the S-wave duration have been approximated for regions such as California and Arizona [W. Silva, *personal communication*, 2013]:

$$T_{d-prop} = 0.1 \cdot R_h \tag{2.6}$$

The factor of 0.10 in this expression is consistent with the study by Kempton and Stewart [2006] in which the distance effects on significant durations of D_{a5-75} (5 to 75% duration) and D_{a5-95} (5 to 95% duration) are calculated as 0.07 and 0.15, respectively. After calculating the D_S in Equation (2.3), the start time of the noise window (t_n) was obtained so that the noise duration equals the S window duration if possible, thus:

$$t_n = \max\left(0, t_p - D_s\right) \tag{2.7}$$

The start time of the coda window $\left(t_c\right)$ was selected by following the theoretical coda definition [Aki 1969; Philips and Aki 1986; Kato et al. 1995]. This definition gives the onset of the coda at a time equal to twice the S-wave travel time after the S-wave onset. However, to estimate this window for as many recordings as possible, we defined the end of coda window, t_c^f, by this formula:

$$t_c^f = \min\left(t_{end}, t_s + 3 \cdot D_s\right) \tag{2.8}$$

Hence the start time of the coda window is obtained by using the same window length as that of the S window.

$$t_c = t_c^f - D_s \tag{2.9}$$

Finally, the entire time window was selected from t_n to t_c^f.

Table 2.3   Base duration used in the analysis.

Magnitude (M_w)	Base duration (sec)
M< 4.5	10
$4.5 \leq M < 6.9$	15
$6.9 \leq M < 7.6$	1.4/ f_c
$7.6 \leq M \leq 7.9$	33

2.3.2 Filtering of the Time Series

Figure 2.8 shows the Fourier velocity amplitude spectra of different windows for the example recording of Figure 2.7. It shows that Fourier amplitude drops sharply above 16 Hz, which is expected based on the instrument response shown in Figure 2.5. Low-pass (LP) filtering is provided in most cases by the anti-alias filter for the TA instrumentation; for recordings with noise at high frequencies, additional LP filtering was applied. It also shows that the FAS of the noise window overlaps with the FAS of the entire window at frequencies below about 0.5 Hz. This is also reflected by the decrease in the signal-to-noise ratio (SNR) to less than 3 near 0.5 Hz. These observations are interpreted to indicate that in this example the noise from microseisms and other sources are dominant at frequencies less than about 0.5 Hz. The high-pass (HP) corner frequency (HP f_c) was selected at 0.5 Hz to remove long-period noise from the recording. Figure 2.9 shows the velocity time series of the same example recording after applying a 5-pole acausal filter at 0.5 Hz. Comparing Figure 2.6 with Figure 2.9 confirms that much of the long-period noise is removed by applying the HP filter. The maximum velocity decreased by approximately 10% due to the LP filtering.
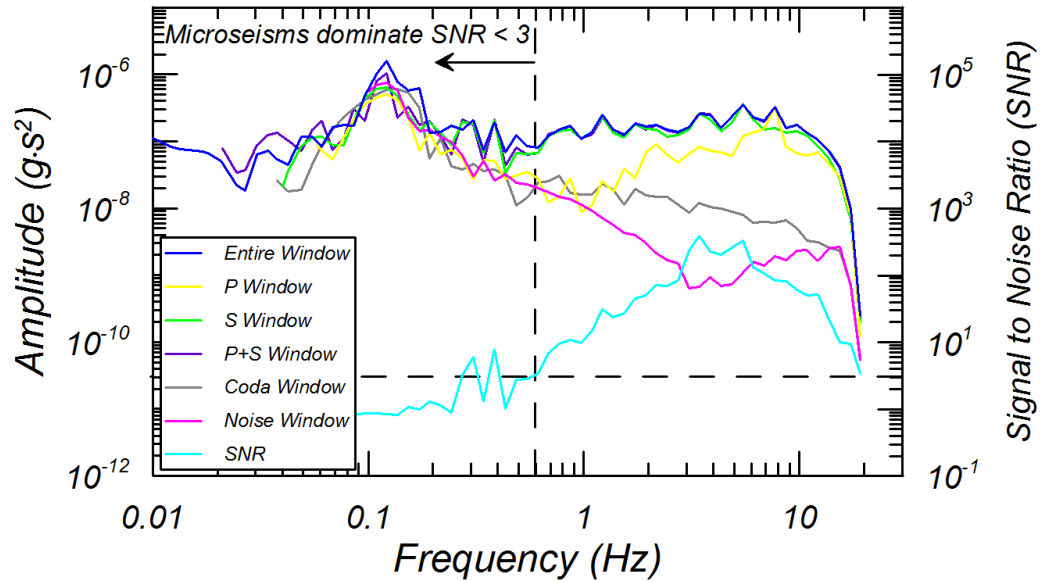
Figure 2.8   Fourier velocity amplitude spectra for an example recording.
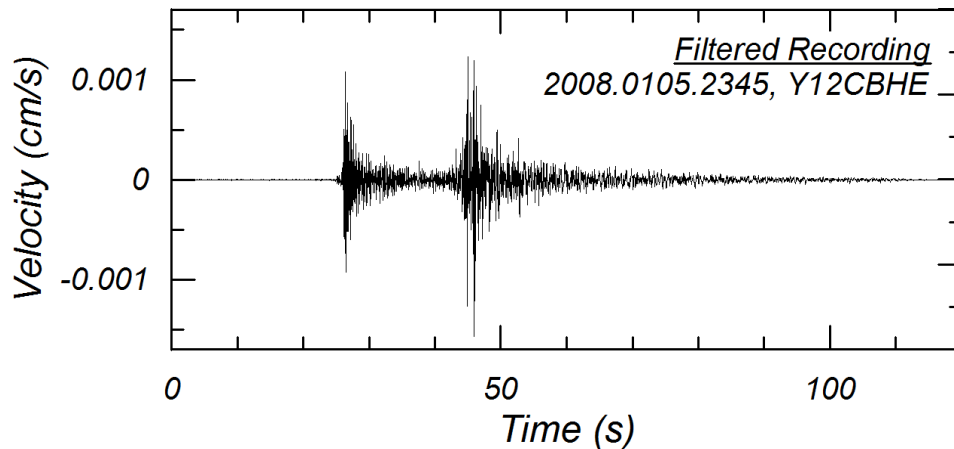
Figure 2.9   Example velocity time series after filtering.

2.3.3 Integration and Derivative of Time Series

The filtered velocity time series were converted into acceleration time series in the frequency domain as briefly described in this section. Let the Fourier spectra (*FS*) be expressed by the following formula:

$$FS(\omega) = A(\omega) + iB(\omega) \tag{2.10}$$

The *FS* was multiplied by $i\omega$ to obtain the derivative (acceleration). Similarly, the *FS* was multiplied by $-i/\omega$ to obtain the integral (displacement). On the basis of these equations, the conversion from velocity to acceleration time series was performed. Figure 2.10 shows an example conversion of velocity time series in the frequency domain to verify that the newly added subroutine works correctly in the *R* code used for signal processing within the NGA-West2 project. Figure

2.10(a) shows an original velocity time series. Figure 2.10(b) shows the converted acceleration time series from velocity time series in Figure 2.10(a) in frequency domain by multiplying by $i\omega$. Figure 2.10(c) shows the velocity time series integrated from the acceleration time series in Figure 2.10b in frequency domain by multiplying $-i/\omega$. Comparing Figures 2.10(a) and 2.10(c) confirms that the derivative and integration of time series are correctly performed by using the above described method. Figure 2.11 shows the comparison of Figure 2.10(a) to 2.10(c) in magnified scale, verifying that the newly added R code of time derivative and integral in frequency domain worked correctly during the data processing.

In the data processing, the filtered velocity time series was converted to an acceleration time series in the frequency domain at the first step. Then, the velocity and displacement time series were calculated from the converted acceleration time series in time domain with the standard PEER baseline correction algorithm [Chiou et al. 2008; Ancheta et al. 2013].
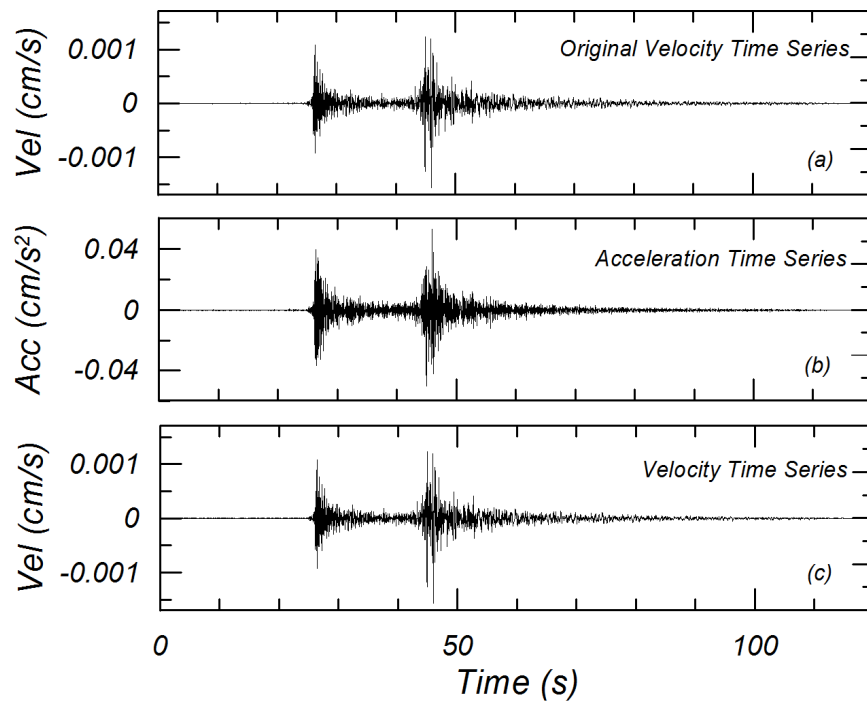
Figure 2.10   **Example conversion from velocity time series to acceleration and velocity time series in frequency domain.**
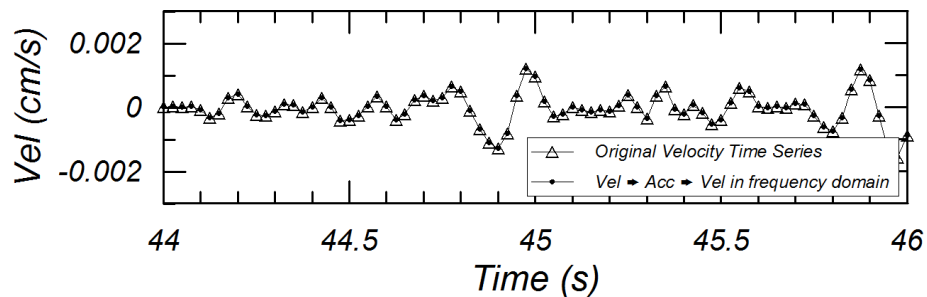
Figure 2.11   **Comparison of velocity time series.**

2.3.4 Pseudo-Spectral Acceleration and RotDnn

Pseudo-spectral accelerations are calculated from the acausal filtered acceleration time series. An acausal filter was selected, as in NGA-West2 research project, because it has less phase distortion compared to causal filters [Boore and Akkar 2003]. Figure 2.12 shows the PSA for the example recording. The black line shows the PSA for which the time series are interpolated linearly at short periods [Nigam and Jennings 1969]. The dashed line shows the PSA for which time series are interpolated in the frequency domain (sinc interpolation) by padding zeros to a higher frequency than the Nyquist frequency. Boore and Goulet [2014] discussed the differences in PSA from these two different interpolation methods and have recommended sinc interpolation because linear interpolation may introduce spurious energy at high frequencies. As shown in Figure 2.12, this energy can be observed in at 0.04 sec (25 Hz) where a small bump is observed in the PSA obtained from linear interpolation; however, it is not observed in the PSA obtained by sinc interpolation. Boore and Goulet [2014] also discussed potential errors on the short-period PSA when the true ground motion has significant energy at frequencies above that of the anti-aliasing filter. This error may occur at low sampling rate recordings, such as those provided by the TA array, especially at hard rock sites at close distances; hence we may expect errors in PSA above 15–16 Hz for very few, if any, of the TA recordings shown in Figure 2.4 based on the distance (generally < 50 km) and the shear-wave velocity measurements (Chapter 3 and Table 2.1). Using the sinc interpolation method, the orientation-independent horizontal spectra proposed by Boore [2010] (RotDnn) was calculated for the Arizona dataset.

Figure 2.13 shows the ratio of 5% damped PSA between sinc and linear interpolations in Figure 2.12; the linear interpolation underestimates the PSA compared to sinc interpolation by 35% at a period of 0.07 sec (14 Hz) but overestimates the PSA by17% at a period of 0.04 sec (25 Hz).
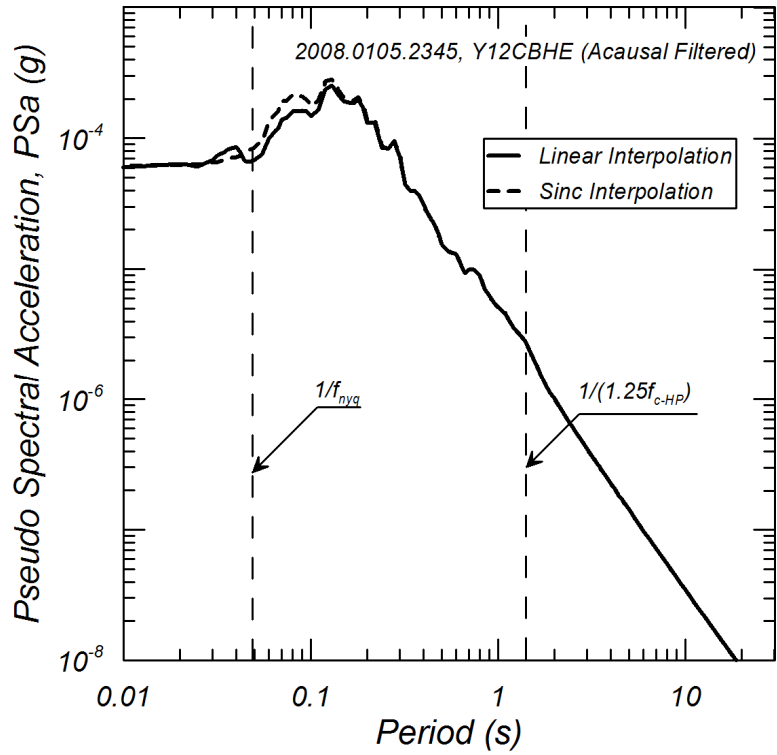
Figure 2.12   PSA for example records with different interpolation methods (solid: linear interpolation, dash: sinc interpolation).
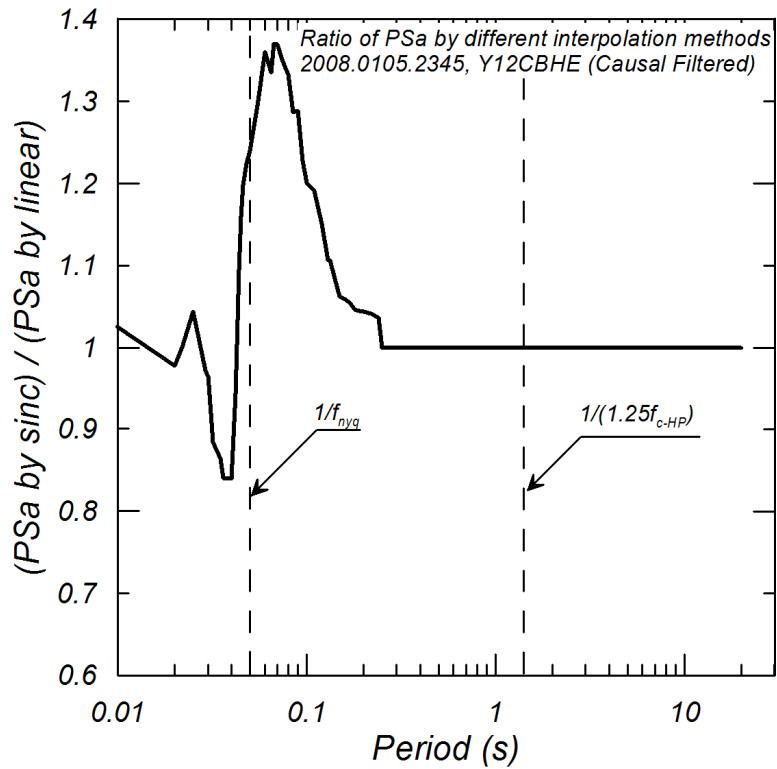
Figure 2.13   Ratio of PSA for example records with different interpolation methods.

2.3.5 Verification of Data Processing

Several routines were added to the standard PEER NGA *R* processing code to process the Arizona time series data recorded by the TA array for this study. For example, the filtering of velocity spectra and the conversion from velocity to acceleration time series in the frequency domain had not been performed in the *R* code during the NGA-West2 project. Therefore, to verify these newly added processing steps, we performed an independent analysis and compared the resulting PSA to each other. Pacific Engineering & Analysis (PE&A) performed an analysis starting from the downloaded ASCII file from IRIS. Figures 2.14 and 2.15 compare plots of the PSA obtained from the PEER processing code (*R* and Fortran) and the PE&A Fortran code, and the ratio of the PSA (5% damped) between these calculations, respectively. These figures show that the resulting PSA are consistent within a couple of percent, which verifies that the data-processing methods for time series and PSA were correctly implemented in this study.

There are also three co-located records between NGA-West2 and Arizona dataset at NEE2 on standard CI instrumentation and TA recorders. Comparisons were also performed for these recordings to verify the data-processing methodology of this study. Figure 2.16 shows an example comparison of the 5% damped PSA from the 2010 El Mayor-Cucapah earthquake. The record in NGA-West2 database was measured on a broadband acceleration instrument with the Nyquist frequency of 50 Hz, whereas that in the Arizona database was measured by TA array with a Nyquist of 20 Hz. On the basis of the excellent agreement demonstrated in Figure 2.16 and two others, it is verified that the data-processing methods for time series and PSA were correctly implemented in this study.
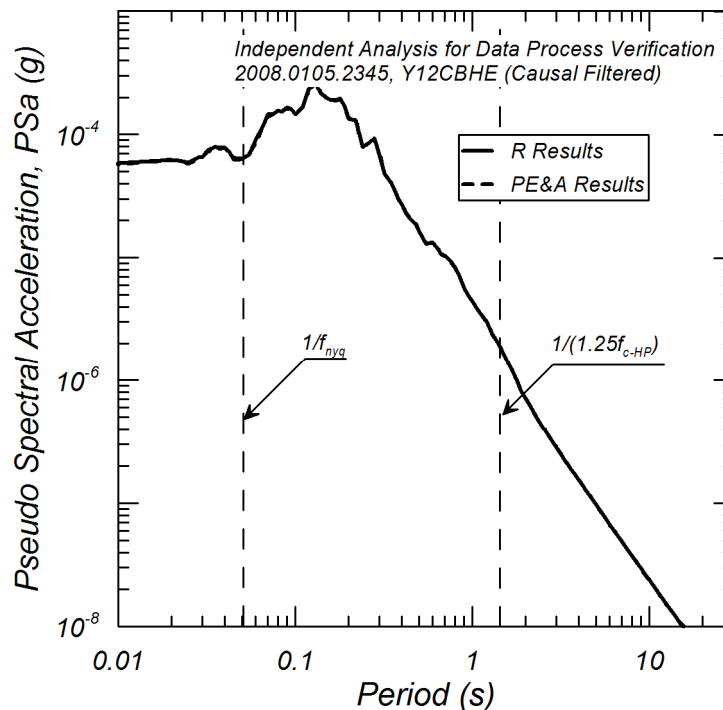
Figure 2.14 **Comparison of PSA for the example recording from *R* and PE&A data processing.**
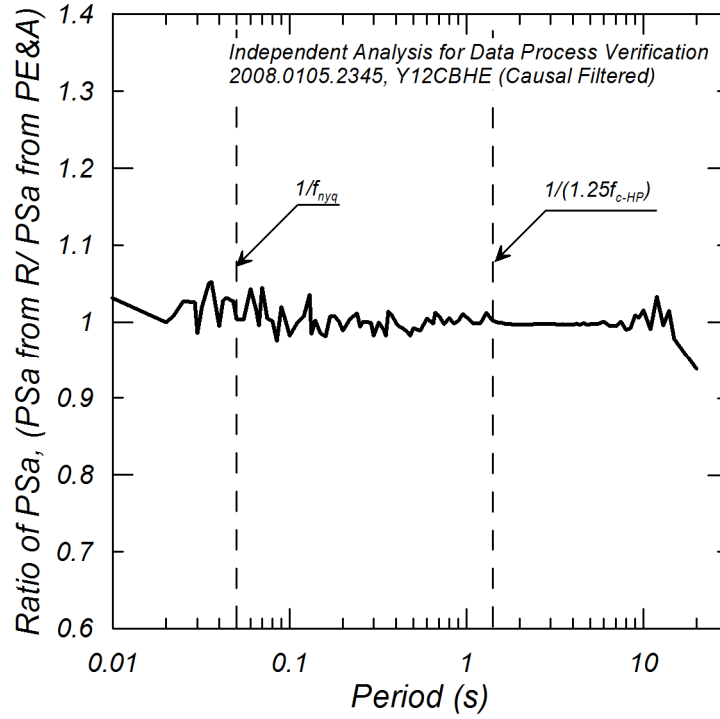
Figure 2.15 Ratio of PSA for the example recording between *R* and PE&A data processing.
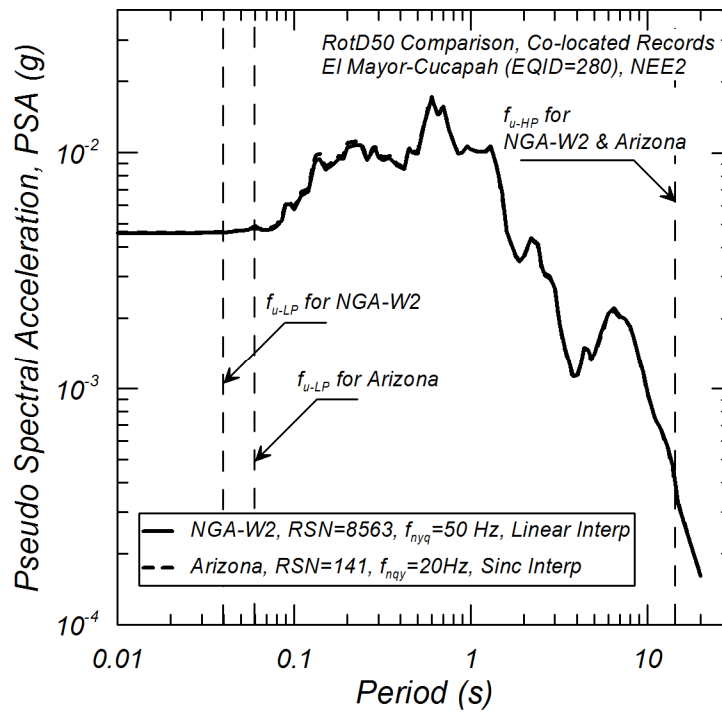
Figure 2.16 PSA comparison for co-located records at Station NEE2 between NGA-West2 and Arizona database.

2.3.6　Usable Frequencies for Processed Data

Several intensity measures were calculated during data processing: the three-component as-recorded PSA, RotDnn, Arias intensity, and related durations. Pseudo spectral accelerations were calculated at 111 periods ranging from 0.01 to 20 sec and for 11 different damping ratios ranging from 0.5 to 30%. These results are tabulated into a spreadsheet (xls file) and named "Arizona Flatfile.xls" on the PEER website. Figure 2.17 shows the HP- and LP-filter corner frequencies (f_{c-HP}, f_{c-LP}, respectively) selected during data processing. It shows that the f_{c-HP} becomes lower as magnitude increases because low-frequency signal amplitude generally increases as magnitude increases relative to noise from microseisms and other sources. It also shows that the f_{c-HP} becomes lower significantly as **M** becomes greater than 4.0 because some recordings have larger amplitudes at low frequency compared to peak values from microseisms, which allow low frequencies extending into and beyond the period range of microseisms (around 3–7 sec). Figure 2.18 shows the number of available recordings as a function of highest usable period. It shows that the number of usable recordings starts to decrease at the period greater than 0.3 sec for Arizona events, but does not decrease until about a period of 2 sec for the larger events in the NGA-West2 database. Finally, the maximum f_{c-LP} is equal to 16 Hz, i.e., 80% of the Nyquist frequency, which is given by the anti-alias filter of the TA data (see also Figure 2.8).
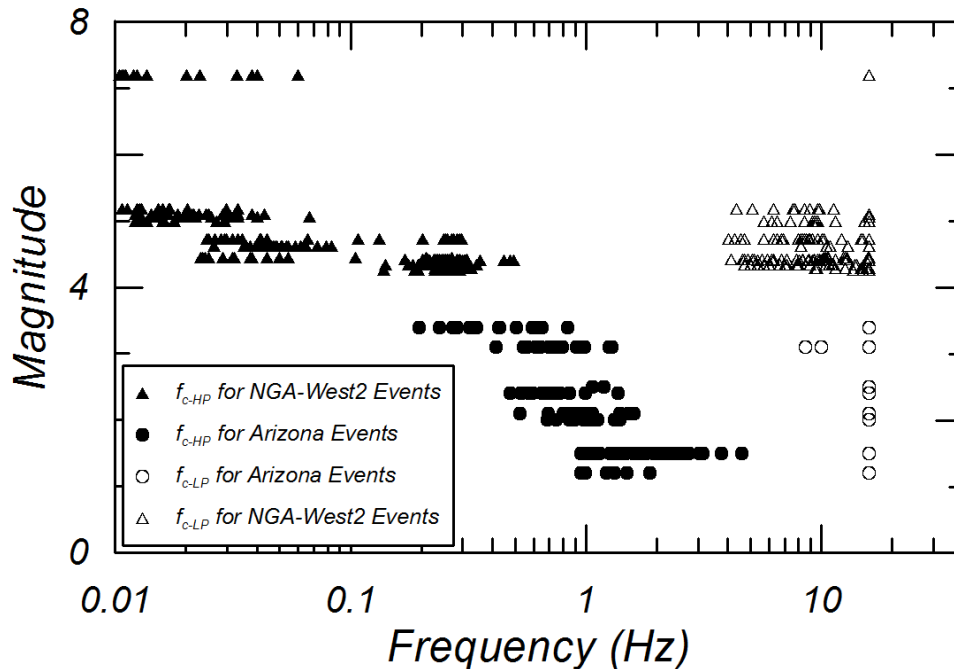
Figure 2.17　　Variation in HP and LP corner frequencies with magnitude.
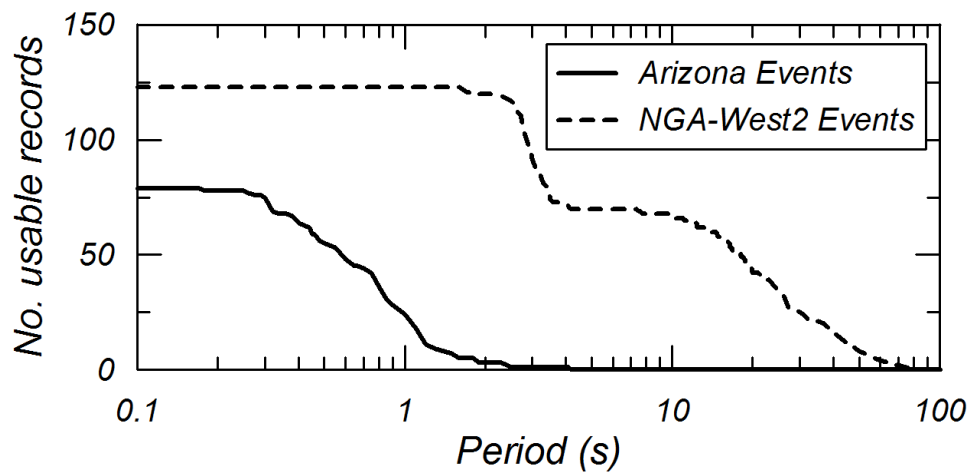
Figure 2.18 **Comparison of number of records with a highest useable period versus period.**

3   Seismic Velocity Site Characterization of Ten Arizona Strong-Motion Recording Stations by Spectral Analysis of Surface Wave Dispersion

3.1   ABSTRACT

Vertical one-dimensional shear-wave velocity (V_S) profiles are presented for strong-motion sites in Arizona for a suite of stations surrounding the PVNGS. The purpose of the study is to determine the detailed site velocity profile, the average velocity in the upper 30 m of the profile ($V_{S,30}$), the average velocity for the entire profile ($V_{S,Z}$), and the NEHRP site classification. The V_S profiles are estimated using a non-invasive continuous-sine wave method for gathering the dispersion characteristics of surface waves. Shear-wave velocity profiles were inverted from the averaged dispersion curves using three independent methods for comparison, and the root-mean square combined coefficient of variation (COV) of the dispersion- and inversion-calculations were estimated for each site.

3.2   INTRODUCTION

This project focuses on the measurement of shear-wave velocity (V_S) of the near-surface materials at strong-motion recording stations in Arizona. During two data collection campaigns, data were collected at ten stations with recordings from prior earthquakes. These stations were regionally instrumented with permanent seismometer recording stations, some now moved or abandoned. The V_S profiles presented in this report are collected for input to GMPEs, factoring in the effects of site amplification. Data presented here were gathered using the continuous harmonic sine wave approach for the SASW presented by Kayen et al. [2004; 2013], which is a stepped-sine wave method that utilizes a notch-filter methodology that improves on the approach of Satoh et al. [1991]. The CSS-SASW is an inexpensive and efficient means of non-invasively estimating the near-surface V_S of the ground. Though it is possible to measure V_S in cased boreholes or during penetration tests, these approaches tend not to be useful as they cannot reach the meaningful depths required for seismic site response analysis without expensive drilling and casing. Because many of the Arizona sites are stiff soil profiles or weathered bedrock profiles, penetration methods are not useful.

3.3   ARIZONA STUDY SITES

The V_S profiles presented here are for strong-motion seismometer stations whose records are identified in the database of PEER and the Southwestern U.S. Ground Motion Characterization SSHAC Level 3 Project (SWUS). The sites surround the PVNGS in central Arizona (see Table 3.1 and Figure 3.1) to a range of approximately 100 miles.
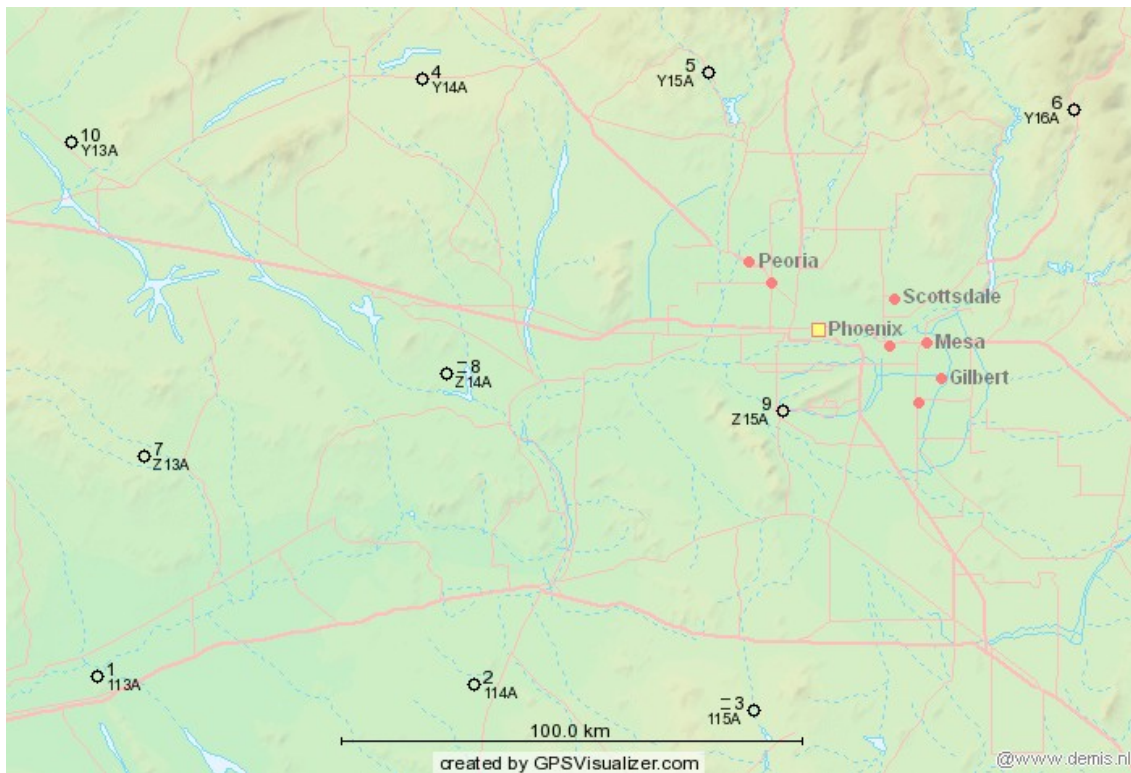
Figure 3.1   Surface wave test locations of 10 sites in central and southern Arizona.

Table 3.1 Sites investigated in this study. The table includes the SWUS site ID, USGS test ID, NEHRP site class, latitude, longitude, V_{s30} from the automated inversion, $V_{S,30}$ from the manual Inversion, $V_{S,30}$ from the Occam Inversion, the maximum depth (m) of the inversion, the average $V_{S,z}$ for the entire profile depth from the automated inversion, the average $V_{S,z}$ for the manual Inversion, the average $V_{S,z}$ for the Occam Inversion, the average COV of the group dispersion profile, the average COV of the inversion, and the combined joint-COV.

Site ID	Z14A	115A	Y16A	Y15A	Z15A	113A	Y14A Stigler ranch	Y13A-2 Plog Ranch	114A Gila Bend	Z13A
USGS Test ID	994 Z14A PV NPP	995 115A Sonora Natl Mon	997 Y16A Beeline Rd.	998 Y15A Lake Pleasant	999 Z15A Komtake	1000AZ 113a	1001AZ	1002AZ	1003AZ	1004AZ Z13a
NEHRP CLASS:	C	C	B	C	C	B	C	C	C	C
Latitude (°)	33.3627	32.7006	33.8798	33.9535	33.2893	32.7683	33.9383	33.816246	32.7513	33.1999
Longitude (°)	-112.9458	-112.2279	-111.4783	-112.3331	-112.1581	-113.7667	-113.0048	-113.8292	-112.8830	-113.6568
$V_{S,30}$ automated inversion	524	460	1028	566	407	1237	520	560	398	689
$V_{S,30}$ manual Inversion	508	443	988	545	464	1232	526	559	404	670
$V_{S,30}$ Occam Inversion	490	424	970	499	373	1140	473	532	380	652
MAX Inversion Depth(m)	108	99	40	40	39	38	50	50	50	50
V_S-MAX automated inversion	522	528	1102	583	434	1599	576	611	424	778
V_S-MAX manual Inversion	689	541	1071	570	431	1385	586	608	445	763
V_S-MAX Occam Inversion	749	473	1023	476	437	1140	572	640	438	740
Dispersion ave. COV	0.035	0.027	0.072	0.041	0.035	0.106	0.074	0.033	0.059	0.043
Inversion ave. COV	0.025	0.019	0.109	0.095	0.042	0.200	0.021	0.021	0.024	0.019
Combined COV	0.043	0.033	0.131	0.103	0.055	0.226	0.077	0.039	0.064	0.047

3.4   RAYLEIGH WAVE DISPERSION

Active-source surface wave analysis testing typically profiles the upper tens of meters of the ground using drop weights or harmonic sources. The upper 30 m is needed to compute the widely used site parameter $V_{S,30}$, defined as 30 m divided by the shear-wave travel time to 30 m depth. The SASW method employed in this study by the USGS uses a parallel array of mass shakers, which allows for profiling to depths up to 100 m without the use of massive drop weights or heavy track-mounted machinery. For this method, we substitute an array of many low frequencies in the 100–1 Hz range with electro-mechanical shakers. Surface waves are generated with an array of up to several APS Dynamics Model 400 shakers and amplifier units, powered by a generator and controlled by a spectral analyzer.

The shakers have a long-stroke capable of cycling to as low as 1 Hz. The output signal from the spectral analyzer is split into a parallel circuit and sent to the separate amplifiers. The amplifiers power the shakers to produce a continuously vibrating, coherent, in-phase harmonic-wave that vertically loads the ground. Most of this energy produces Rayleigh retrograde elliptical surface waves that propagate away from the source in a vertical cylindrical wavefront perpendicular to the ground surface. The amplitude of the surface waves decay exponentially with depth, such that the energy of the wavefront is centered at a depth of approximately 1/3 to 1/2 the wavelength.

Frequency domain analyses are made on two or more signals received by sensors placed in the field in the linear array some distance from the source. First, all channels of time domain data are transformed into their equivalent linear spectrum in the frequency domain using a Fourier transform. One of the sensor's signals (typically the sensor closest to the source) is used for a reference input signal, and the other sensor signals are used to compute the linear spectrums of the output. The separation of the reference seismometer and output seismometer $\left(d_s - d_{ref} \right)$ radially from the source is later used to compute the wave velocity. The cross power spectrum $G_{xy}(\omega)$ is determined by multiplying the complex conjugate of the linear spectrum of the input signal $S_x^*(\omega)$, and the real portion of the linear spectrum of the output signal $S_y(\omega)$. The cross power spectrum is defined as

$$G_{xy}(\omega) = S_x^*(\omega) * S_y(\omega) \tag{3.1}$$

The autopower spectrum, which is a measure of the energy at each frequency of the sweep, can be used to determine the strength of individual frequencies, and is equal to the linear spectrum of a given sensor times its complex conjugate pair:

$$G_{xx}(\omega) = S_x(\omega) * S_x^*(\omega) \tag{3.2}$$

and

$$G_{yy}(\omega) = S_y(\omega) * S_y^*(\omega) \tag{3.3}$$

A cross-power spectrum can be represented by its real and imaginary components by its phase θ and magnitude m. The phase θ is the relative lag between the signals at each frequency, and the magnitude is a measure of the power between the two signals at each frequency. Because the phases are relative, they can be stacked to enhance the SNR of the phase lag at each frequency.

The phase of the cross-power spectrum is computed as the inverse tangent of the ratio of the imaginary and real portions of the cross-power spectrum:

$$\theta_{xy}(\omega) = \tan^{-1} \frac{\text{Im}\left[G_{xy}(\omega)\right]}{\text{Re}\left[G_{xy}(\omega)\right]} \tag{3.4}$$

The travel time $t(f)$ of one cycle of a wave of frequency (f) is computed as

$$t(f) = \theta(\omega)/\omega \tag{3.5}$$

and the wavelength, λ, at each frequency is

$$\lambda(\theta) = \left(d_s - d_{ref}\right)/\theta(f) \tag{3.6}$$

The Rayleigh wave velocity, V_r, is computed as

$$\begin{aligned} V_r(f) &= \left(d_s - d_{ref}\right)/t(f) \\ &= f \bullet \left(d_s - d_{ref}\right)360°/\theta \text{ (degrees)} \\ &= f \bullet \left(d_s - d_{ref}\right)2\pi/\theta(\phi) \text{ (radians)} \\ &= f \bullet \lambda(f) \end{aligned} \tag{3.7}$$

The SASW procedure maps the change in θ across the frequency spectrum, and merges these phase lags with the sensor array geometry to measure velocity. Typically with the shaker source, the discrete frequencies are cycled in a swept- (stepped-) sine fashion across a range of low frequencies (1–200 Hz). Rayleigh-wave phase velocity is then mapped in frequency or wavelength space. This velocity map or profile is called a dispersion curve and characterizes changes in the frequency-dependent Rayleigh wave velocity. The evaluation of velocities is constrained to the wavelength zone where $\lambda(f)/3 < (d_s-d_{ref}) < 2\,\lambda(f)$ for typical data and $\lambda(f)/3 < (d_s-d_{ref}) < 3\lambda(f)$ for excellent data, corresponding to phase lags of 180°–1080° (typical data) and 120°–1080° (excellent data). At longer and shorter wavelengths the data become unreliable for computing velocities.

As the useable wavelengths are constrained by the seismometer separation, the array is expanded to capture Rayleigh wave dispersion representative of a specific range of wavelengths. The near surface is characterized by short wavelengths and high frequencies, whereas the deeper portion of the profile is characterized by long wavelengths and low frequencies. Each wavelength range requires a separate independent test that is merged together with other wavelength ranges to determine an average dispersion curve for the site.

At the largest seismometer separations, the increasing area of the wave front causes the wave amplitude to diminish due to geometric damping, and the overall quality of the data diminishes. Two

measures of data quality are used to evaluate the field measurements in the frequency domain. Coherence, $\gamma^2(\omega)$, is a normalized real function with values between 0 and 1 corresponding to the ratio of the power of the cross-power spectrum, $G_{yx}(\omega) \bullet G_{yx}^*(\omega)$, to the auto-power spectrum of the outboard seismometer, $G_{xx}(\omega) \bullet G_{yy}(\omega)$. Values close to 1 indicate high correlation between the reference and outboard seismometers across narrow frequency bands. This is a useful data quality parameter for hammer impact data.

$$\gamma_{xy}^2(\omega) = \frac{G_{yx}(\omega) \bullet G_{yx}^*(\omega)}{G_{xx}(\omega) \bullet G_{yy}(\omega)} \qquad (3.8)$$

For swept-sine data, where discrete frequencies are used to compute phase rather than narrow frequency bands, the frequency response function, *FRF*, is a complex measure of the data quality of the output (outboard) seismometer, and is sometimes called the transfer function:

$$FRF(\omega) = \frac{G_{yx}(\omega)}{G_{xx}(\omega)} \qquad (3.9)$$

where *x* is the input (reference) signal, and *y* is the response (output) signal. The FRF is a two-sided complex parameter. To convert to the frequency response gain (magnitude) that is used to evaluate the amplitude of the output response to the input stimulus, a rectangular-to-polar coordinate conversion is used.

3.4.1 Adjustments for Missing 1st Wrapped Phase

At some sensor separations the field data have a poorly formed 1st phase such that the first clear wrapped phase crossing occurs not at 180° but at 540°. For these dispersion data files, a simple reprocessing was done to add one phase jump (360°, 2π) to the dispersion curves preceding the 540° jump to adjust the file to the correct wrapped phase number. This adjustment corrects the wavelength calculation as follows:

$$\lambda_{(corrected)} = 2\pi d / (\theta + 2\pi) \qquad (3.10)$$

With the wavelength adjusted, the velocity, V_r, decreases by

$$V_r = f \bullet 2\pi d / (\theta + 2\pi) \qquad (3.11)$$

The effect of correcting the phase wrap and reducing the calculated wavelength is to reduce the depth of influence of the adjusted dispersion curve.

3.5   INVERSION OF THE V_S PROFILE

The relation between Rayleigh wave (V_R), shear wave (V_S), and compression wave (V_P) velocities can be formulated through Navier's equations for dynamic equilibrium. On the surface of the ground, and in the case of plane strain, the following characteristic equation applies:

$$\frac{V_r^6}{V_s} - 8\frac{V_r^4}{V_s} + \left\{24 - 16\left[\frac{1-2v}{2(1-v)}\right]\right\}\frac{V_r^2}{V_s} + 16\left\{\left[\frac{1-2v}{2(1-v)}\right] - 1\right\} = 0 \qquad (3.12)$$

where v is Poisson's ratio and

$$\frac{V_S}{V_P} = \gamma = \sqrt{\left[\frac{1-2v}{2(1-v)}\right]} \qquad (3.13)$$

For reasonable values of Poisson's ratio for earth materials, which are between 0.30 and 0.49, Viktorov [1967] shows that the shear-wave velocity ranges between 105–115% of the measured Rayleigh wave velocity.

$$\frac{V_R}{V_S} = K = \frac{0.87 + 1.12v}{1+v} \qquad (3.14)$$

such that across the range $0.2 < v < 0.49$, the range of K is $0.87 < K < 0.96$.

The inversion method seeks to infer an acceptable best-fit *model* of seismic shear-wave velocity, V_S, of the ground given the *measured* dispersive characteristics of Rayleigh waves observed in the frequency domain, and the estimated profile of Poisson's ratio and material density. The inversion attempts to build a model from observations as opposed to the normal prediction of behavior based upon a model. If the inversion model is simple and linear, it will result in a unique and stable solution. French mathematician Hadamard defined mathematical problems that have solutions that exist, are unique, and are stable as "well-posed" [Zhdanov 2002]. However, surface wave inversion is an "ill-posed" inverse problem as the solutions are not unique; therefore, the solutions may become unstable, and multiple shear way velocity profiles can result in approximately the same dispersion curve [Zhdanov 2002].

The dispersive characteristic of Rayleigh wave propagation allows us to infer the V_S at depth based on measurements at the free surface. The inversion problem computes the Rayleigh wave phase velocity (V_R) from laterally constant layers of an infinite half space. For each of these layers the shear modulus, Poisson's ratio, density, and thickness are unknown. Displacements for a vertically acting harmonic point load can be computed in the far field if we neglect body wave components, thus:

$$u_\beta(r,z,\omega) = F_z \cdot G_\beta \cdot (r,z,\omega) \cdot e^{i[\omega t - \psi_\beta(r,z,\omega)]} \qquad (3.15)$$

where β stands for the generic component either vertical or radial, $G_\beta(\rho,\zeta,\omega)$ is the Rayleigh geometrical spreading function, and $\psi_\beta(\rho,\zeta,\omega)$ is the composite phase function [Lai and Rix 1998].

Regularization methods have been developed for solving the ill-posed inversion problem, e.g., the velocity profiles computed here. The Levenberg-Marquardt method, also called damped least squares, is one example of a regularization method. These and other techniques, such as artificial neural networks and genetic algorithms, are discussed by Santamarina and Fratta [1998].

One drawback of these stochastic methods is that they often require many more iterations, and so they are much more computationally intensive.

The parameters of the inversion problem can be chosen such that the difference between the observational dispersion data and the output of the inversion problem are minimized. Such a constraint is insufficient for ill-posed problems because many solutions can fit the data equally well, and some of these solutions will be physically unrealistic. The most common approach is to constrain the inversion solution space by selecting the smoothest solution from a suite of solutions that all exhibit a sufficient goodness-of-fit to the observed data, as indicated by a root mean square (RMS) error minimum.

An empirical approach serves as a counterpoint to the inversion methods used in this report. Pelekis and Athanosopoulos [2011] advanced the work of Satoh et al. [1991] in a technique termed the simplified inversion method (SIM) that computes the shear-wave velocity profile as a function of the incremental slope of the Rayleigh wave dispersion curve where:

$$V_{Sn,normal\ dispersion} = 1.1 \cdot \frac{\bar{V}_{Rn}D_n - \bar{V}_{Rn-1}D_{n-1}}{D_n - D_{n-1}} \tag{3.16}$$

$$V_{Sn,inverted\ dispersion} = 1.1 \cdot \frac{D_n - D_{n-1}}{D_n/\bar{V}_{Rn} - D_{n-1}/\bar{V}_{Rn-1}} \tag{3.17}$$

The dispersion curve V_R plotted against λ_R is converted into an apparent velocity $\left(\bar{V}_R\right)$ and depth (z) by converting λ_R to an estimated depth of $z_{eq} = a_R \cdot \lambda_R \approx 0.635\lambda_R$. The parameter a_R is a penetration depth coefficient optimized to achieve a minimum weighted average difference between the simplified velocity profile and that computed through the more advanced inversion of Pelekis and Athanosopoulos [2011]. The apparent phase velocity, $\bar{V}_R$, is approximated as the velocity at each segment node (layer interface) of a multi-linear curve fit to the dispersion curve. A positive slope of a segment indicates normal dispersion; a negative slope indicates inverted dispersion. The value of V_S for each individual layer is calculated using the equations above for the cases of normal dispersion or inverted dispersion, respectively. The approach of Pelekis and Athanosopoulos [2011] improves on the Satoh et al. [1991] method notably by optimizing the penetration depth coefficient a_R.

3.6   RESULTS

We provide two profile solutions at each site (Inversion and SIM model). We varied the assumptions about the layer thicknesses and the threshold RMS error that determines if the inversion has converged to best characterize the site. The decision is subjective as to whether or not the more complex model is warranted by the fit of the theoretical dispersion curve (TDC) to the empirical dispersion curve (EDC). Table 3.1 summarizes results and provides the SASW site ID, the site description, the date of data collection, the latitude and longitude of the SASW test site, and the $V_{S,30}$. Section 3.7 includes plots of the model profiles and the EDC and TDC's for each site. Section

3.7 also includes the site photos and a vicinity map for each site. Where possible we have indicated the location of the strong-motion station in the site photographs and vicinity maps to assess the distance between the SASW survey and the strong-motion station. The NEHRP classification is used to average the site conditions in the upper-30 m of ground ($V_{S,30}$ from the IBC [ICC 2002]). Equation (3.18) is used to compute this average velocity based on the unit layer thickness (d_i) and the corresponding interval-velocity (V_{Si}).

$$V_{S-depth-averaged} = \frac{\sum_{i=1}^{n} d_i}{\sum_{i=1}^{n} \frac{d_i}{V_{Si}}} \qquad (3.18)$$

These site categories are used to assign design spectra in the evaluation of performance for new and built structures.

A statistical analysis of the shear-wave velocity of the upper 30 m was computed by determining the average coefficient of variation (COV_{DIS}) of the dispersion curve from the group phase velocity, and the average coefficient of variation (COV_{INV}) of shear-wave velocity profiles computed in the inversions that satisfied the minimum acceptable inversion model variance.

The mean values of the group dispersion curves were calculated by binning the dispersion curve values in terms of wavelength (e.g., in 1-m bins), or frequency (e.g., 1-Hz bins), and then averaging the values within each bin. The coefficient of variation was calculated by dividing the binned-standard deviation of the velocity values by the binned-mean values. The mean and standard deviation of the shear-wave velocity layers of the inversion were calculated by averaging the layer values for the suite of profiles that satisfy the lowest possible root-mean square error separating the theoretical inversion-based and empirical field-dispersion curves.

For both the dispersion curve and the inversion-based coefficients of variation, the average COV was determined for the profiles. The overall model coefficient of variation was computed as the root-mean-square of the dispersion COV and the inversion COV [Equation (3.19)].

$$COV_{MODEL} = \sqrt{COV_{DIS}^2 + COV_{INV}^2} \qquad (3.19)$$

For deep, stiff soil sites the combined dispersion and inversion COV was typically less than 0.07, reflecting the remarkably good dispersion datasets and the gentle monotonic increasing nature of the velocity profiles. For sites situated on rock, the combined COV ranges from 0.12–0.23, reflecting greater variance in the field dispersion data and the inverted profiles.

3.7 SITE DATA

The following section presents the individual site location photographs, location map, field and computed velocity data, dispersion curves, and inversion profiles. *Vs* values for 30 m and the maximum profile depth are presented for the three inversion methods as well as the coefficient of variation of these parameters.
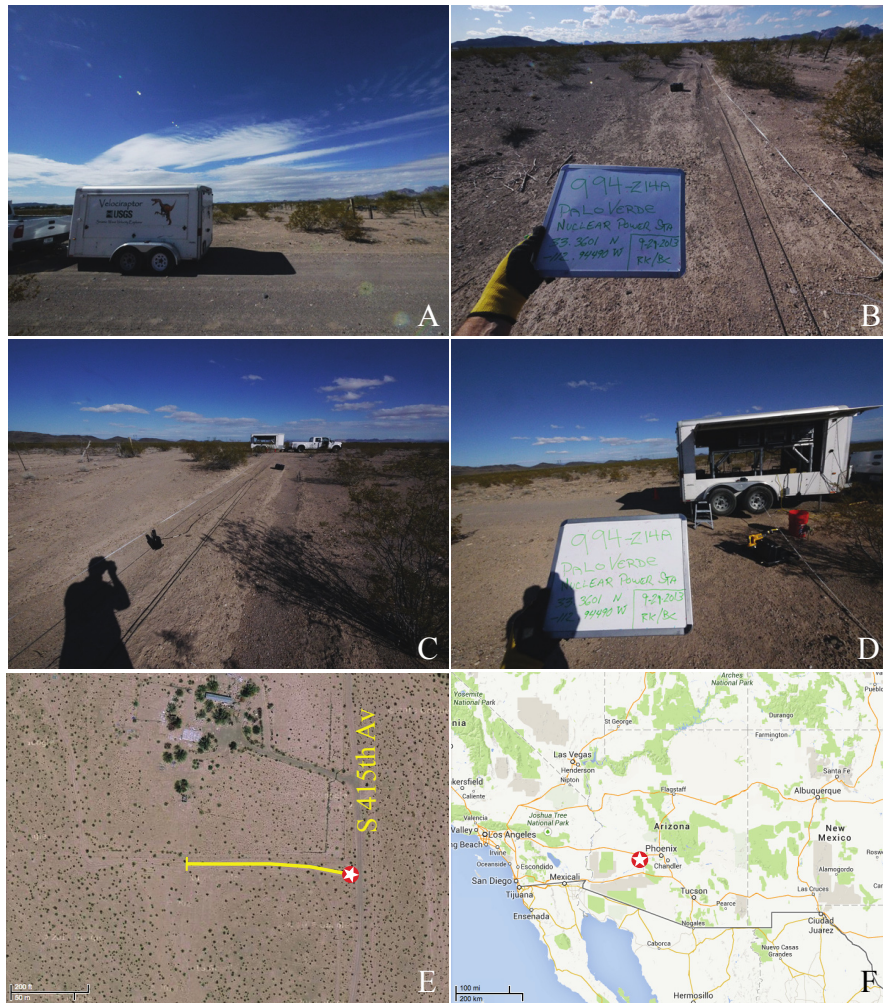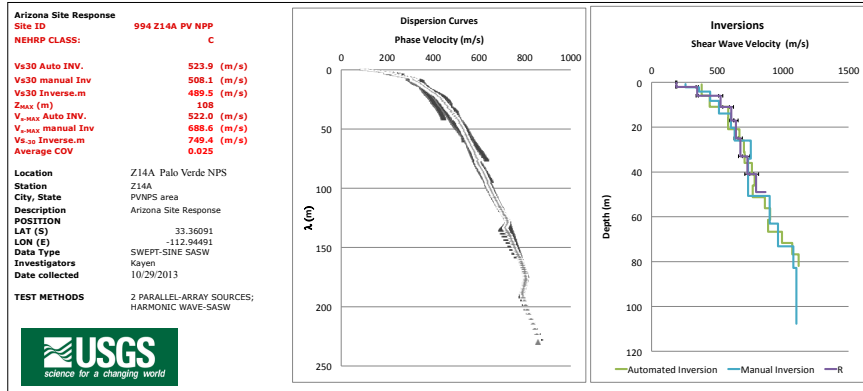
Figure 3.2   Station Z14A: (a) shear-wave velocity profile and (b) surface-wave test site 994-Z14A located (33.3601, -112.94490) on South 415th Av., 8 km SW of the Palo Verde Nuclear Generating Station, Arizona. The test site is located about 200 m S-SE of the US Array seismometer location (33.36275, -112.94577). (A) View towards the west from the shaker trailer; (B) Another view to the west along the seismometer array; (C) View to the east to the shaker trailer; (D) Another view to the east; (E) satellite view of the local site, yellow bar is seismometer array; and (F) site location in Arizona.
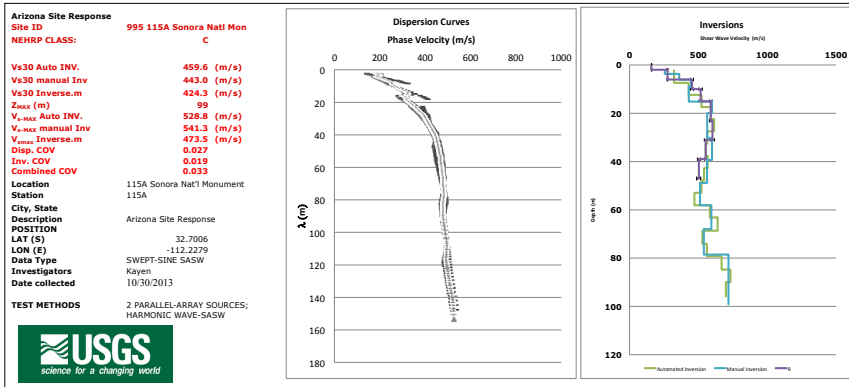
Figure 3.3 **Station 115A: (a) shear-wave velocity profile and (b) surface-wave test site 995-115A located (lat 32.70885, long -112.23207) adjacent to Vekol Valley Road in the Sonoran Desert National Monument, 15 km south of Interstate 8, Arizona. The test site is about 1 km N-NW of the location of the US Array seismometer (lat. 32.7006, long. -112.2279). (A) view looking eastward to the shaker trailer; (B) view westward along the seismometer array; (C) another view eastward to the shaker trailer; (D) sign on Vekol Valley Road near Interstate 8; (E) satellite view of the local site, yellow bar is seismometer array; and (F) site location in Arizona.**
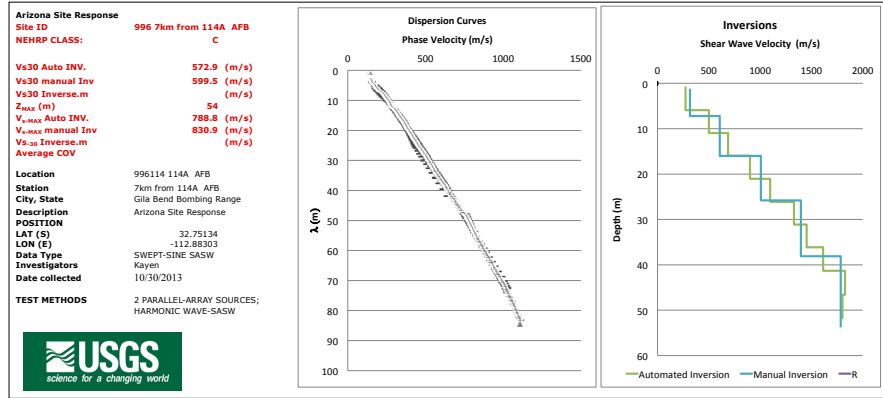
Figure 3.4 **Station 114A: (a) shear-wave velocity profile and (b) surface-wave test site 996-114A located (lat 32.82366, long -112.91518) on the U.S. Air Force Barry M. Goldwater Gunnery Range, Arizona. The test site is located 8.7 km N-NW of the US Array seismometer installation (32.75134, -112.88303). (A) view northward to the shaker trailer, the seismometer array extends to the left; (B) View to the SE across the seismometer array; (C) View SW to the shaker trailer; (D) another view to the SE to the shaker trailer; (E) satellite view of the local site, yellow bar is seismometer array; and (F) site location in Arizona.**
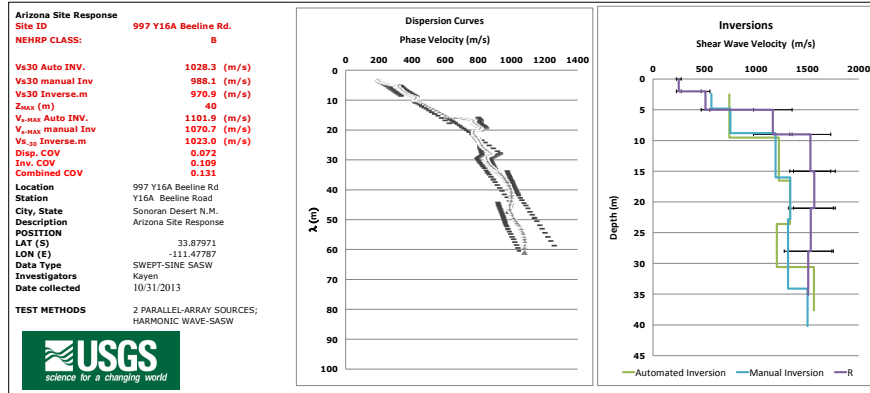
Figure 3.5 **Station Y16A: (a) shear-wave velocity profile and (b) surface wave test site 997-Y16A located (lat 33.87971, long -111.47787) near N. Beeline Highway, about 1.7 km from Highway 87 and about 70 km NE of Phoenix, Arizona. (A) view to the west to the shaker trailer; (B) view to the east to the shaker trailer; (C) view west along the seismometer array; (D) view to the east from the shaker trailer; (E) satellite view of the local site, yellow bar is seismometer array, the yellow star is the US Array seismometer location, Beeline Highway is at the upper right; and (F) site location in Arizona.**
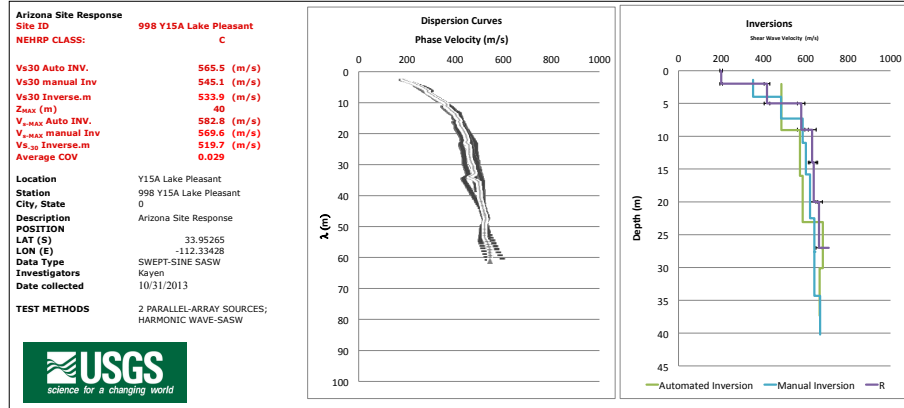
Figure 3.6   Station Y15A: (a) shear-wave velocity profile and (b) surface-wave test site 998-Y15A located (lat 33.95265, long -112.33428 W) on N. Castle Hot Springs Road, NW of Lake Pleasant, Arizona. (A) view to the SW to the shaker trailer; (B) another view to the SW along the seismometer array; (C) view NE on the seismometer array; (D) US Array seismometer; (E) satellite view of the local site, yellow bar is seismometer array, the yellow star is the US Array seismometer location; and (F) site location in Arizona.
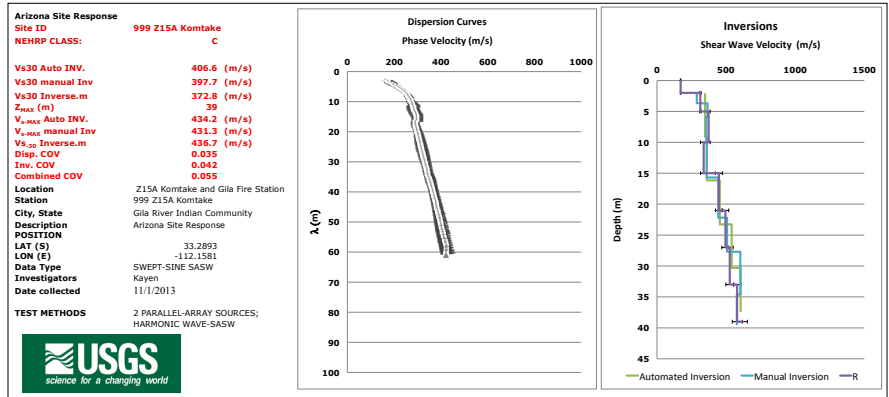
Figure 3.7 Station Z15A: (a) shear-wave velocity profile and (b) surface-wave test site 999-Z15A located (lat 33.2893, long -112.1581) in District 6 (Komatke), Gila River Indian Community, Arizona. (A) view looking westward to the seismometer array location (dashed yellow line); (B) view west to the shaker trailer parked on S. Health Care Drive; (C) view NE to the shaker trailer; (D) view SW to the shaker trailer; (E) satellite view of the local site, yellow bar is seismometer array, the yellow star is the location of the US Array seismometer; and (F) site location in Arizona.
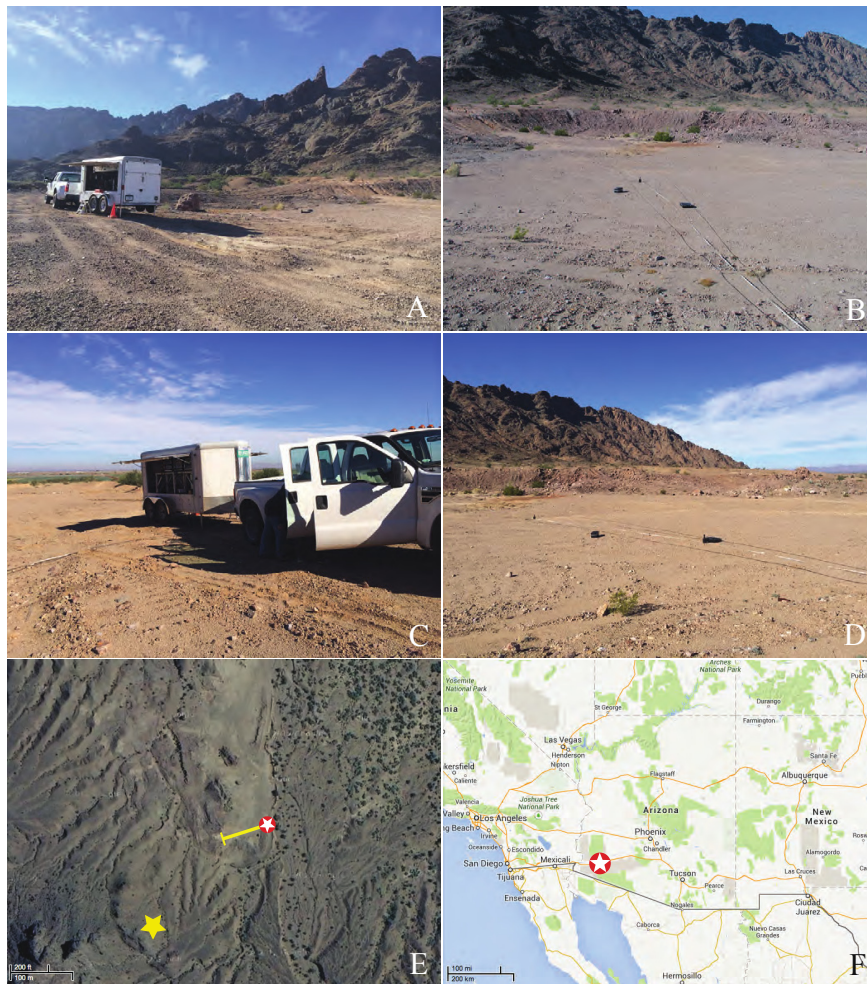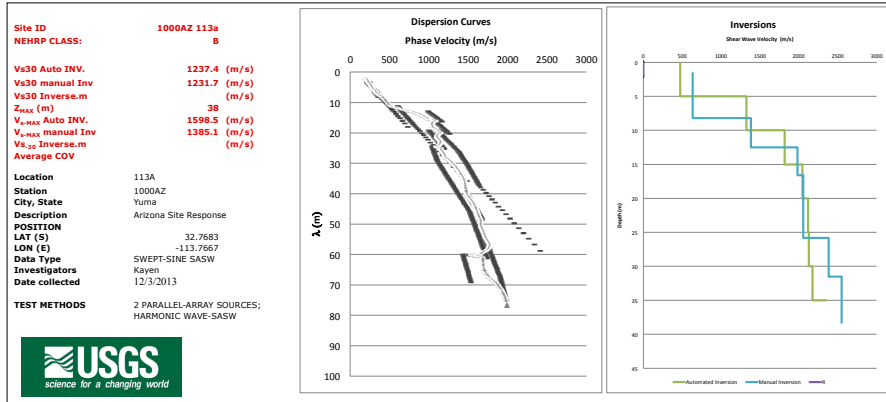
Figure 3.8   Station 113A: (a) shear-wave velocity profile and (b) surface-wave test site 1000AZ-113A located (lat 32.76984, long -113.76493) 76 km east of Yuma, Arizona. (A) view to the SW to the shaker trailer; (B) view westward to the seismometer array; (C) view NE to the shaker trailer; (D) view NW to the seismometer array; (E) satellite view of the local site, yellow bar is seismometer array, the yellow star is the location of the US Array seismometer; and (F) site location in Arizona.
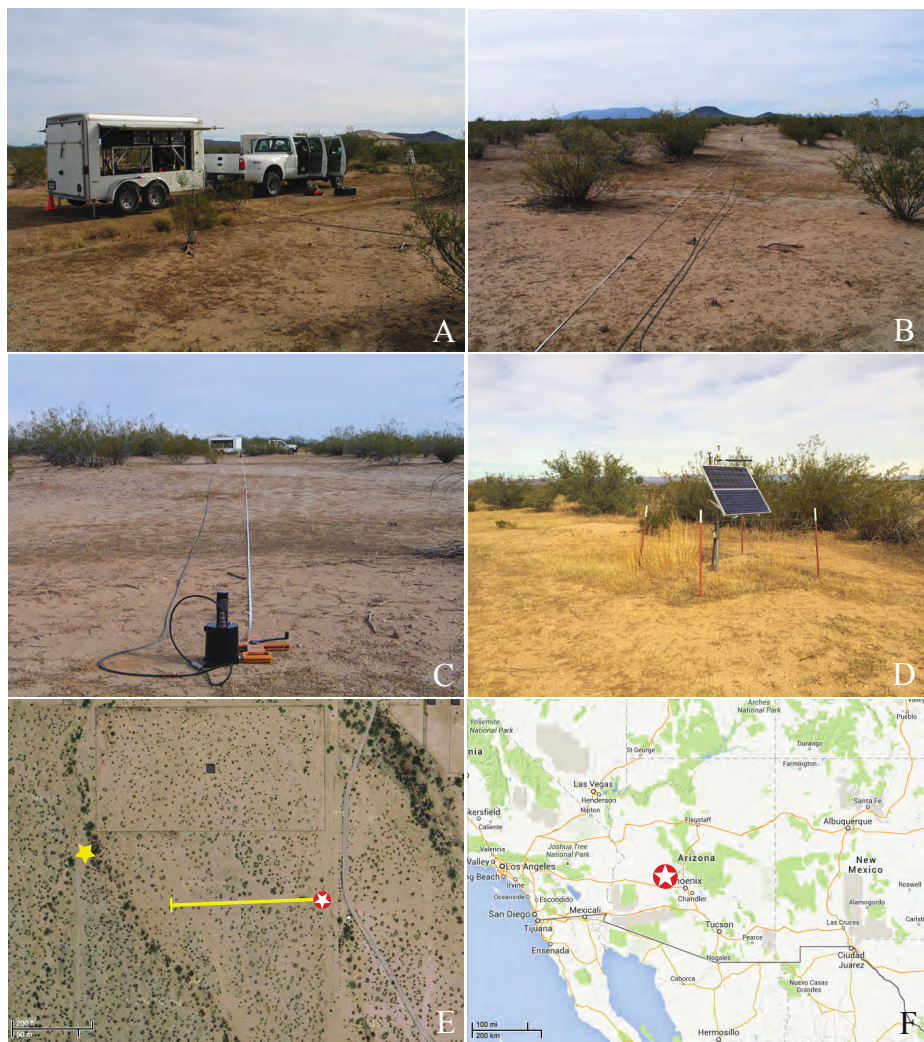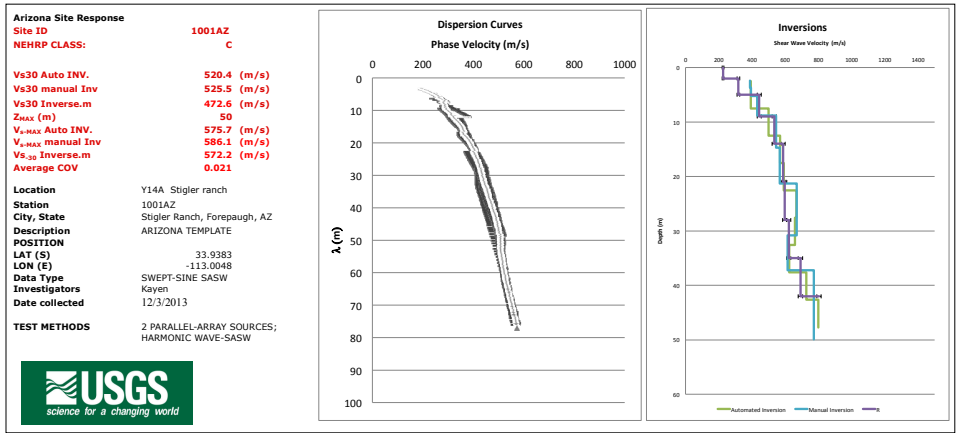
Figure 3.9 Station Y14A: (a) shear-wave velocity profile and (b) surface-wave test site 1001AZ-Y14A located (lat 33.93792, long -113.00282) 25 km west of Wickenburg, Arizona. (A) view to the SE to the shaker trailer; (B) view west to the seismometer array; (C) view east to the shaker trailer; (D) view NE to the US Array seismometer location; (E) satellite view of the local site, yellow bar is seismometer array, yellow star is the US Array seismometer location; and (F) site location in Arizona.
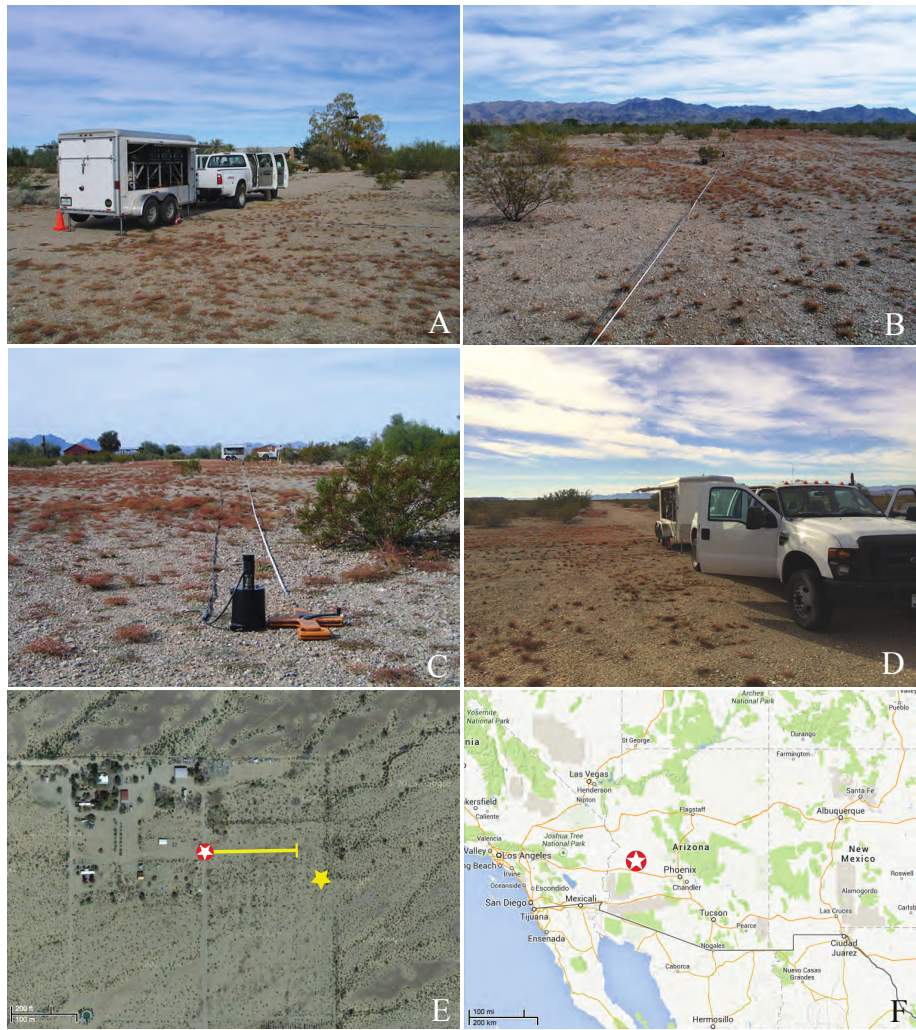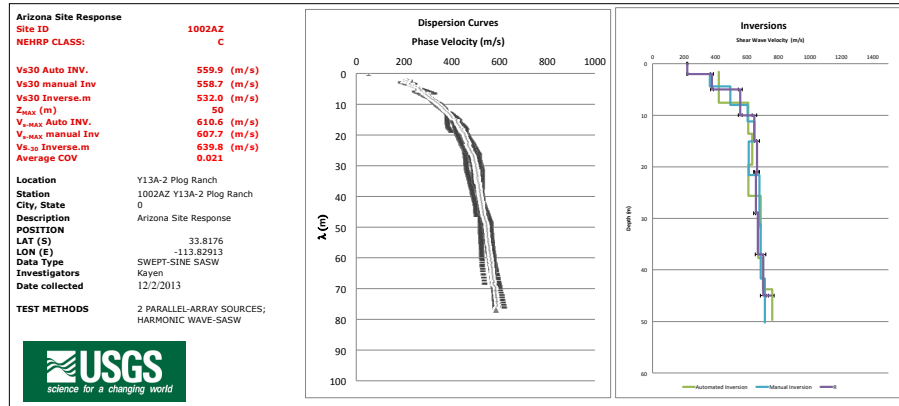
Figure 3.10 Station Y13A: (a) shear-wave velocity profile and (b) surface-wave test site 1002-Y13A-2 located (lat 33.8176, long -113.82913), 20 km W-NW of Salome, Arizona. (A) view northward to the shaker trailer; (B) view to the east to the seismometer array; (C) view west to the shaker trailer, 100 m from the trailer; (D) view to the south from the shaker trailer; (E) satellite view of the local site, yellow bar is seismometer array, the yellow star is the former location of the US Array seismometer; and (F) site location in Arizona.
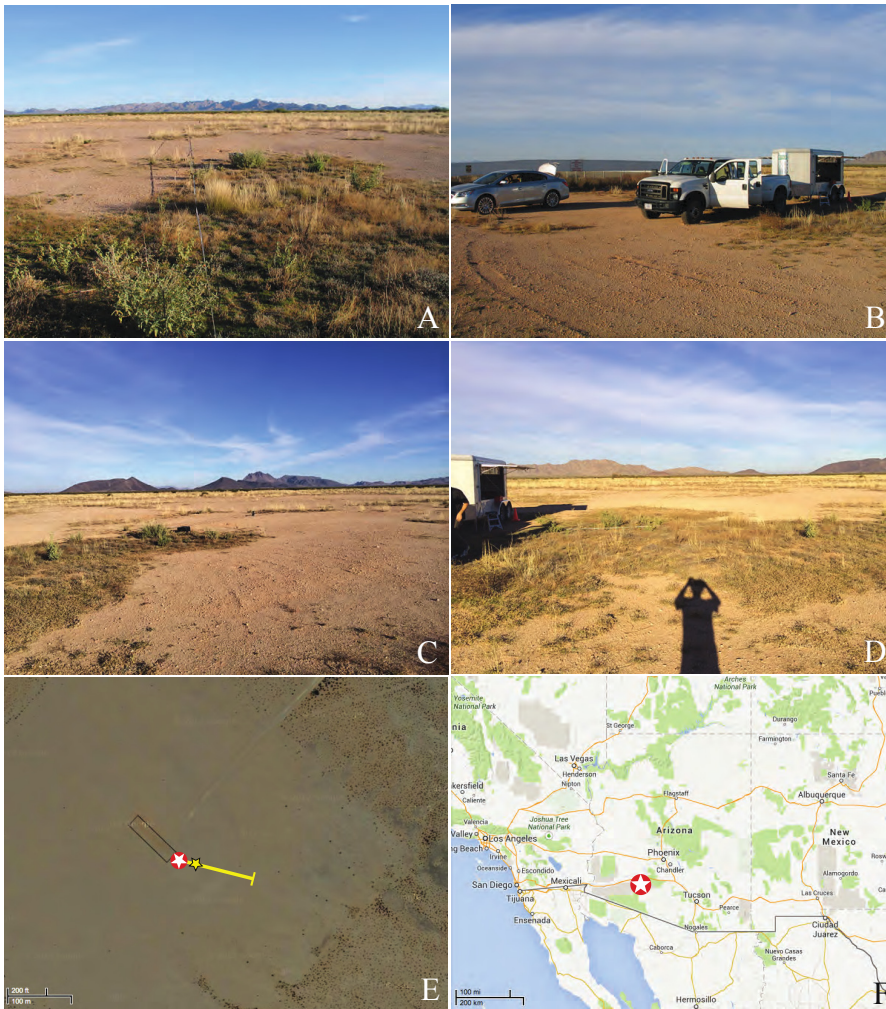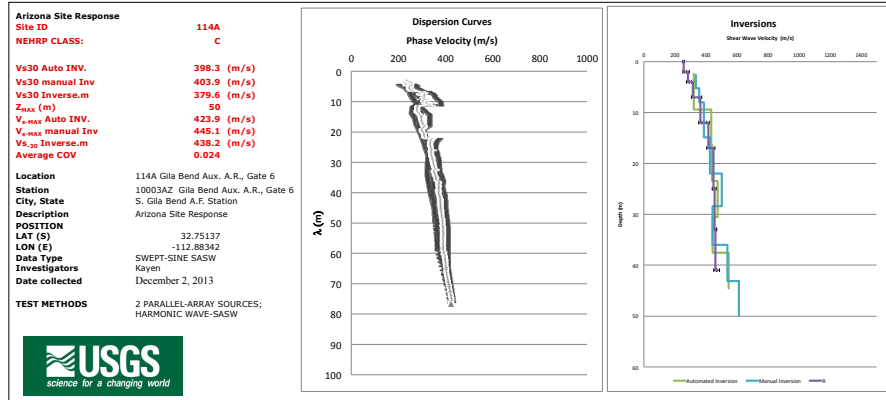
Figure 3.11 Station 114A: (a) shear-wave velocity profile and (b) surface-wave test site 1003AZ-114A located (lat 32.75137, long -112.88342) on the Barry M Goldwater Gunnery Range (BMGR East), Range 4, 26 km SW of Gila Bend, Arizona. (A) view towards the east from the shakers to the trend of the seismometer array; (B) view northward to the shaker trailer; (C) view NE across the seismometer array; (D) another view to the north near the shaker trailer; (E) satellite view of the local site, yellow bar is seismometer array, the yellow star is the location of the US Array seismometer; and (F) site location in Arizona.
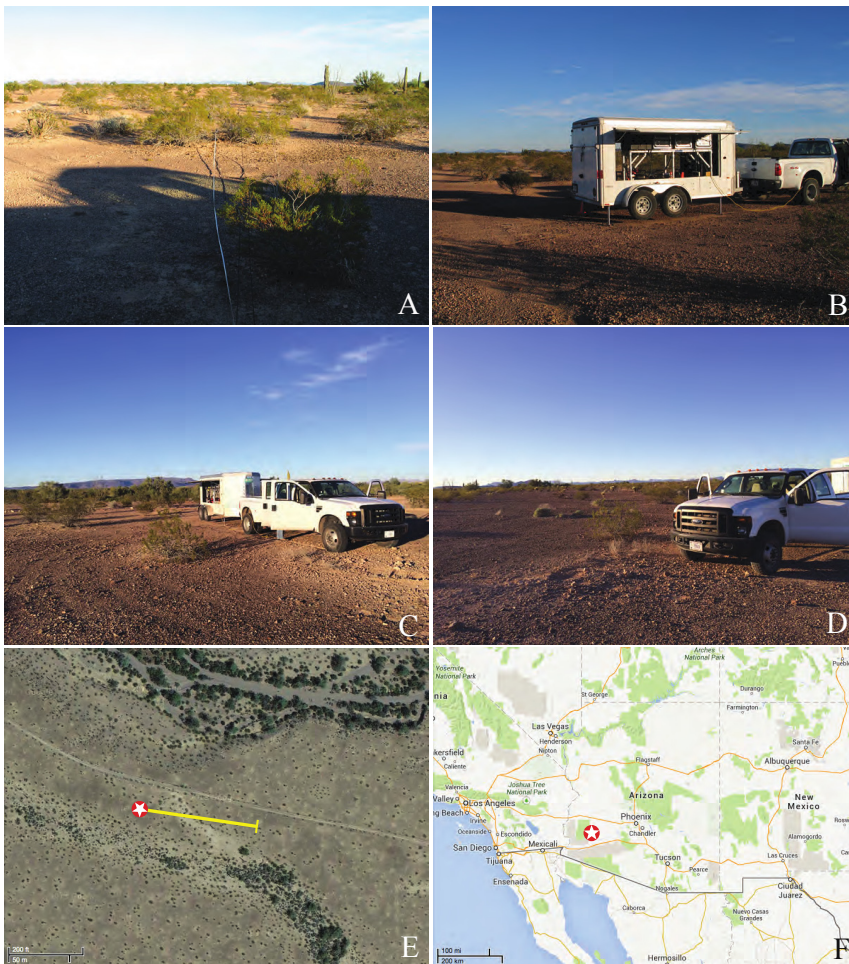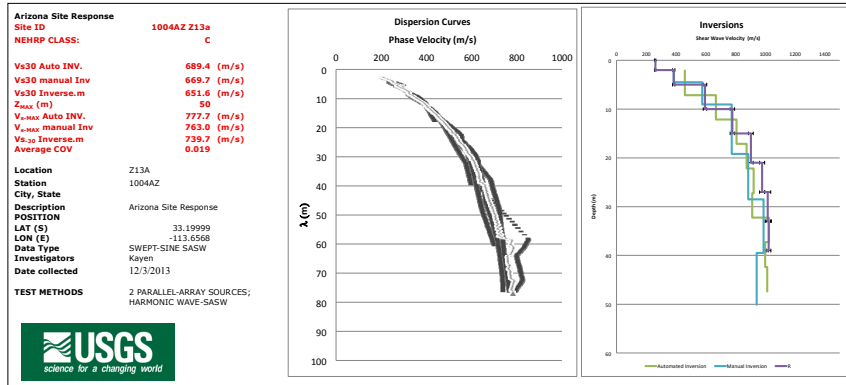
Figure 3.12 Station Z13A: (a) shear-wave velocity profile and (b) surface-wave test site 1004AZ-Z13A located (lat 33.20064, long -113.6506) 90 km NW of Gila Bend, Arizona. The test site is located about 600 m E-NE of the US Array seismometer location. (A) view eastward from the shaker trailer to the seismometer array; (B) view eastward to the shaker trailer; (C) view NE to the shaker trailer; (D) view to the NW; (E) satellite view of the local site, yellow bar is seismometer array; and (F) Site location in Arizona.

4 Kappa (κ) Measurements at Sites in Arizona

4.1 OVERVIEW

The parameter kappa (κ) models the empirical observation of energy dissipation occurring in the top 1–2 km of the crust [Anderson and Hough 1984]. The damping in the top part of the crust appears to be frequency independent (hysteretic), occurs at low strains, and is the principal site or path property controlling the limitation of high-frequency (> 5 Hz) strong ground motion at close in (≤ 50 km) sites. As a result, its value or range of values is important in characterizing strong ground motions for engineering design, particularly in regions of sparse seismicity like Arizona. Additionally, because it is generally independent of the level of motion at rock or very stiff sites, small local or regional earthquakes may be used to estimate its value or range in values. For the Arizona sites (Figure 2.1 and Table 2.1), the estimation of the damping in the profiles is important to assessing appropriate levels of high-frequency design motions.

Acceleration time series from the Arizona dataset described in Chapter 2 were used to estimate κ in the region using three different methods. Following the nomenclature proposed by Ktenidou et al. [2014], these approaches include the acceleration spectrum approach $\left(\kappa_{\_AS}\right)$, the displacement spectrum approach $\left(\kappa_{\_DS}\right)$, and the broadband approach $\left(\kappa_{\_BB}\right)$. The primary references for these approaches are Anderson and Hough [1984], Biasi and Smith [2001], EPRI [1993], and Schneider et al [1993], as well as Silva et al. [1997]. Table 4.1 outlines the approaches based on certain common features, such as the principle behind the approach and the frequency range over which κ is estimated.

We make a clear distinction between κ_r and κ_0. The aim here is to estimate κ_0, the zero-distance, site-specific attenuation factor. Some of the approaches to measure κ, such as AS and DS, generally start with individual measurements of κ_r (i.e., observations on individual spectra at distance "r"), which must then be combined, interpreted, and extrapolated to zero distance to obtain an estimate of κ_0 for the site. Others, such as BB, yield directly the κ_0 (i.e., the site-specific, zero-distance κ derived from many observations), after having corrected for path attenuation and near-surface amplification. There are different ways of extrapolating κ_r values to zero distance (i.e., correcting for the path contribution); these are discussed in the Section 4.4.

Table 4.1   Approaches used for estimating κ (adapted from Ktenidou et al. [2014]).

Notation	Principle	Main references	Measurement / computation	Frequency range
$\kappa_{\_AS}$	High-frequency decay of the S-wave Fourier spectrum	Anderson and Hough [1984], Hough and Anderson [1988]	Direct measurement on the S-wave Fourier **acceleration spectrum** above f_c, where it is theoretically flat	High (above f_c)
$\kappa_{\_DS}$	Small magnitudes (strong trade-off with source)	Biasi and Smith [2001]	Direct measurement on low-frequency part of the Fourier **displacement spectrum** (much below f_c) where it is theoretically flat	Below f_c
$\kappa_{\_BB}$	Inversion of the entire frequency band of the spectrum	Anderson and Humphrey [1991], Humphrey and Anderson [1992], EPRI [1993], Schneider et al. [1993], Silva et al. [1997], Edwards et al. [2011]	**Broadband** inversion of the entire spectrum for source, path and site terms (usually for moment, f_c and κ_0)	Entire band

f_c : source corner frequency

4.2   DESCRIPTION OF THE METHODS TO ESTIMATE KAPPA

4.2.1 Method 1

Following the classic definition of Anderson and Hough [1984], κ_r can be directly measured in log-linear space on the high-frequency part of the Fourier acceleration spectrum of the S waves, between frequencies f_1 and f_2, where the decay is approximately linear. We will refer to this original definition as κ_{r_AS}. Since a component of horizontal wave propagation—affected by Q—is present in these measurements, an extrapolation to zero distance (assuming frequency-independent Q) will lead to the site-specific attenuation component, κ_{0_AS}. This approach can only be used for relatively large earthquake magnitudes, as f_1 must exceed the source corner frequency (f_c) to avoid any trade-off with the source. We also correct the Fourier amplitude spectra for crustal amplification in order to avoid the site amplification from affecting κ estimation (i.e., by distorting the shape of the spectrum).

The main steps for applying this approach are outlined in Ktenidou et al. [2013]. The main considerations include:

- using frequencies above f_c, which is estimated from a range of stress drop values from 1 to 50 bars
- using frequencies where the instrument response can be considered as flat (up to 15 Hz, the corner of the LP filter is at 16 Hz for stations in the TA)

- using frequencies within this range with an acceptable SNR (which is taken to be 3)
- working with an adequate frequency band ($D_f = f_2 - f_1$) (which is taken to be at least 7 Hz)
- checking that κ is not strongly biased by local site resonances in the FAS

4.2.2 Method 2

The traditional approach uses relatively large magnitude earthquakes in order to measure spectral decay above f_c. Biasi and Smith [2001] proposed an approach that extends the method to very small magnitudes where ground motion data are more abundant. They proposed to measure κ_r directly on the Fourier displacement spectrum, using frequencies below the (rather above) f_c, in contrast to using the Fourier acceleration spectrum and keeping above the (rather low) f_c. Rather than measuring κ_r as the departure of the acceleration spectrum from a horizontal line ($\kappa = 0$ sec, no attenuation), we use records from small earthquakes and measure κ_r as the departure of the displacement spectrum from a horizontal line ($\kappa = 0$ sec, no attenuation) over potentially the same frequency range (D_f). Again, we analyze Fourier amplitude spectra that have been corrected for crustal amplification.

One advantage of this method is that the theoretical basis for treating the displacement spectrum at the source as flat below f_c is actually stronger than the basis for treating the acceleration spectrum as flat above f_c, since the latter depends on the validity of the ω^{-2} assumption. Let us denote individual κ_r values thus measured as κ_{r_DS}, and the extrapolated zero-distance site parameter as κ_{0_DS} (this is also referred to as κ_{0_mini}).

4.2.3 Method 3

An inversion process [Silva et al. 1997] was used to estimate κ (κ_0) in which the earthquake source, path, and site parameters were obtained by using a nonlinear least-squares fit to the Fourier amplitude spectra using the point-source model [Boore 1983; EPRI 1993]. The useable bandwidth for each amplitude spectrum was site and earthquake specific based on a visual examination of the pre-event FAS noise levels compared to the windowed shear-wave FAS and with the maximum frequency constrained by anti-alias filters of only 15 Hz. The inversion scheme treats multiple earthquakes and sites simultaneously with the common crustal path damping parameter $Q(f)$. The parameter covariance matrix was examined to determine which parameters may be resolved for each dataset. Asymptotic standard errors were computed at the final iteration. The five parameters that may be determined from the data are κ (κ_0), Q_0 (the value of Q for f equal to 1 Hz), and η (frequency-dependent path Q model), **M**, and corner frequency (stress drop). The procedure uses the Levenberg-Marquardt algorithm [Press et al. 1986] with the inclusion of the second derivative. Crustal profile amplification was accommodated in the inversion scheme by incorporating the

appropriate rock or soil transfer functions (shear-wave velocity from source depth to the surface) in estimating the point-source surface spectra.

To reduce the potential for non-uniqueness inherent in inversion results, a suite of starting models was employed. The final set of parameters was selected based upon a visual inspection of the model fit to the Fourier amplitude spectrum, the χ-square values, and the parameter covariance matrix. The stress drop was calculated from the moment and corner frequency using the relation

$$f_c = \beta \left(\frac{\Delta_\sigma}{8.44 \cdot M_0} \right)^{1/3} \tag{4.1}$$

The inversions were done on log amplitude spectra (vector average of the two horizontal components), as strong ground motion data appear to be log normally distributed. This is consistent with the model being represented as a product (rather than sum) of models [EPRI 1993]. A feature of the inversion scheme is the flexibility to distinguish between sites, for which κ is determined, and stations for which recordings are available. As a result, several stations may share a common site or κ estimate. For the inversions, due to the narrow bandwidth and limited distance range (about 9 km to 300 km, see Table 4.4) $Q(f)$ was fixed at $200(f)^{0.68}$ (Erickson et al. [2004] for the Basin and Range Province). The assumed $Q(f)$ is comparable with the models of Beck et al. [2013], Phillips et al. [2013], and Pasyanos [2013]. For the transfer functions, amplification (FAS) from the source region (nominal depth of about 10 km, see Table 4.3) to the surface, two profiles were used: one representing stiff soil and one representing firm rock with shallow portions (top 100 ft to about 350 ft, see Figure 4.14) based on recent SASW measurements (Chapter 3). Figure 4.14 shows the SASW shear-wave velocity profiles and corresponding $V_{S,30}$ estimates for the sites surveyed.

As Figure 4.14 illustrates, at depths below about 20 ft, the profiles tend to cluster into two groups or classes, which were characterized as stiff soil ($V_{S,30} \leq 670$ m/sec) and firm rock ($V_{S,30} > 670$ m/sec) irrespective of material description. Class-specific amplification factors were developed by selecting representation profiles: Z14A for stiff soil and 113A for firm rock (solid lines in Figure 4.14, respectively). The two class specific profiles were extrapolated to source depths at a shear-wave velocity of 3.5 km/sec using a generic WNA profile (760 m/sec, Kamai et al. [2014]) and shown in Figure 4.15. For sites without SASW or other shear-wave velocity measurements, an appropriate profile was chosen based on the inferred $V_{S,30}$ from the Geomatrix 3rd letter. Stations W13A and Y12C were assigned Geomatrix "A" site category with a proxy based $V_{S,30}$ estimate of 630 m/sec [Ancheta et al. 2013] and Station X13A was assigned "Geomatrix B with a proxy $V_{S,30}$ estimate of 425 m/sec with all three sites considered reflective of stiff soil amplification. The case-specific transfer functions or amplification factors are illustrated in Figure 4.16 along with unity, which was used in the sensitivity analyses to estimate epistemic uncertainty in κ (Section 4.4.5).

Care was taken in the analysis to consider the subset of small magnitude ($\mathbf{M} < 2$) earthquakes based on a similar analysis of κ at a site in Washington [Silva and Darragh 2014]. In this study, the best solution (minimum chi-square) resulted in corner frequencies below 15 Hz and very low stress drops (< 1 bar); however, another more consistent solution existed fixing corner frequencies beyond 15 Hz with stress drops not resolvable with the 15 Hz high-frequency limit. Similarly, for the small Arizona events the corner frequencies for $\mathbf{M} < 1.6$ were also fixed beyond 15 Hz with the high-

frequency limit retained at 15 Hz. Note for the point-source model with a corner frequency beyond 15 Hz, the corner frequency will have little effect for frequencies below about 15 Hz.

4.3   ARIZONA DATASET

The Arizona data from the TA deployment [US Array 2003] and CIT\SCSN arrays are shown in Figure 4.1. Magnitudes range from 1.2 to 3.4. Hypocentral distances range from about 10 to greater than 300 km. Recordings that sampled various near-surface crustal structures were windowed to include both shear-wave and pre-event noise samples. Fourier amplitude spectra were provided for the sites listed in Table 2.1 from 11 earthquakes recorded in 2008 with epicenters in Arizona [Figure 2.2 and Table 2.2]. All of the recordings reflect broadband velocity instruments with sampling at 40 SPS and a corresponding high-frequency limit of about 15 Hz. The narrow bandwidth for the TA broadband data (15 Hz) severely limits the resolving power for κ resulting in some ambiguity (uncertainty) in the current analyses.

Kappa estimates were made for selected sites and earthquakes in Tables 2.1 and 2.2. This analysis dataset consists of the 11 earthquakes recorded at 14 sites (Table 4.3). Tables 4.3 and 4.4 show the range of magnitude, hypocentral depth, and distance, as well as their distributions between the recordings stations. These data have been discussed in more detail in Chapter 2.

4.4   RESULTS

4.4.1 Method 1

The uncertainty in the stress drop for these small-magnitude events led us to consider a range of possible stress drops between two limiting values: (1) a typical (upper bound) value for the large magnitude earthquakes in WNA equal to 50 bars [W. Silva, *personal communication*, 2013]; and (2) a value of 1 bar (lower bound), which is the mean value found for small events in Phillips et al. [2013], which also used data from the TA array. The possible source f_c values derived based on these two stress drop values are shown in Figure 4.2. The uncertainty in the f_c values is large, especially for low magnitudes. Moreover, the usable bandwidth of the data is very small and also limited by the 16 Hz anti-alias corner frequency for these data. The conflicting frequency requirements from this combination of magnitude and bandwidth rendered this study particularly difficult. Hence we decided to use only the largest magnitude events (M3.1 and M3.4, red in Figure 4.1) when applying the AS method and only the smallest magnitudes (M1.2 and M1.5, blue in Figure 4.1) when applying the DS method, so that we can be fairly certain of working above and below the f_c, respectively. We do not use the intermediate-magnitude Arizona events (1.9<M<2.6) because the range of possible f_c values spans the entire usable frequency range of these data.
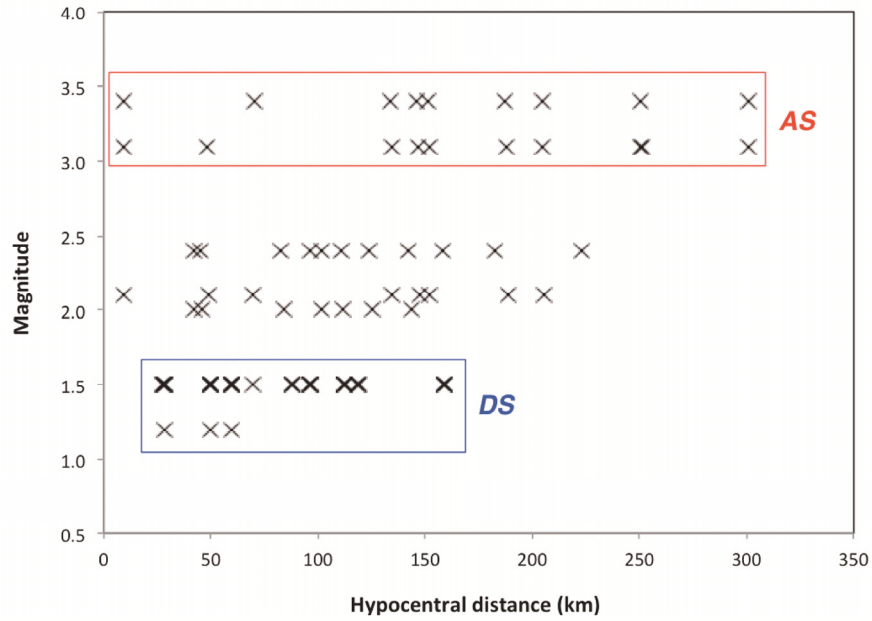
Figure 4.1 The magnitude and distance range of the Arizona records chosen for κ estimation using the AS and DS approaches.
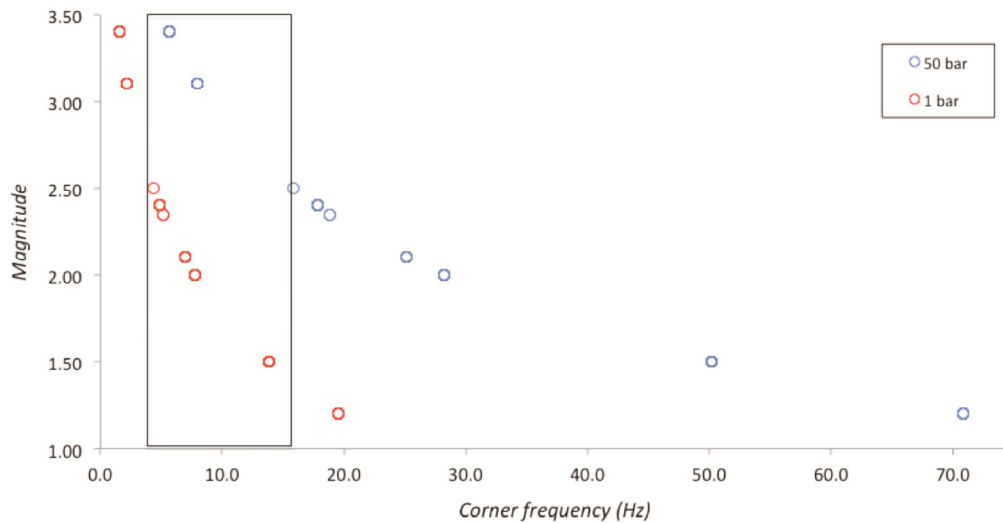
Figure 4.2 The range of possible source corner frequencies assuming stress drops of 1 and 50 bars. The box indicates the usable frequency range of the records based on noise level and LP filtering.

The stations and events considered for applying the AS approach are shown in Figure 4.3. The two epicenters are located about 200 km from the PVNGS. The nearest stations to the epicenters (NEE2, Y12C, X13A, and W13A) are not among the 9 sites lying directly around the PVNGS. Due to the scarcity of data (without these sites there are no data at epicentral distances less than 100 km), all FAS were divided by the smoothed case-specific transfer functions shown in Figure 4.16 to correct for crustal amplification,. Site 113A is considered a rock site (as is site Y16A, which is not analyzed with Method 1). Due to the small magnitudes recorded at this site, Method 2 is appropriate, and all others sites are considered stiff soil. More details about the estimation of these transfer functions are given in Section 4.4.4.

We considered both possibilities of low and high stress drop (the spectral shapes can be interpreted either as a combination of high stress drop and high attenuation or low stress drop and low attenuation). After visual inspection of the spectral shapes, we consider the high stress drop possibility as more probable. The shape can be interpreted as having either a low (~2 Hz) or high (~8 Hz) corner frequency, though the former interpretation cannot be made at all sites (e.g., Figure 4.4). Figure 4.5 shows the results if the AS approach is applied, assuming both interpretations; the low stress drop assumption leads to low κ_r values, including one value less than zero.
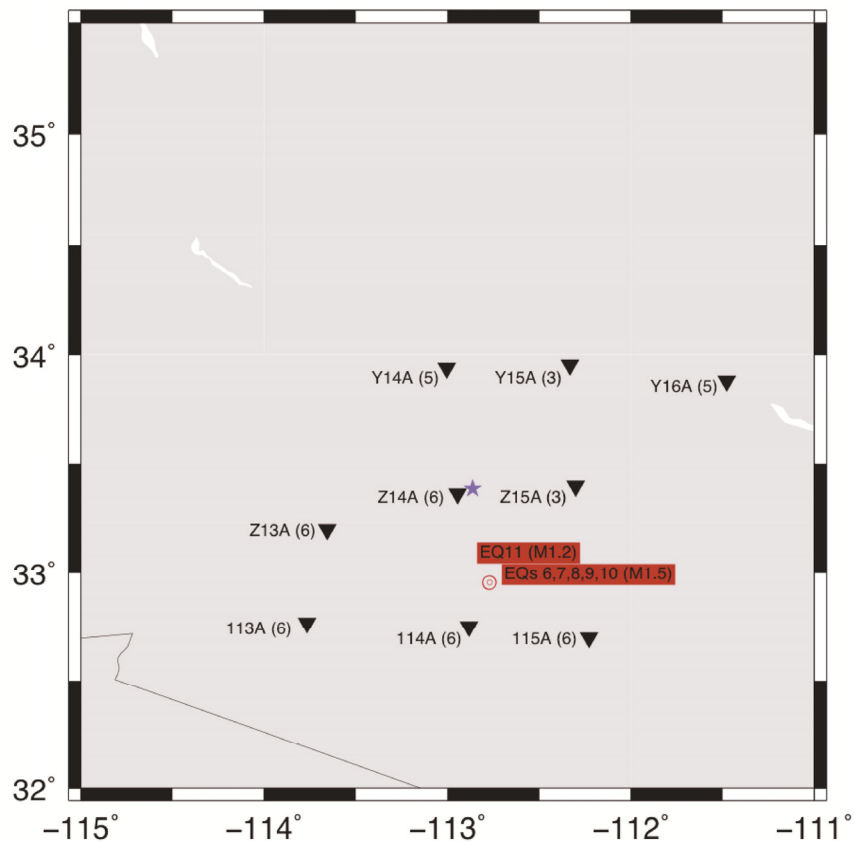
Figure 4.3   The stations and events used for the AS approach.

Consequently, we choose the frequency range between 9–16 Hz as lying most likely above the source corner frequency. (We use the data up to 16 Hz despite the 3 dB amplitude drop at that frequency in order to maximize the usable bandwidth to 7 Hz). We measure κ_{r_AS} in that range in two ways: on each individual acceleration spectrum (1 or 2 events and 2 horizontal components per station) and on a single spectrum computed by logarithmically stacking the individual spectrum at each station. Figure 4.6 shows the resulting κ_{r_AS} values versus epicentral distance. All of the individual values (circles) along with the value from the stacked spectra (cross) are shown for each station. On the same figure we note the station name and $V_{S,30}$ value in parenthesis (blue indicates the 9 stations around the PVNGS and red indicates the more distant stations; an asterisk indicates $V_{S,30}$ values were not measured but were determined from the assigned Geomatrix 3rd classification and $V_{S,30}$ proxy. We included results from spectral stacking to provide more robust κ estimates since it improves the SNR and should still capture the overall trend of the spectral decay.
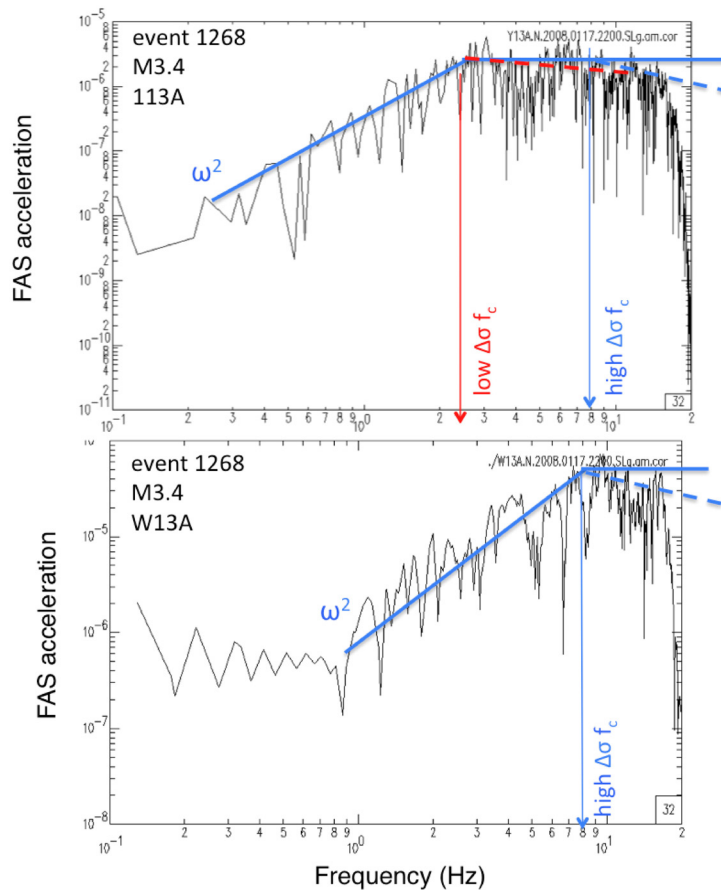
Figure 4.4 An example of the acceleration spectra at two sites (113A and W13A) and the possible corner frequency interpretations for low (red) and high (blue) stress-drop assumptions; also shown are the possible κ_r slopes. The low-stress drop corner may not be discernible.
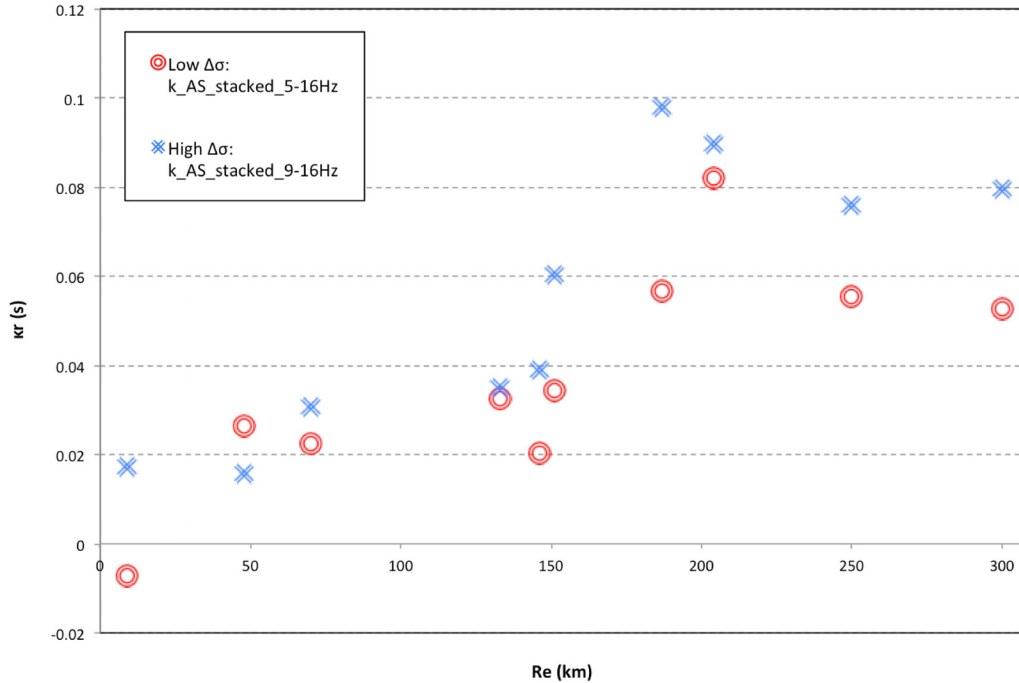
Figure 4.5 **Results of the AS approach (κ_r versus distance) for low and high stress drop assumptions.**

Despite the smoothing provided by the stacking, the scatter in the results remains large. There may be several reasons for the scatter: (1) foremost is the limited bandwidth of the data at high frequencies; (2) the estimates of κ are sensitive to the choice of window (Although this limitation may be overcome by using multiple moving windows or one very wide frequency window, such an approach is not possible with these data due to the narrow bandwidth available of only about 7 Hz [J. Anderson, *personal communication* 2013].); and (3) it may be due to the different site conditions. Nearly all the sites (see Chapter 3) have $V_{S,30}$ values around 500±50 m/sec, except for sites 113A and Y16A, which are the only stiff rock sites, with a $V_{S,30}$ of 1232 and 1028 m/sec, respectively (in Method 1 no records from Y16A are included due to their small magnitude). The κ measurements for 113A are much smaller than those from the stiff soil sites. Fourth, the measurement of κ may be biased by high-frequency resonance at some of the sites. This may be the case for site Y15A, which plots above all sites in Figure 4.6. We computed horizontal-to-vertical spectral ratios (HVSR), [Lermo and Chávez-García 1993] for S-wave and coda windows, and observed a broadband amplification between 7–10 Hz at Y15A. This resonance may bias κ_{r_AS}, leading to an overestimation [Parolai and Bindi 2005] since κ is measured in the frequency range adjacent to this broadband amplification peak, which trends downwards as shown in Figure 4.7 (blue box). For site 113A, however, the HVSR shape is flat over the entire frequency range; hence the low value we computed is probably not due to bias caused by resonance.

Having accounted for the two largest outliers (sites 113A and Y15A), we focus the analysis on the remaining κ estimates. Note that there is the possibility of a constant κ_r in the first 50 km from the source, as indicated by the data from W13A and X13A, as noted by Kilb et al. [2012] for

earthquakes in Southern California. The site-specific value of κ_{0_AS}—assuming this 'hockey-stick' dependence with distance—is about $\kappa_{0\_AS} = 0.017$ sec, as shown in Figure 4.6 (dashed line). As is typical, we note an overall increase of κ_{r_AS} with epicentral distance.

This increase with distance corresponds to an overall frequency-independent regional Q attenuation of about 900 in the frequency range studied, assuming a crustal S-wave velocity of 3.5 km/sec (the range in Q is from 600 to1300, depending on whether we include data at all distances or only greater than 50 km, and whether we include the two aforementioned outliers or not). This range of Q values is shown in Figure 4.6 in green. Pasyanos [2013] found crustal Q_s values around 500–600, between 6–10 Hz, for the area plotted in Figure 4.3 (southern Arizona belongs to the 'Basin and Range' area of his study). Assuming that this $Q(f)$ follows a power law and extrapolating to 16 Hz, it may reach a value of about 850. This range is shown in the figure in red. On the other hand, for the 'Colorado Plateau' area of his study, which includes northern Arizona, he found Q values between 2000–5000 (6000 when extrapolated to 16 Hz). For the same area, Phillips et al. [2013] found Q_{Lg} in the range of 500–1200, between 6–12 Hz (this range of Q values is shown in Figure 4.6 in blue). This study also shows that, in the area sampled by the rays passing from the earthquake epicenters to the stations, the Q structure is very complex, with significant lateral variations. This may be another reason behind the large scatter in the κ_r values with distance (i.e., each κ_r measurement may contain different path contributions). Beck et al. [2013] found an average Q_c of 450 for the Basin and Range area between 6–10 Hz (including stations 113A and 114A), and 400 further north in the transition zone (including Station W13A), although their ray coverage for those stations is poor. Erikson et al. [2004] computed power law formulas that yield Q_{Lg} values around 875–1300 for the Basin and Range area between 9–16 Hz (purple zone in Figure 4.6). Our estimated Q value generally falls within these estimates.

Chapter 5 compares ground motions at the Arizona and California stations and no significant regional attenuation difference can be inferred between them. Assuming typical Q values for California [$Q(f) = 150f^{0.6}$] (W. Silva, *personal communication* [2013]) in the frequency range we used (9–16 Hz), the expected Q is 560–790 with a mean value of 680 (this range of Q values is shown in Figure 4.6 in brown). In the same frequency range, Erikson et al. [2004] found Q_{Lg} between 500–800. The California values are very similar to those given for southern Arizona by Pasyanos [2013]. Both Beck et al. [2013] and Erikson et al. [2004] make the case that Q in Arizona may be significantly lower than Q values from stable continental regions like CEUS and closer to values from California. The Q values inferred from our data points in Figure 4.6 are somewhat higher than those of California, but still relatively low compared to CEUS values.
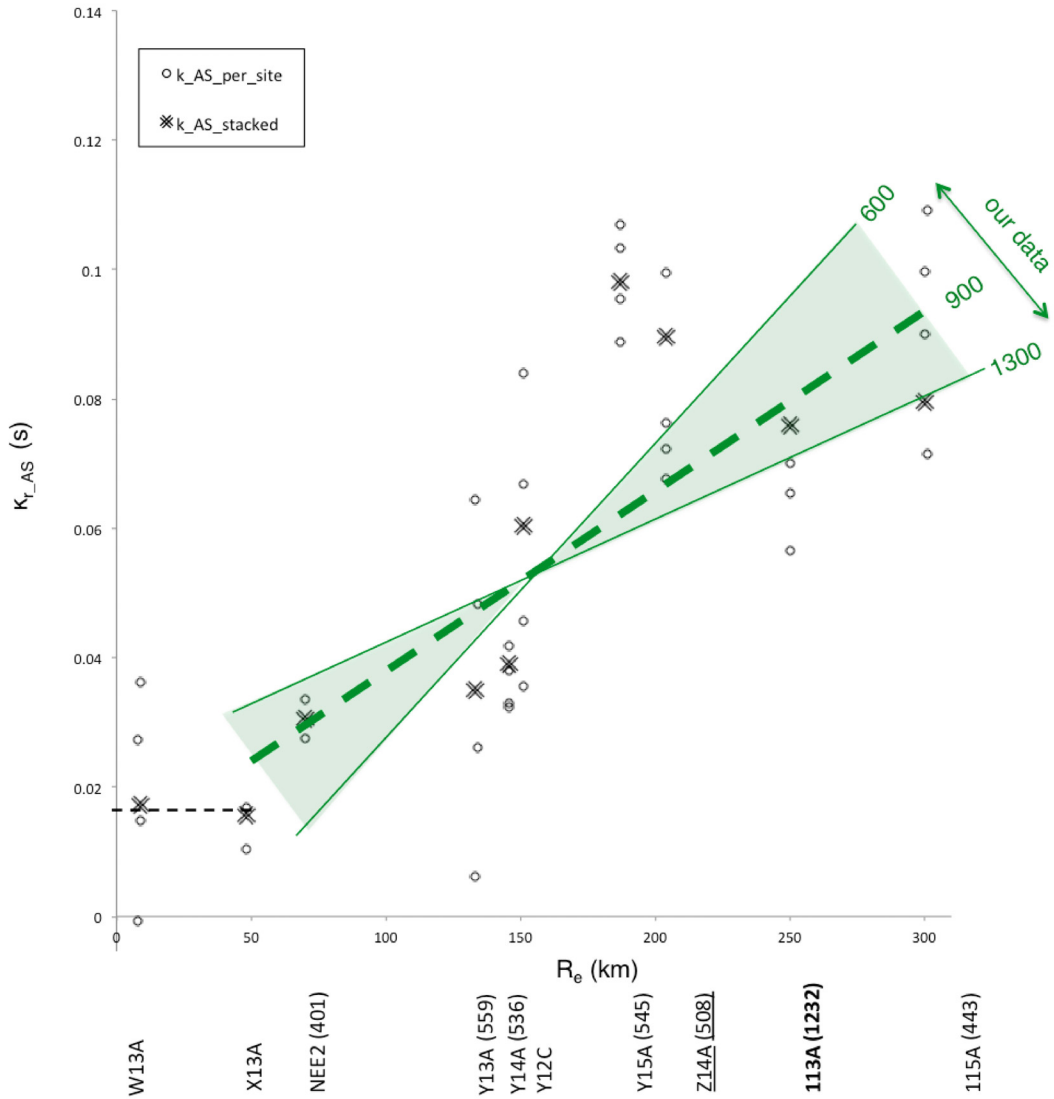
(a)

Figure 4.6(a) The measured κ_{r_AS} values versus epicentral distance for individual spectra (circles) and stacked spectra (crosses). Also shown are the possible models of κ_r with distance corresponding to κ_{0_AS} = 17 m/sec (dashed line) and Q = 600–1300 (green range, with a mean of around 900) based on the values from the Arizona records. The names of the stations are accompanied by Vs_{30} values (blue for nearby and red for distant stations from the PVNGS; asterisk means inferred value).
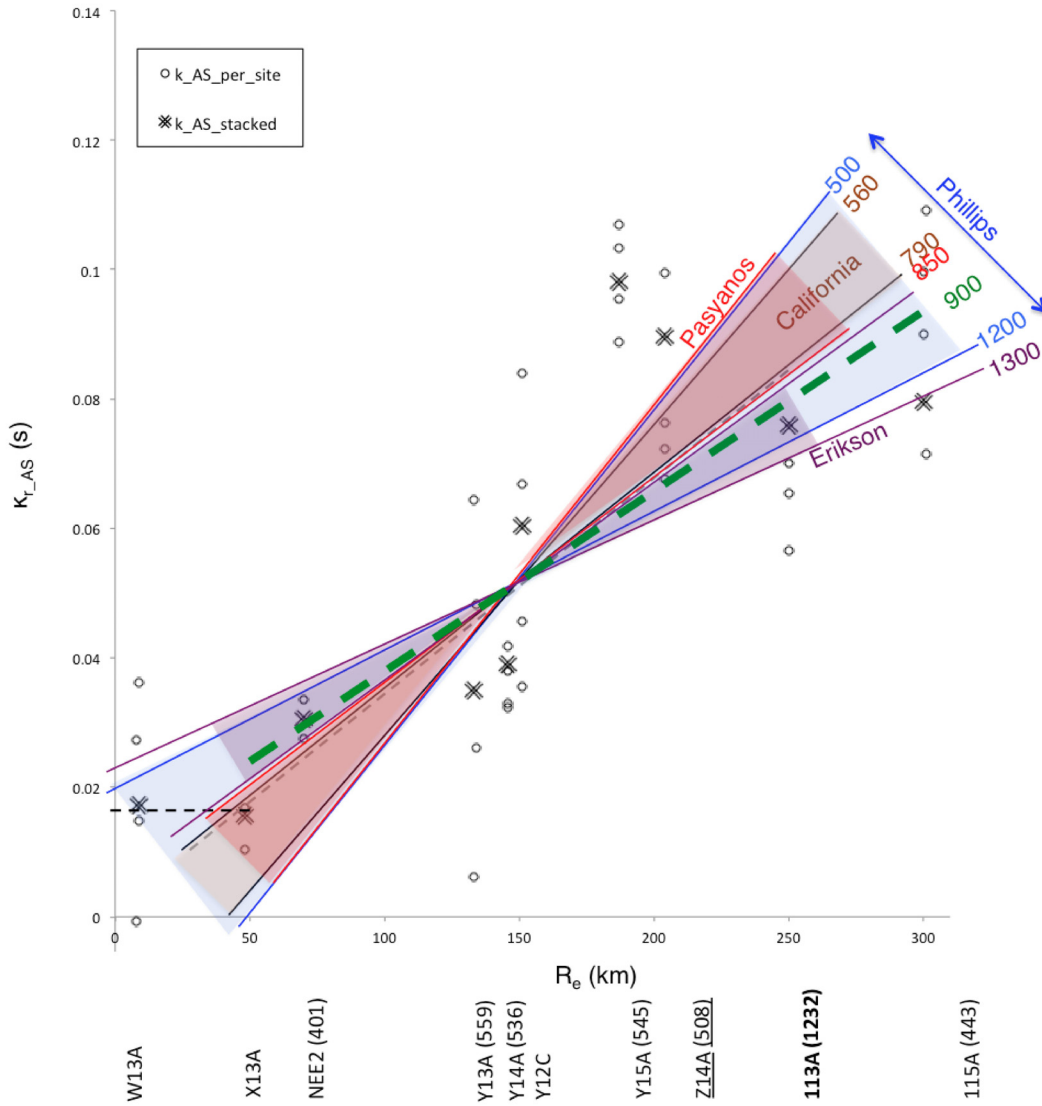
(b)

Figure 4.6(b) Comparison of our mean Q of 900 with Q models from literature. Blue range: Arizona Q_{Lg} values of Phillips et al. [2013] for 6–12 Hz. Red range: southern Arizona Q_s values from Pasyanos [2013] for 9–16 Hz. Brown range: typical California Q values for 9–16 Hz. Purple range: Erikson et al. [2004] Q_{Lg} values for the Basin and Range between 9–16 Hz.
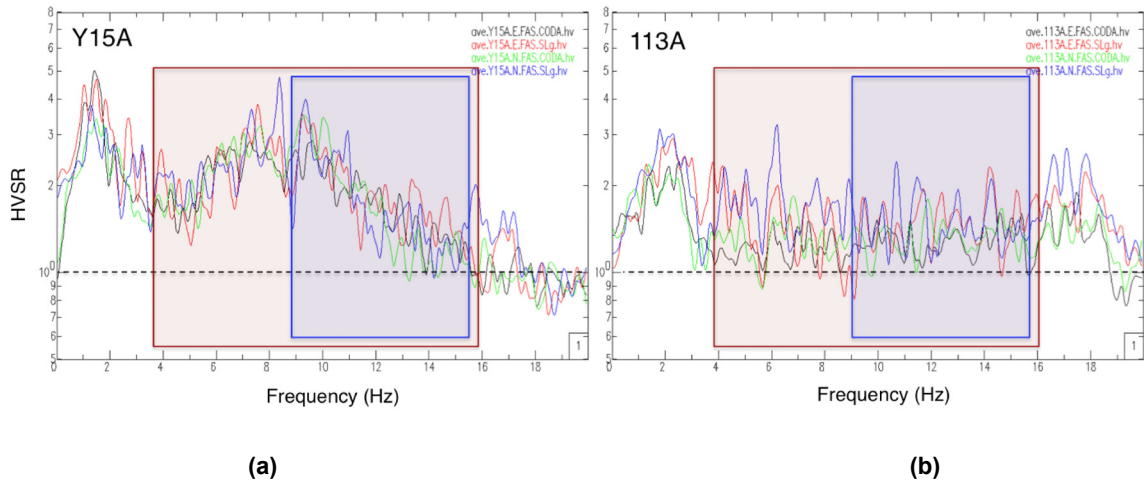
Figure 4.7   The mean HVSR over all events recorded at site Y15A (a) and 113A (b). The mean is computed using S-wave windows (mean over 8 and 11 events) and coda windows (mean over 7 and 10 events), for both horizontal components. The blue box indicates the frequency range used to compute $\kappa_{\_AS}$ and the red one the range used to compute $\kappa_{\_DS}$.

4.4.2 Method 2

The stations and events considered for applying the DS approach are shown in Figure 4.8. The epicenters are located in the vicinity of the PVNGS (<50 km), and all stations are within 120 km of the sources, except Y16A, which lies at 160 km. We again consider the two possible combinations to interpret the spectral shapes: low stress drop and low attenuation (which would mean a low f_c, which would in turn allow use of the AS approach), versus high stress drop and high attenuation (which would mean a high f_c and require use of the DS approach). After inspection of the spectral shapes (in Figure 4.9 the acceleration spectrum continues to increase above 5 Hz) and the estimated κ values (in Figure 4.10 all κ_{r_AS} values are negative), we consider the corner frequency to lie most likely above the usable bandwidth for these small magnitude earthquakes (M<2). Hence we prefer to apply the DS approach in the usable frequency range between 4–16 Hz.

We compute the displacement FAS by multiplying the acceleration FAS by ω^2 where ω is the angular frequency $(\omega = 2\pi f)$. We measure κ_{r_DS} in two ways: first, we stack the displacement spectrum for all events and horizontal components (i.e., 12 spectra per site for sites that recorded all 6 events) and compute κ_{r_DS} on each one. We also stack different sites together based on epicentral distance in four groups (0 to 40 km, 40 to 80 km, 80 to 120 km, and 120 to 160 km; see Figure 4.11) and measure κ_{r_DS} on each of the four groups of sites. Stacking improves the SNR given the low magnitudes of these events and provides a more robust estimate of κ_{r_DS}. The stacking is justified given the nearly collocated hypocenters of all 6 events and their similar magnitudes.

Figure 4.11 shows the resulting κ_{r_DS} values versus epicentral distance. For each station we show the value from the stacked spectrum over all the events and components per site (circle), and for each group of stations we show the value of the stacked spectra over those stations (cross). On the same figure we note each station and its $V_{S,30}$ value in parenthesis. The inset sketch shows how the stations were grouped by distance.

We do not observe a significant increase of κ_{r_DS} with epicentral distance out to about 80 km; that is, we do not clearly see the path Q contribution to overall attenuation out to this distance. The average value is $\kappa_{0\_DS} = 0.050$ sec.

In contrast to the previous method, we do not observe a strong correlation of the measured values with $V_{S,30}$. In the third group of sites (distances 80–120 km), the firmest rock site, 113A ($V_{S,30}$ of 1232 m/sec), has a higher κ_{r_DS} value than any other site, which is contrary to our expectations. Furthermore, site Y16A has a very high κ_{r_DS} value even though it is the second firmest site in the dataset. At these large epicentral distances the complex regional Q attenuation may mask the effect of site attenuation (κ). The other outlier is site Y15A, with a very low measured κ_{r_DS} (near 0.015 sec). Once again we attribute this outlier to possible bias from a site resonance. In Figure 4.7 (red box), the broadband resonance peak observed on the empirical HVSR ratios is between 7–10 Hz; therefore, it lies exactly in the middle of the frequency range where the κ measurement is performed (4–16 Hz). Because the spectral decay is masked by the resonance peak, fitting a line through the peak yields a nearly horizontal line (κ near zero). Based on this observation, we do not include the κ value from this station in stacking the spectra or in deriving the final model.
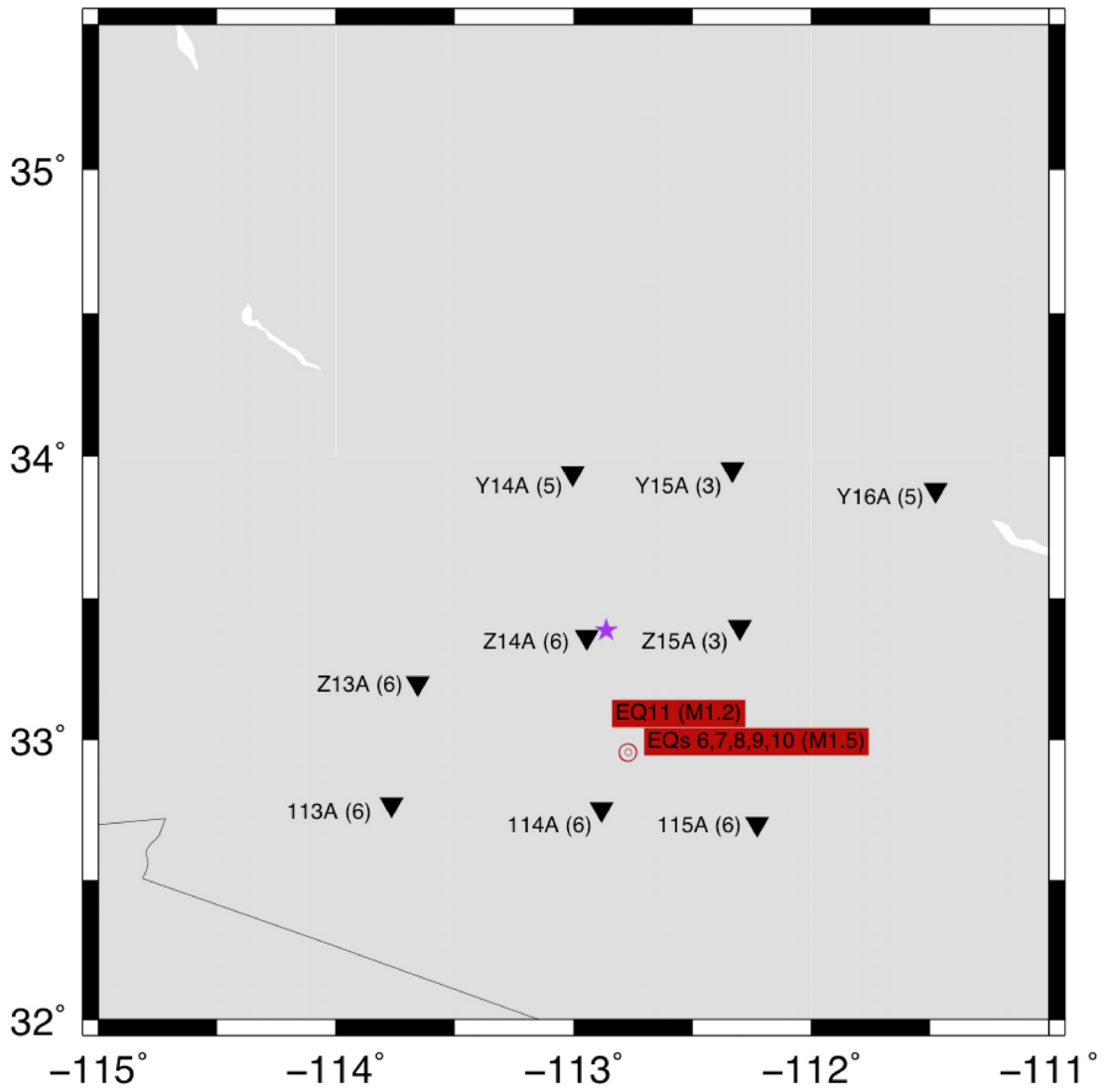
Figure 4.8 The stations and events used for the DS approach.
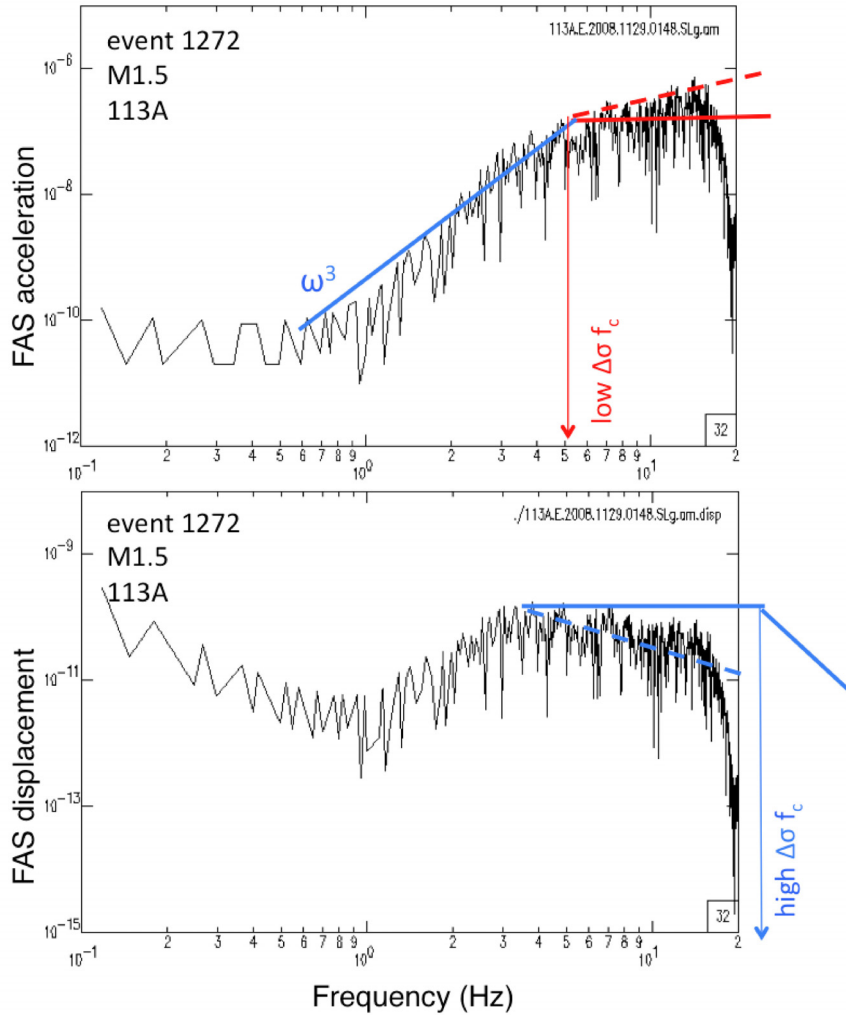
Figure 4.9 An example at site 113A of the acceleration and displacement spectrum of an M1.5 event and the possible corner frequency interpretations for low (red) and high (blue) stress-drop assumptions. Also shown, the possible κ_r slopes; for the low-stress drop assumption they are positive.
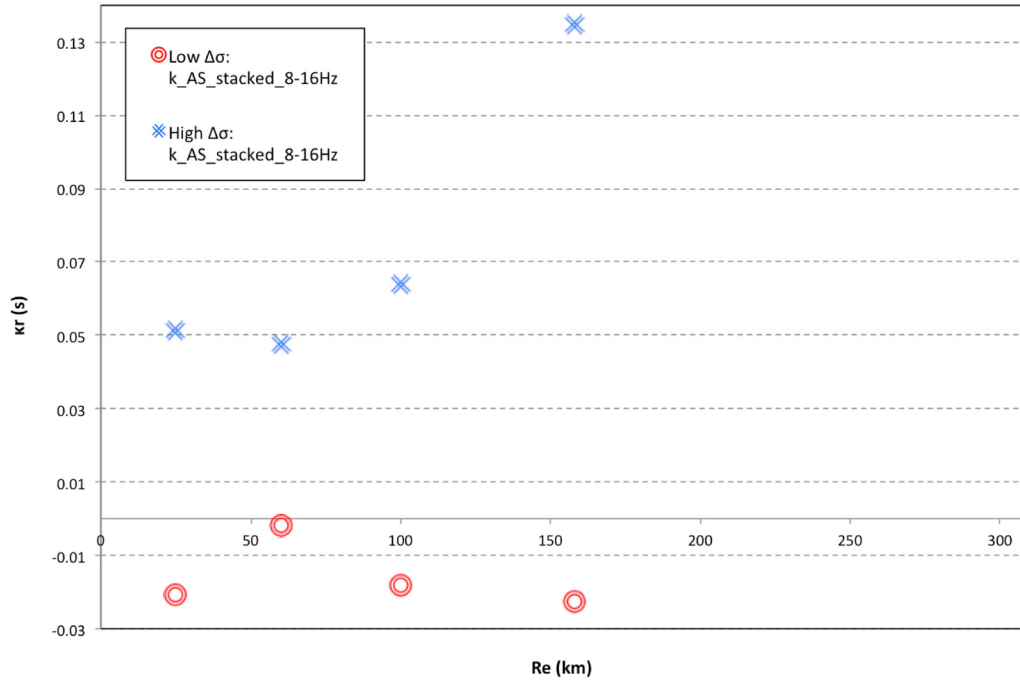
Figure 4.10 Results of the AS and DS approach (κ_r versus distance) for low (red) and high (blue) stress-drop assumptions. For the low stress-drop assumption, the κ values are always negative.
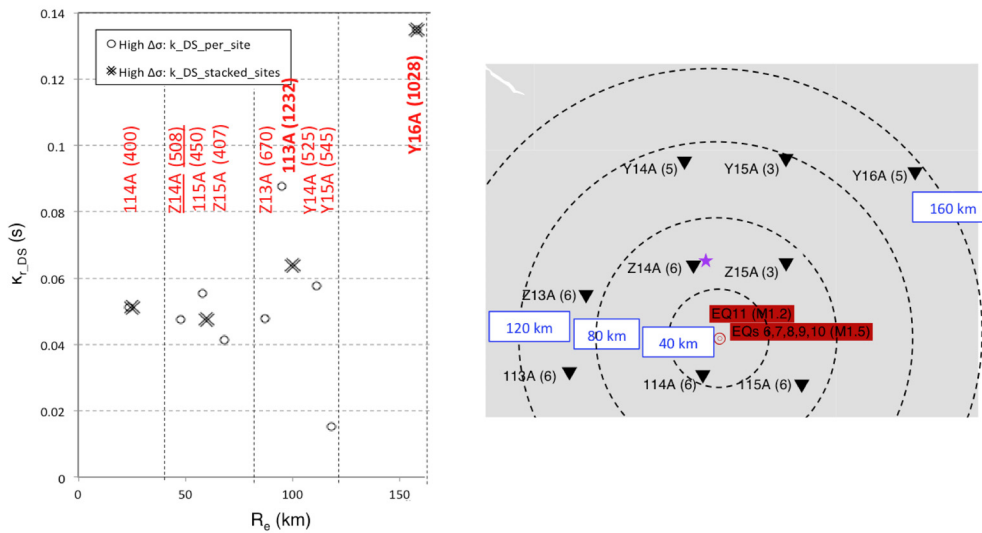
Figure 4.11 The measured κ_{r_DS} values versus epicentral distance for each station (circles) and for groups of stations (crosses). Out to 100 km the average κ_{0_DS} =0.050 sec. The names of the stations are accompanied by the Vs_{30} values. The inset shows how stations were grouped by distance.

Figure 4.12 shows all the measured κ_r values using both approaches, AS (black) and DS (red), and both stacking options (the individual values can be found in Table 4.2). The DS approach seems to yield an upper bound on κ at all distances; out to 70 km the estimated κ values are about three times higher than the corresponding κ values measured with the AS approach. This observation is in agreement with previous findings (e.g., Biasi and Anderson [2007] and Kilb et al. [2012]), although those authors found that the two methods differed by a factor of 2. This discrepancy may be due to the distribution of Arizona earthquake magnitudes. The range of magnitudes from M 1.2–3.4 is exactly the range in which Kilb et al. [2012] consider κ to be "somewhat ill defined." We have used the κ_{DS} method on data from earthquakes with magnitude 1.2 and 1.5, whereas the suggested range is below M 1. Similarly, we have used the κ_{AS} method on data from earthquakes with magnitude 3.1 and 3.4, whereas the suggested range of use is above M 3.5 or higher.
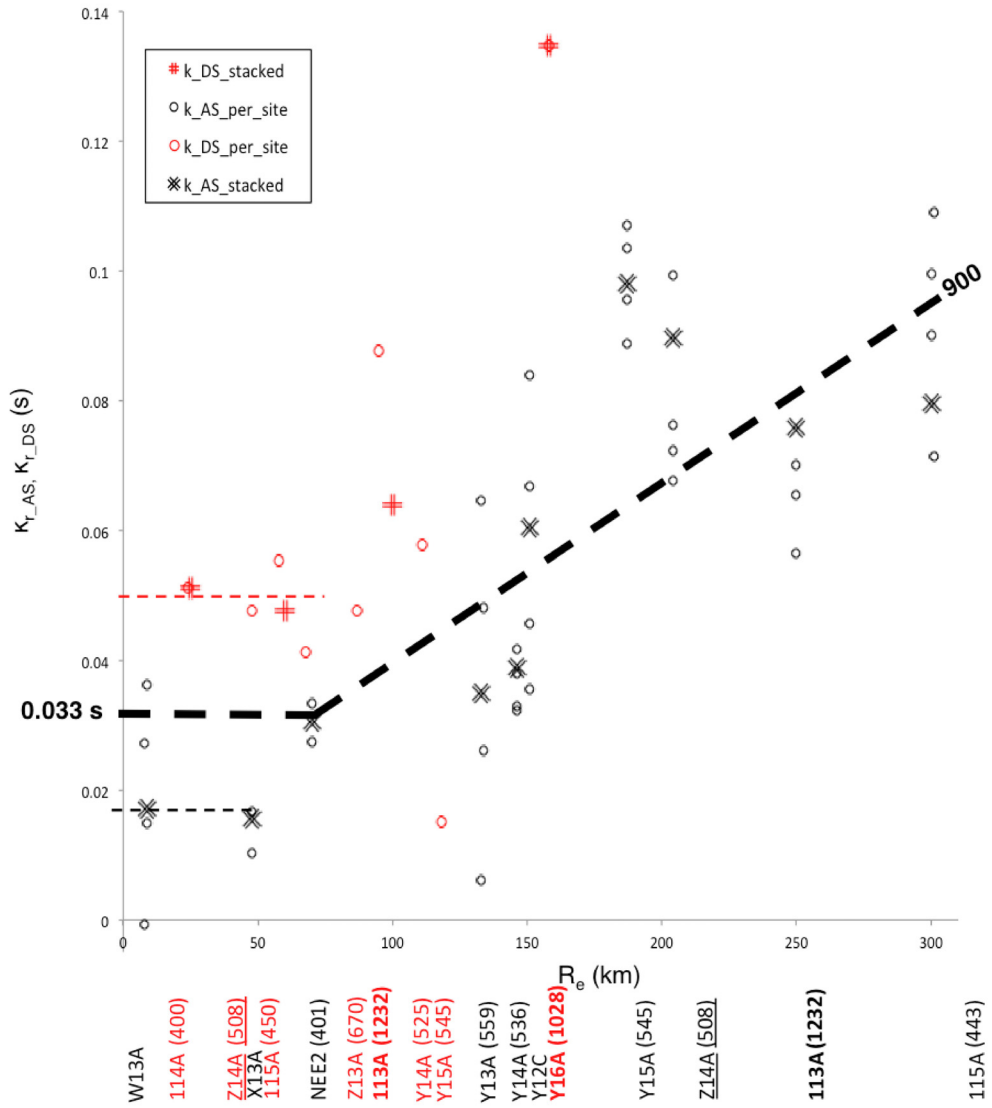
Figure 4.12(a) All measured κ_{r_DS} (red) and κ_{r_AS} (black) values versus epicentral distance. The names of the stations are accompanied by the $V_{S,30}$ values and the same color code (asterisk means inferred value). The final proposed model (thick dashed line) over all the sites studied has κ_0 = 0.033 sec and Q = 900. The green range shows possible Q values from regressions on our data points from the Arizona records.
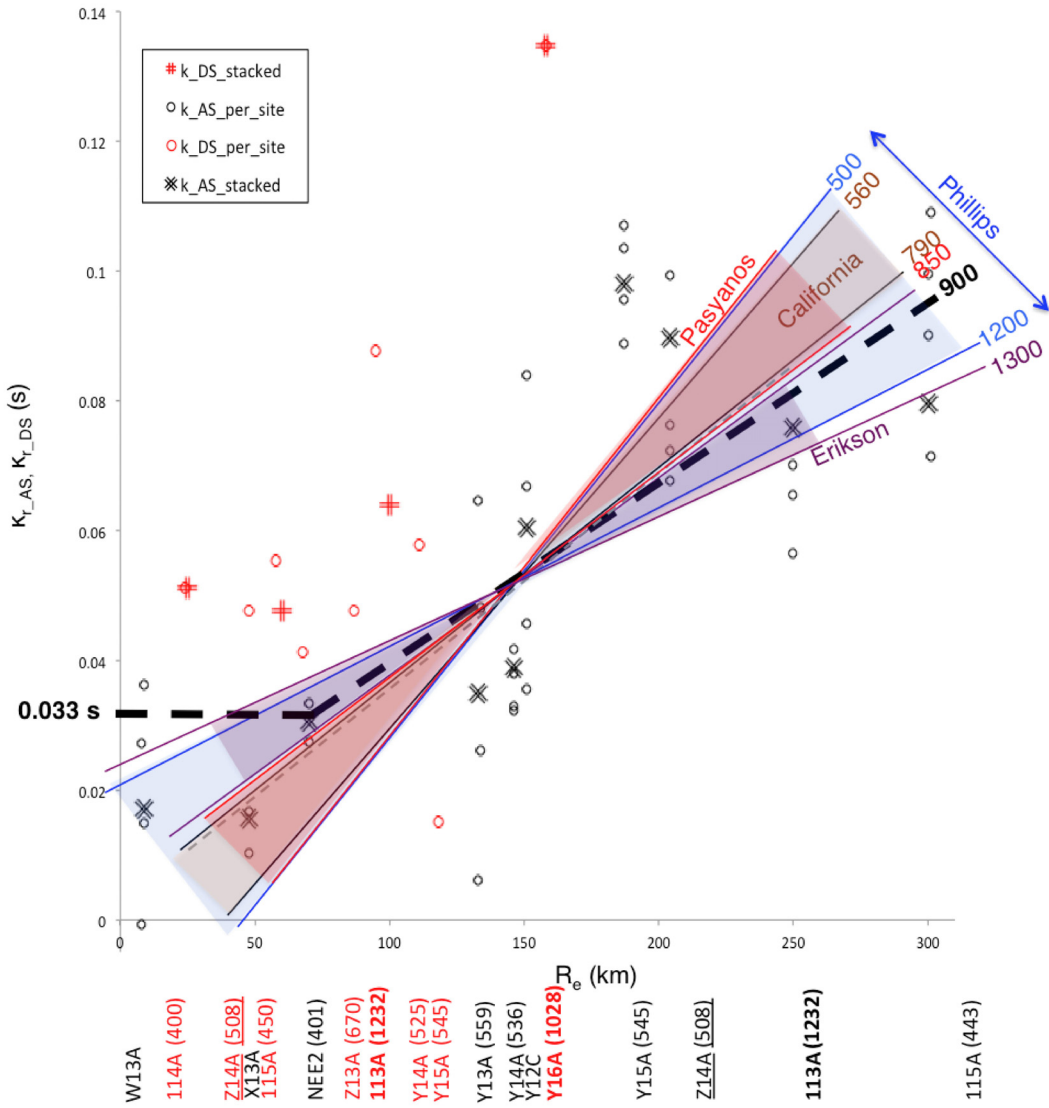
Figure 4.12(b) Comparison with *Q* models from literature. Blue range: Arizona Q_{Lg} values of Phillips et al. [2013] for 6–12 Hz. Red range: southern Arizona Q_s values from Pasyanos [2013] for 9–16 Hz. Brown range: typical California *Q* values for 9–16 Hz. Purple range: Erikson et al. [2004] Q_{Lg} values for the Basin and Range between 9–16 Hz.

4.4.3 Preferred Model from Methods 1 and 2, and Assessment of Uncertainty

Combining all the results from Methods 1 and 2, we propose a 'hockey-stick' dependence of κ_r with distance; κ_r may remain constant over the first 50–100 km from the source (Figure 4.12). This will yield a value of κ_0 ranging from 19–47 m/sec, depending on the hockey-stick distance selected. κ_r then increases with distance due to path attenuation at a slope that depends on the hockey-stick distance and whether or not we use the results from several outliers discussed earlier. The slope corresponds to a mean underlying crustal Q of 900 (shown in the figure in green), with a range from 600 to 1300. Again the range in Q depends on the hockey-stick distance assumed and whether outliers are included or not. This range of Q values is somewhat higher than typical Californian Q_s values (brown) and southern Arizona values by Pasyanos [2013] (red). Our range is near the lower bound of the Q_{Lg} given by Phillips et al. [2013] (blue) and falls within the Q_{Lg} values of Erikson et al. [2004], (purple). Our preferred model (thick dashed line) has $\kappa_0 = 0.033\pm14$ sec out to 70 km, at which point κ_0 increases with distance assuming a Q of 900±300. Figure 4.13 shows the residuals between the data and the final proposed model shown in Figure 4.12 versus distance and $V_{S,30}$. The residuals are well centered, with the exception of site Y16A, which has an unusually high κ value for a stiff rock site.

This preferred κ model averages over all stations, whose Vs_{30} values range from 400–1232 m/sec, but lie mostly between 450–550 m/sec. The site investigation at Z14A (the closest station to the PVNGS) has a $V_{S,30}$ of 508 m/sec (Chapter 3). Previous measurements at the PVNGS itself yielded a value of 350 m/sec [Walling, *personal communication*, 2012], which is lower than all other sites investigated in this study (the velocities measured at sites NEE2 and 114A are the lowest with $V_{S,30}$ of 400 m/sec). In the DS approach, we observe no clear scaling of $\kappa_{\_DS}$ with $V_{S,30}$; furthermore, the closest observation is from 114A at 25 km, which may be representative of the PVNGS in terms of distance and $V_{S,30}$. Hence we consider that the value of $\kappa_{0\_DS} = 0.050$ sec to be a reasonable upper limit for κ_0 for the surface conditions at the PVNGS. The lower limit of $\kappa_{0\_AS} = 0.017$ sec for distances less than 50 km is controlled by sites W13A and X13A, with inferred $V_{S,30}$ values of 425 and 660 m/sec. For site NEE2 (which should be representative of the PVNGS in terms of measured Vs_{30}, if not distance), the prediction of the preferred model lies near the measured value.

We also checked the sensitivity of our results to the correction for crustal amplification. If we consider a unit transfer function (i.e., if we use the Fourier amplitude spectra without correcting them with site crustal amplification transfer function), then the κ values estimated for both methods are lower. Out to 60 km, we find mean $\kappa_{0\_DS} = 0.034$ sec and mean $\kappa_{0\_AS} = 0.011$ sec, with an overall mean $\kappa_0 = 0.021$ sec (55% lower than our preferred κ_0 in this study). The Q model we find is almost the same as for the corrected data, i.e., around 900. For Methods 1 and 2 the change in the crustal amplification (Figure 4.16) strongly affects the κ estimates. In Method 3, as discussed below, similar changes in crustal amplification affect primarily the moment magnitude, leaving κ essentially unaffected.

Finally, we attempt to interpret the scatter in the measured κ_r values by accounting for site conditions. Chapter 3 estimates *Vs* profiles for 10 of these stations. Based on those profiles, and assuming an empirical rule of thumb for *Q* (*Q*~0.10*Vs* m/sec according to K. Olsen [*Personal communication*, 2014], we estimate the amount of κ_r at each site due to the near-surface stiff soil layers. Hough and Anderson [1988] proposed that κ_0 could be integrated along the raypath in an analogy to t^* based on *Q* and *Vs* in the shallow crust layers, and under the conditions described by Anderson [1991]; this can be written as a sum over each layer:

$$t^* = \int\limits_{path} \frac{dr}{V_s(z)Q(z)} = \sum \frac{H}{V_s Q} = \kappa_0 \tag{4.2}$$

For several sites where the SASW measurements penetrated bedrock (113A, 114A, Z13A, Z14A, and Y16A), the κ_r for the underlying rock should be equal to or lower than the total measured κ_r value at the site after this t^* quantity due to the stiff soil has been removed. However, t^* is less than 3 m/sec at these sites, and hence the large scatter in measured κ_r values cannot be explained by the differences in the *Q* (damping) of the near-surface materials. It is more likely that the band limitation of the data and the earthquake magnitudes (which may cause trade-offs with the source), the large distances (which cause trade-offs with path *Q*), and possible local resonance effects prevent us from achieving a more accurate estimate of κ.
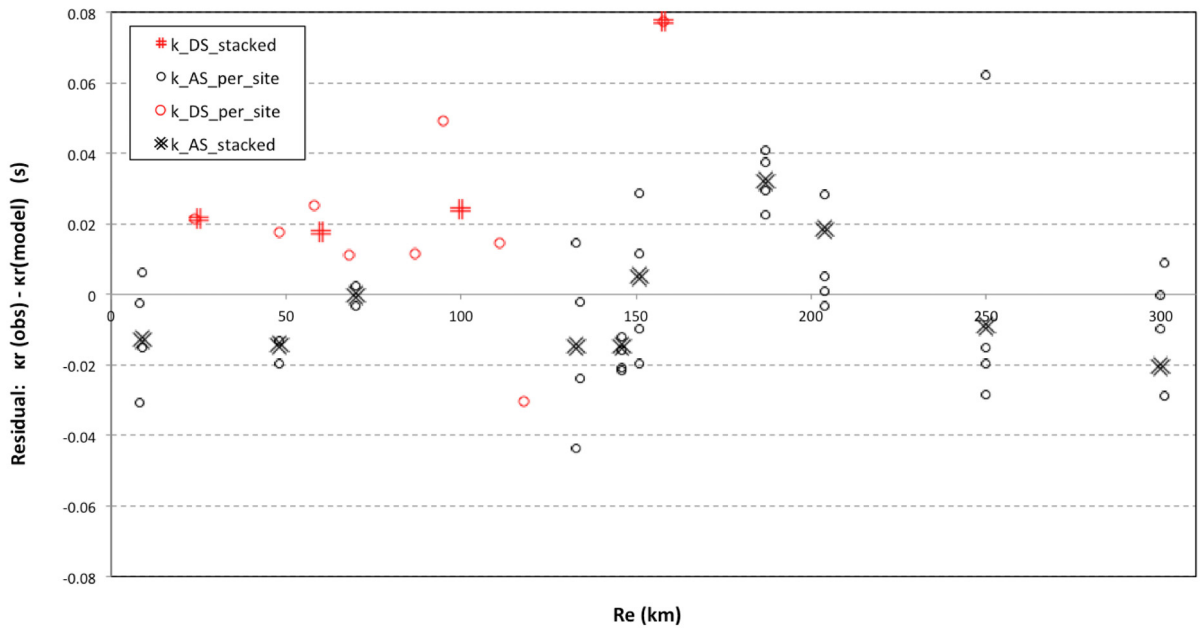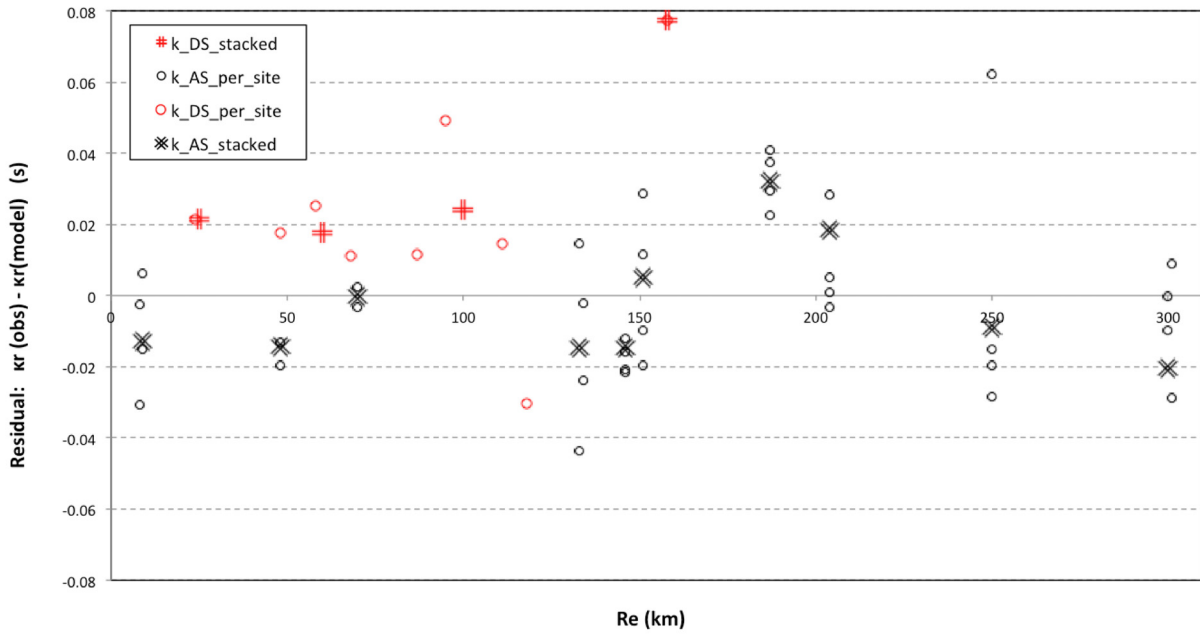
Figure 4.13   Residuals of all measured $\kappa_{\mathrm{r\_DS}}$ (red) and $\kappa_{\mathrm{r\_AS}}$ (black) values with respect to the final proposed model versus epicentral distance (top) and $V_{S,30}$ (bottom). The largest outlier is site Y16A.

Table 4.2   Individual measured κ_{r} values using different approaches and stacking options.

Site	$\kappa_{\mathrm{r}}(s)$	Method	Site	$\kappa_{\mathrm{r}}(s)$	Method	Site	$\kappa_{\mathrm{r}}(s)$	Method
113A	0.057	AS_individual	Y13A	0.028	AS_individual	X13A	0.016	AS_stacked
113A	0.090	AS_individual	Y13A	0.015	AS_individual	Y12C	0.060	AS_stacked
113A	0.034	AS_individual	Y13A	0.036	AS_individual	Y13A	0.035	AS_stacked
113A	0.036	AS_individual	Y13A	0.065	AS_individual	Y14A	0.039	AS_stacked
115A	0.046	AS_individual	Y14A	0.042	AS_individual	Y15A	0.098	AS_stacked
115A	0.006	AS_individual	Y14A	0.107	AS_individual	Z14A	0.090	AS_stacked
115A	0.038	AS_individual	Y14A	0.076	AS_individual	113A	0.088	DS_per_site
115A	0.103	AS_individual	Y14A	0.070	AS_individual	114A	0.051	DS_per_site
W13A	0.068	AS_individual	Y15A	0.071	AS_individual	115A	0.055	DS_per_site
W13A	0.147	AS_individual	Y15A	-0.001	AS_individual	Y14A	0.058	DS_per_site
W13A	0.109	AS_individual	Y15A	0.010	AS_individual	Y15A	0.015	DS_per_site
W13A	0.027	AS_individual	Y15A	0.067	AS_individual	Z13A	0.048	DS_per_site
X13A	0.017	AS_individual	Z14A	0.026	AS_individual	Z14A	0.048	DS_per_site
X13A	0.084	AS_individual	Z14A	0.033	AS_individual	Z15A	0.041	DS_per_site
X13A	0.048	AS_individual	Z14A	0.089	AS_individual	Y16A	0.135	DS_per_site
X13A	0.032	AS_individual	Z14A	0.099	AS_individual	25-km radius	0.051	DS_per_R_bin
Y12C	0.096	AS_individual	113A	0.076	AS_stacked	55-km radius	0.048	DS_per_R_bin
Y12C	0.072	AS_individual	115A	0.080	AS_stacked	95-km radius	0.064	DS_per_R_bin
Y12C	0.065	AS_individual	NEE2	0.031	AS_stacked	160-km radius	0.135	DS_per_R_bin
Y12C	0.100	AS_individual	W13A	0.017	AS_stacked			

4.4.4 Method 3

The broadband inversion model parameters include R_C (cutoff distance from $1/R$ to $1/\sqrt{R}$ geometrical spreading), Q_0, η, Δ_σ (bars), Brune point-source shear-wave velocity (β) and density (ρ), **M**, and crustal amplification (*f*). Inversion parameters typically consist of **M**, Q_0, η, R_C, and κ. For datasets with an insufficient range in distances, strong parameter coupling necessitates fixing both Q_0 and η, and occasionally R_C (which was the case for the Arizona data). Initial parameters for the Arizona analyses with crustal amplification are listed in Table 4.5 and illustrated in Figure 4.16. Broadband inversions were done for Δ_σ (f_c), **M**, and κ for 14 sites (see Tables 4.3 and 4.4).

Starting values for Δ_σ and κ were 5 bars and 0.04 sec, respectively. Magnitudes were given as summarized in Table 4.4 (from Table 2.2, Chapter 2). Initial inversions omitted the three earthquakes listed in Table 4.4 with very shallow hypocentral depths equal to 1 km, i.e., earthquakes 1267, 1268, and 1269. Since the major contributions to κ (κ_0) are thought to occur through damping over the top 1 m to several km of the crust, it was considered that the very shallow depth (1 km), if accurate, may bias the recordings by also including the effects of shallow crustal damping below the source depth. However the inversions omitting the three shallow earthquakes resulted in poor convergence due to the limited distance range combined with the limited bandwidth of the

remaining earthquakes and sites (about 50–200 km, see Table 4.4). The three shallow earthquakes span the largest distance range from about 9 to 300 km, and their inclusion provided a significant reduction to the uncertainty in κ. As previously mentioned, Q_0 and η were fixed at 200 and 0.68, respectively, based on the Erickson et al. [2004] $Q(f)$ estimates, relative to a geometrical spreading of $1/\sqrt{R}$, for the Basin and Range province. Initial inversions for **M**, Δ_σ, κ, and R_C both with and without the three shallow earthquakes consistently showed results for R_C of about 40 km, where it was held fixed for all subsequent inversions.

Results of the inversions are listed in Table 4.5, which shows the Q_0 and η values, median κ over the 14 sites, mean magnitude, and the mean/median ratio of the fit to the FAS, which reflects a "goodness of fit" measure. Stress drops were not listed as the narrow bandwidth precludes reliable estimates for **M** less than about **M** 2. The limited bandwidth and limited distance range for several sites also resulted in moderate coupling among κ estimates between sites. As a result, the median estimate of κ is considered significantly more reliable than estimates at individual sites. For example, site Z15A had only two recordings at hypocentral distances of about 70 and 250 km (Table 4.4), site NEE2 had three recordings at about 70, 69, and 96 km, and site Y12C had three recordings each at about 150 km.

To assess stability of the median κ estimate, Table 4.5 shows the inversion results for a suite of $Q(f)$ models as well as unity amplification (Figure 4.16) at all sites. As shown inn Table 4.5, Model 1 reflects the best estimate of the median κ along with the mean **M** and mean/median ratio. In all cases the mean magnitude increased over the network magnitude values by about 10%, along with a considerable improvement in the overall fit, which is illustrated in Figures 4.17–4.38 for Model 1.

Because the region of earthquakes and site locations in Arizona is in the far southern portion of the Basin and Range province, adjacent to Southern California (Figure 2.3), Model 2 examines the effect of the Erickson et al. [2004] Southern California $Q(f)$ model on the inversions. The resulting median κ shows only a very small change from 0.033 sec to 0.034 sec, with a slight increase in mean **M** and mean/median ratio.

To examine the effect of a frequency-independent Q model implied in the Methods 1 and 2 approaches (Sections 4.4.1 and 4.4.2), Model 3 fixed Q_0 at 1000 and η at 0. The value of 1000 is close to the best estimate resulting from Methods 1 and 2. In this case the median κ estimate decreased to about 0.024 sec, a significant reduction of about 40%.

Finally, to assess the potential effect of amplification on the median κ estimate, Model 4 reflects results from an inversion with unity amplification (Figure 4.16). The resulting median κ estimate increased only slightly from 0.033 sec to 0.034 sec, with a significant increase in mean **M** to **M** 2.37, along with a poorer fit reflected in the increased mean/median ratio.

Interestingly, the individual site κ estimates show little dependence on site stiffness. The two stiffest (rock) sites (Table 4.4) have κ estimates of 0.046 sec and 0.051 sec for sites 113A and Y16A, respectively (Table 4.5). These two sites had recordings at closest hypocentral distances of

about 100 km and 160 km for sites 113A and Y16A, respectively. As a result, the effects of $Q(f)$ may have masked the effect of a κ value , which may be much lower than the current median estimate.

These results (Model 4) along with Model 2 results suggest the best estimate of the median κ across all 14 sites (Table 4.4) is about 0.033 sec and is relatively stable, but contingent on a $Q(f)$ model close to that of Erickson et al. [2004] for the region.

Table 4.3   All Arizona events.

Station name	N	M – M	Range hypo dist (km)	Range hypo depth (km)	$V_{S,30}$ (m/sec)
113A	7	1.5 - 3.4	96 - 250	1 – 13	1,237
114A	7	1.2 - 2.4	28 – 183	6 – 13	398
115A	9	1.2 - 3.4	59 – 301	1 – 13	460
NEE2	3	2.0 - 3.4	69 – 96	1 – 7	401
W13A	5	2.0 - 3.4	9 – 101	1 – 7	660
X13A	4	2.0 - 3.1	45 – 49	1 – 7	425
Y12C	3	2.1 - 3.4	152 – 152	1 – 1	660
Y13A	5	2.0 - 3.4	42 – 135	1 – 7	560
Y14A	9	1.5 - 3.4	82 – 147	1 – 13	520
Y15A	8	1.5 - 3.4	119 – 189	1 – 13	566
Y16A	4	1.5 – 1.5	158-159	13	1,028
Z13A	5	1.5 - 2.4	88 – 111	6 – 13	689
Z14A	11	1.2 – 3.4	50 – 206	1 – 13	524
Z15A	2	1.5 – 3.1	69 –251	1 – 13	407

Table 4.4   Arizona event summary.

		Station name	113A	114A	115A	Y14A	Y15A	Z13A	Z14A	Z15A	NEE2	W13A	X13A	Y13A	Y12C	Y16A	
		$V_{S,30}$ (m/sec)	1232	404	443	536	545	670	508	464	401	660*	425**	559	660*	1028	
		Site no.	1	2	3	4	5	6	7	8	9	10	11	12	13	14	
EQ ID	Mag	Hypo Depth (km)	Hypo Dist (km)	Hypo Dist (km)	Hypo Dist (km)	Hypo Dist (km)	Hypo Dist (km)	Hypo Dist (km)	Hypo Dist (km)	Hypo Dist (km)	Hypo Dist (km)	Hypo Dist (km)	Hypo Dist (km)	Hypo Dist (km)	Hypo Dist (km)	Hypo Dist (km)	
1267	3.1	1	250.46		301.16	146.47	187.52		204.65	251.40		8.88	48.27	134.32	151.91		
1268	3.4	1	250.13		300.88	146.20	187.31		204.36		70.25	9.20		133.99	151.60		
1269	2.1	1				147.54	188.79		205.56		69.27	9.08	48.83	134.74	151.72		
1270	2.4	6	157.74	182.77	223.23	82.49	142.00	111.12	123.84		96.10	101.31		45.40	41.92		
1271	2.0	7				84.13	143.68	111.45	125.02			101.32		45.62	42.16		
1272	1.5	13	96.01	27.72	59.68	112.23			50.01							159.00	
1273	1.5	13	96.03	27.81	59.73	112.12	119.01	87.83	49.90							158.93	
1274	1.5	13	96.26	28.06	59.67	111.94	118.74	87.93	49.76	69.47						158.93	
1275	1.5	13	96.35	28.09	59.59	111.96	118.70	88.02	49.79							158.57	
1276	1.5	13		28.04	59.46				49.93								
1277	1.2	13		28.13	59.51				49.82								
Total Recordings			7	7	9	9	8	5	11	2	3	5	4	5	3	4	82

*Geomatrix 3rd letter A proxy $V_{S,30}$ estimate of 660m/sec
**Geomatrix 3rd letter B proxy $V_{S,30}$ estimate of 425m/sec

Table 4.5   **Inversion results.**

	Q	η	$\overline{\kappa}(\text{s})$	$\overline{\mathbf{M}}$	Mean/median	Amplification
Starting Model*	200	0.68	0.040	1.97	1.56	rock/soil
Model 1	200**	0.68**	0.033	2.14	1.13	rock/soil
Model 2	152**	0.72**	0.034	2.17	1.16	rock/soil
Model 3	1000**	0.00**	0.024	2.00	1.12	rock/soil
Model 4	200**	0.68**	0.034	2.37	1.15	unity

*Source Region Shear-wave velocity, density and R_C: 3.5 km/sec, 2.75cgs and 80 km, respectively
**Fixed Parameters, R_C fixed at 40 km

Site no. (Table 4.4)	Site	$\kappa_0(\text{s})$ (Model 1)
1	113A	0.046
2	114A	0.030
3	115A	0.048
4	Y14A	0.023
5	Y15A	0.052
6	Z13A	0.058
7	Z14A	0.032
8	Z15A	0.015
9	NEE2	0.025
10	W13A	0.045
11	X13A	0.024
12	Y13A	0.015
13	Y12C	0.043
14	Y16A	0.051
Median		**0.033**

Table 4.6   Parameter variations.

Parameter variations	Change in median kappa [κ(s)]
$Q_0/1.5$	$\kappa/1.14$
$Q_0 * 1.5$	$\kappa * 1.03$
$\eta/1.5$	$\kappa/1.32$
$\eta * 1.5$	$\kappa * 1.21$
$R_C/1.5$	$\kappa * 1.02$
$R_C * 1.5$	$\kappa * 1.03$
$\kappa/2$	$\kappa * 1.01$
$\kappa * 2$	$\kappa * 1.01$
$\Delta_\sigma * 2$	$\kappa * 1.09$
$\Delta_\sigma/2$	$\kappa/1.06$
amp/1.3[1]	$\kappa * 1.03$

[1] Replaced rock and soil crustal amplification (Figure 4.16) with unity.

Note in all cases relative difference for individual sites varied from less than about 10% to over 100% depending on the parameter varied.
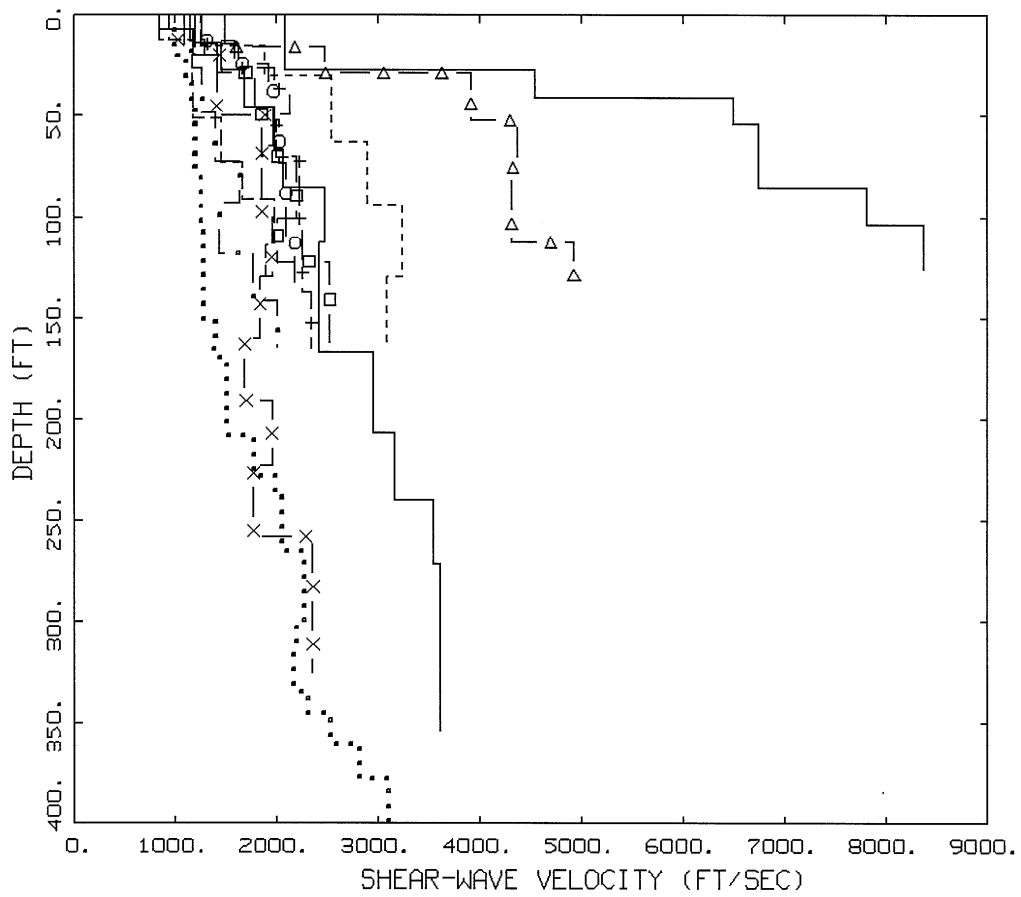
Figure 4.14 Site-specific shear-wave velocity profiles and corresponding $V_{S,30}$ value based on SASW surveys (Chapter 3) at recording sites (Table 4.4) as well as the Palo Verde Nuclear Generating Station.
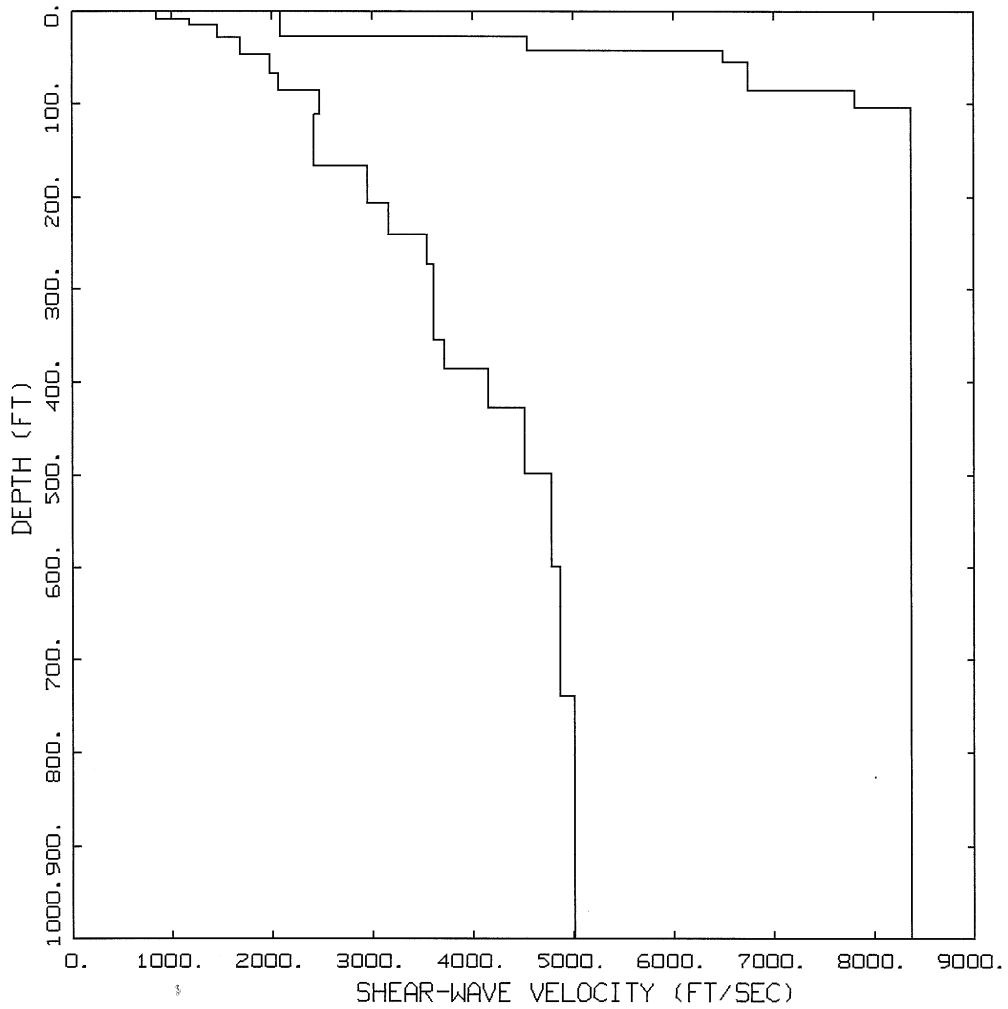
REFERENCE PROFILES

Figure 4.15 **Case-specific reference profiles for stiff soil (VS,30 = 508 m/sec, profile Z14A Figure 4.14) and firm rock ($V_{S,30}$ = 1028 m/sec, profile 113A Figure 4.14).**
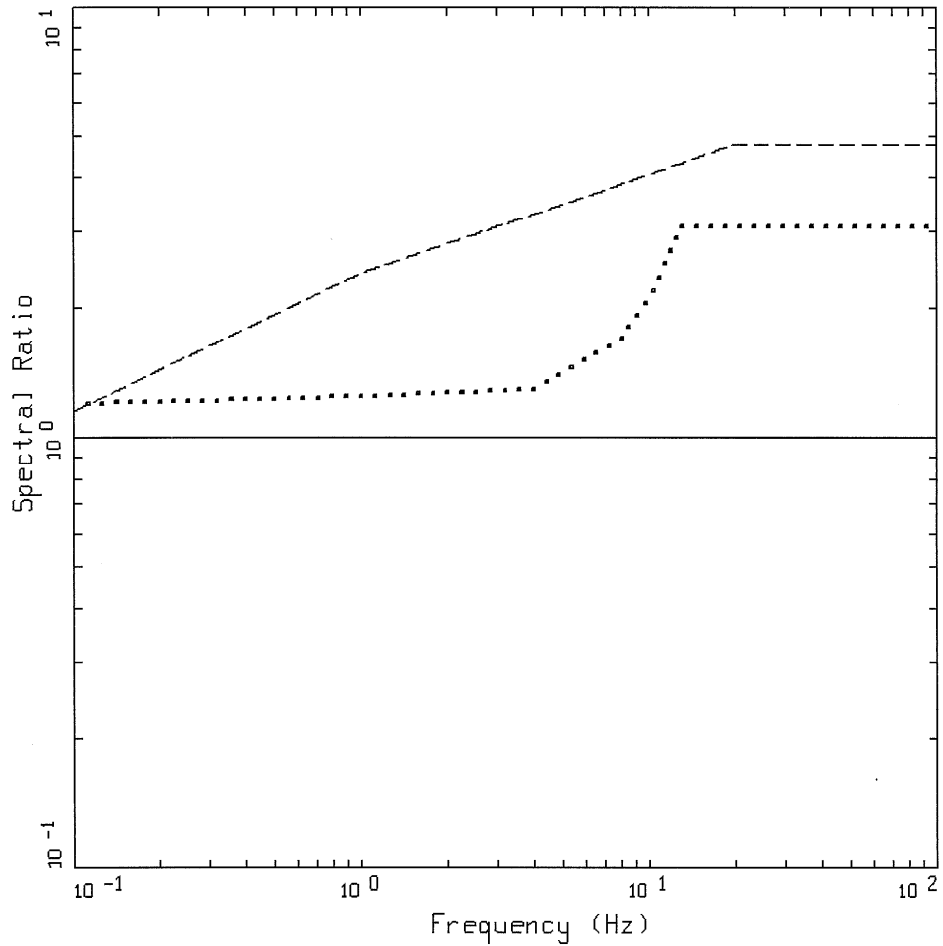
ARIZONA TRANSFER FUNCTIONS

LEGEND
— — — —   Z14A(FIRM SOIL) TRANSFER FUNCTION
• • • •   113A(ROCK) TRANSFER FUNCTION
————   UNITY TRANSFER FUNCTION

Figure 4.16   Smoothed case-specific Arizona crustal transfer functions (FAS) for (1) recording site Z14A (stiff soil); and (2) recording site 113A (firm rock). Both profiles are shown in Figure 4.15.
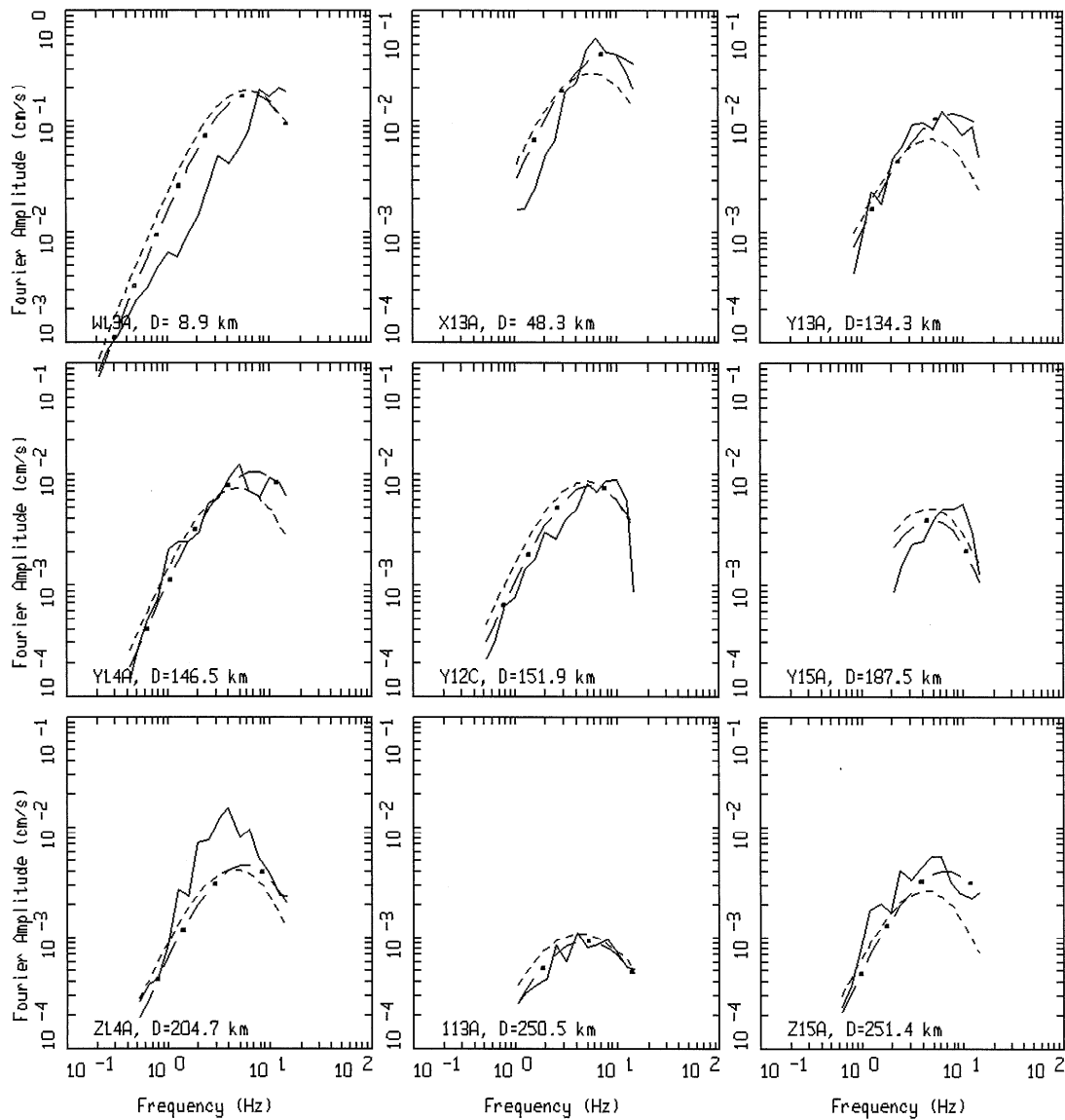
72

ARIZONA EARTHQUAKES: EQID 1267, PAGE 1 OF 2.
BASE CASE RUN: M 3.1, Z=1.0 KM

LEGEND
———————   DATA
– – – –   INITIAL MODEL
— ▪ —   FINAL MODEL

Figure 4.17   Comparison of the Model 1 broadband (initial and final) models with the recorded FAS data at sites that recorded earthquake 1267 (Table 4.4) (logarithmic frequency axes).
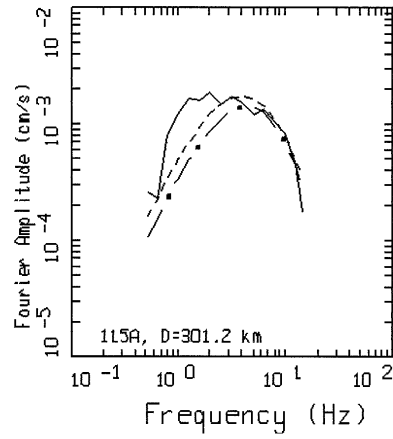
ARIZONA EARTHQUAKES: EQID 1267, PAGE 2 OF 2.
BASE CASE RUN: M 3.1, Z=1.0 KM

LEGEND
—————— DATA
- - - - - INITIAL MODEL
—— • —— FINAL MODEL

Figure 4.16   (Continued)
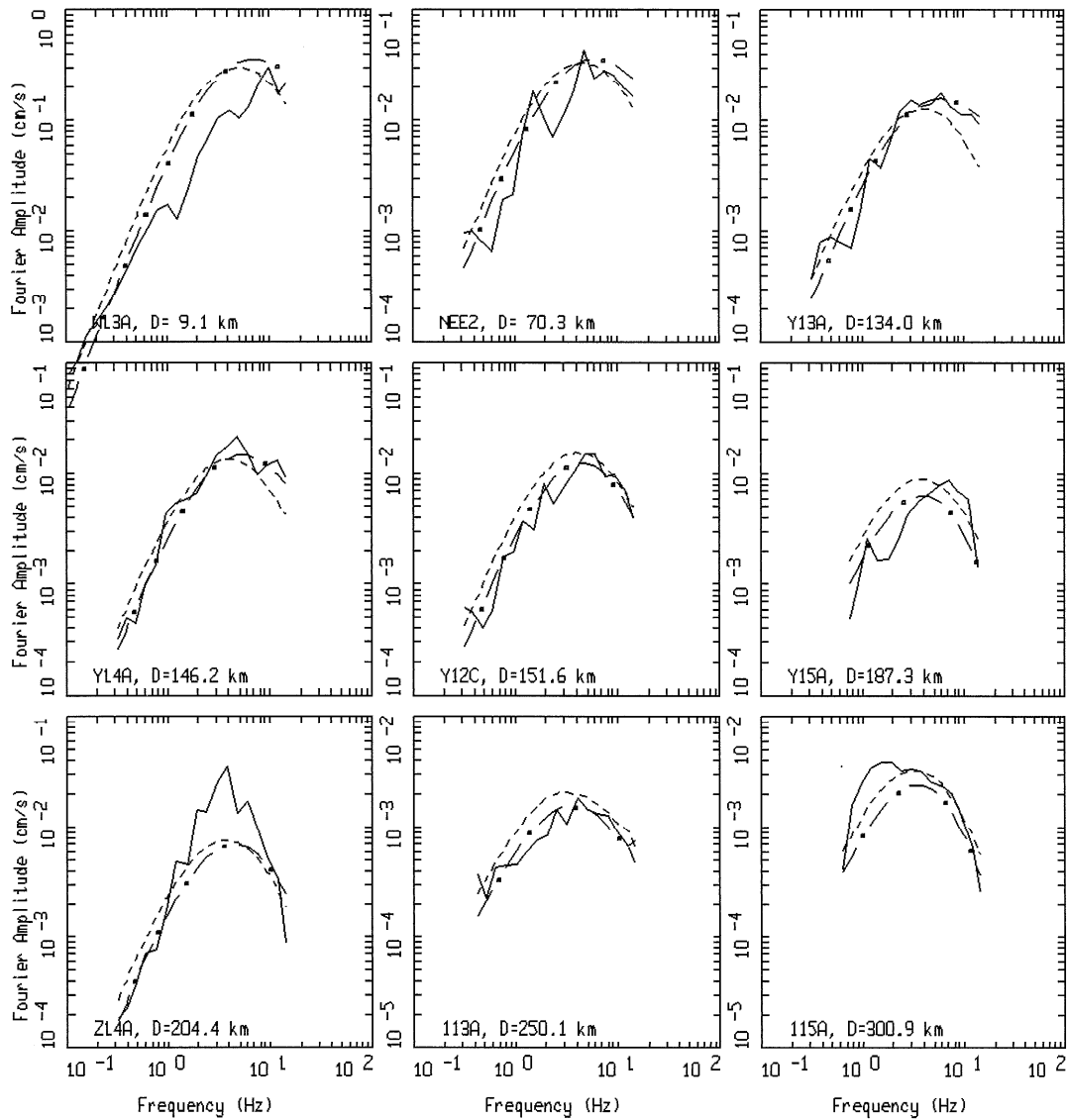
ARIZONA EARTHQUAKES: EQID 1268, PAGE 1 OF 1.
BASE CASE RUN: M 3.4, Z=1.0 KM

	LEGEND
————	DATA
- - - - -	INITIAL MODEL
— • —	FINAL MODEL

Figure 4.17   **Comparison of the Model 1 broadband (initial and final) models with the recorded FAS data at sites that recorded earthquake 1268 (Table 4.4) (logarithmic frequency axes)**
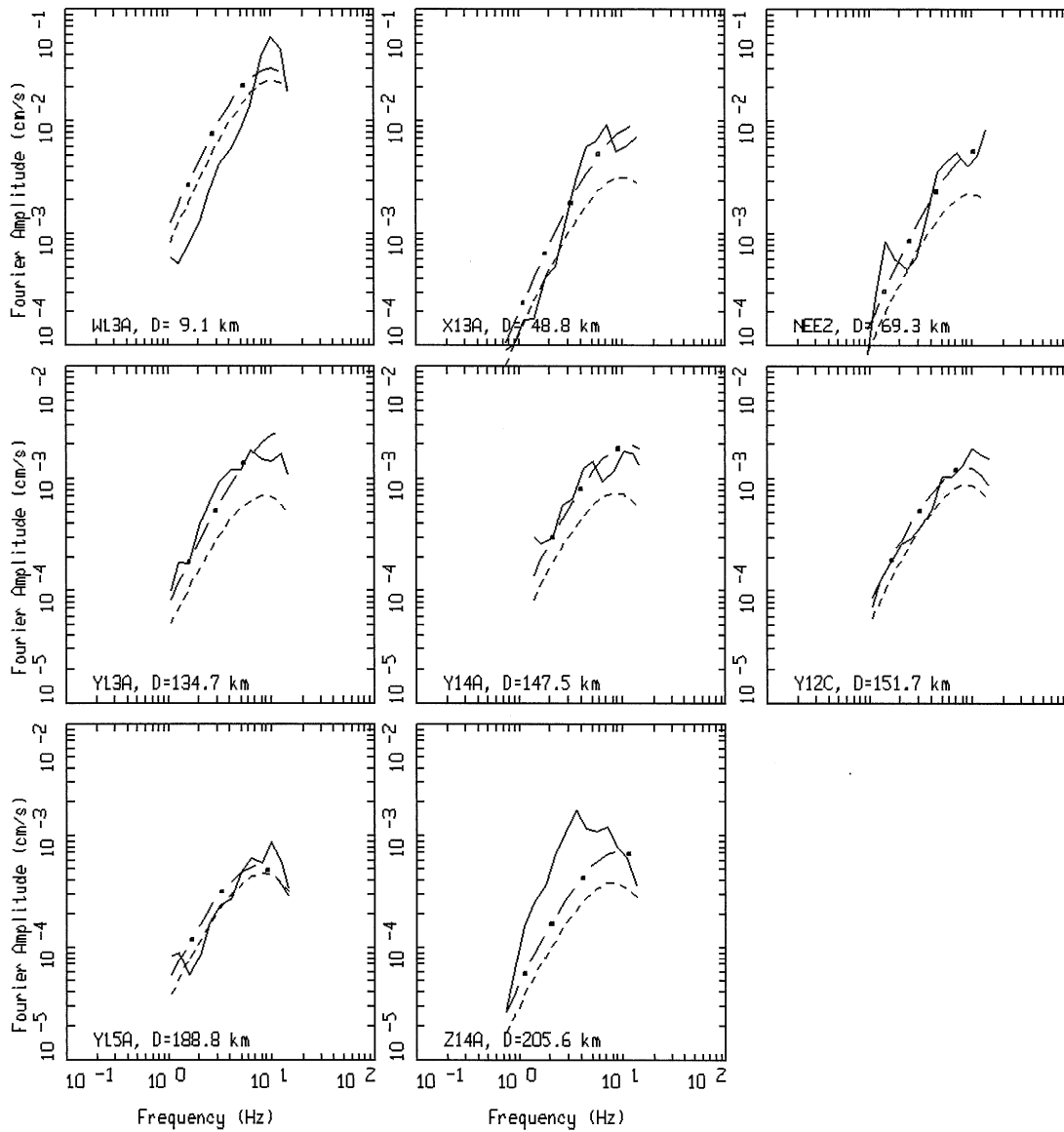
ARIZONA EARTHQUAKES: EQID 1269, PAGE 1 OF 1.
BASE CASE RUN: M 2.1, Z=1.0 KM

LEGEND
DATA
INITIAL MODEL
FINAL MODEL

Figure 4.18   **Comparison of the Model 1 broadband (initial and final) models with the recorded FAS data at sites that recorded earthquake 1269 (Table 4.4) (logarithmic frequency axes)**
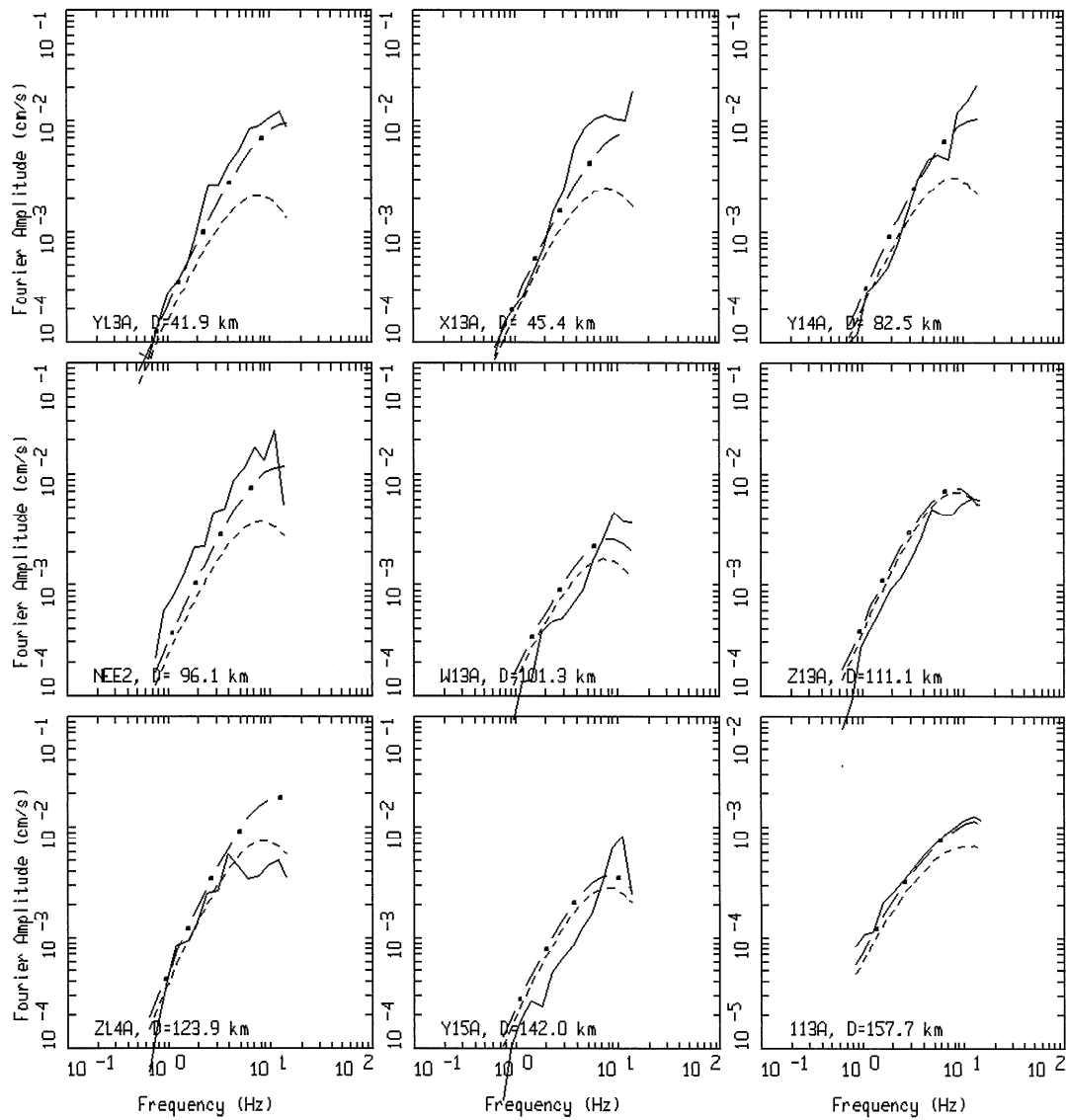
ARIZONA EARTHQUAKES: EQID 1270, PAGE 1 OF 2.
BASE CASE RUN: M 2.4, Z=6.0 KM

LEGEND
—————— DATA
— — — — INITIAL MODEL
—— • —— FINAL MODEL

Figure 4.19   Comparison of the Model 1 broadband (initial and final) models with the recorded FAS data at sites that recorded earthquake 1270 (Table 4.4) (logarithmic frequency axes).
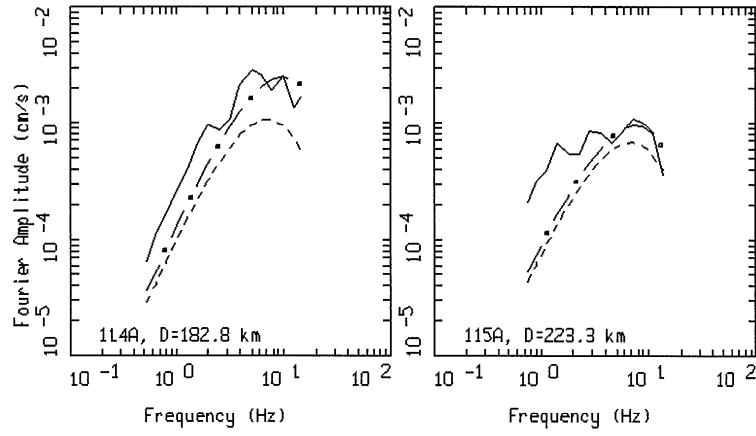
ARIZONA EARTHQUAKES: EQID 1270, PAGE 2 OF 2.
BASE CASE RUN: M 2.4, Z=6.0 KM

LEGEND
——————   DATA
- - - - -   INITIAL MODEL
— ▪ —   FINAL MODEL

Figure 4.20   Continued.
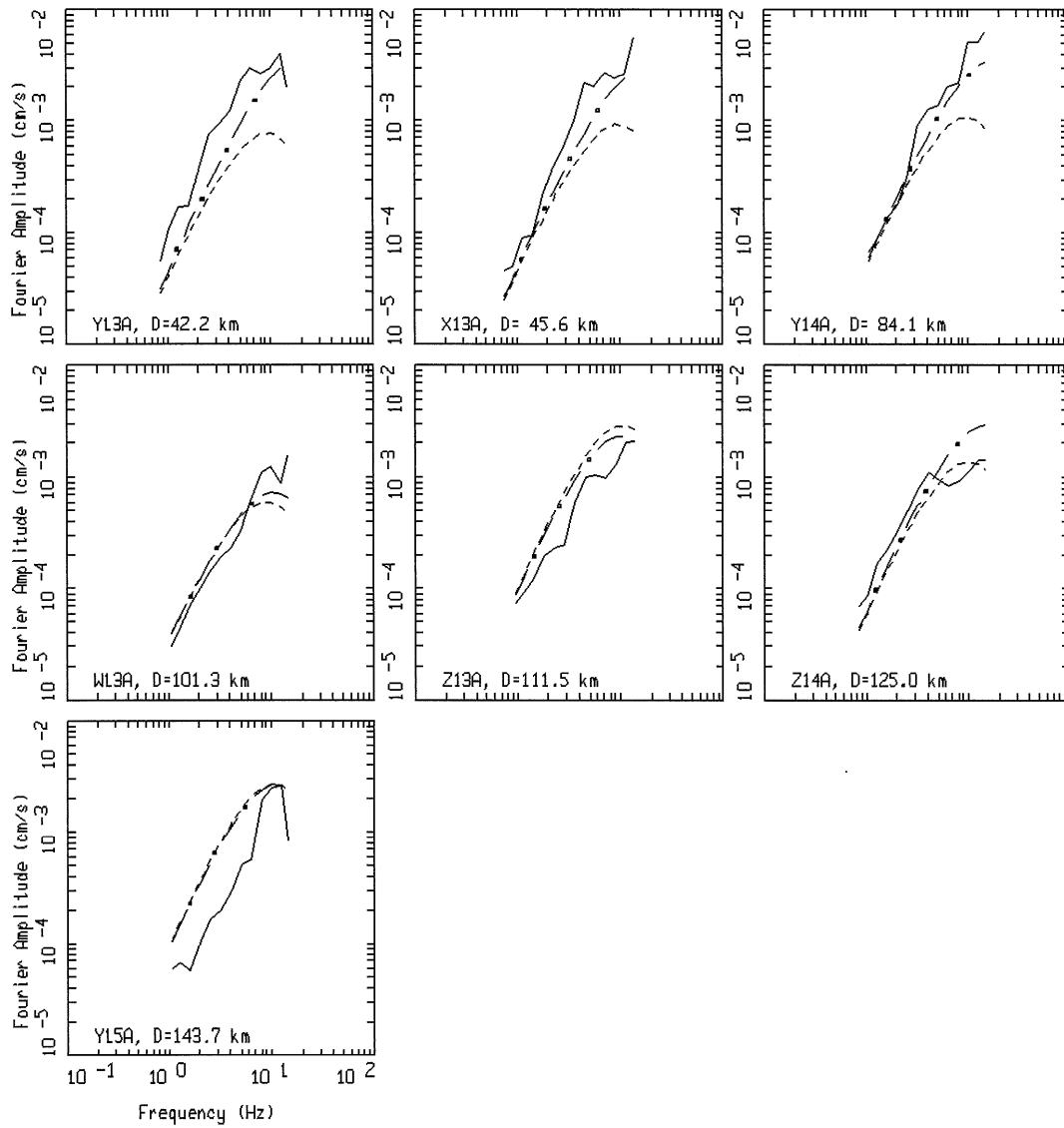
ARIZONA EARTHQUAKES: EQID 1271, PAGE 1 OF 1.
BASE CASE RUN: M 2.0, Z=7.0 KM

LEGEND
DATA
INITIAL MODEL
FINAL MODEL

Figure 4.20 **Comparison of the Model 1 broadband (initial and final) models with the recorded FAS data at sites that recorded earthquake 1271 (Table 4.4) (logarithmic frequency axes).**
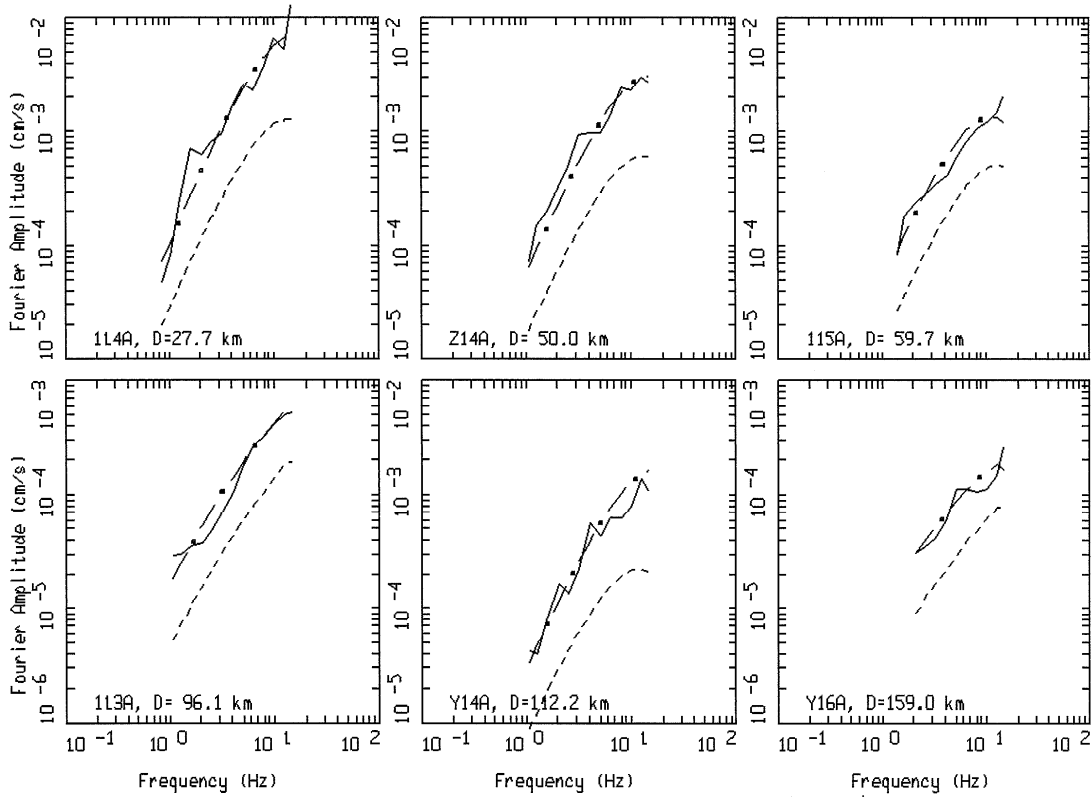
ARIZONA EARTHQUAKES: EQID 1272, PAGE 1 OF 1.
BASE CASE RUN: M 1.5, Z=13.0 KM

LEGEND
——————— DATA
— — — — — INITIAL MODEL
— • — FINAL MODEL

Figure 4.21 **Comparison of the Model 1 broadband (initial and final) models with the recorded FAS data at sites that recorded earthquake 1272 (Table 4.4) (logarithmic frequency axes).**
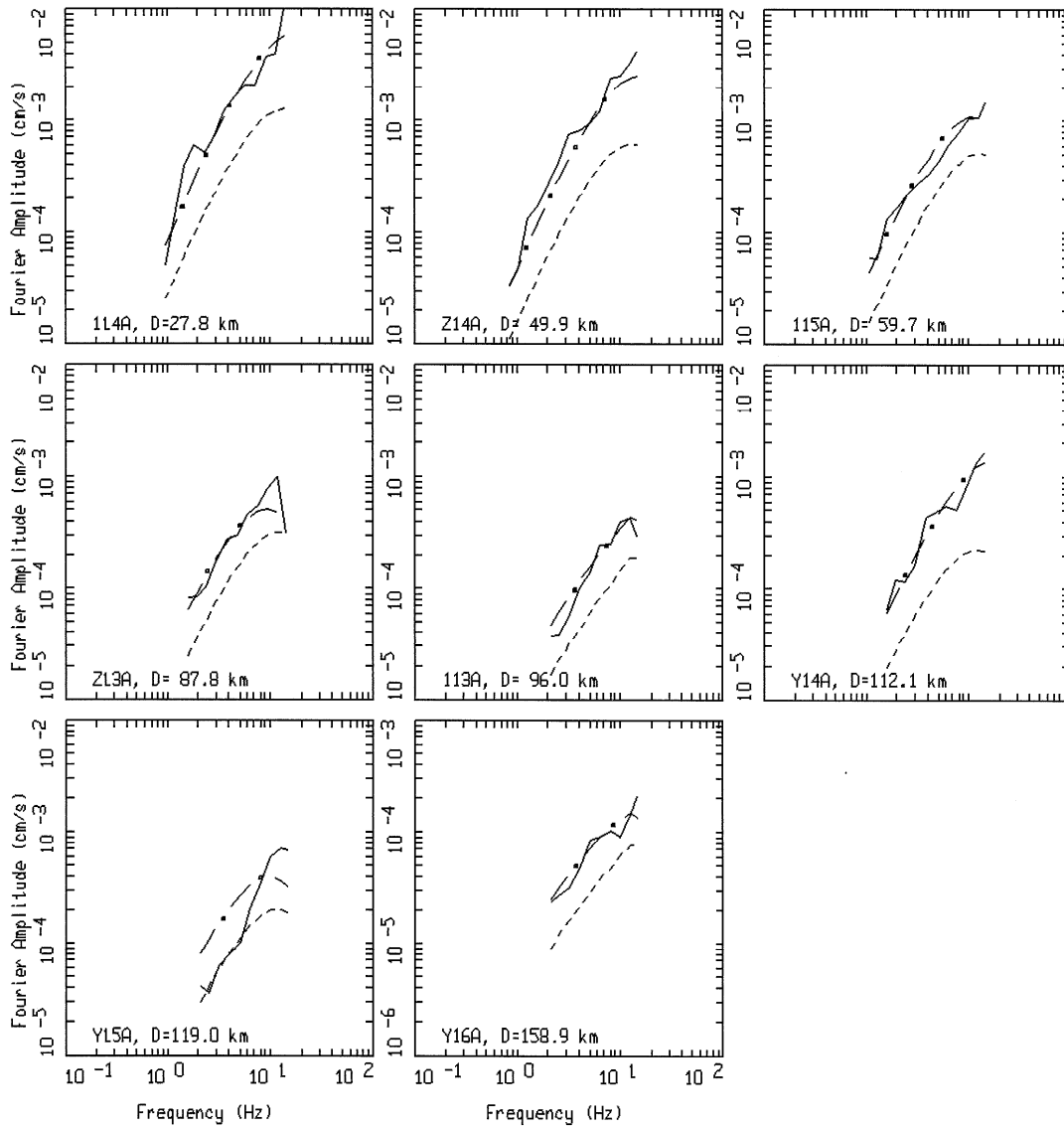
ARIZONA EARTHQUAKES: EQID 1273, PAGE 1 OF 1.
BASE CASE RUN: M 1.5, Z=13.0 KM

LEGEND
———————— DATA
- - - - - INITIAL MODEL
— · — FINAL MODEL

Figure 4.22   **Comparison of the Model 1 broadband (initial and final) models with the recorded FAS data at sites that recorded earthquake 1273 (Table 4.4) (logarithmic frequency axes).**
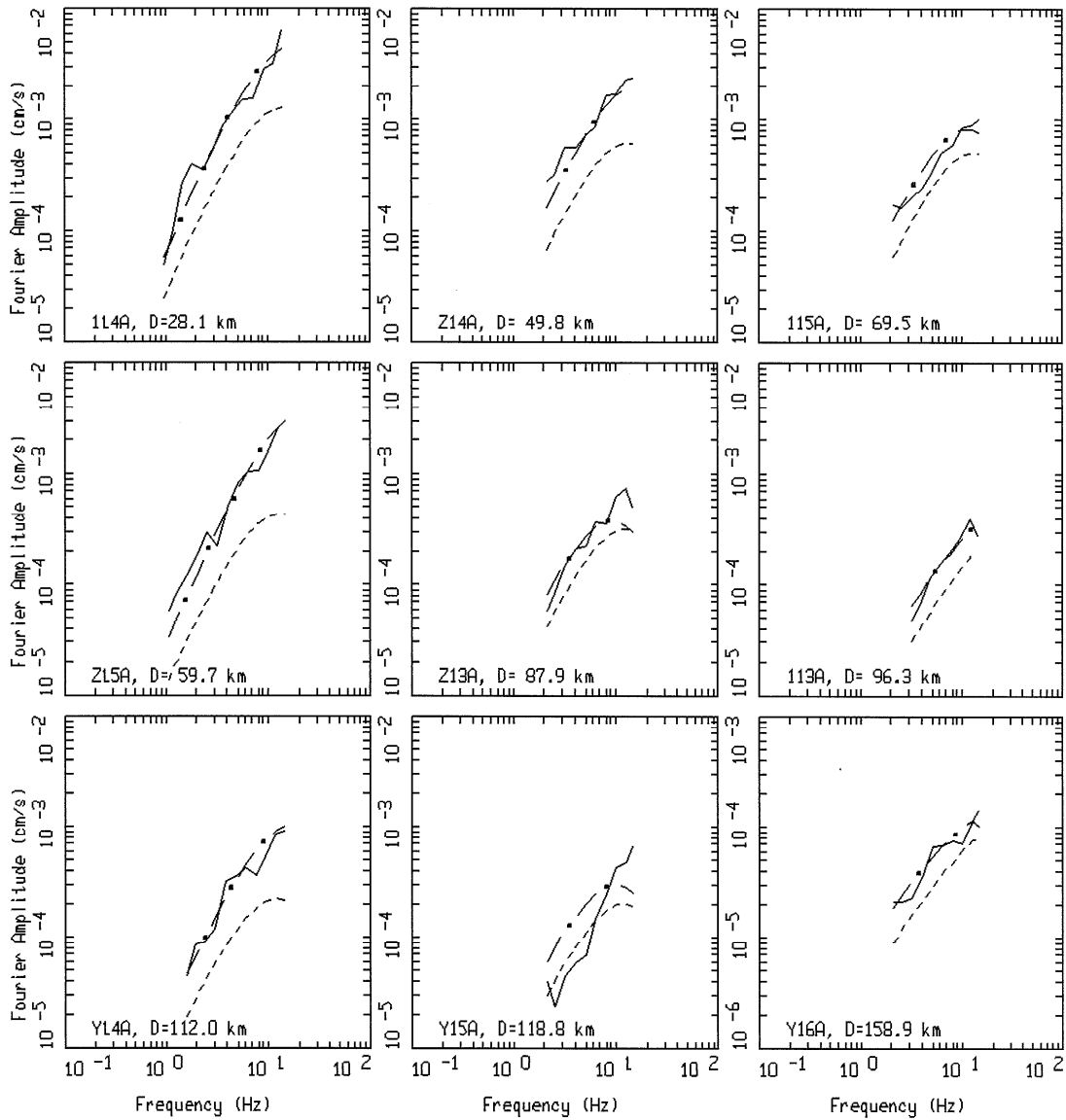
ARIZONA EARTHQUAKES: EQID 1274, PAGE 1 OF 1.
BASE CASE RUN: M 1.5, Z=13.0 KM

LEGEND
——————— DATA
- - - - - INITIAL MODEL
—— • —— FINAL MODEL

Figure 4.23   Comparison of the Model 1 broadband (initial and final) models with the
recorded FAS data at sites that recorded earthquake 1274 (Table 4.4)
(logarithmic frequency axes).
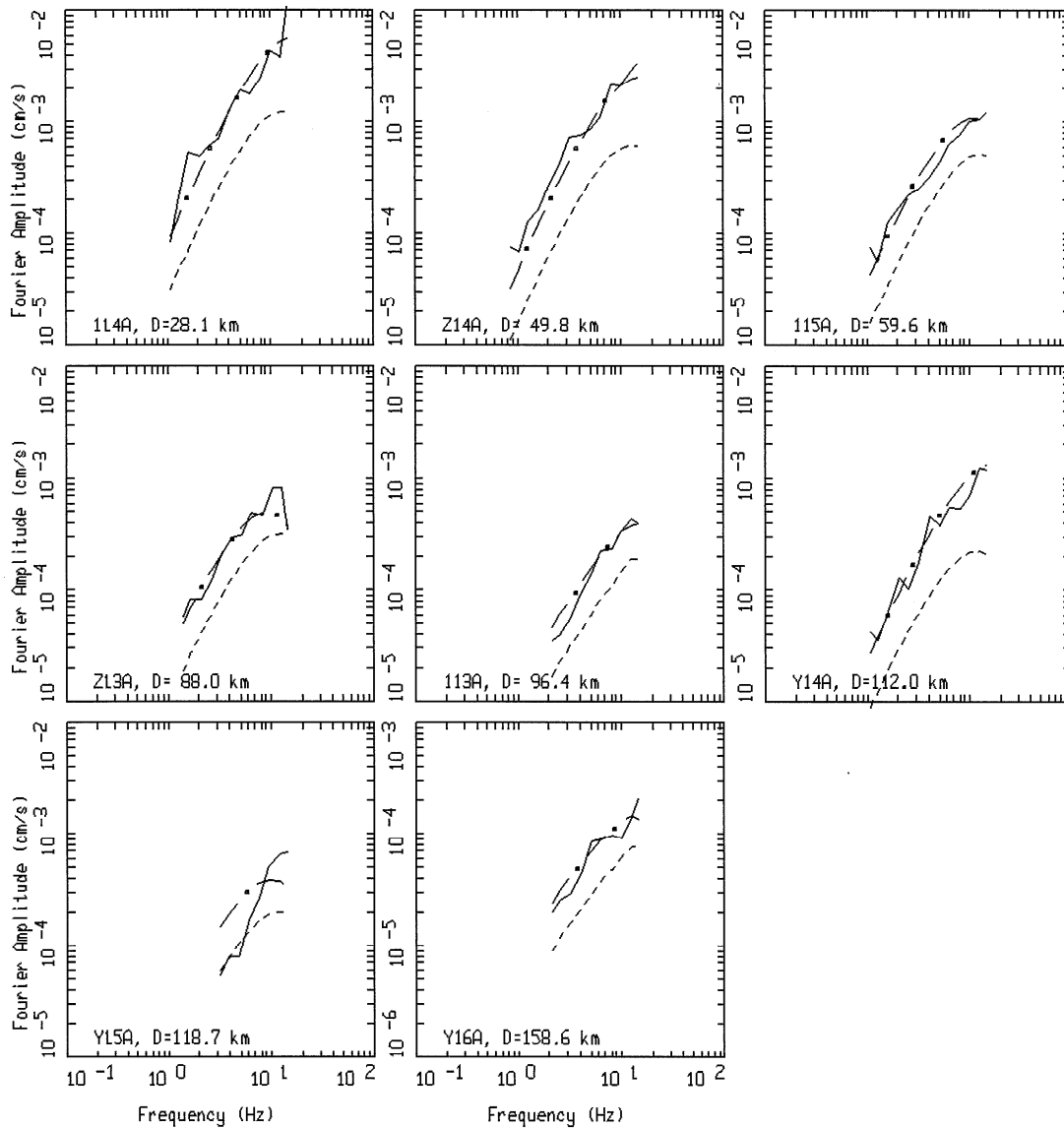
ARIZONA EARTHQUAKES: EQID 1275, PAGE 1 OF 1.
BASE CASE RUN: M 1.5, Z=13.0 KM

LEGEND
DATA
INITIAL MODEL
FINAL MODEL

Figure 4.24 Comparison of the Model 1 broadband (initial and final) models with the recorded FAS data at sites that recorded earthquake 1275 (Table 4.4) (logarithmic frequency axes).
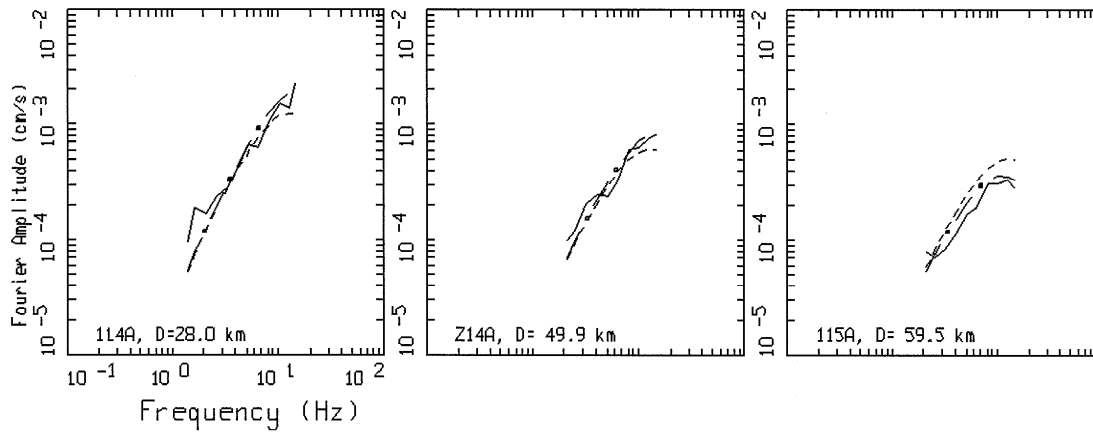
ARIZONA EARTHQUAKES: EQID 1276, PAGE 1 OF 1.
BASE CASE RUN: M 1.5, Z=13.0 KM

LEGEND
—————— DATA
- - - - - INITIAL MODEL
— • — FINAL MODEL

Figure 4.25   **Comparison of the Model 1 broadband (initial and final) models with the recorded FAS data at sites that recorded earthquake 1276 (Table 4.4) (logarithmic frequency axes).**
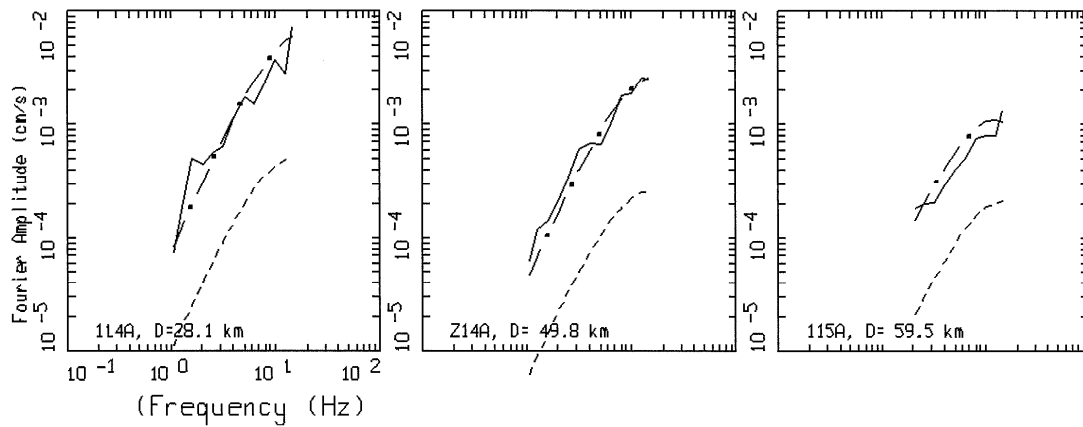
ARIZONA EARTHQUAKES: EQID 1277, PAGE 1 OF 1.
BASE CASE RUN: M 1.5, Z=13.0 KM

LEGEND
—————— DATA
- - - - - INITIAL MODEL
— • — FINAL MODEL

Figure 4.26   **Comparison of the Model 1 broadband (initial and final) models with the recorded FAS data at sites that recorded earthquake 1277 (Table 4.4) (logarithmic frequency axes).**
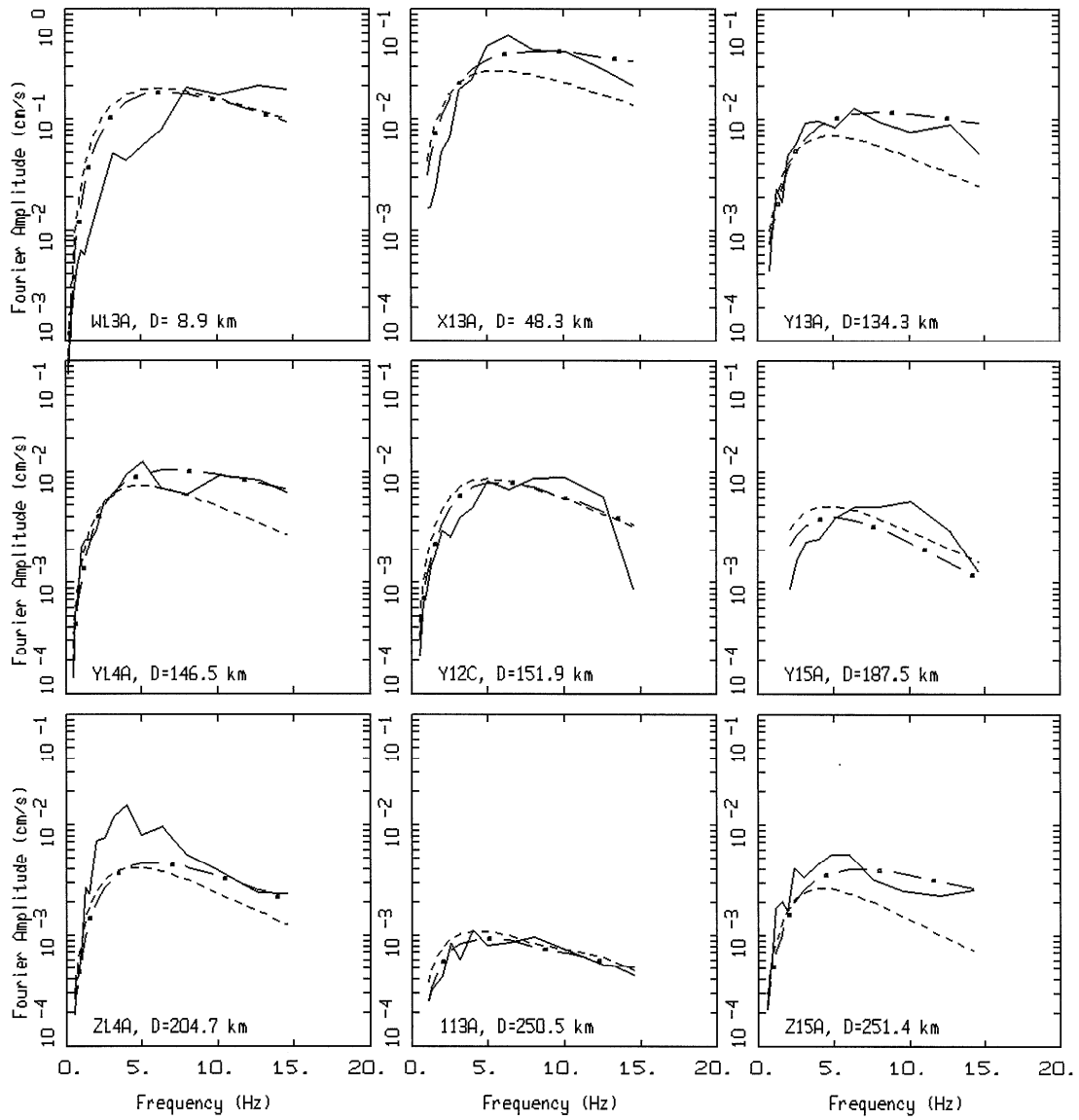
ARIZONA EARTHQUAKES: EQID 1267, PAGE 1 OF 2.
BASE CASE RUN: M 3.1, Z=1.0 KM

LEGEND
——————— DATA
- - - - - INITIAL MODEL
— · — FINAL MODEL

Figure 4.27   **Comparison of the Model 1 broadband (initial and final) models with the recorded FAS data at sites that recorded earthquake 1267 (Table 4.4) (linear frequency axes).**
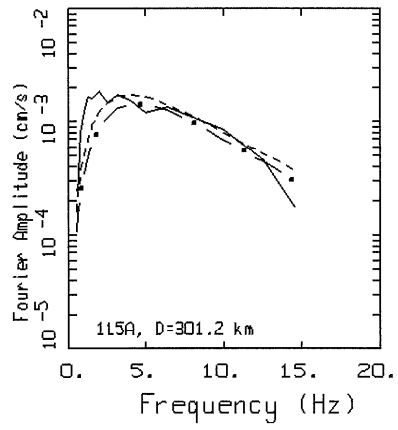
85

ARIZONA EARTHQUAKES: EQID 1267, PAGE 2 OF 2.
BASE CASE RUN: M 3.1, Z=1.0 KM

LEGEND
—————— DATA
- - - - - INITIAL MODEL
—— • —— FINAL MODEL

Figure 4.28   Continued.

ARIZONA EARTHQUAKES: EQID 1268, PAGE 1 OF 1.
BASE CASE RUN: M 3.4, Z=1.0 KM

LEGEND
DATA
INITIAL MODEL
FINAL MODEL

Figure 4.28   **Comparison of the Model 1 broadband (initial and final) models with the recorded FAS data at sites that recorded earthquake 1268 (Table 4.4) (linear frequency axes).**
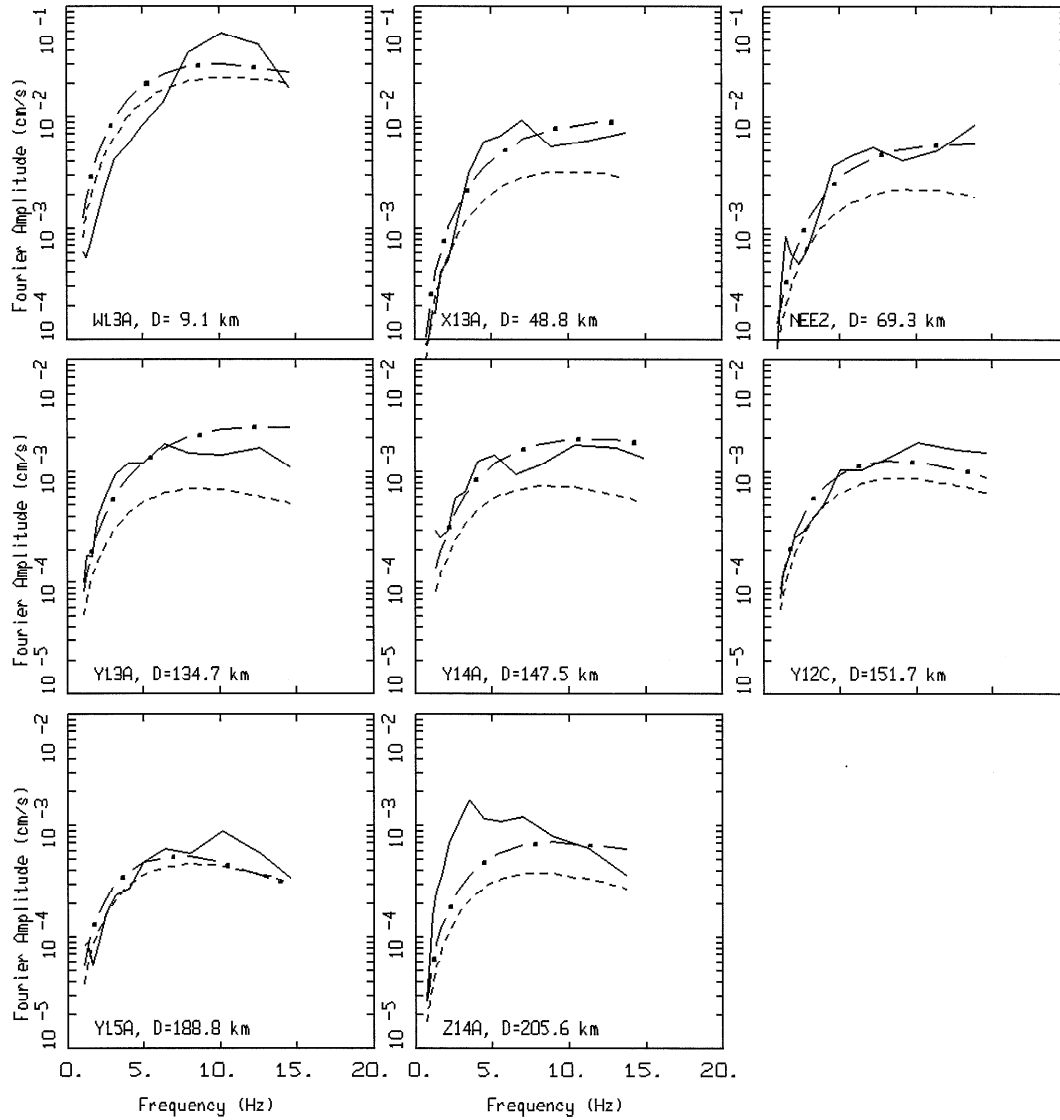
Figure 4.29 Comparison of the Model 1 broadband (initial and final) models with the recorded FAS data at sites that recorded earthquake 1269 (Table 4.4) (linear frequency axes).
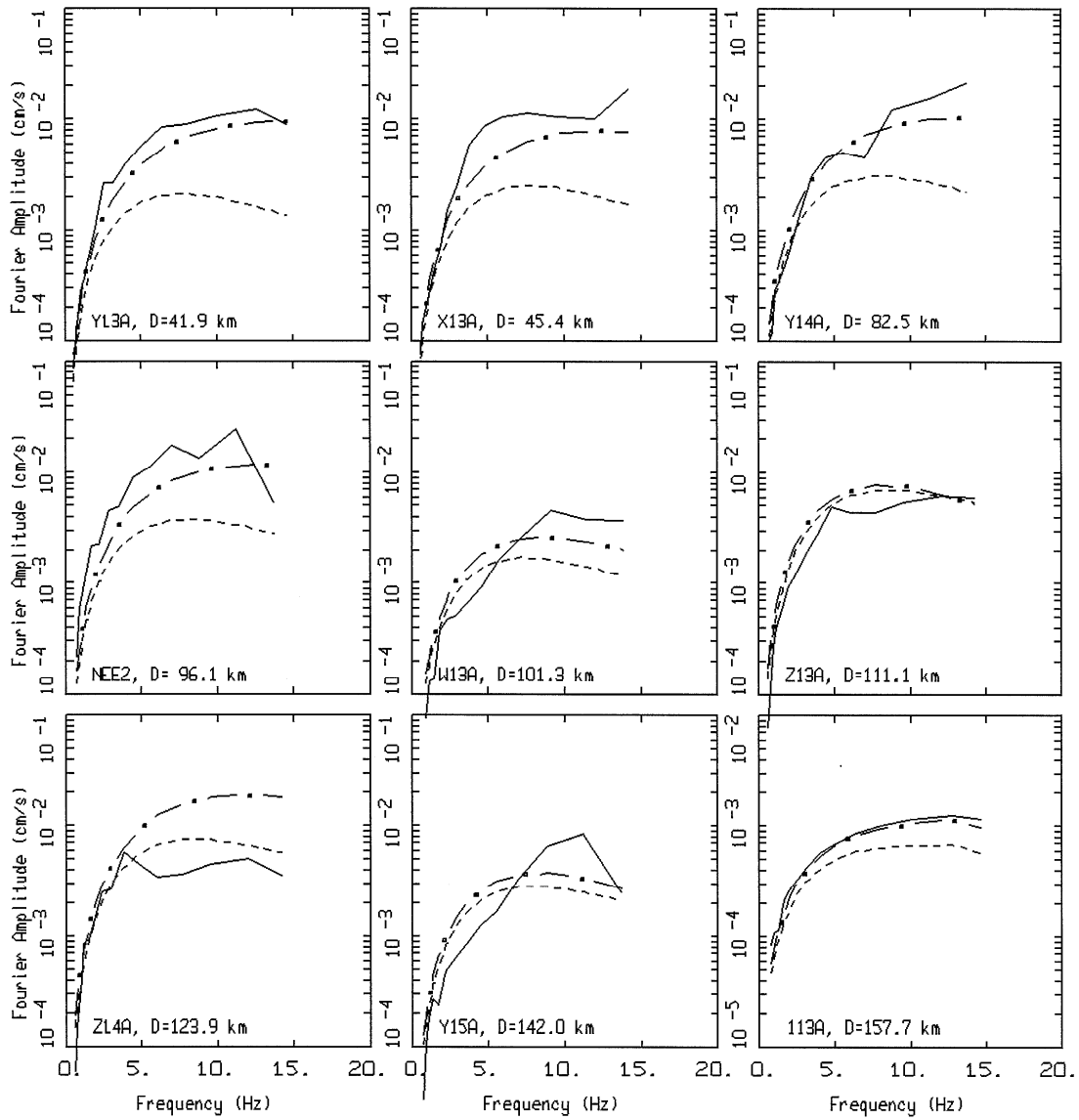
ARIZONA EARTHQUAKES: EQID 1270, PAGE 1 OF 2.
BASE CASE RUN: M 2.4, Z=6.0 KM

LEGEND
——————— DATA
— — — — INITIAL MODEL
— • — FINAL MODEL

Figure 4.30   Comparison of the Model 1 broadband (initial and final) models with the recorded FAS data at sites that recorded earthquake 1270 (Table 4.4) (linear frequency axes).
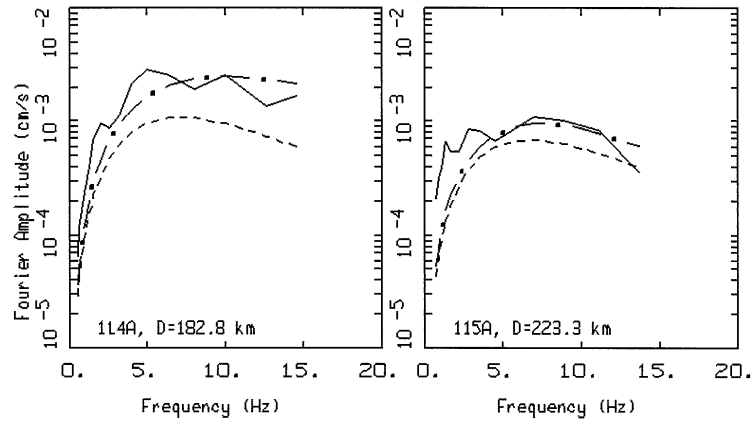
Fourier Amplitude (cm/s)

114A, D=182.8 km

115A, D=223.3 km

Frequency (Hz)

Frequency (Hz)

ARIZONA EARTHQUAKES: EQID 1270, PAGE 2 OF 2.
BASE CASE RUN: M 2.4, Z=6.0 KM

LEGEND

——————— DATA

- - - - - INITIAL MODEL

—— ▪ —— FINAL MODEL

Figure 4.31   Continued.
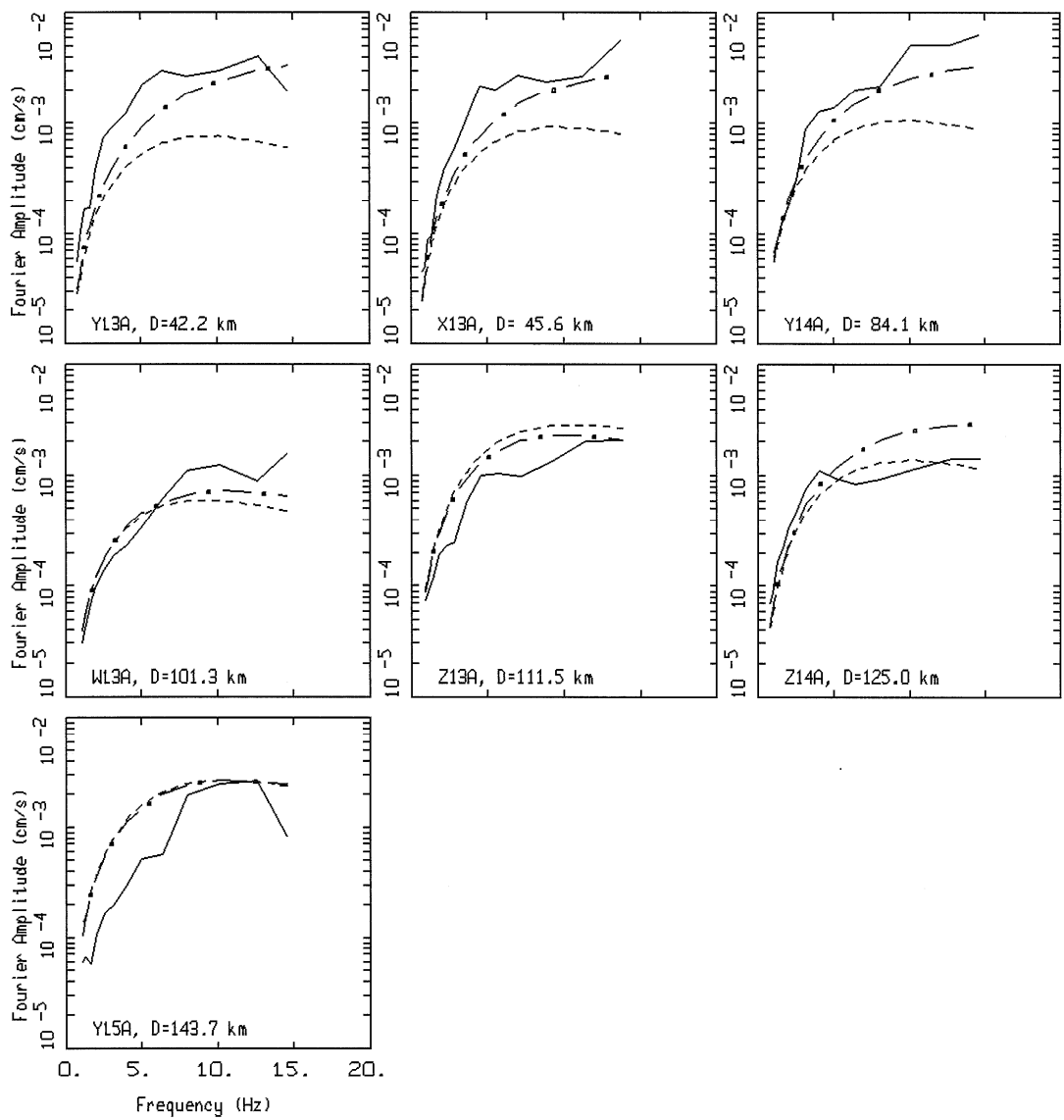
90

ARIZONA EARTHQUAKES: EQID 1271, PAGE 1 OF 1.
BASE CASE RUN: M 2.0, Z=7.0 KM

LEGEND
——————— DATA
- - - - - INITIAL MODEL
— · — FINAL MODEL

Figure 4.31 **Comparison of the Model 1 broadband (initial and final) models with the recorded FAS data at sites that recorded earthquake 1271 (Table 4.4) (linear frequency axes).**
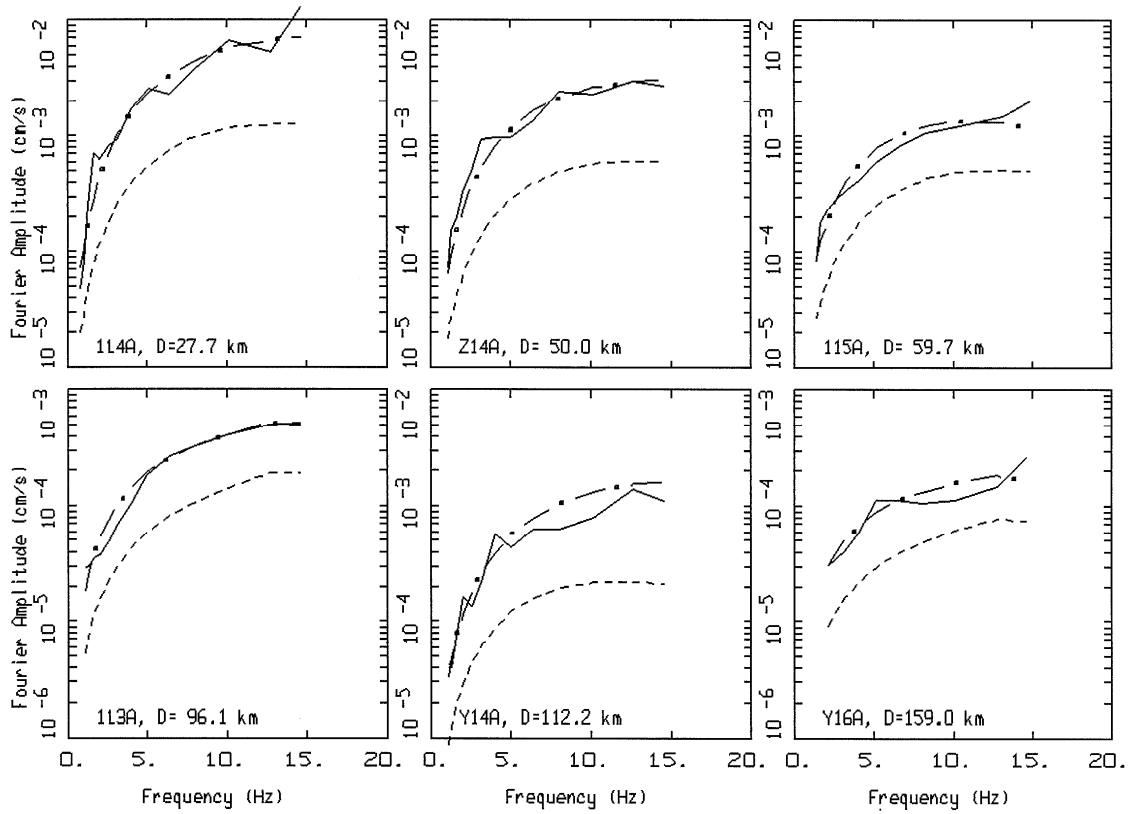
91

ARIZONA EARTHQUAKES: EQID 1272, PAGE 1 OF 1.
BASE CASE RUN: M 1.5, Z=13.0 KM

LEGEND
——————— DATA
— — — —   INITIAL MODEL
— • —   FINAL MODEL

Figure 4.32   **Comparison of the Model 1 broadband (initial and final) models with the recorded FAS data at sites that recorded earthquake 1272 (Table 4.4) (linear frequency axes).**
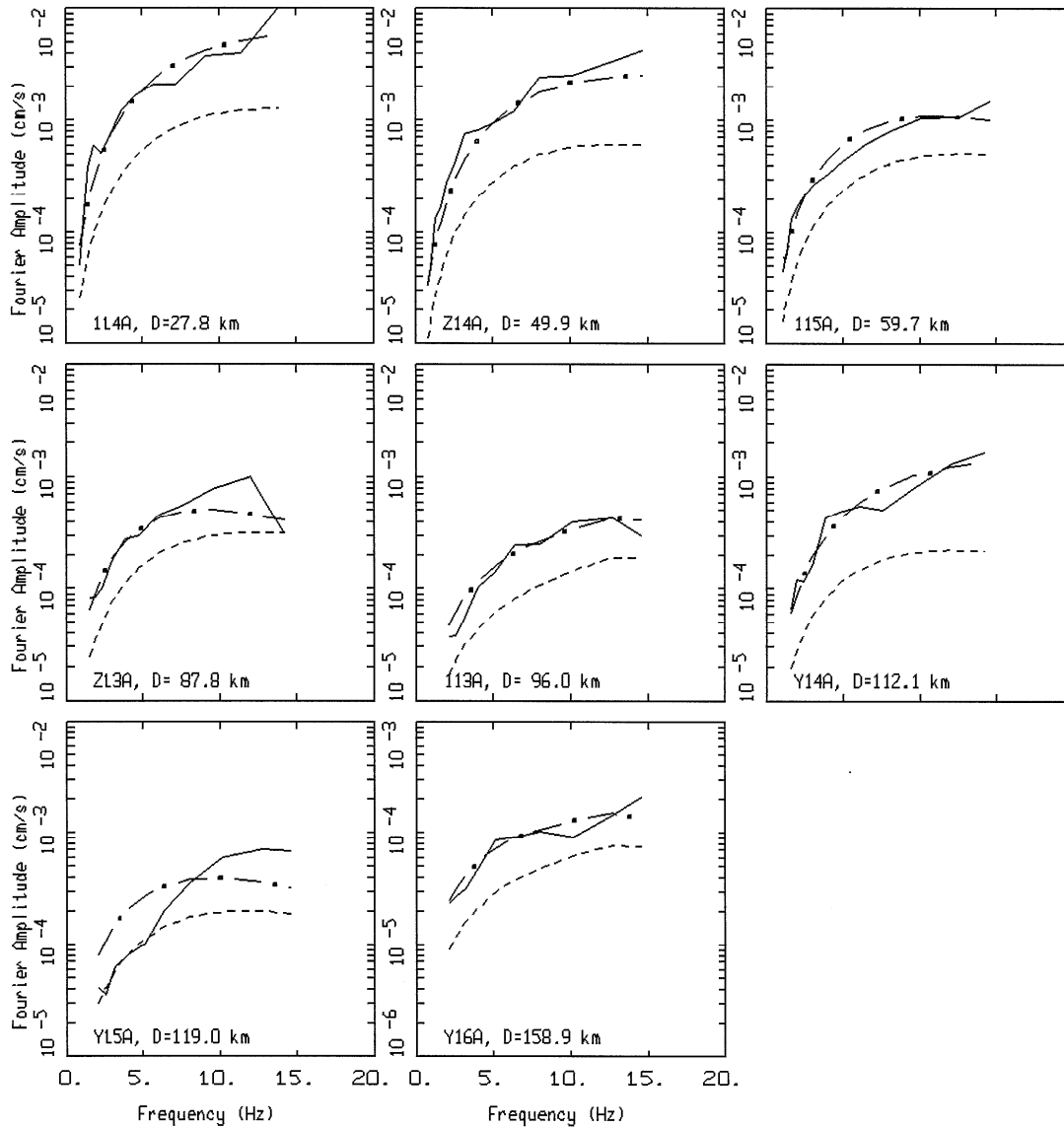
92

ARIZONA EARTHQUAKES: EQID 1273, PAGE 1 OF 1.
BASE CASE RUN: M 1.5, Z=13.0 KM

LEGEND
——————   DATA
– – – – –   INITIAL MODEL
—— ■ ——   FINAL MODEL

Figure 4.33   **Comparison of the Model 1 broadband (initial and final) models with the recorded FAS data at sites that recorded earthquake 1273 (Table 4.4) (linear frequency axes).**
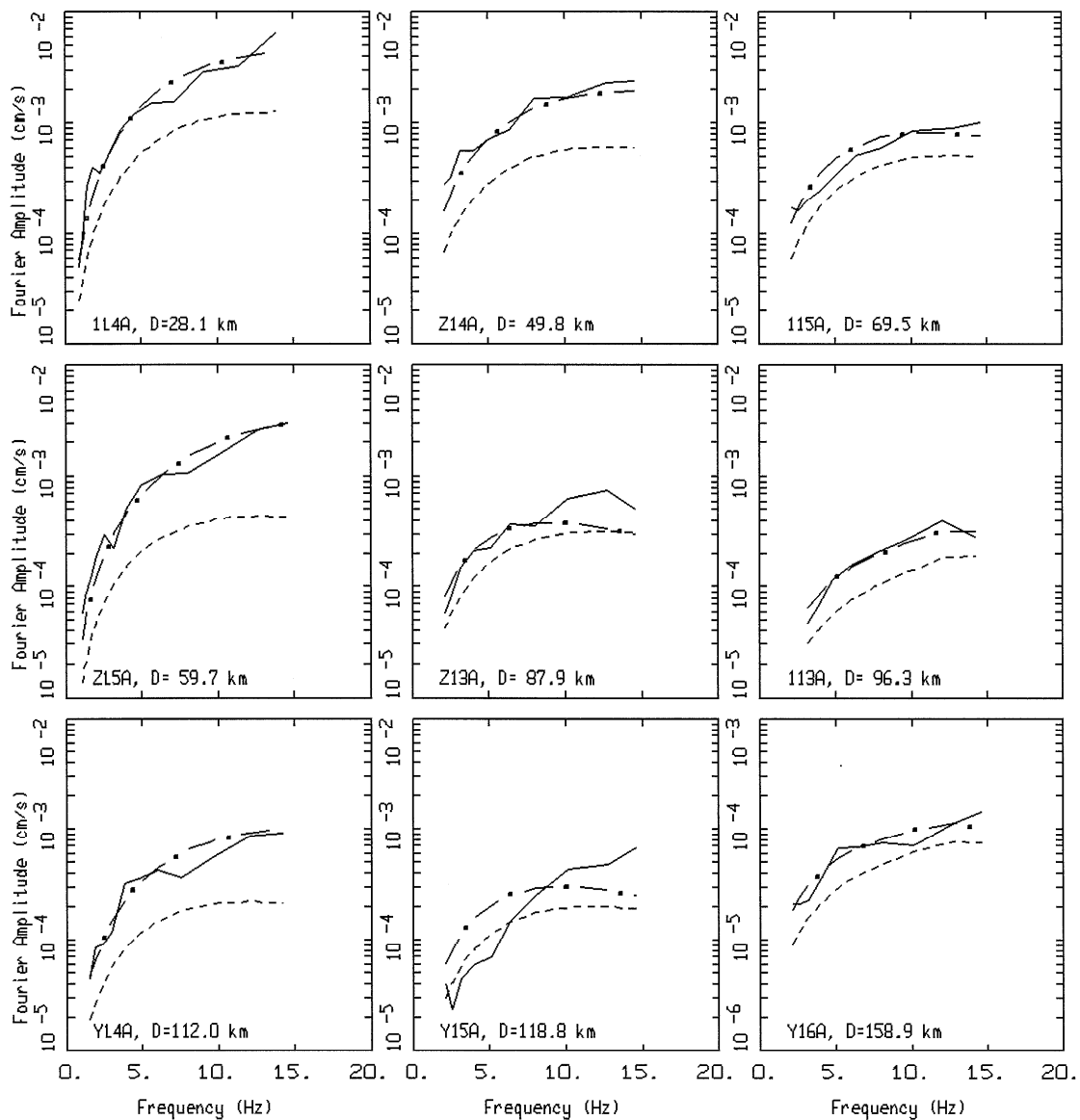
93

ARIZONA EARTHQUAKES: EQID 1274, PAGE 1 OF 1.
BASE CASE RUN: M 1.5, Z=13.0 KM

LEGEND
———————— DATA
- - - - - INITIAL MODEL
—— ∎ —— FINAL MODEL

Figure 4.34   **Comparison of the Model 1 broadband (initial and final) models with the recorded FAS data at sites that recorded earthquake 1274 (Table 4.4) (linear frequency axes).**
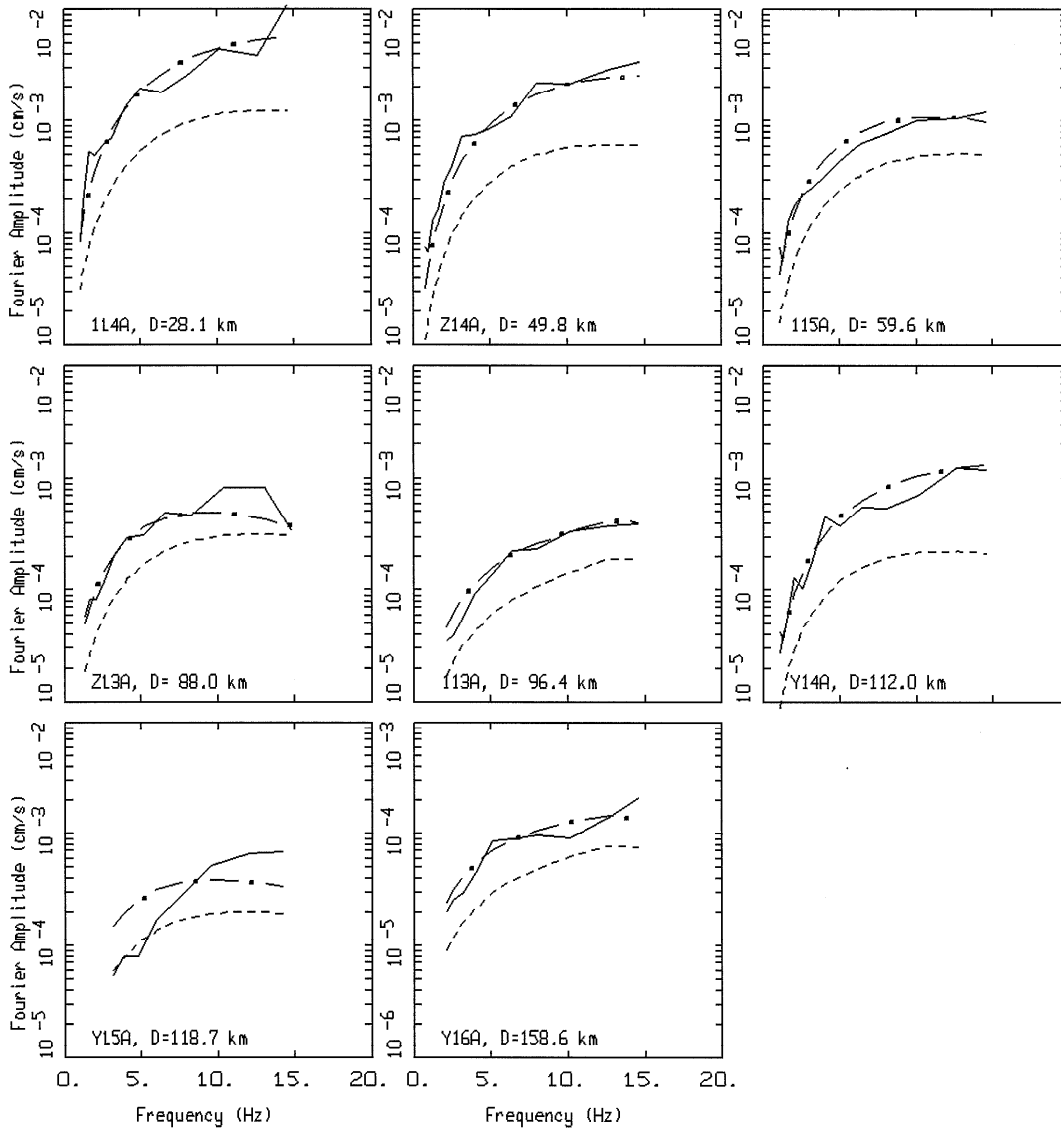
Figure 4.35 Comparison of the Model 1 broadband (initial and final) models with the recorded FAS data at sites that recorded earthquake 1275 (Table 4.4) (linear frequency axes).
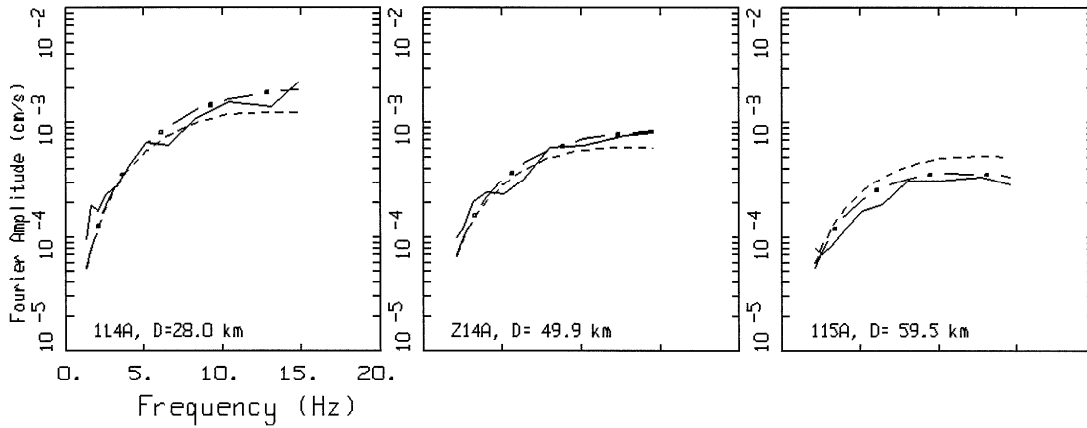
ARIZONA EARTHQUAKES: EQID 1276, PAGE 1 OF 1.
BASE CASE RUN: M 1.5, Z=13.0 KM

LEGEND
———————— DATA
– – – – – INITIAL MODEL
—— • —— FINAL MODEL

Figure 4.36   **Comparison of the Model 1 broadband (initial and final) models with the recorded FAS data at sites that recorded earthquake 1276 (Table 4.4) (linear frequency axes).**
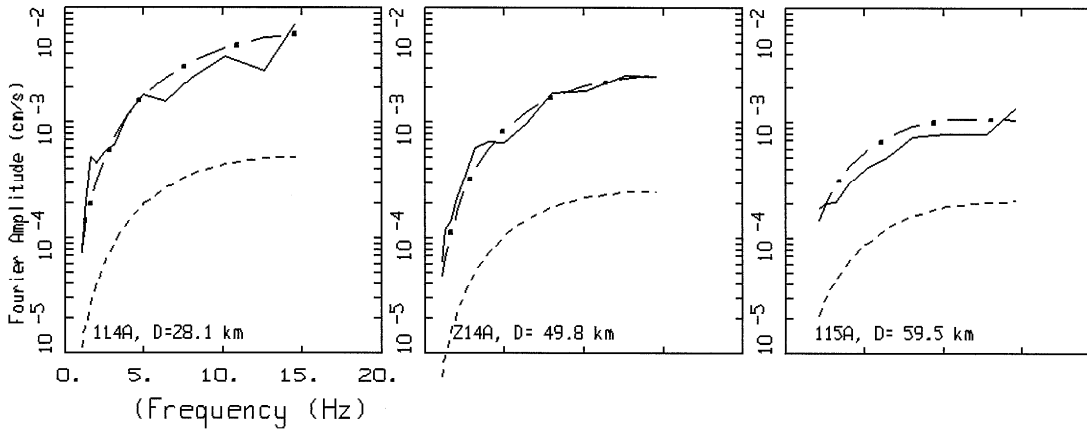
ARIZONA EARTHQUAKES: EQID 1277, PAGE 1 OF 1.
BASE CASE RUN: M 1.5, Z=13.0 KM

LEGEND
———————— DATA
– – – – – INITIAL MODEL
—— • —— FINAL MODEL

Figure 4.37   **Comparison of the Model 1 broadband (initial and final) models with the recorded FAS data at sites that recorded earthquake 1277 (Table 4.4) (linear frequency axes).**

96

4.4.5 Assessment of Uncertainty in Kappa using Method 3

To examine model (κ) sensitivity and provide a basis for model uncertainty, fixed parameters were varied by realistic amounts to assess differences in κ. Table 4.6 shows the change in κ for a given change in *each* parameter as well as starting models for κ and Δ_σ. Note all of the inversion parameters (**M**, Δ_σ) change along with κ. From Table 4.6, the strongest coupling was with η with a 30% reduction in median κ for a 50% reduction in η. Recall our κ estimates must be viewed as relative to $Q(f)$ and R_C, which suggests an uncertainty in median (over the 14 sites) κ of at least $\sigma_{\mu\ln}$ = 0.3 for a realistic range in parameters taken independently. Considering the coupling that exists between Q_0, η, and κ with this dataset due to the limited bandwidth and range in distances, epistemic uncertainty in the median estimate of κ should be increased to a recommended value of 0.5(ln).

As an additional approach to estimate epistemic uncertainty in κ, inversions with different subsets of the data (jackknife) were considered; upon examination, however, there were insufficient data to meaningfully constrain the inversions.

Additional insight into κ uncertainty is the effect of smoothing on the estimated values. Inversions may be done on FAS with smoothing using a constant frequency increment or a constant logarithmic frequency increment. Use of a constant frequency increment results in an increased number of points at high frequency compared to low frequency. A constant log frequency increment, as used in the Models 1–4 inversions and parameter sensitivity analyses, results in a uniform distribution of points at high and low frequency. Inversions with a set of points (smoothed or unsmoothed) using constant frequency increment results in increased weighting at high frequency compared to low frequency, which emphasizes high-frequency parameters such as κ, stress drop, and $Q(f)$ at larger distances, compared to the parameter magnitude (**M**).

Such unequal weighting is most appropriate at large magnitude earthquakes where the point-source model tends to over predict low-frequency motions [EPRI 1993; Silva et al. 1997; Atkinson and Silva 2000]. Increased weighting at high frequency for large magnitude recordings places more emphasis over the frequency range where the point-source model works well, conversely decreasing the emphasis where the model does not perform as well. Constant log frequency increment smoothing results in equal weighting across the inversion bandwidth and is more appropriate for small magnitude recordings where the point-source model appears to work equally well at both high and low frequency for small magnitude earthquakes. This sensitivity analysis between constant and constant logarithmic frequency interval showed a difference (reduction) in median κ between unsmoothed and smoothed (log frequency increment = 0.1) FAS inversions of about 1.10 or 10%.

Epistemic uncertainty in κ, due largely to the sensitivity with η in this dataset along with a limited bandwidth and limited range in distances, around a value of 0.5($\sigma_{\mu\ln}$) seems warranted. With cross correlations between site κ values of about 0.8, a maximum individual site uncertainty of about 0.6(ln) may be reasonable for a median κ uncertainty of 0.5(ln).

Eleven earthquakes in the magnitude range 1.2 to 3.4 (Table 2.2) were inverted for κ, stress drop, and moment magnitude. Due to limitations in both bandwidth (TA array data) and hypocentral distance range, both $Q(f)$ and geometrical attenuation were fixed, resulting in non-uniqueness in the median κ estimate of 0.033 sec. Sensitivity analyses varying $Q(f)$, geometrical attenuation, and amplification suggested that, for reasonable values of these parameters, the median κ estimate of 0.033 sec was reasonably stable with an uncertainty of 0.5(ln).

4.5   MODEL COMPARISON AND CONCLUSIONS

Two κ models have been derived. The first κ model combined the results from Methods 1 and 2. These methods try to avoid frequencies near the source corner frequency; instead they use a frequency range where the source spectrum should be flat to estimate κ. The models work only with Arizona earthquakes, whose magnitudes are either above M 3 or below M 1.6. The second κ model was derived from the broadband Method 3, which makes use of all events and inverts Fourier amplitude spectra over the entire usable frequency range.

The combined results from Methods 1 and 2 over the frequency range of 8−16 Hz yielded the model shown in Figure 4.39 (black line). The model has a hockey-stick-type dependence of κ_r with distance, a mean $\kappa_0 = 33\pm14$ m/sec, and a mean frequency-independent regional Q of 900 ± 300 in this frequency range. The DS method (Method 2) provided an upper bound for estimated κ_r values, which are up to three times higher than the AS (Method 1) values within the first 50 km. κ_0 is sensitive to the assumptions we made regarding crustal amplification, and if the latter is not accounted for (set equal to unity), the mean κ_0 drops by 35% to 21 m/sec. In contrast, for these models Q is not very sensitive to crustal amplification corrections. The mean Q is slightly higher than typical California values and is consistent with independent attenuation studies for the region. The scatter in the Q values reported in the literature is large, not only due to the differences in methods and data, but also because the sites lie close to the border between the Basin and Range and the Southern California provinces. There is a large scatter in the individual measured κ_r values versus distance (Figure 4.39, black symbols) that is not explained by the effect of distance or site stiffness (e.g., the two hardest sites, 113A and Y16A, have surprisingly high κ values compared to the other stiff soil sites). The large scatter in κ_r values may be partly due to the actual Q structure being much more complex, with raypaths for different events crossing different parts of the upper crust. Furthermore, the large epicentral distances make the trade-off between κ_0 and Q difficult to resolve in all the methods used. In some cases the scatter can also be due to shallow site resonances, which are not fully accounted for by the simple one-dimensional crustal amplification transfer functions. Our knowledge of the site profiles at depth also does not allow us to estimate the damping component from the stiff soils at all sites, but at the sites where this is possible; accounting for the soil damping does not render the remaining "rock" κ values more consistent. We believe that the most severe obstacles in resolving κ in this study are the band limitation of the recorded data, in combination with the event magnitudes and large distances.

Method 3 inverted the FAS from station that recorded eleven earthquakes in the magnitude range 1.2 to 3.4 for κ, stress drop, and moment magnitude. Due to limitations in both bandwidth (TA array data) and hypocentral distance range, both $Q(f)$ and geometrical attenuation were fixed, resulting in non-uniqueness in the median κ estimate of 0.033 sec. Sensitivity analyses varying $Q(f)$, geometrical attenuation, and amplification suggested that, for reasonable values of these parameters, the median κ estimate of 0.033 sec was reasonably stable with an uncertainty of 0.5(ln).

Method 3 yielded κ_0 values for each site, while the combination of Methods 1 and 2 yielded an overall κ model with distance, averaged over all sites. The two approaches came to several similar results:

1. The preferred value for the total average κ_0 estimated for all sites is essentially the same (33 m/sec, see black line and orange symbols in Figure 4.39 and Table 4.5). The results from broadband inversion (Method 3, Model 3), with the assumption of a constant Q (frequency independent) produced a κ_0 of 24 m/sec, which is within the range of uncertainty (standard deviation of 14 m/sec) of the κ_0 derived from the preferred broadband model (Model 1) and the combined Methods 1 and 2 (green line in Figure 4.39).

2. The mean Q is consistent between the techniques to estimate κ. Models 1, 2, and 4 of the broadband (Method 3) inversion give a log-average Q over 8–16 Hz ranging from 850 to 1050. These values are close to the mean constant Q of 900 obtained from the combination of Methods 1 and 2. These Q values are slightly higher than typical California values.

3. The stiffest rock sites had some of the highest estimates of κ from both methods. Due to large epicentral distances from the Arizona sites, the effects of $Q(f)$ may have masked the effect of κ at these two sites. Kappa may be much lower than the median estimates from both approaches. Another reason may be the contribution from site effects that are not discernible in the empirical spectral ratios.

4. The stress drop for several of these events appears to be higher than the value in Phillips et al. [2013]. Hence the source corner frequency for the small earthquakes in the dataset is likely higher than the data Nyquist frequency. Phillips et al. [2013] also did not address the possibility of contributions from f_{max} [Hanks 1982], which may also mask the source corner frequency for small events (see Frankel, [1982]). This may have led to very low stress drop values due to κ effects.

The results from the two approaches have different sensitivities:

1. The two approaches differed in the sensitivity of their results to the correction for crustal amplification. Changes in site amplification changed the estimate of κ in Methods 1 and 2, but primarily changed the estimate of moment magnitude in Method 3.

2. The two approaches differed in the sensitivity of κ_0 results to $Q(f)$ models. In the broadband analysis (Method 3), Models 1, 2, and 4 all use various frequency-dependent Q functions to check the sensitivity of κ_0 results to Q_0 and η. The κ_0 values did not change significantly. In contrast, a constant-Q model used in Model 3 reduced κ_0 by 40%. In Methods 1 and 2, the hockey-stick model helps to constrain κ_0 using nearby records. This does not allow for changes in the slope (Q) to change κ_0, which is based on the nearby data. This constraint does not allow for the large reduction seen in the broadband method (Model 3).
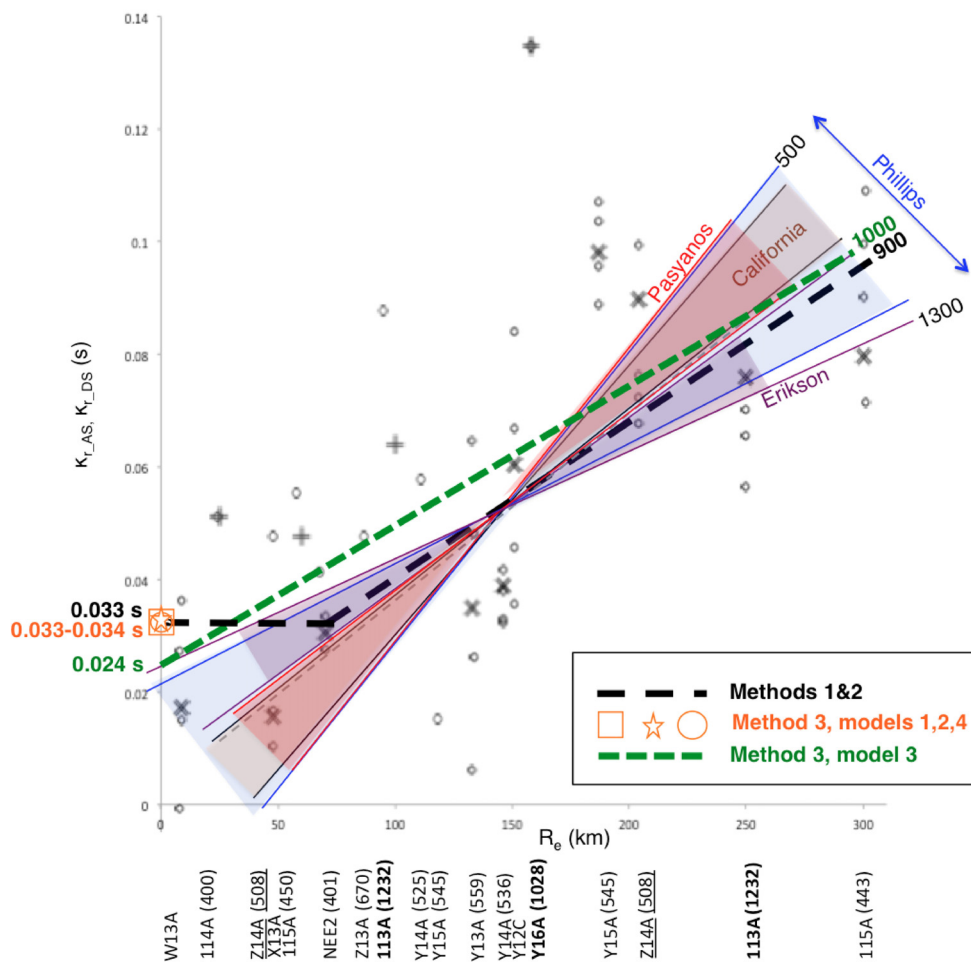
Figure 4.38   Comparison of models from the different methods applied: Methods 1 and 2 (κ_{DS} and κ_{AS}, black line for the final model, and black symbols for all the data points) and Method 3 (κ_{BB}, orange symbols for models 1, 2, and 4, and green line for the constant-Q Model 3). Also shown are the different Q models summarized from the literature.

5 Comparison of Data with NGA-West2 Ground Motion Prediction Equations

Several studies have estimated higher Q, and thus lower attenuation, in Arizona as compared to California (e.g., Phillips et al. [2013]). If the effect of the higher Q is significant, then the ground motion at Arizona stations should be larger than those of California stations for the same earthquake and distance. This would necessitate a change to GMPEs in order for them to be applicable to Arizona. This chapter compares the 5% damped pseudo acceleration spectra from Arizona stations described in Chapter 2 with the NGA-West2 data and GMPEs to determine if such a change is necessary.

5.1 NGA-WEST2 EARTHQUAKES SELECTED FOR ANALYSIS

The California and Mexico earthquakes described in Chapter 2 were separated into regions of distinct source or Q values in an attempt to separate potential source and path effects. Region 3 earthquakes are those whose raypaths to southwest Arizona cross through the Gulf of California source zone. Region 2 earthquakes are those whose raypaths to southwest Arizona cross the extensional zone, characterized by low Q, north of the Gulf of California source zone. Region 1 earthquakes are those whose raypaths to southwest Arizona lie north of the extensional zone. The earthquakes selected for this analysis are listed in Table 5.1 and shown in Figure 5.1.

Table 5.1   NGA-West2 earthquakes selected for analysis.

NGAW2 EQID	Hypocenter latitude	Hypocenter longitude	Depth (km)	Magnitude	Region
280	32.300	-115.267	0	7.2	3
1004	32.4105	-115.3120	18.65	5.1	3
1005	34.8118	-116.4227	9.33	5.06	1
1009	36.4011	-117.8397	7.419	4.73	1
1017	32.3362	-115.2425	17.16	4.63	3
1018	34.1081	-117.3062	14.795	4.45	2
1020	33.8776	-116.2019	10.062	4.26	2
1028	33.7328	-117.4921	10.018	4.73	2
1047	35.4744	-118.4262	6.678	4.43	1
1053	35.8373	-117.678	6.864	4.34	1
1058	32.707	-116.040	10.16	4.41	3
1067	33.2262	-116.1472	10.889	4.29	2
1182	36.3864	-117.8583	7.408	5.0	1
1186	36.4034	-117.8499	9.418	5.19	1
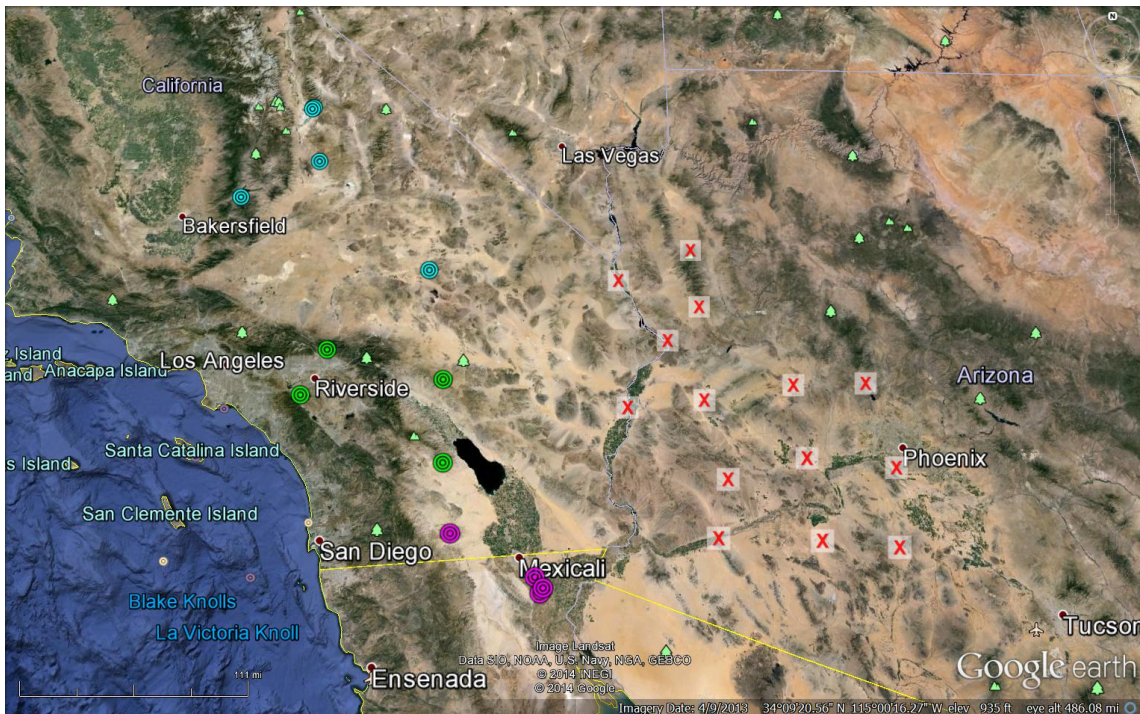
Figure 5.1   NGA-West2 earthquakes selected for analysis. Region 1 earthquakes are shown as blue circles, Region 2 earthquakes are shown as green circles, and Region 3 earthquakes are shown as purple circles. Arizona recording stations are shown as red "X"s.

5.2   ESTIMATION OF *Q* VALUES FOR REGIONS 1, 2, AND 3

The Q data from Phillips et al. [2013] are used as the basis for the Q estimates along the path between the earthquake epicenter and recording station. The data has a spacing of 0.5° and is interpolated to 0.01° spacing. Bresenham's [1965] line algorithm is then used to determine the path from earthquake to station. The inverse value of Q has been summed for every grid along the path, and an average path Q has been estimated from this sum.

5.2.1 *Q* Values for NGA-West2 Data

Average path Q values were estimated from the Phillips et al. [2013] data for the NGA-West2 dataset to provide a baseline and are shown in Figure 5.2. For rupture distances less than 100 km there are clear regional differences in the Q values at all four center frequencies. Region 2 has the highest average path Q values and Region 3 the lowest. Region 1 may be split into two groups, with some values in between Regions 2 and 3, and some path Q values near 500 within 100 km. The earthquakes in Region 1 are centered at latitude 36.0 longitude -118.0 where the Q value [Phillips et al. 2013] for the frequency range 0.75–1.5 Hz is approximately 140. The earthquakes in Region 2 are centered at latitude 34.0 longitude -117.0 where the Q value for the frequency range 0.75–1.5 Hz is approximately 225. The earthquakes in Region 2 are centered at latitude 32.5 longitude -115.5 where the Q value for the frequency range 0.75–1.5 Hz is approximately 110. The Q values at distances less than 100 km are similar to the Q value closest to the earthquake for the three Regions except for the higher Q values in Region 1. At distances beyond about 100 km the regional differences become less pronounced as the raypaths from earthquake to station sample a wider range of Q structures. Beyond 200 km the regional differences have disappeared with the exception of the lowest Q raypaths in Region 3.
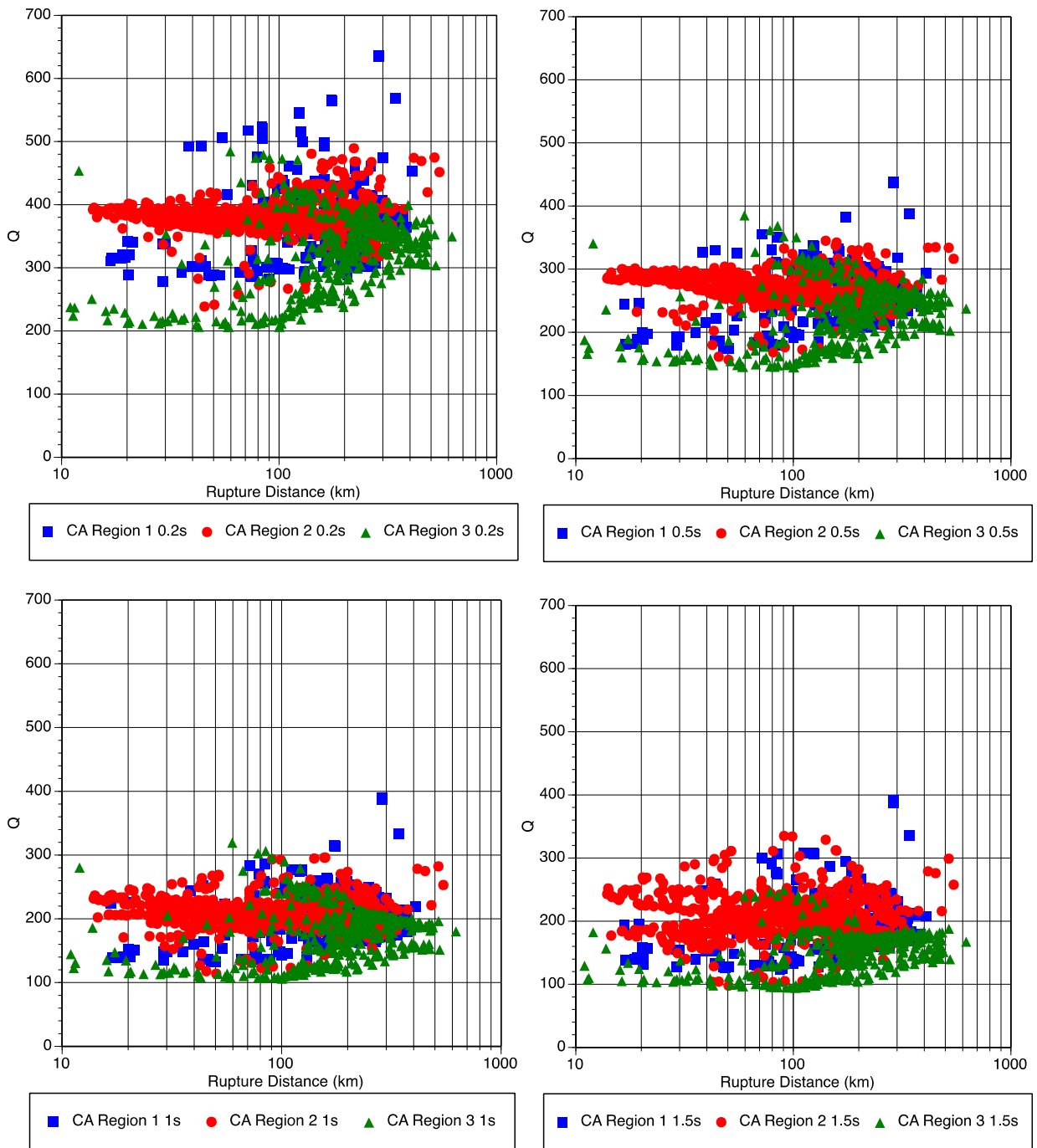
Figure 5.2 *Q* values for NGA-West2 data from earthquakes in Region 1, 2, and 3 over frequency ranges with average periods of 0.2, 0.5, 1, and 1.5 sec.

5.2.2 *Q* Values for Arizona Data

The average path Q values were also calculated for the Arizona recordings of the NGA-West2 earthquakes and are shown in Figure 5.3. This dataset does not include any estimates for rupture distances less than 100 km where differences were observed in Figure 5.2.

Region 1 has the highest average path Q value and Region 3 the lowest, with Region 2 somewhere in the middle for all distances and periods. There is a clear distance trend for the Region 2 and 3 data. To illustrate how the regional differences occur, Figure 5.4 shows the Q values along the path from the earthquake epicenter to an example recording station for three earthquakes recorded at Y14A, one earthquake from each of the three Regions (1, 2 and 3). The paths from the earthquakes in Regions 2 and 3 both cross the extensional zone, which exhibits Q values in the low hundreds averaged over frequencies from 0.75–1.5 Hz, and then continue into the higher Q region in Arizona [Phillips et al. 2013]. The longer the path from earthquakes in Region 2 or 3 to the station in Arizona, the greater the fraction of the raypath spent in the higher Q region of Arizona and thus the higher the average path Q (Figure 5.3). The raypaths from the earthquakes located in Region 1 head southeast and pass through a region with a high Q corresponding with the Mojave Block. The Q values from Phillips et al. [2013] peak near latitude 35.0, longitude -117.5 with a value of approximately 445 for the frequency range of 0.75–1.5 Hz. This high Q zone causes the average Q values for raypaths from earthquakes in Region 1 to southwest Arizona to be the highest of the three Regions within about 200 km (Figure 5.4).
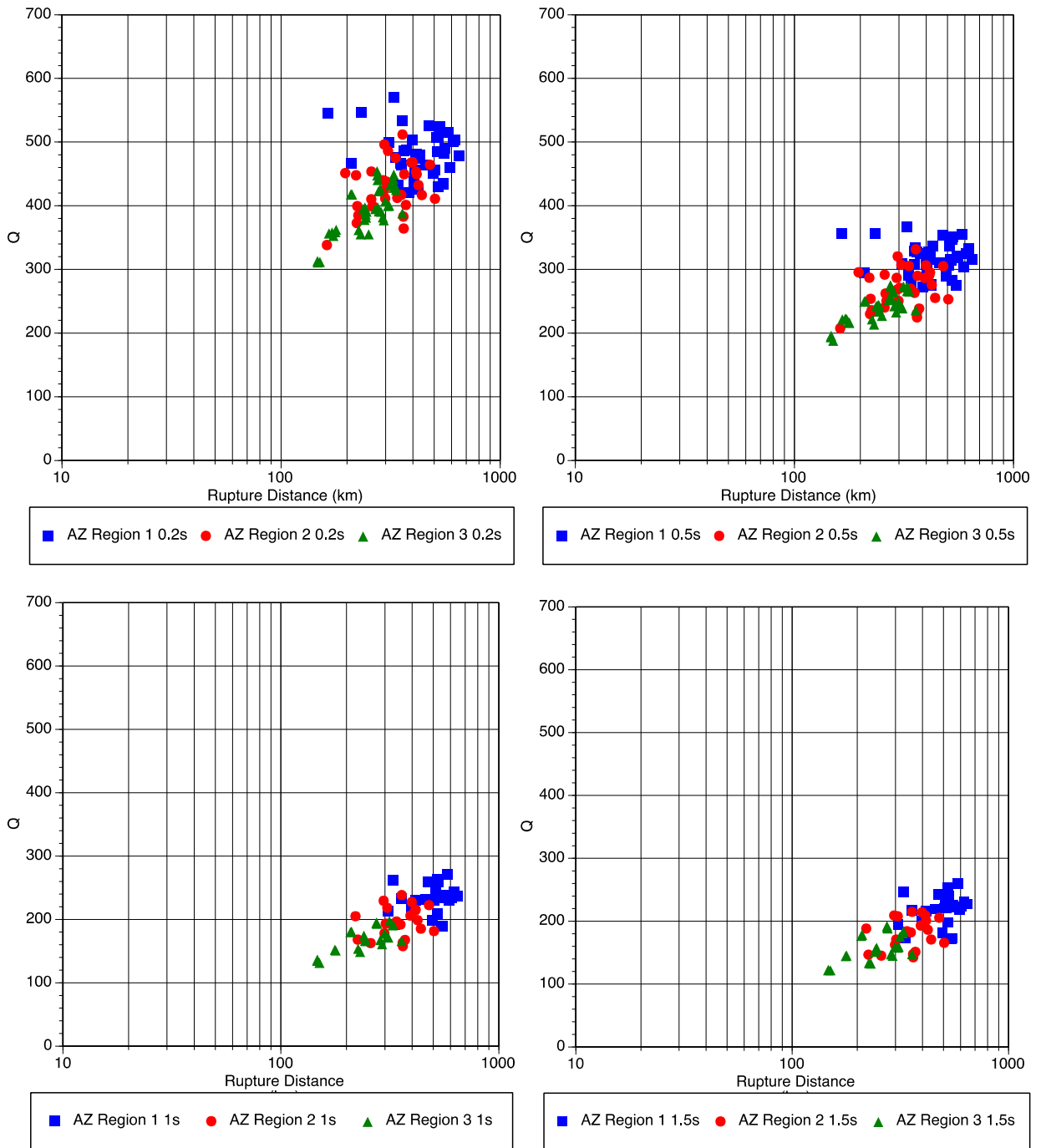
Figure 5.3 *Q* values for NGA-West2 data from earthquakes in Region 1, 2, and 3 over frequency ranges with average periods of 0.2, 0.5, 1, and 1.5 sec.
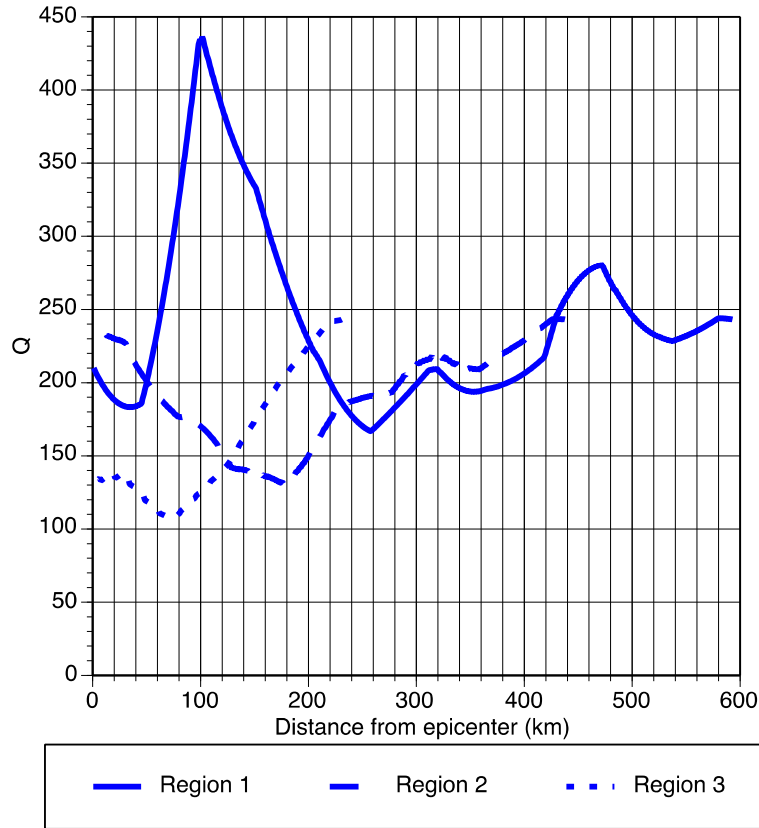
Figure 5.4 *Q* values for the frequency range 0.75 to 1.5 Hz along raypaths from earthquakes located in Region 1, 2, or 3 to a station (Y14A) located in southwest Arizona.

5.2.3 Conclusions

Average path Q values for earthquakes from Regions 1, 2, and 3 from NGA-West2 and Arizona data at a distance of 200–400 km are calculated and shown in Figure 5.5. For this distance range there is little difference between path Q values in California and Arizona for earthquakes in Regions 2 and 3 except at periods less than about 0.4 sec. There is a difference between Q values in California and Arizona for earthquakes in Region 1 at periods from 0.08 to 1.5 sec.
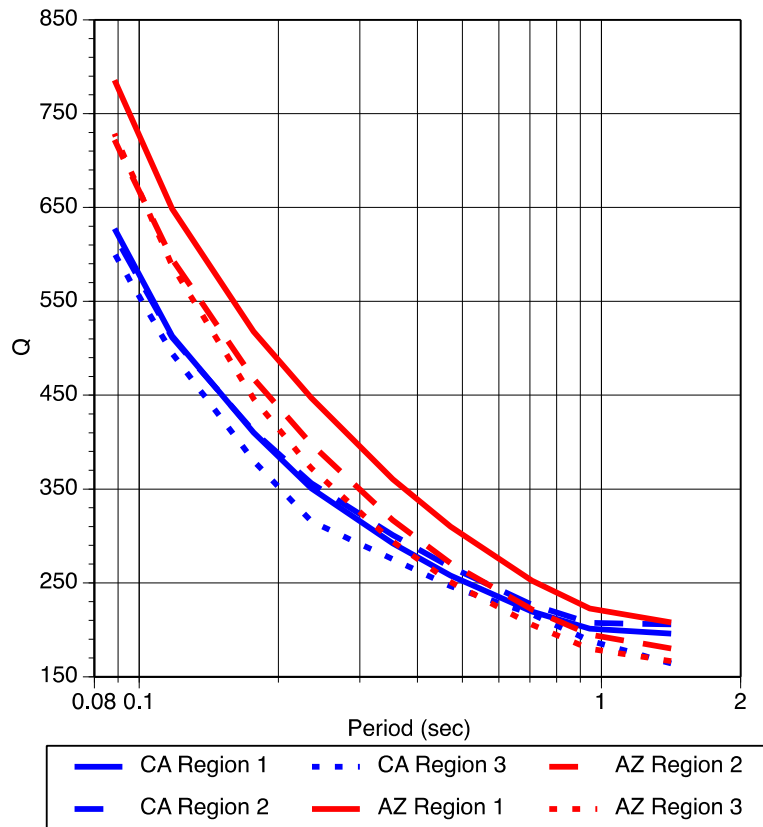
Figure 5.5 **Comparison of *Q* values from earthquakes located in Regions 1, 2, and 3 to stations in California and Arizona at a rupture distance of 200–400 km.**

5.3 COMPARISON OF ARIZONA RECORDINGS WITH NGA-WEST2 RECORDINGS AND GROUND MOTION PREDICTION EQUATIONS

To determine if the higher Q in Arizona is significant enough to impact ground motion values, this section compares the 5% damped pseudo-spectral acceleration values for the Arizona recording stations and NGA-West2 earthquakes described in Chapter 2 with additional recordings made of those earthquakes from the NGA-West2 database. There is also the possibility of a difference in attenuation at the Arizona recording stations between earthquakes that originate in Regions 1, 2, and 3, thus the comparison of PSA values from the NGA-West2 earthquakes is separated into three subsection comprising earthquakes from Regions 1, 2, and 3.

Ground motion recorded at the Arizona stations and from the NGA-West2 dataset for each of the earthquakes in Regions 1, 2 and 3 are corrected to a uniform $V_{S,30}$ of 500 m/sec using an average site term from four NGA-West2 GMPEs and plotted with respect to closest distance (Abrahamson, Silva, and Kamai [2014] (ASK), Boore, Stewart, Seyhan and Atkinson [2014] (BSSA), Campbell and Bozorgnia (2014) (CB), and Chiou and Youngs [2014] (CY)). Predictions from the NGA-West2 GMPEs are plotted at a $V_{S,30}$ of 500 m/sec with the event term removed. Event terms were requested from the NGA-West2 developer teams. Event terms were received for the Abrahamson, Silva and

Kamai [2014], Boore, Stewart, Seyhan and Atkinson [2014], Campbell and Bozorgnia [2014], and Chiou and Youngs [2014] GMPEs. If an event term is unavailable for an earthquake and ground motion prediction pair then the GMPE is not plotted. The event terms are given in Table 5.2. These plots are shown in the following three subsections broken down by Regions 1, 2, and 3.

Table 5.2   NGA-West2 event terms for selected earthquakes in Regions 1, 2, and 3.

NGA-West2	Abrahamson, Silva and Kamai [2014]				Boore, Stewart, Seyhan and Atkinson [2014]				Campbell and Bozorgnia [2014]				Chiou and Youngs [2014]			
EQID	0.2 s	0.5 s	1.0 s	2.0 s	0.2 s	0.5 s	1.0 s	2.0 s	0.2 s	0.5 s	1.0 s	2.0 s	0.2 s	0.5 s	1.0 s	2.0 s
280	-0.078	-0.403	-0.491	-0.231	-0.110	-0.137	-0.216	0.034	0.496	0.291	0.286	0.031	-0.010	-0.060	-0.294	-0.237
1004	-0.605	-0.325	0.294	-	-0.113	0.174	0.589	0.370	-	-	-	-	-	-	-	-
1005	0.195	-0.322	0.231	0.103	0.358	-0.020	0.470	0.469	-0.070	-0.230	-0.140	-0.143	-0.199	-0.256	-0.143	0.018
1009	-	-	-	-	-0.738	-0.244	-0.063	-0.202	-0.621	-0.236	-0.229	-0.358	-0.576	-0.296	-0.129	-0.239
1017	-	-	-	-	-1.527	-0.896	-0.378	-0.087	-	-	-	-	-0.172	0.090	0.104	0.396
1018	0.418	0.485	0.401	0.285	0.696	0.747	0.622	0.473	0.679	0.698	0.582	0.525	0.559	0.768	0.730	0.580
1020	-0.179	-0.683	-0.917	-0.886	-0.118	-0.507	-0.784	-0.862	-0.453	-0.712	-0.959	-1.093	-0.134	-0.524	-0.797	-0.949
1028	-0.420	-0.585	-0.693	-0.830	-0.267	-0.386	-0.499	-0.625	-0.094	-0.383	-0.626	-0.751	-0.238	-0.452	-0.617	-0.790
1047	-	-	-	-	-	-	-	-	-	-	-	-	-0.205	-0.241	-0.518	-0.711
1053	-0.188	-0.209	-0.326	-0.500	-0.204	-0.053	-0.102	-0.305	0.025	-0.097	-0.478	-0.775	-0.158	-0.027	-0.257	-0.604
1058	-1.243	-0.911	-0.858	-0.943	-1.025	-0.707	-0.696	-0.911	-0.741	-0.826	-0.847	-	-0.694	-0.752	-0.752	-0.822
1067	-0.228	-0.723	-0.853	-1.090	-0.028	-0.470	-0.657	-0.933	0.026	-0.529	-0.840	-0.955	-0.040	-0.386	-0.608	-0.903
1182	-0.472	-0.426	-0.314	-0.003	-0.423	-0.247	-0.159	0.252	-0.269	-0.144	-0.453	-0.287	-0.287	-0.244	-0.539	-0.250
1186	-0.666	-0.686	-0.524	-0.469	-0.907	-0.739	-0.574	-0.284	-0.399	-0.515	-0.615	-0.553	-0.328	-0.552	-0.631	-0.566

5.3.1 Region 1
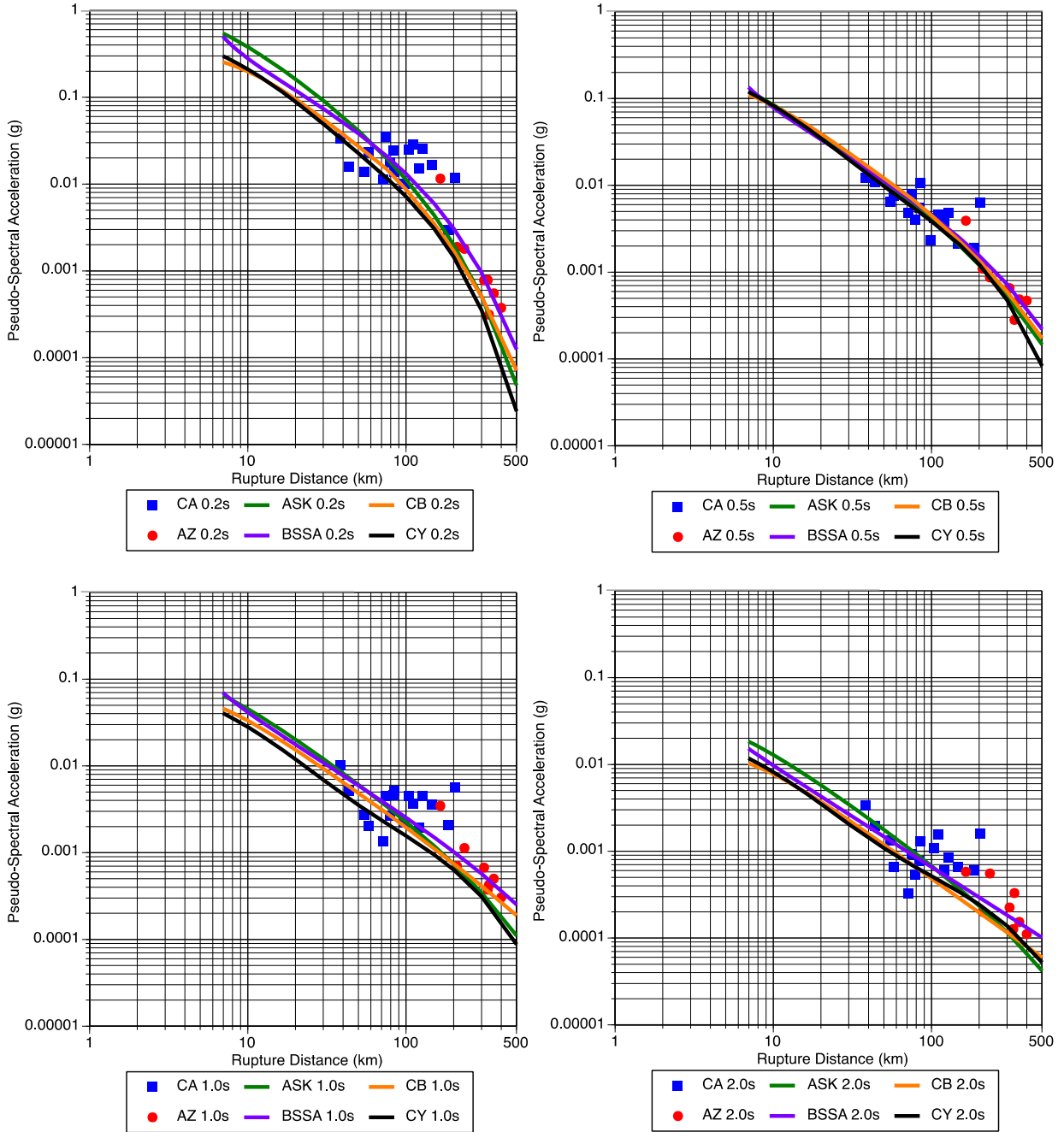
Figure 5.6   **EQID 1005: pseudo-spectral acceleration (*g*) at periods of 0.2, 0.5, 1.0, and 2.0 sec from the NGA-West2 dataset, Arizona stations, and the 2014 NGA-West2 GMPEs are shown for which an event term is available.**
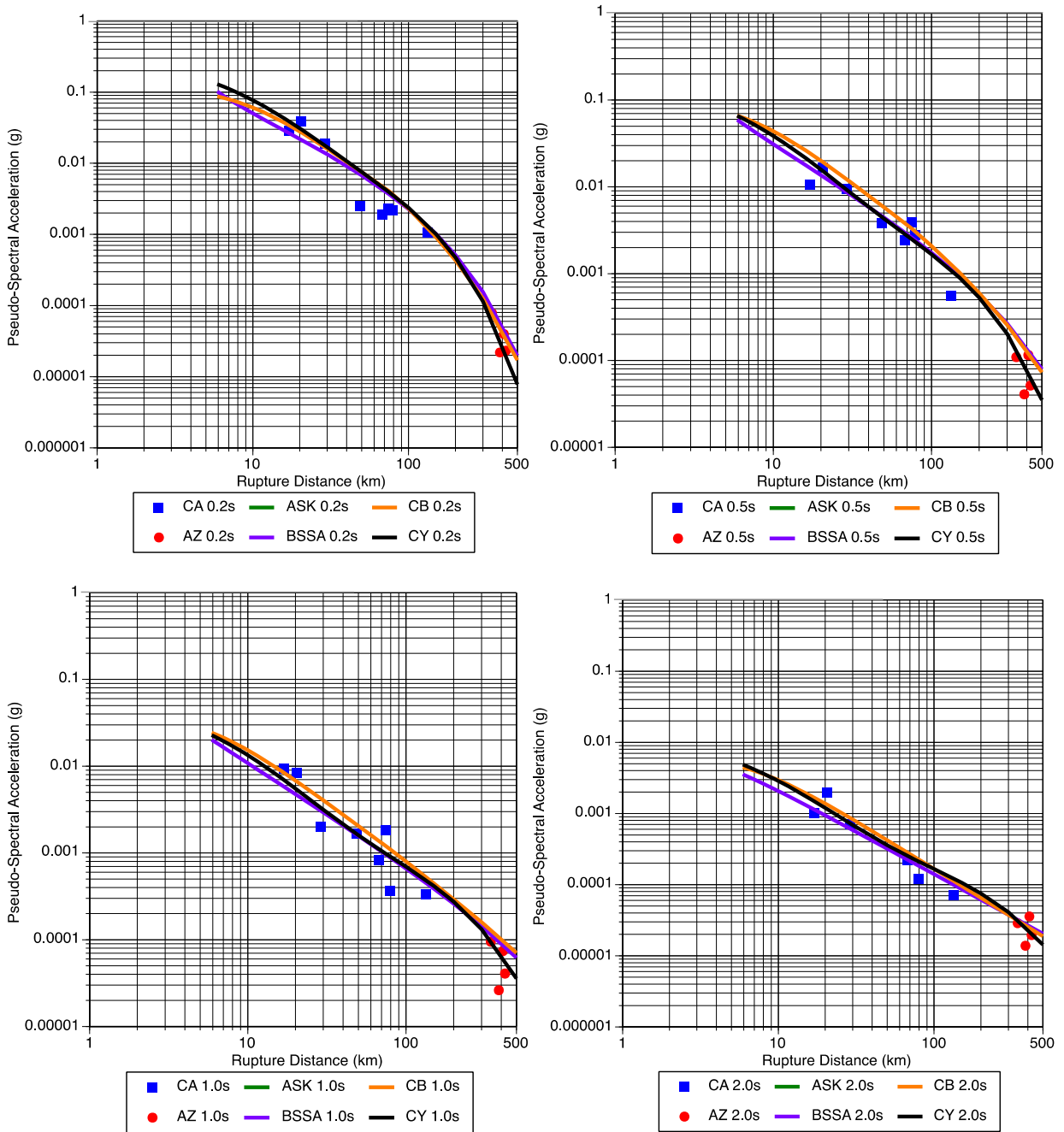
Figure 5.7 EQID 1009: pseudo-spectral acceleration (*g*) at periods of 0.2, 0.5, 1.0, and 2.0 sec from the NGA-West2 dataset, Arizona stations, and the 2014 NGA-West2 GMPEs are shown for which an event term is available.
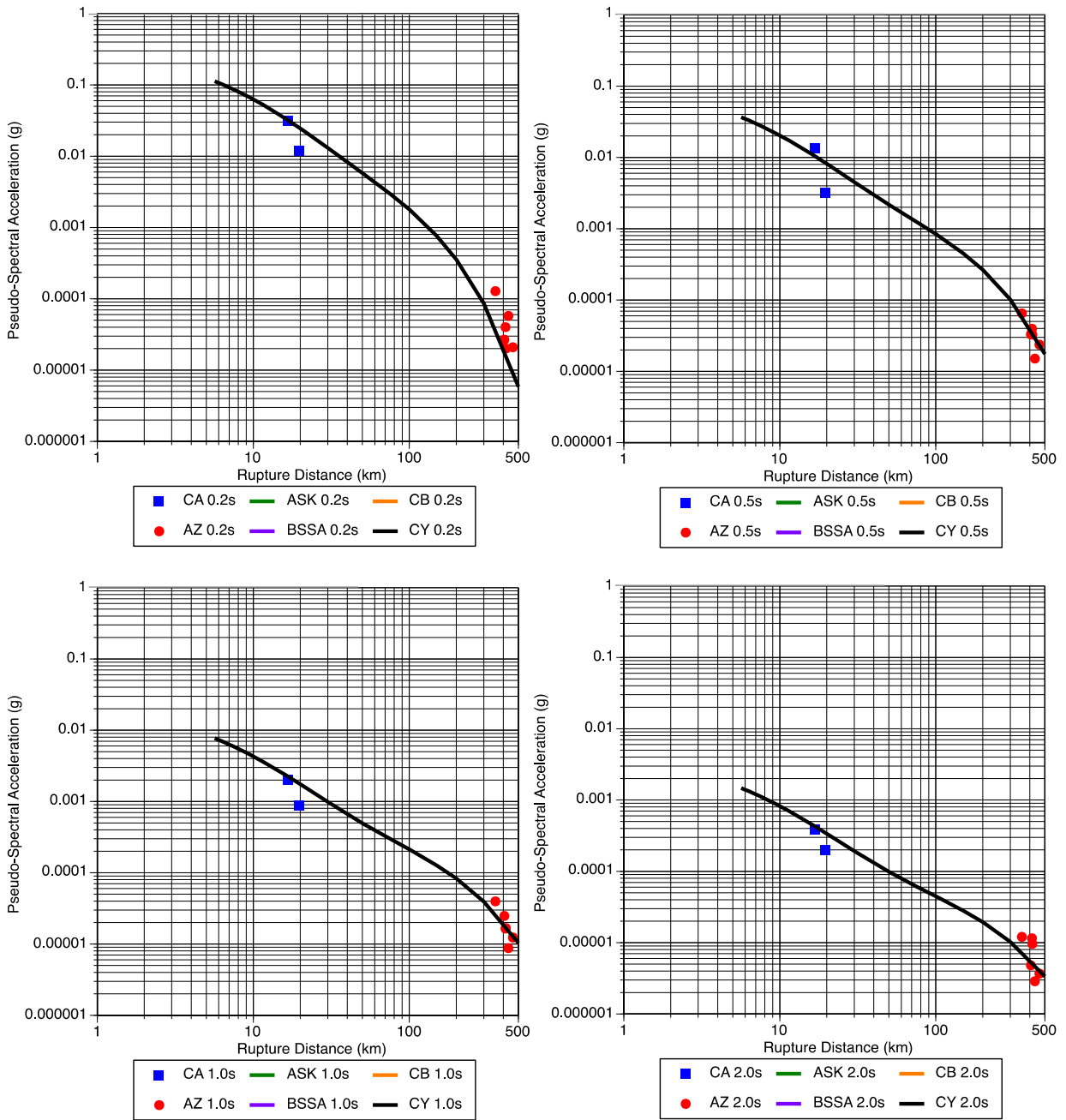
Figure 5.8 **EQID 1047: pseudo-spectral acceleration (*g*) at periods of 0.2, 0.5, 1.0, and 2.0 sec from the NGA-West2 dataset, Arizona stations, and the 2014 NGA-West2 GMPEs are shown for which an event term is available.**
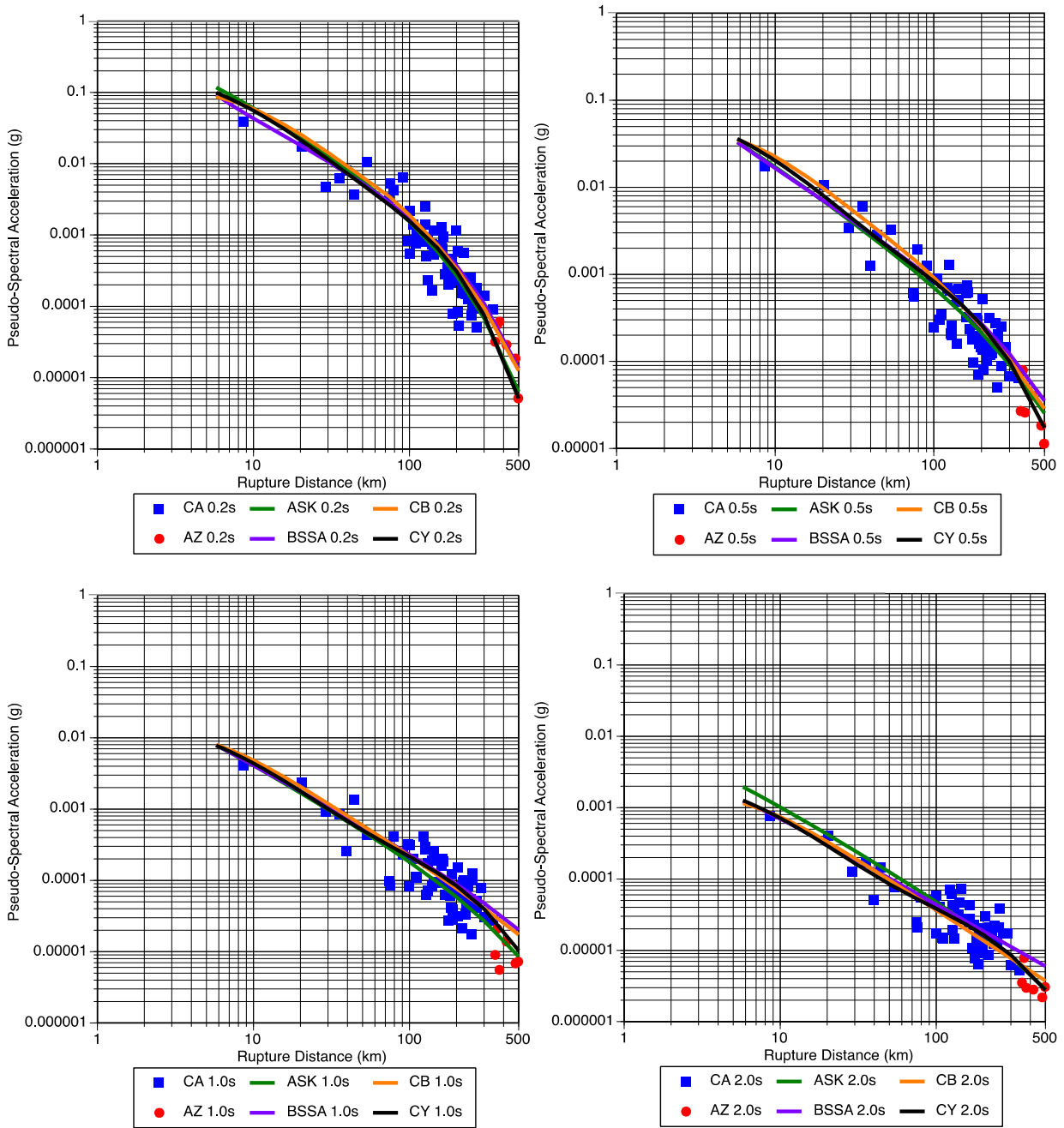
Figure 5.9 **EQID 1053: pseudo-spectral acceleration (*g*) at periods of 0.2, 0.5, 1.0, and 2.0 sec from the NGA-West2 dataset, Arizona stations, and the 2014 NGA-West2 GMPEs are shown for which an event term is available.**
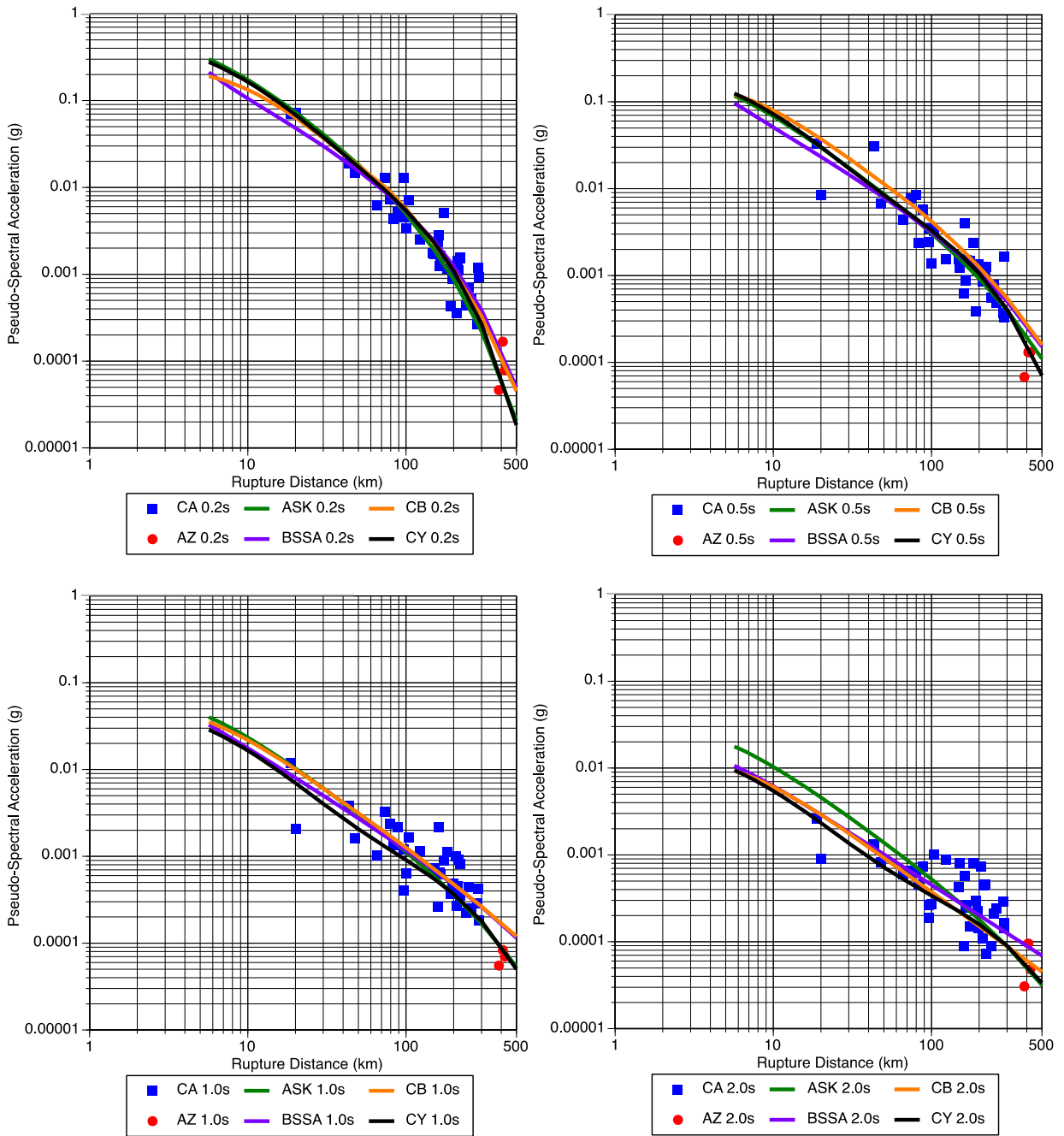
Figure 5.10 EQID 1182: pseudo-spectral acceleration (*g*) at periods of 0.2, 0.5, 1.0, and 2.0 sec from the NGA-West2 dataset, Arizona stations, and the 2014 NGA-West2 GMPEs are shown for which an event term is available.
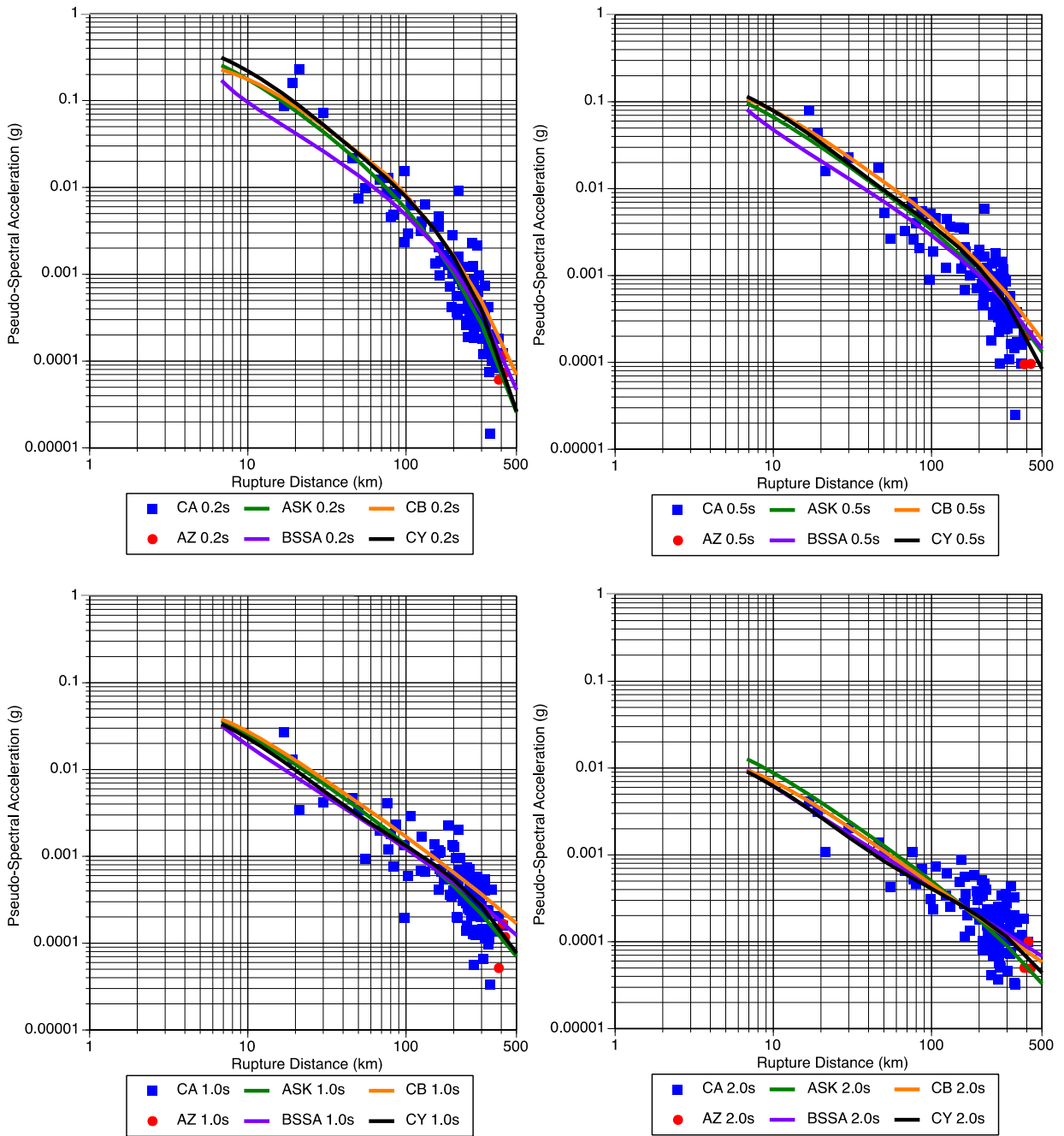
Figure 5.11 EQID 118: pseudo-spectral acceleration (*g*) at periods of 0.2, 0.5, 1.0, and 2.0 sec from the NGA-West2 dataset, Arizona stations, and the 2014 NGA-West2 GMPEs are shown for which an event term is available.

5.3.2   Region 2
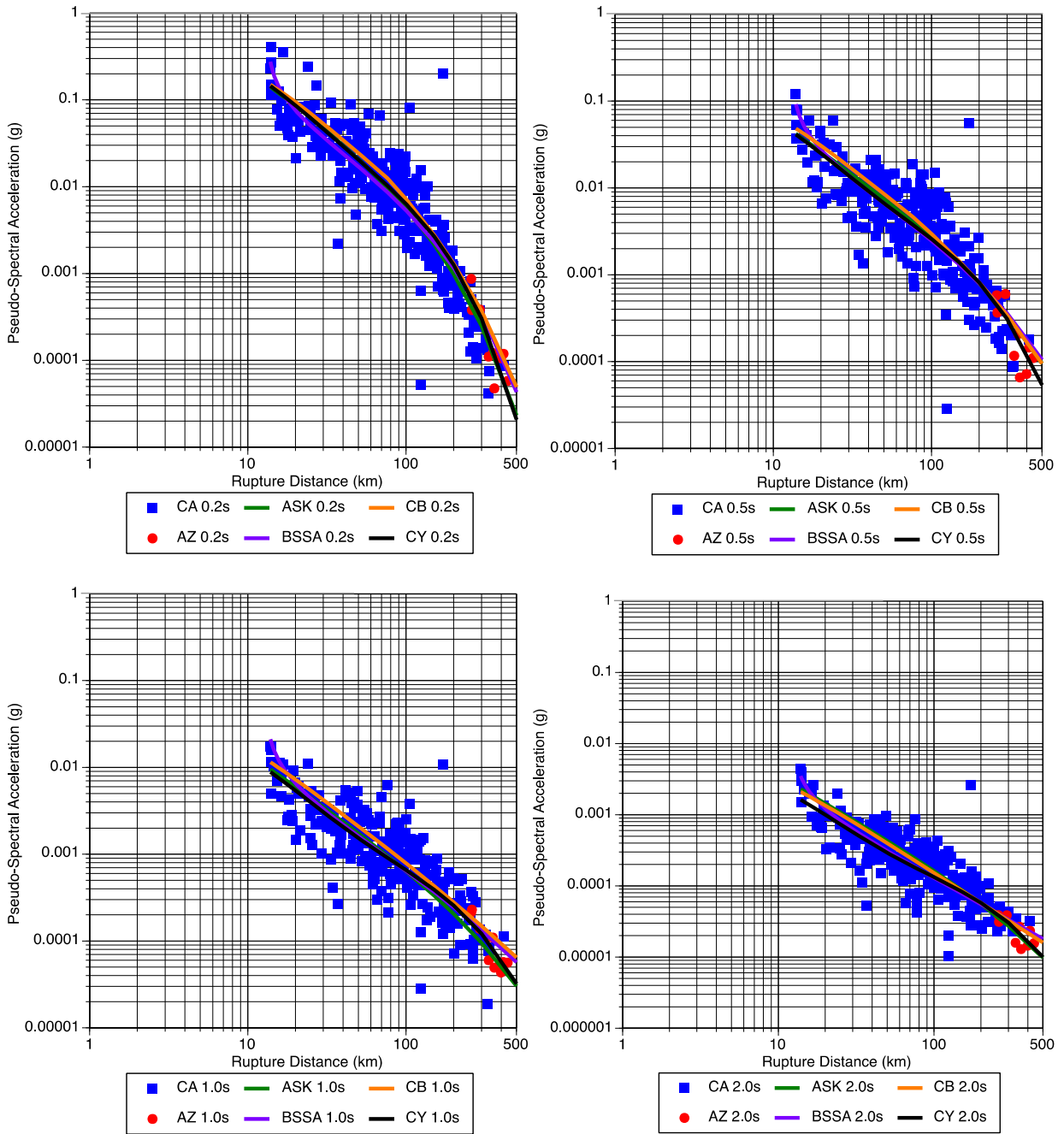
Figure 5.12   EQID 1018: pseudo-spectral acceleration (*g*) at periods of 0.2, 0.5, 1.0, and 2.0 sec from the NGA-West2 dataset, Arizona stations, and the 2014 NGA-West2 GMPEs are shown for which an event term is available.
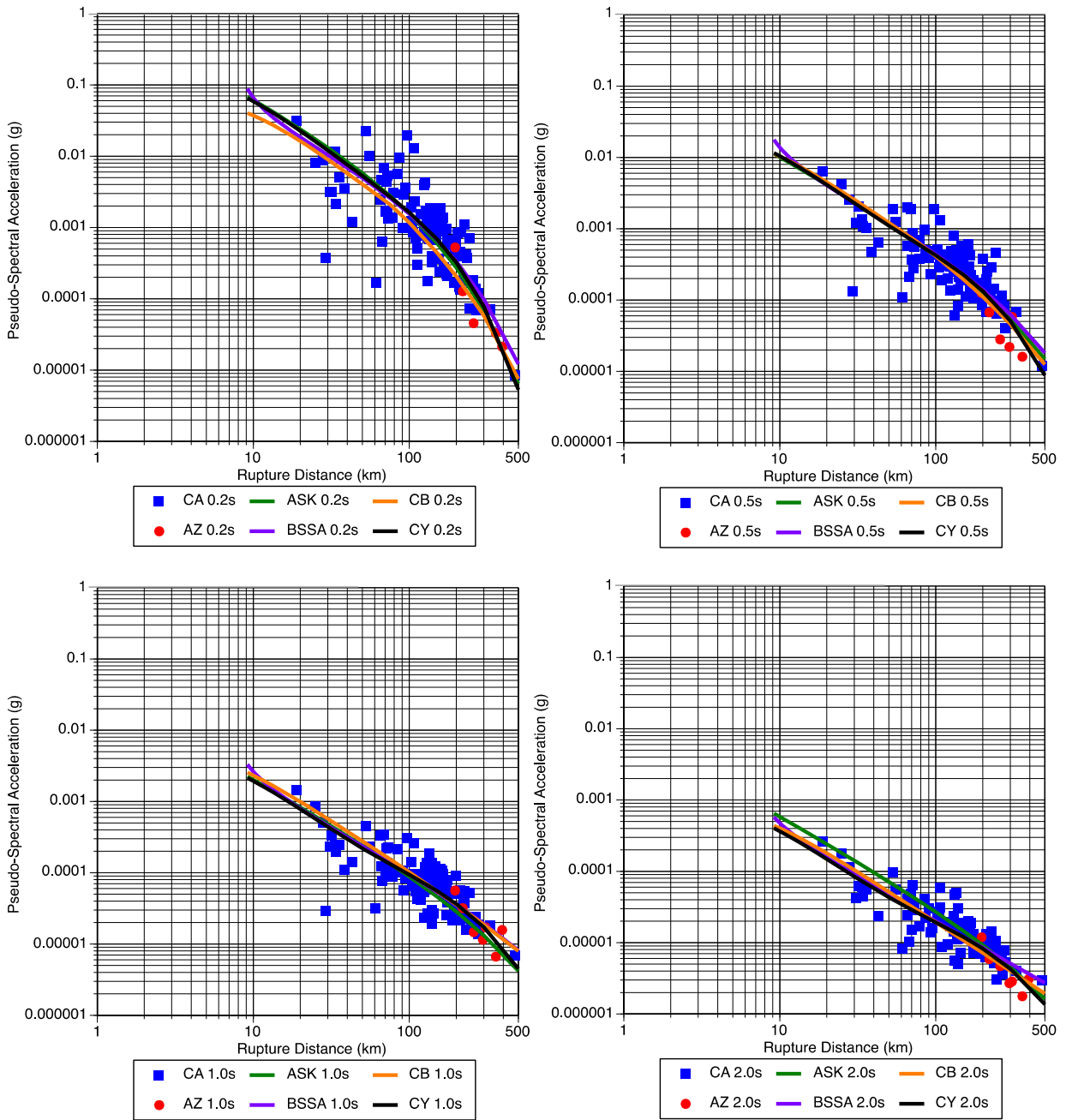
Figure 5.13 **EQID 1020: pseudo-spectral acceleration (*g*) at periods of 0.2, 0.5, 1.0, and 2.0 sec from the NGA-West2 dataset, Arizona stations, and the 2014 NGA-West2 GMPEs are shown for which an event term is available.**
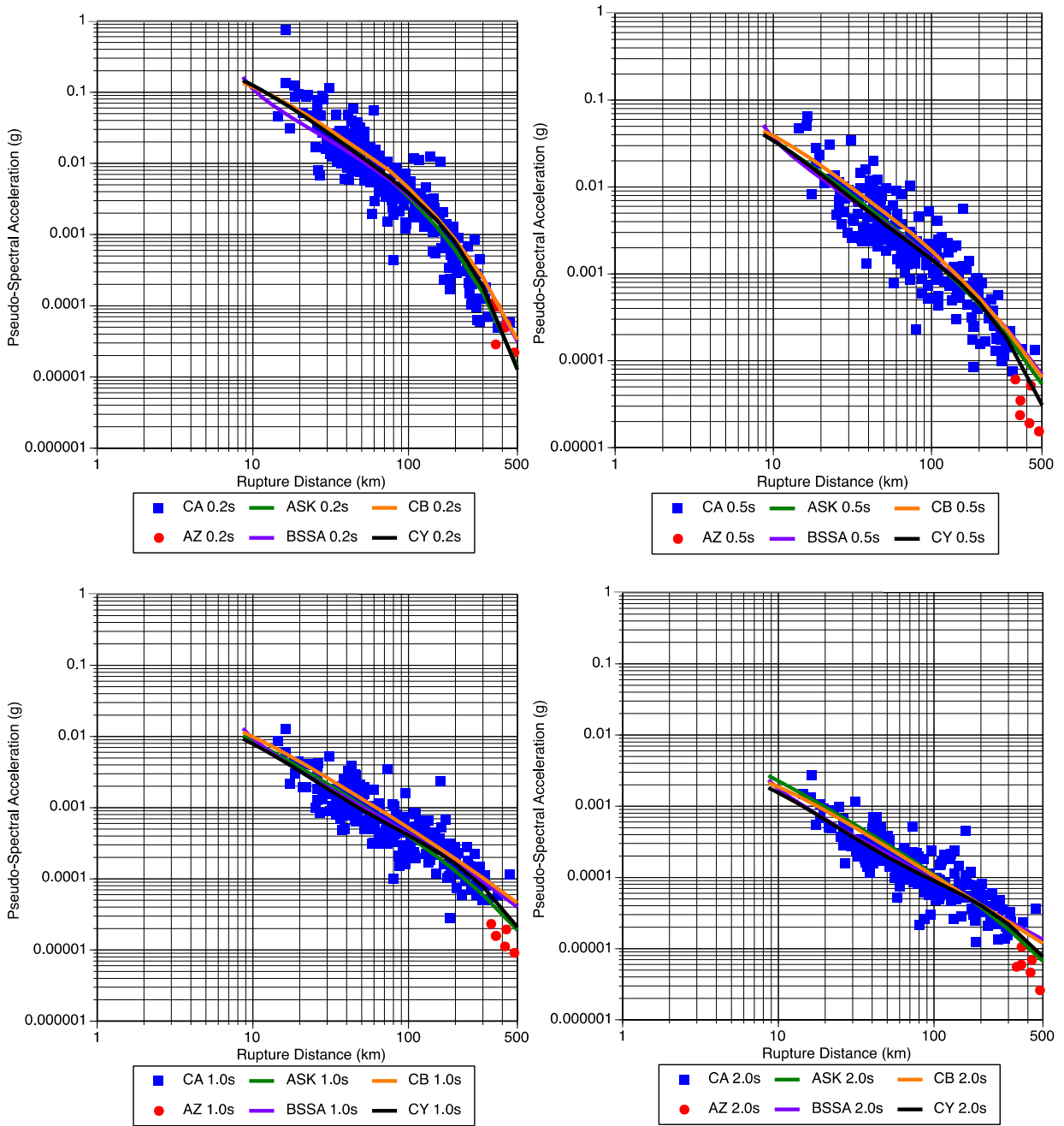
Figure 5.14   **EQID 1028: pseudo-spectral acceleration (*g*) at periods of 0.2, 0.5, 1.0, and 2.0 sec from the NGA-West2 dataset, Arizona stations, and the 2014 NGA-West2 GMPEs are shown for which an event term is available.**
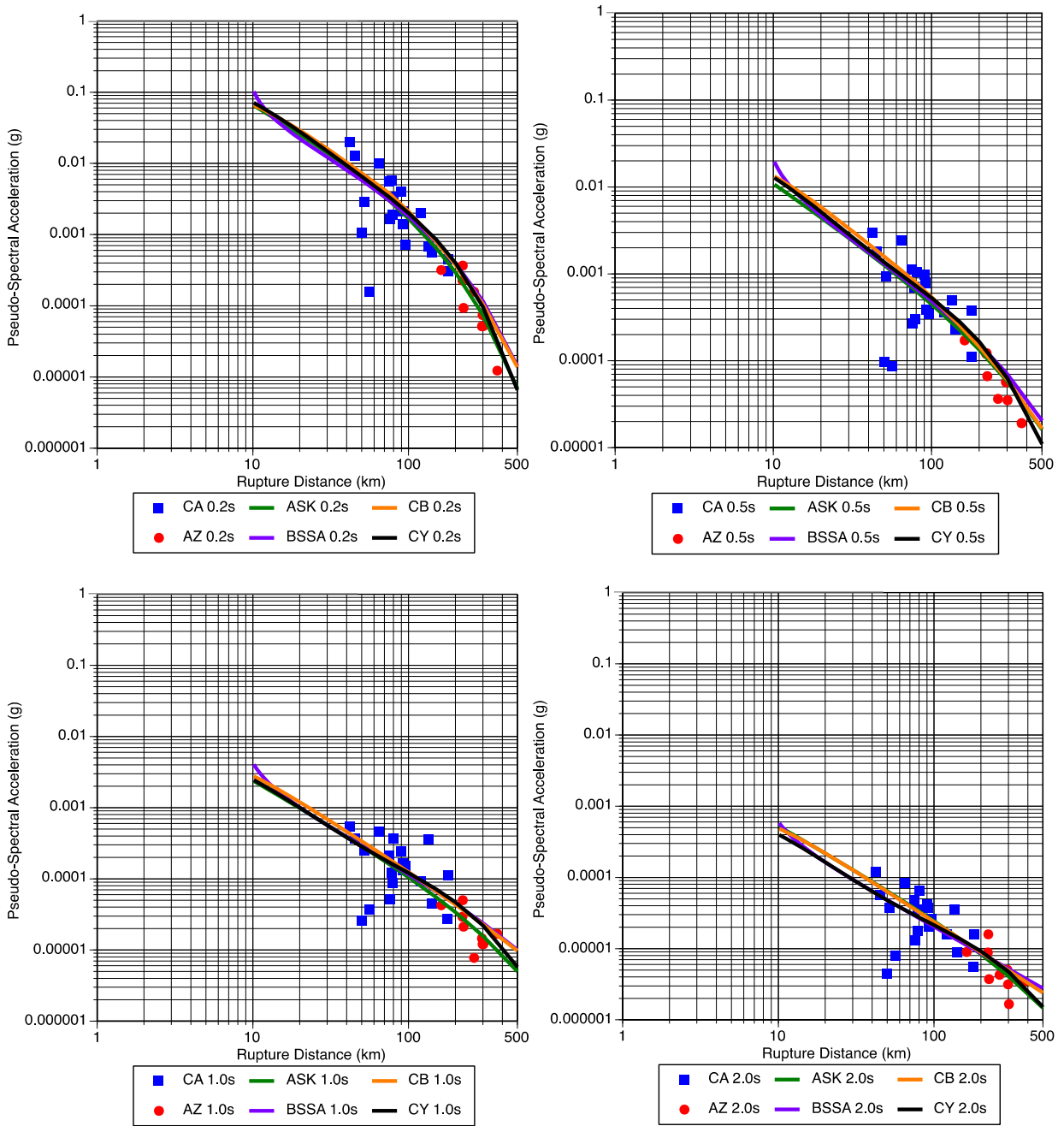
Figure 5.15 EQID 1067: pseudo-spectral acceleration (*g*) at periods of 0.2, 0.5, 1.0, and 2.0 sec from the NGA-West2 dataset, Arizona stations, and the 2014 NGA-West2 GMPEs are shown for which an event term is available.

5.3.3 Region 3
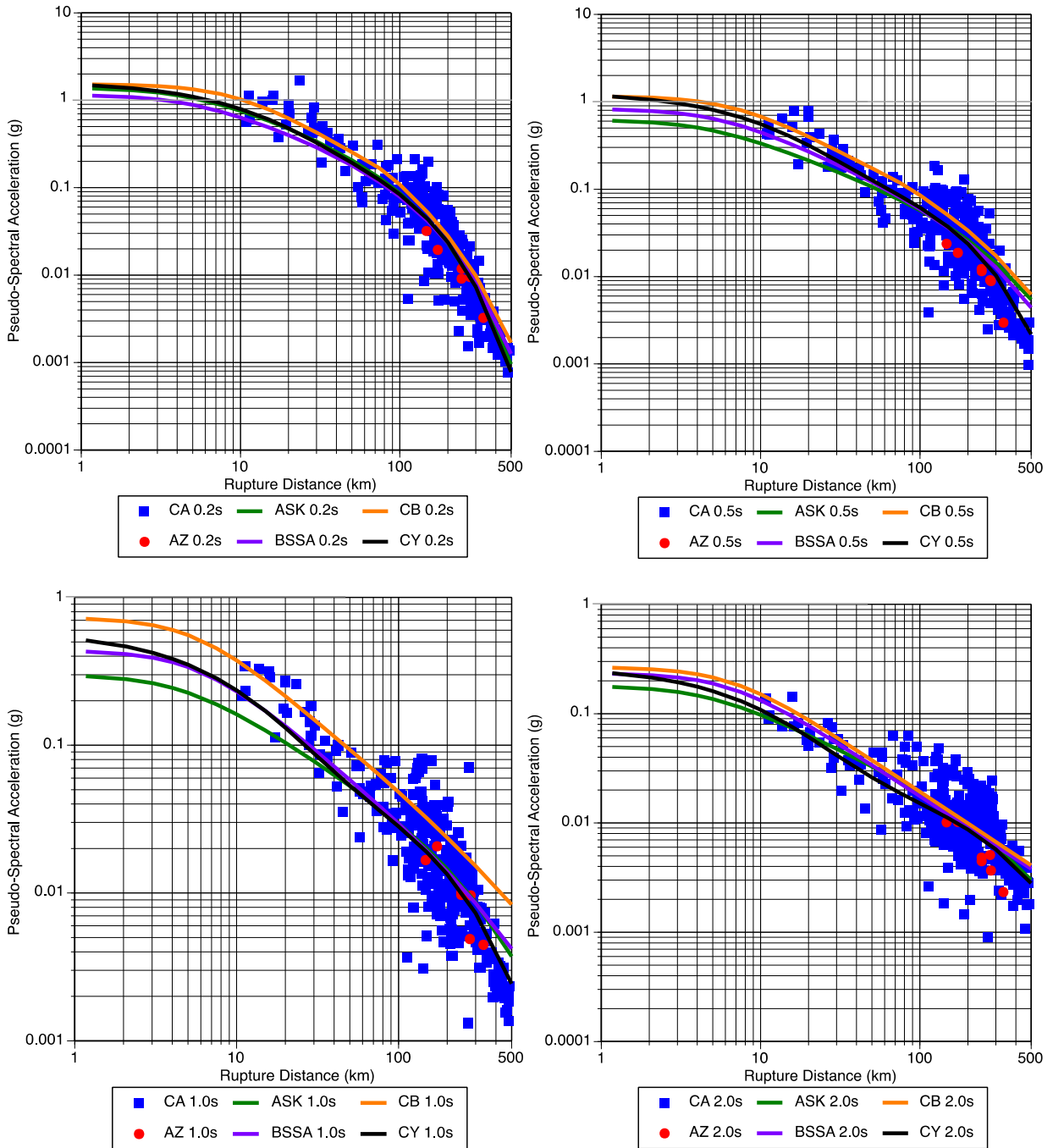
Figure 5.16   EQID 280: pseudo-spectral acceleration (*g*) at periods of 0.2, 0.5, 1.0, and 2.0 sec from the NGA-West2 dataset, Arizona stations, and the 2014 NGA-West2 GMPEs are shown for which an event term is available.
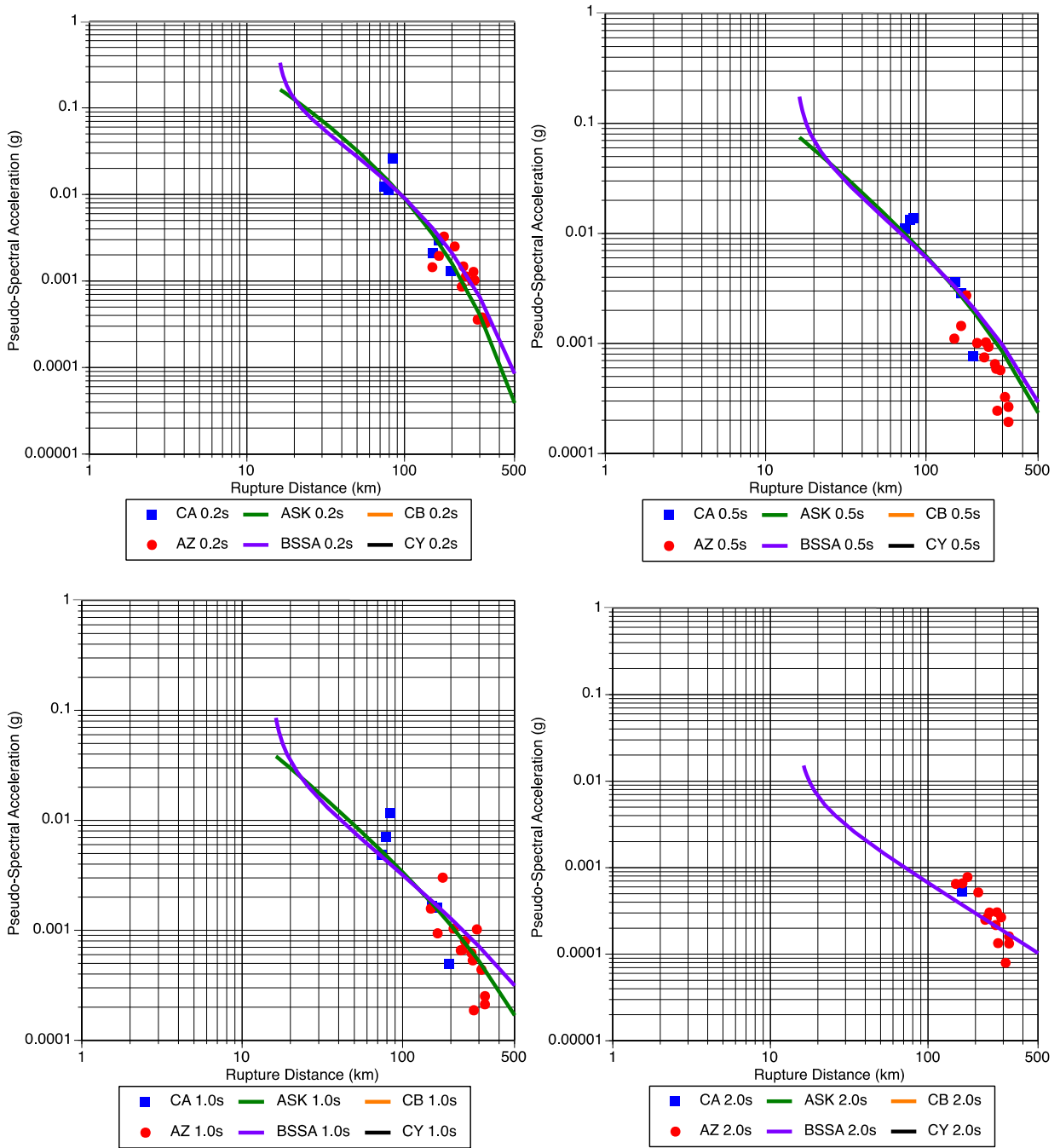
Figure 5.17   EQID 1004: pseudo-spectral acceleration (*g*) at periods of 0.2, 0.5, 1.0, and 2.0 sec from the NGA-West2 dataset, Arizona stations, and the 2014 NGA-West2 GMPEs are shown for which an event term is available.
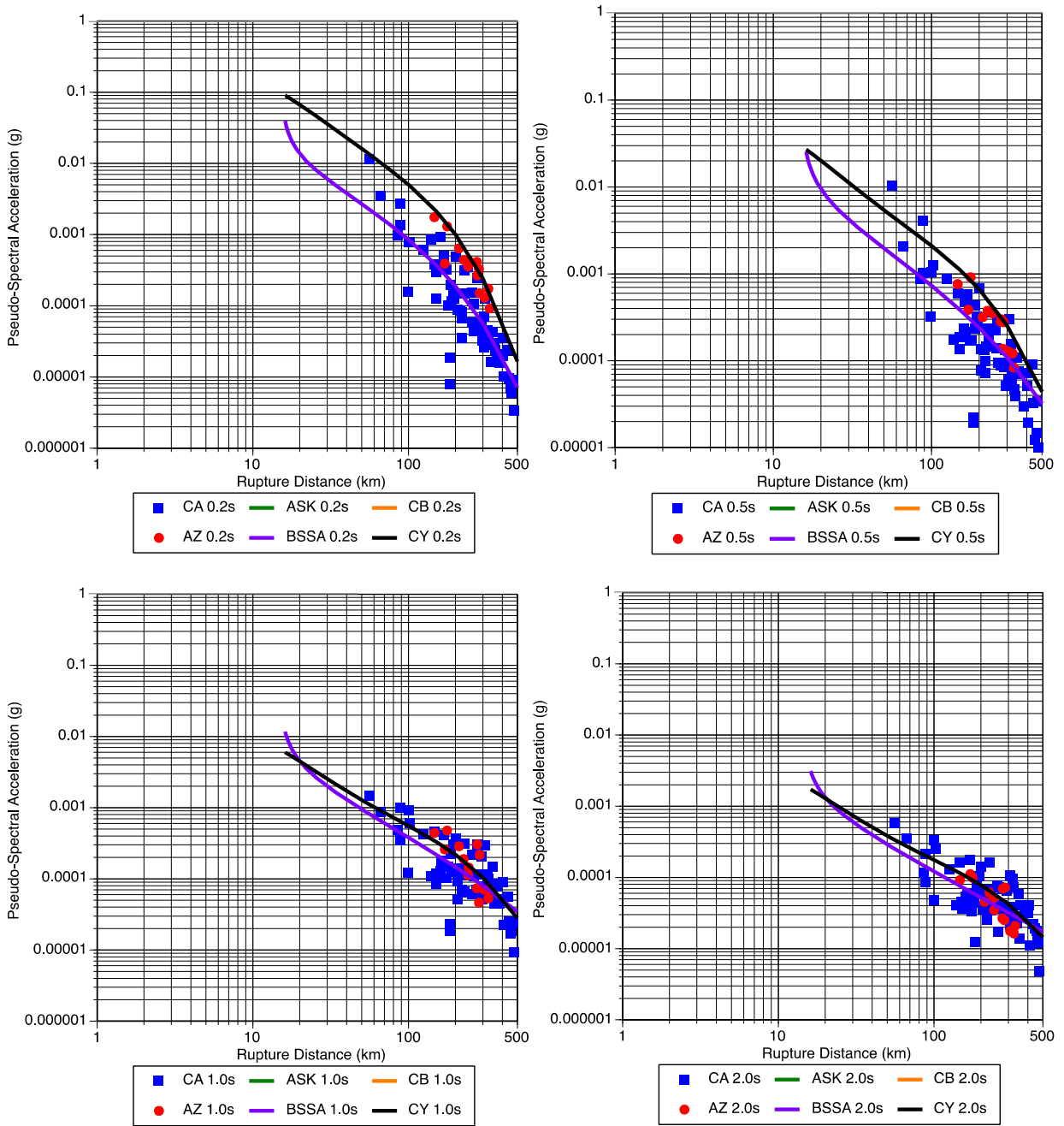
Figure 5.18   **EQID 1017: pseudo-spectral acceleration (*g*) at periods of 0.2, 0.5, 1.0, and 2.0 sec from the NGA-West2 dataset, Arizona stations, and the 2014 NGA-West2 GMPEs are shown for which an event term is available.**
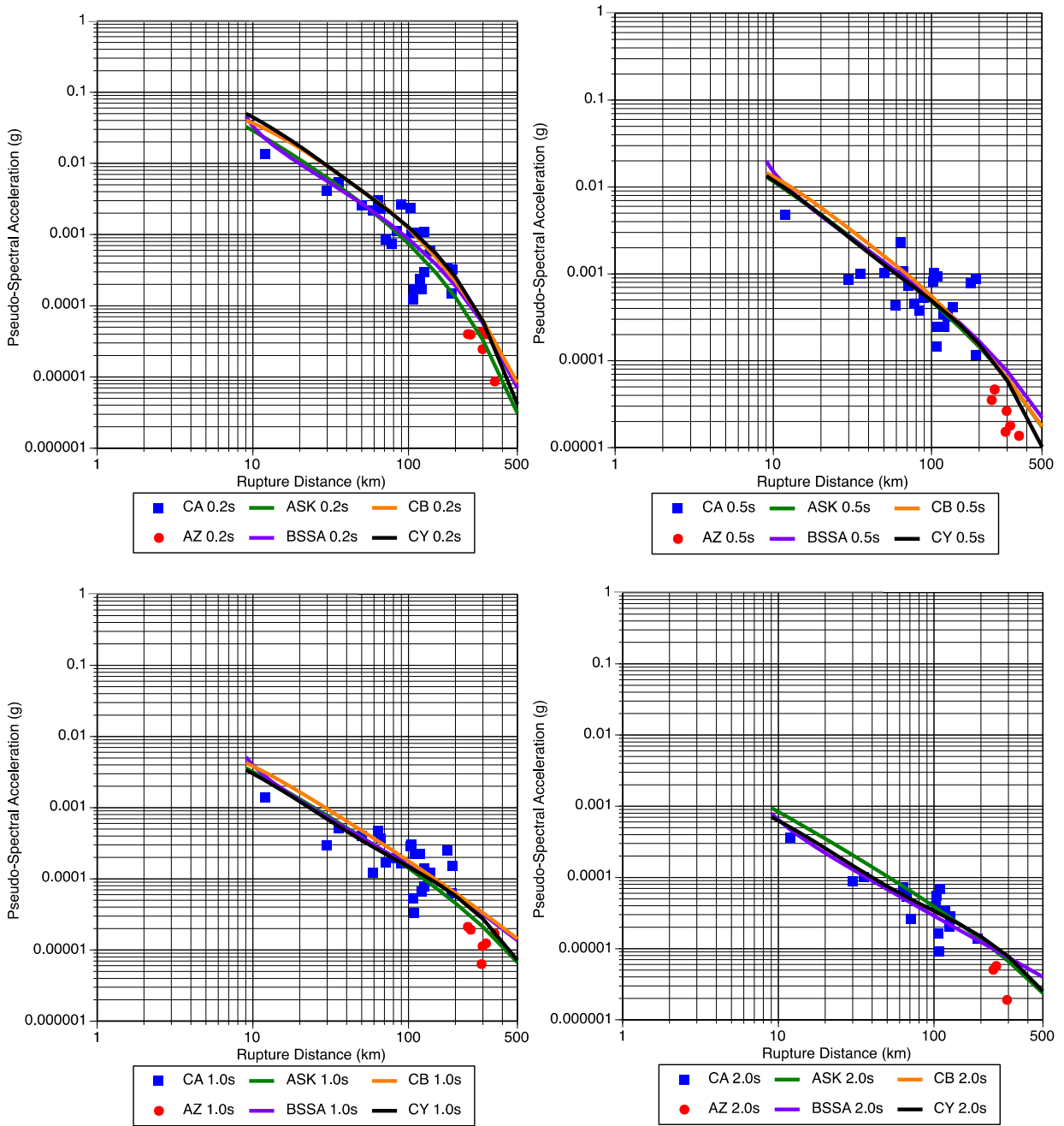
Figure 5.19   EQID 1058: pseudo-spectral acceleration (*g*) at periods of 0.2, 0.5, 1.0, and 2.0 sec from the NGA-West2 dataset, Arizona stations, and the 2014 NGA-West2 GMPEs are shown for which an event term is available.

5.3.4 Conclusions

Section 5.2 showed that the Arizona recordings from earthquakes in Region 1 have a higher average Q than the California data, thus the 5% damped PSA at the four periods in Section 5.3.1 from stations in Arizona should be above the predictions from the NGA-West2 GMPEs and the data from the NGA-West2 database, but this is not observed. The ground motion from both the NGA-West2 database and the Arizona recordings fall off faster with distance than the NGA-West2 GMPEs predict. The difference in path Q between the Arizona recordings of the Region 1 earthquakes is being masked by the overprediction of the southeastern California earthquakes at long distances of the NGA-West2 GMPEs.

5.4   RESIDUALS FROM NGA-WEST2 GROUND MOTION PREDICTION EQUATIONS FOR ARIZONA DATA

The figures in Section 5.3 show that the NGA-West2 GMPEs overpredict the NGA-West2 and Arizona data at long distances from earthquakes in southeastern California. To evaluate the extent of this overprediction, the intra-event residuals from the NGA-West2 ground motion predictions are shown in Figures 5.20, 5.21, and 5.22 for Regions 1, 2, and 3, respectively. Figure 5.20 shows that the NGA-West2 GMPEs are most similar to the Arizona data from earthquakes in Region 1, overpredicting at periods of 0.5 and 1 sec, but nearly unbiased at periods of 0.2 and 2 sec. Figures 5.21 and 5.22 show that the NGA-West2 GMPEs overpredict the Arizona data at all periods for both Regions 2 and 3. Figure 5.23 summarizes these observations.
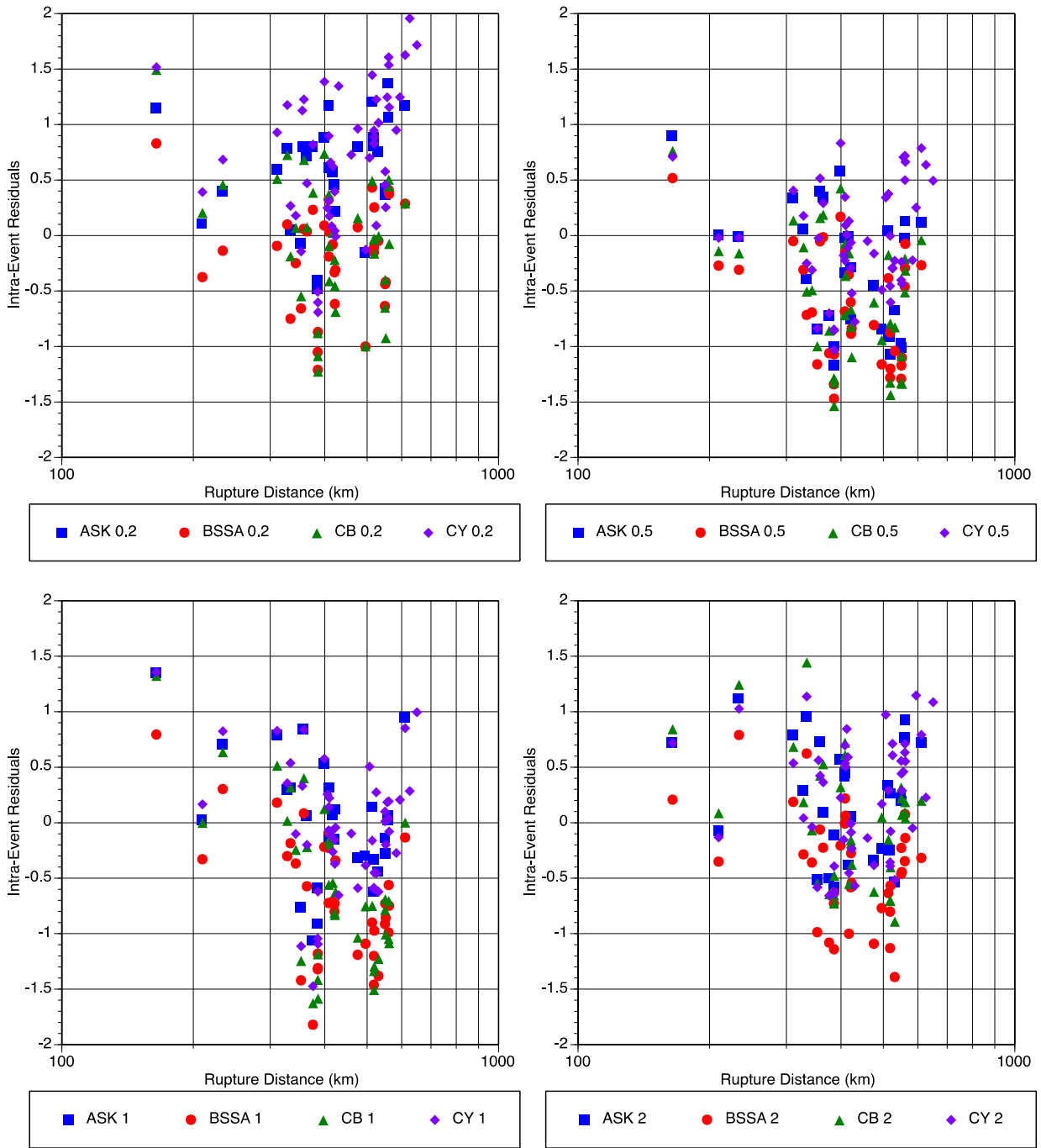
Figure 5.20 **Intra-event residuals for Arizona data from earthquakes in Region 1 for the 2014 NGA-West2 GMPEs for which event terms are available at periods of 0.2, 0.5, 1.0, and 2.0 sec.**
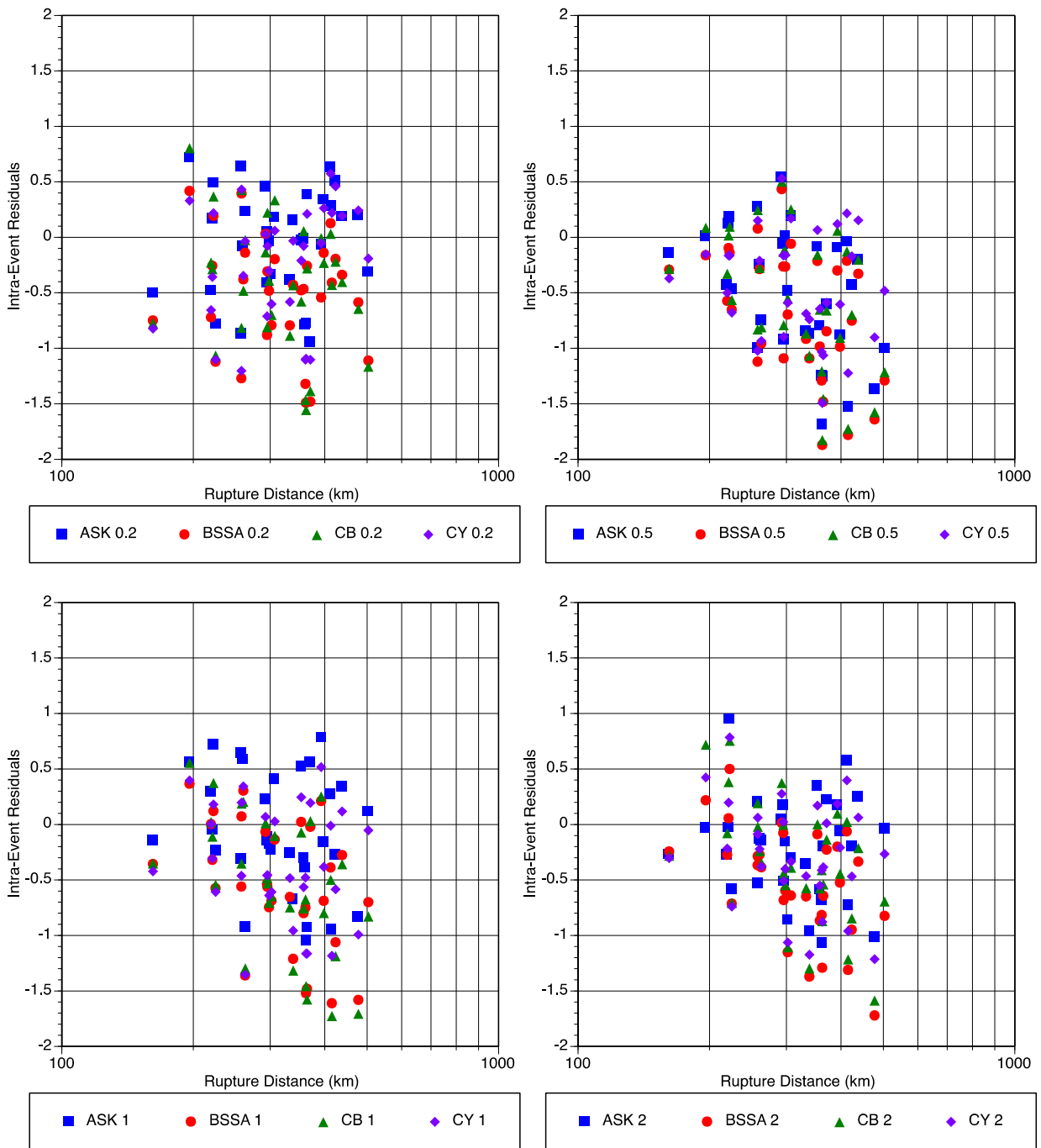
Figure 5.21 Intra-event residuals for Arizona data from earthquakes in Region 2 for the 2014 NGA-West2 GMPEs for which event terms are available at periods of 0.2, 0.5, 1.0, and 2.0 sec.
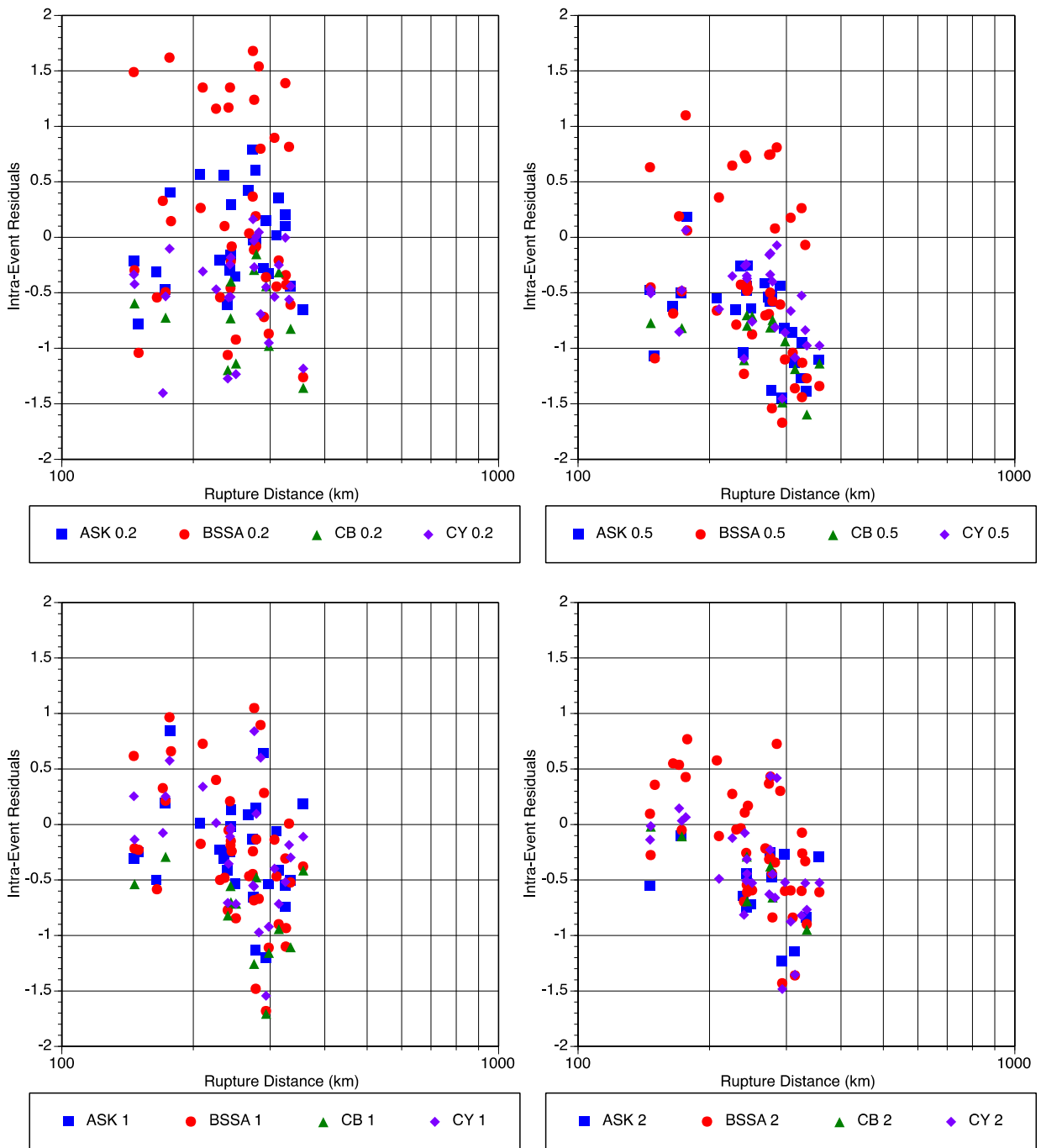
Figure 5.22 **Intra-event residuals for Arizona data from earthquakes in Region 3 for the 2014 NGA-West2 GMPEs for which event terms are available at periods of 0.2, 0.5, 1.0, and 2.0 sec.**
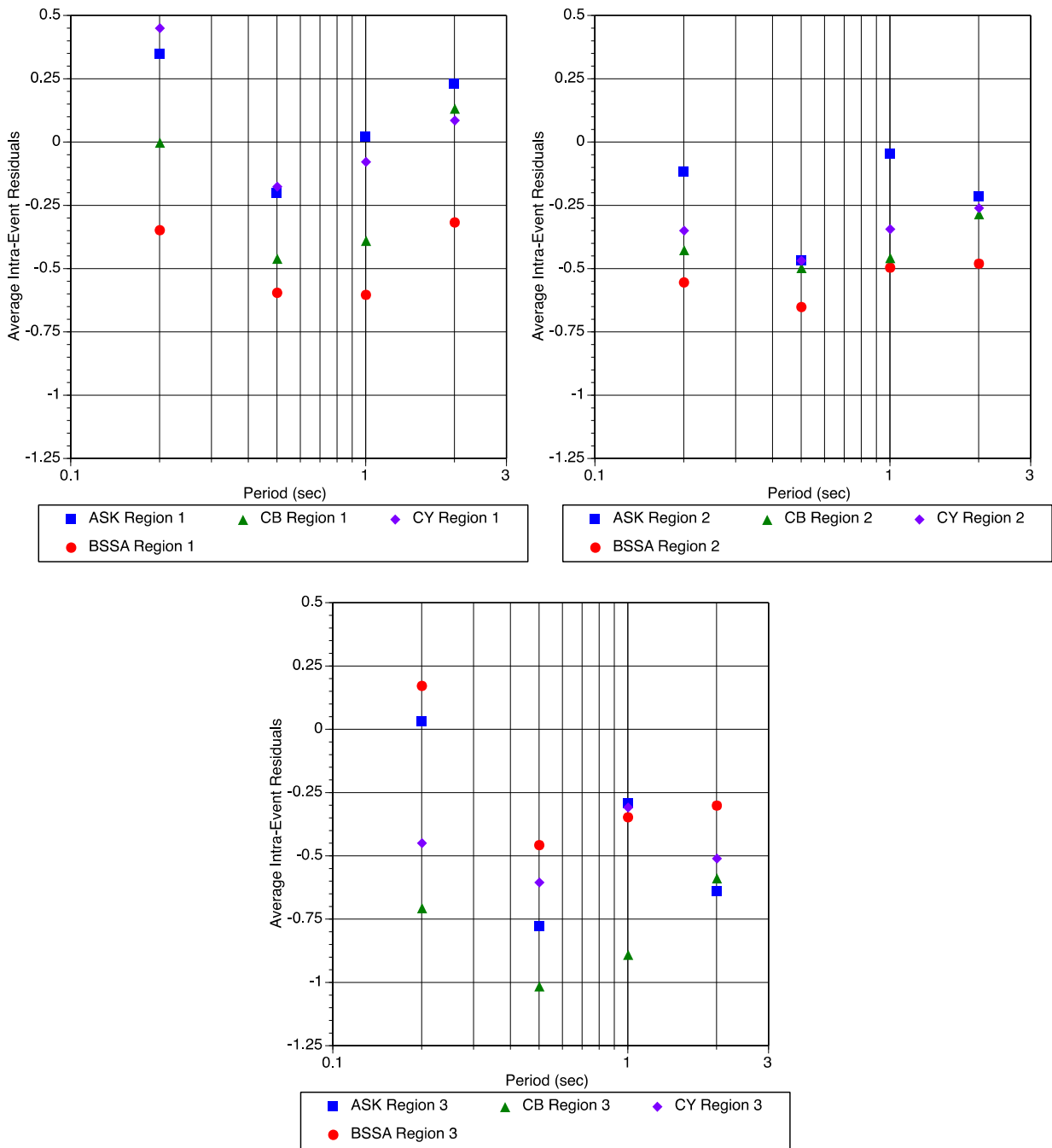
Figure 5.23 Average intra-event residuals for Arizona data from earthquakes in Regions 1, 2, and 3 for the 2014 NGA-West2 GMPEs for which event terms are available at periods of 0.2, 0.5, 1.0, and 2.0 sec.

To estimate how much of the overprediction is due to the shape of the NGA-West2 GMPEs, the same procedure is followed with the NGA-West2 data to look at the overprediction to this set. Figure 5.24 shows how the overprediction of the NGA-West2 data compares with the overprediction of the Arizona data. The NGA-West2 data is broken down into two subsets, the first with rupture distances of 200–300 km, and the second with rupture distances of 300–400 km. The steepness of the NGA-West2 GMPEs with respect to distance indicates that the overprediction will be larger for larger distances; Figure 5.26 shows this to be the case for the NGA-West2 data.

The Arizona data are primarily at rupture distances of 300–400 km, thus it is possible to compare the bias of the Arizona data from Regions 1, 2, and 3 with the bias of the NGA-West2 data with rupture distances of 300–400 km. The bias for the NGA-West2 data lies primarily in the middle of the range from Regions 1, 2, and 3. This demonstrates that there is a component of the bias in the Arizona data that is due to the NGA-West2 models being too steep. The NGA-West2 bias is most similar to Region 2, which has the most similar average path Q to California. The Region 1 bias is above the NGA-West2 data bias, which may be due to the average Q path being larger than path Q in California. The Region 3 bias is primarily below the NGA-West2 data bias, which may be due to the average Q path being slightly smaller than path Q in California.
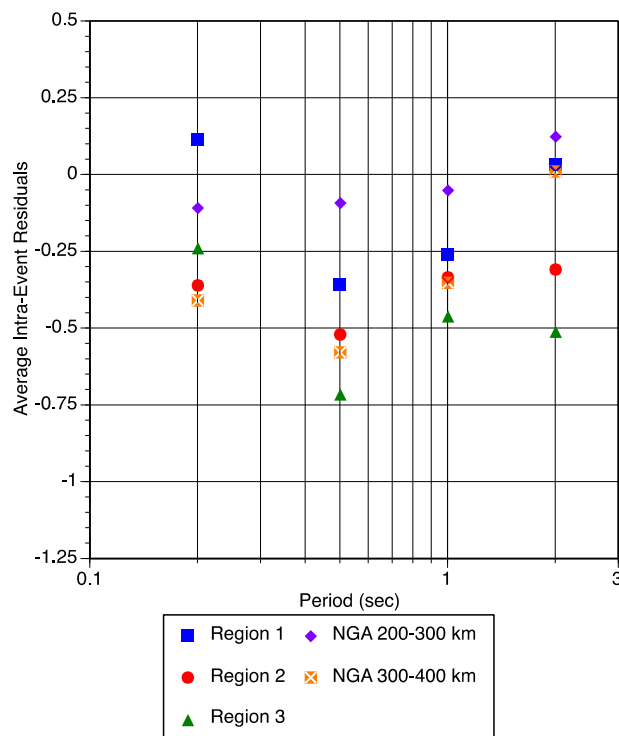
Figure 5.24   **Average intra-event residuals for Arizona data from earthquakes in Regions 1, 2, and 3 and NGA-West2 data at distances of 200–300 km and 300–400 km averaged across the NGA-West2 relationships at periods of 0.2, 0.5, 1.0, and 2.0 sec.**

5.5   CONCLUSIONS

There are regional differences in the path Q from earthquakes in California and Mexico to sites in Arizona that have effects on the 5% damped pseudo-spectral acceleration. The effect from Q is complicated by the overprediction of the NGA-West2 GMPEs at large distances in Arizona. Three regions in California are created to estimate the combined effect of NGA-West2 overprediction of southeastern California earthquakes at large distances and path Q differences to Arizona. The Arizona data from earthquakes in Region 1 are overpredicted by 0–0.35 natural log units. The Arizona data from earthquakes in Regions 2 and 3 are overestimated by an additional 0.1–0.4 natural log units for a total overprediction of between 0.2 and 0.7 natural log units for periods between 0.2–2 sec.

REFERENCES

Abrahamson N.A., Silva W.J., Kamai, R. (2014). Summary of the AKS14 ground-motion relation for active crustal regions, *Earthq. Spectra*, Vol. 30, DOI: 10.1193/070913EQS198M, (in press).

Aki K. (1967). Scaling law of seismic spectrum, *J. Geophys. Res.*, 72: 1217−1231.

Aki K. (1969). Analysis of the seismic coda of local earthquakes as scattered waves, *J. Geophys. Res.*, 74: 615−631.

Ancheta T.D., Darragh R.B., Stewart J.P., Seyhan E., Silva W.J., Chiou B.S.-J., Wooddell K.E., Graves R.W., Kottke A.R., Boore D.M., Kishida, T., Donahue J.L. (2013). PEER NGA-West2 database, *PEER Report 2013/03*, Pacific Earthquake Engineering Research Center, University of California, Berkeley, CA.

Anderson J.G. (2013). *Personal communication*.

Anderson J.G. (1991). A preliminary descriptive model for the distance dependence of the spectral decay parameter in southern California, *Bull. Seismol. Soc. Am.*, 81: 2186–2193.

Anderson J.G., Hough S.E. (1984). A model for the shape of the Fourier amplitude spectrum of acceleration at high frequencies, *Bull. Seismol. Soc. Am.*, 74: 1969–1993.

Anderson J.G., Humphrey J.R. (1991). A least squares method for objective determination of earthquake source parameters, *Seismol. Res. Lett.*, 62: 201–209.

Arizona Geological Survey (2011). <http://www.azgs.az.gov/eq_monitor.shtml> (Dec. 15, 2013).

Atkinson G.M., Silva W.J. (1997). An empirical study of earthquake source spectra for California earthquakes, *Bull. Seismol. Soc. Am.,* 87: 97−113.

Atkinson G.M., Silva W.J. (2000). Stochastic modeling of California ground motions, *Bull. Seismol. Soc. Am.*, 90: 255–274.

Bakun W.H. (1984). Seismic moments, local magnitudes, and coda-duration magnitudes for earthquakes in central California, *Bull. Seismol. Soc. Am.*, 74: 439–458.

Beck S., Linkimer L., Zandt G., Holland A. (2013). Focal mechanisms and preliminary attenuation measurements in Arizona, *Report CR-13-C*, Arizona Geological Survey, (repository.azgs.az.gov), 21 pgs.

Biasi G.P., Anderson J.G. (2007). Measurement of the parameter kappa, and reevaluation of kappa for small to moderate earthquakes at seismic stations in the vicinity of Yucca Mountain, Nevada, *Final Technical Report TR-07-007*, Nevada System of Higher Education (NSHE), University of Nevada, Las Vegas (UNLV), 232 pgs.

Biasi G.P., Smith K. D. (2001). Site effects for seismic monitoring stations in the vicinity of Yucca Mountain, Nevada, *MOL20011204.0045*, a report prepared for the US DOE/University and Community College System of Nevada (UCCSN) Cooperative Agreement.

Boore D.M. (1983). Stochastic simulation of high frequency ground motions based on seismological models of the radiated spectra, *Bull. Seismol. Soc. Am.*, 73: 1865–1894.

Boore D.M. (2010). Orientation-independent, nongeometric-mean measures of seismic intensity from two horizontal components of motion, *Bull. Seismol. Soc. Am.*, 100: 1830–1835.

Boore D.M., Akkar S. (2003). Effect of causal and acausal filters on elastic and inelastic response spectra, *Earthq. Eng. Struct. Dyn.*, 32: 1729–1748.

Boore D.M., Goulet C.A. (2014). The effect of sampling rate and anti-aliasing filters on high-frequency response spectra, Bull. Earthq. Eng*.,* 12: 203–216.

Boore D.M., Stewart J.P., Seyhan E., Atkinson G.M. (2014). NGA-West 2 equations for predicting PGA, PGV, and 5%-damped PSA for shallow crustal earthquakes, *Earthq. Spectra*, DOI: 10.1193/070113EQS184M (in press).

Bozorgnia Y., Abrahamson N.A., Al Atik L., Ancheta T.D., Atkinson G.M., Baker J.W., Baltay A., Boore D.M., Campbell K.W., Chiou B.S.-J., Darragh R.B., Day S., Donahue J., Graves R.W., Gregor N., Hanks T., Idriss I.M., Kamai R., Kishida T., Kottke A., Mahin S.A., Rezaeian S., Rowshandel B., Seyhan E., Shahi S., Shantz T., Silva W.J., Spudich P., Stewart J.P., Watson-Lamprey J., Wooddell K.E., Youngs R.R. (2014). NGA-West2 research project, *Earthq. Spectra*, DOI: 10.1193/072113EQS209M (in press).

Bresenham J.E. (1965). Algorithm for computer control of a digital plotter, *IMC Systems J.*, 4(1): 25−30.

Brune J.N. (1970). Tectonic stress and the spectra of seismic shear waves from earthquakes, *J. Geophys. Res.*, 75: 4997–5002.

Campbell K.W., Bozorgnia Y. (2014). NGA-West2 ground motion model for the average horizontal components of PGA, PGV, and 5%-damped linear acceleration response spectra, *Earthq. Spectra*, Vol. 30, DOI: 10.1193/062913EQS175M (in press).

Chiou B.S.-J., Darragh R.B., Gregor N., Silva W.J. (2008). NGA project strong-motion database, *Earthq. Spectra*, 24: 23–44.

Chiou= B.S-J., Youngs R.R. (2014). Update of the Chiou and Youngs NGA model for the average horizontal component of peak ground motion and response spectra, *Earthq. Spectra*, Vol. 30, DOI: 10.1193/072813EQS219M (in press).

Edwards B., Faeh D., Giardini D. (2011). Attenuation of seismic shear wave energy in Switzerland. *Geophys. J. Int.*, 185: 967–984.

EPRI (1993). Guidelines for determining design basis ground motions, Electric Power Research Institute, Vol. 1-5, *EPRI TR-102293*, Palo Alto, CA.

Erickson D., McNamara D., Benz H. (2004). Frequency dependent Lg Q within the continental United States, *Bull. Seism. Soc. Am.*, 94: 1630–1643.

Frankel A. (1982). The effects of attenuation and site response on the spectra of microearthquakes in the Northeastern Caribbean, *Bull. Seismol. Soc. Am.*, 72: 1379–1402.

Goldstein P., Dodge D., Firpo M., Minner L. (2003). SAC2000: Signal processing and analysis tools for seismologists and engineers, in: *The IASPEI International Handbook of Earthquake and Engineering Seismology*, W.H.K. Lee, H. Kanamori, P.C. Jennings, C. Kisslinger (eds.), Academic Press, London.

Hanks T. C. (1982). f max, *Bull. Seismol. Soc. Am.*, 72: 1867–1879.

Hanks T.C., Bakun W.H. (2008). M - log A observations of recent large earthquakes, *Bull. Seismol. Soc. Am.,* 98(1): 490–494.

Hanks T.C., Boore D.M. (1984). Moment-magnitude relations in theory and practice, *J. Geophys. Res.*, 89: 6229–6235.

Hanks T.C., Kanamori H. (1979). A moment magnitude scale, *J. Geophys. Res.*, 84: 2348–2350.

Hough S.E., Anderson J.G. (1988). High-frequency spectra observed at Anza, California: Implications for Q structure, *Bull. Seismol. Soc. Am.*, 78: 692–707.

Humphrey J.R., Jr., Anderson J.G. (1992). Shear wave attenuation and site response in Guerrero, Mexico, *Bull. Seismol. Soc. Am.,* 81, 1622–1645.

ICC {2002). *International Building Code*, International Code Council, Country Club Hills, IL.

IRIS (2013). Incorporated Research Institutions for Seismology, < http://www.iris.edu/hq/> (Dec. 15, 2013).

Kamai R., Abrahamson N.A., Silva, W.J. (2013). Nonlinear horizontal site response for the NGA-West2 project*, PEER Report 2013/12*, Pacific Earthquake Engineering Research Center, University of California, Berkeley, CA.

Kato K., Aki K., Takemura M. (1995). Site amplification from coda waves: validation and application to S-wave site response, *Bull. Seismol. Soc. Am.*, 85: 467–477.

Kayen R., Moss R.E.S., Thompson E., Seed R.B., Cetin K.O., Der Kiureghian A., Tanaka Y., Tokimatsu K. (2013) Shear-wave velocity–based probabilistic and deterministic assessment of seismic soil liquefaction potential, *J. Geotech. Geoenviron. Eng.*, 139(3): 407–419.

Kayen R., Seed R.B., Moss R.E.S., Cetin K.O., Tanaka Y., Tokimatsu K. (2004) Global shear wave velocity database for probabilistic assessment of the initiation of seismic soil liquefaction, *Proceedings, 11th International Conference on Soil Dynamics and Earthquake Engineering (The 3rd International Conference on Earthquake Geotechnical Engineering),* 2: 506–513, Berkeley, CA.

Kempton J.J., Stewart J.P. (2006). Prediction equations for significant duration of earthquake ground motions considering site and near-source effects, *Earthq. Spectra*, 22: 985–1013.

Kilb D., Biasi G., Anderson J.G., Brune J., Peng Z., Vernon F.L. (2012). A comparison of spectral parameter kappa from small and moderate earthquakes using southern California ANZA seismic network data, *Bull. Seismol. Soc. Am.*, 102: 284–300.

Kishida T., Ktenidou O.-J., Darragh R.B., Silva W.J. (2014). Data processing for Fourier amplitude spectrum (FAS) estimation from NGA-West2 processed accelerations, Chapter 7 in the PEER NGA-East Database Report Pacific Earthquake Engineering Research Center, University of California, Berkeley, CA (in preparation).

Ktenidou O.-J., Gelis C., Bonilla F. (2013). A study on the variability of kappa in a borehole. Implications on the computation method used, *Bull. Seismol. Soc. Am.*, 103(2a): 1048–1068.

Ktenidou O.-J., Cotton F., Abrahamson N.A., Anderson J.G. (2014). Taxonomy of kappa: a review of definitions and estimation methods targeted to applications, *Seismol. Res. Letts.* 85(1): 135–146.

Lai C.G., Rix G. J. (1998). Simultaneous inversion of Rayleigh phase velocity and attenuation for near-surface site characterization, *Report No. GIT-CEE/GEO-98-2*, Georgia Institute of Technology, School of Civil and Environmental Engineering, Atlanta, GA, 258 pgs.

Lermo J., Chávez-García F.-J. (1993). Site effect evaluation using spectral ratios with only one station, *Bull. Seismol. Soc. Am.*, 83: 1574–1594.

Lettis Consultants International Inc. (2012). *Characterization of Ground Motion Propagation for Palo Verde SSHAC Level 2 PSHA,* Internal Project Report.

Nigam N., Jennings P.C. (1969). Calculation of response spectra from strong-motion earthquake records, *Bull. Seismol. Soc. Am.*, 59(2): 909–922.

Olsen K. (2014). *Personal communication*.

Parolai S., Bindi D.(2004). Influence of soil-layer properties on k evaluation, *Bull. Seismol. Soc. Am.*, 94, 349–356.

Pasyanos M.E. (2013). A lithospheric attenuation model of North America, *Bull. Seismol. Soc. Am.*, 103: 3321–3333.

Pelekis P.C, Athanasopoulos G.A. (2011). An overview of surface wave methods and a reliability study of a simplified inversion technique, *Soil. Dyn. Earthq. Eng.*, 31(12): 1654−1668.

Phillips S.W., Aki K. (1986). Site amplification of coda waves from local earthquakes in central California, *Bull. Seismol. Soc. Am.*, 76: 627−648.

Phillips W.S., Mayeda K., Malagnini L. (2013). How to invert multi-band, regional phase amplitudes for 2-D attenuation and source parameters: Tests using the US Array, *Pure. Appl. Geophys.*, 171: 469–484.

Press W.H., Flannery B.P., Teukolsky S.A., Vetterling W.T. (1986). *Numerical Recipes*, Cambridge University Press, Cambridge, UK.

Richter C. (1958). *Elementary Seismology*, W. H. Freeman and Co., San Francisco, CA.

Santamarina J.C., Fratta D. (1998). *Introduction to Discrete Signals and Inverse Problems in Civil Engineering*, Amer. Society of Civil Engineers, 327 pgs.

Satoh T., Poran C.I., Yamagata K., Rodriquez J.A. (1991). Soil profiling by spectral analysis of surface waves. In: *Proceedings, 2nd International Conference on Recent Advances In Geotechnical Earthquake Engineering and Soil Dynamics*, Vol. II; pp, 1429–1434.

Schneider J., Silva W.J., Stark C. (1993). Ground motion model for the 1989 **M** 6.9 Loma Prieta Earthquake including effects of source, path, and site, *Earthq. Spectra*, 9(2): 251−287.

Seyhan E., Stewart, J.P., Ancheta T. D., Darragh R.B., Graves R.W. (2014). NGA-West 2 site database, *Earthq. Spectra*, doi: http://dx.doi.org/10.1193/062913EQS180M.

Silva W.J. (2013). *Personal communication*.

Silva W.J. Darragh R.B. (2014). Estimation of kappa, *Report Submitted to Pacific Northwest National Laboratory*, Richland, WA.

Silva W.J., Abrahamson N., Toro G., Costantino C. (1997). Description and validation of the stochastic ground motion model, *Report submitted to Brookhaven National Laboratory, Contract No. 770573*, Associated Universities, Inc., Upton, NY.

Thatcher W., Hanks T.C. (1973). Source parameters of southern California earthquakes, *J. Geophys. Res.*, 78: 8547−8576.

US Array (2003). <http://www.usarray.org/researchers/obs/transportable> (Dec. 15, 2013).

Viktorov I.A. (1967). *Rayleigh and Lamb Waves: Physical Theory and Applications*, Plenum Press, New York.

Webb S.C. (2002). Seismic noise on land and on the sea floor, in: *The IASPEI International Handbook of Earthquake and Engineering Seismology*, W.H.K. Lee, H. Kanamori, P.C. Jennings, C. Kisslinger (eds.), Academic Press, London.

Walling M. (2012). *Personal communication*.

Wesnousky S.G. (2008). Displacement and geometrical characteristics of earthquake surface ruptures: Issues and implications for seismic hazard analysis and the process of earthquake rupture, *Bull. Seismol. Soc. Am.*, 98(4): 1609–1632.

Wessel P., Smith W. H. F. (1998). New, improved version of the generic mapping tools released, *EOS, Trans. Am. Geophys. Union*, 79 (47): 579.

Yen Y.-T., Ma K.-F. (2011). Source-scaling relationship for M 4.6–8.1 earthquakes, specifically for earthquakes in the collision zone of Taiwan, *Bull. Seismol. Soc. Am.*, 101(2): 464–481.

Young J. (2013). *Personal communication.*

Youngs R.R. (2012). *Personal communication*.

Zhdanov M.S. (2002). *Geophysical Inverse Theory and Regularization Problems*, Elsevier Science, 633 pgs.

PEER REPORTS

PEER reports are available as a free PDF download from http://peer.berkeley.edu/publications/peer_reports_complete.html. Printed hard copies of PEER reports can be ordered directly from our printer by following the instructions at http://peer.berkeley.edu/publications/peer_reports.html. For other related questions about the PEER Report Series, contact the Pacific Earthquake Engineering Research Center, 325 Davis Hall mail code 1792, Berkeley, CA 94720. Tel.: (510) 642-3437; Fax: (510) 665-1655; Email: peer_editor@berkeley.edu

PEER 2014/09 *PEER Arizona Strong-Motion Database and GMPEs Evaluation.* Tadahiro Kishida, Robert E. Kayen, Olga-Joan Ktenidou, Walter J. Silva, Robert B. Darragh, and Jennie Watson-Lamprey. June 2014.

PEER 2014/08 *Unbonded Pretensioned Bridge Columns with Rocking Detail.* Jeffrey A. Schaefer, Bryan Kennedy, Marc O. Eberhard, John F. Stanton. June 2014.

PEER 2014/07 *Northridge 20 Symposium Summary Report: Impacts, Outcomes, and Next Steps.* May 2014.

PEER 2014/06 *Report of the Tenth Planning Meeting of NEES/E-Defense Collaborative Research on Earthquake Engineering.* December 2013.

PEER 2014/05 *Seismic Velocity Site Characterization of Thirty-One Chilean Seismometer Stations by Spectral Analysis of Surface Wave Dispersion.* Robert Kayen, Brad D. Carkin, Skye Corbet, Camilo Pinilla, Allan Ng, Edward Gorbis, and Christine Truong. April 2014.

PEER 2014/04 *Effect of Vertical Acceleration on Shear Strength of Reinforced Concrete Columns.* Hyerin Lee and Khalid M. Mosalam. April 2014.

PEER 2014/03 *Retest of Thirty-Year-Old Neoprene Isolation Bearings.* James M. Kelly and Niel C. Van Engelen. March 2014.

PEER 2014/02 *Theoretical Development of Hybrid Simulation Applied to Plate Structures.* Ahmed A. Bakhaty, Khalid M. Mosalam, and Sanjay Govindjee. January 2014.

PEER 2014/01 *Performance-Based Seismic Assessment of Skewed Bridges.* Peyman Kaviani, Farzin Zareian, and Ertugrul Taciroglu. January 2014.

PEER 2013/26 *Urban Earthquake Engineering. Proceedings of the U.S.-Iran Seismic Workshop.* December 2013.

PEER 2013/25 *Earthquake Engineering for Resilient Communities: 2013 PEER Internship Program Research Report Collection.* Heidi Tremayne (Editor), Stephen A. Mahin (Editor), Jorge Archbold Monterossa, Matt Brosman, Shelly Dean, Katherine deLaveaga, Curtis Fong, Donovan Holder, Rakeeb Khan, Elizabeth Jachens, David Lam, Daniela Martinez Lopez, Mara Minner, Geffen Oren, Julia Pavicic, Melissa Quinonez, Lorena Rodriguez, Sean Salazar, Kelli Slaven, Vivian Steyert, Jenny Taing, and Salvador Tena. December 2013.

PEER 2013/24 *NGA-West2 Ground Motion Prediction Equations for Vertical Ground Motions.* September 2013.

PEER 2013/23 *Coordinated Planning and Preparedness for Fire Following Major Earthquakes.* Charles Scawthorn. November 2013.

PEER 2013/22 *GEM-PEER Task 3 Project: Selection of a Global Set of Ground Motion Prediction Equations.* Jonathan P. Stewart, John Douglas, Mohammad B. Javanbarg, Carola Di Alessandro, Yousef Bozorgnia, Norman A. Abrahamson, David M. Boore, Kenneth W. Campbell, Elise Delavaud, Mustafa Erdik and Peter J. Stafford. December 2013.

PEER 2013/21 *Seismic Design and Performance of Bridges with Columns on Rocking Foundations.* Grigorios Antonellis and Marios Panagiotou. September 2013.

PEER 2013/20 *Experimental and Analytical Studies on the Seismic Behavior of Conventional and Hybrid Braced Frames.* Jiun-Wei Lai and Stephen A. Mahin. September 2013.

PEER 2013/19 *Toward Resilient Communities: A Performance-Based Engineering Framework for Design and Evaluation of the Built Environment.* Michael William Mieler, Bozidar Stojadinovic, Robert J. Budnitz, Stephen A. Mahin and Mary C. Comerio. September 2013.

PEER 2013/18 *Identification of Site Parameters that Improve Predictions of Site Amplification.* Ellen M. Rathje and Sara Navidi. July 2013.

PEER 2013/17 *Response Spectrum Analysis of Concrete Gravity Dams Including Dam-Water-Foundation Interaction.* Arnkjell Løkke and Anil K. Chopra. July 2013.

PEER 2013/16 *Effect of hoop reinforcement spacing on the cyclic response of large reinforced concrete special moment frame beams.* Marios Panagiotou, Tea Visnjic, Grigorios Antonellis, Panagiotis Galanis, and Jack P. Moehle. June 2013.

PEER 2013/15 *A Probabilistic Framework to Include the Effects of Near-Fault Directivity in Seismic Hazard Assessment.* Shrey Kumar Shahi, Jack W. Baker. October 2013.

PEER 2013/14 *Hanging-Wall Scaling using Finite-Fault Simulations.* Jennifer L. Donahue and Norman A. Abrahamson. September 2013.

PEER 2013/13 *Semi-Empirical Nonlinear Site Amplification and its Application in NEHRP Site Factors.* Jonathan P. Stewart and Emel Seyhan. November 2013.

PEER 2013/12 *Nonlinear Horizontal Site Response for the NGA-West2 Project.* Ronnie Kamai, Norman A. Abramson, Walter J. Silva. May 2013.

PEER 2013/11 *Epistemic Uncertainty for NGA-West2 Models.* Linda Al Atik and Robert R. Youngs. May 2013.

PEER 2013/10 *NGA-West 2 Models for Ground-Motion Directionality.* Shrey K. Shahi and Jack W. Baker. May 2013.

PEER 2013/09 *Final Report of the NGA-West2 Directivity Working Group.* Paul Spudich, Jeffrey R. Bayless, Jack W. Baker, Brian S.J. Chiou, Badie Rowshandel, Shrey Shahi, and Paul Somerville. May 2013.

PEER 2013/08 *NGA-West2 Model for Estimating Average Horizontal Values of Pseudo-Absolute Spectral Accelerations Generated by Crustal Earthquakes.* I. M. Idriss. May 2013.

PEER 2013/07 *Update of the Chiou and Youngs NGA Ground Motion Model for Average Horizontal Component of Peak Ground Motion and Response Spectra.* Brian Chiou and Robert Youngs. May 2013.

PEER 2013/06 *NGA-West2 Campbell-Bozorgnia Ground Motion Model for the Horizontal Components of PGA, PGV, and 5%-Damped Elastic Pseudo-Acceleration Response Spectra for Periods Ranging from 0.01 to 10 sec.* Kenneth W. Campbell and Yousef Bozorgnia. May 2013.

PEER 2013/05 *NGA-West 2 Equations for Predicting Response Spectral Accelerations for Shallow Crustal Earthquakes.* David M. Boore, Jonathan P. Stewart, Emel Seyhan, Gail M. Atkinson. May 2013.

PEER 2013/04 *Update of the AS08 Ground-Motion Prediction Equations Based on the NGA-West2 Data Set.* Norman Abrahamson, Walter Silva, and Ronnie Kamai. May 2013.

PEER 2013/03 *PEER NGA-West2 Database.* Timothy D. Ancheta, Robert B. Darragh, Jonathan P. Stewart, Emel Seyhan, Walter J. Silva, Brian S.J. Chiou, Katie E. Wooddell, Robert W. Graves, Albert R. Kottke, David M. Boore, Tadahiro Kishida, and Jennifer L. Donahue. May 2013.

PEER 2013/02 *Hybrid Simulation of the Seismic Response of Squat Reinforced Concrete Shear Walls.* Catherine A. Whyte and Bozidar Stojadinovic. May 2013.

PEER 2013/01 *Housing Recovery in Chile: A Qualitative Mid-program Review.* Mary C. Comerio. February 2013.

PEER 2012/08 *Guidelines for Estimation of Shear Wave Velocity.* Bernard R. Wair, Jason T. DeJong, and Thomas Shantz. December 2012.

PEER 2012/07 *Earthquake Engineering for Resilient Communities: 2012 PEER Internship Program Research Report Collection.* Heidi Tremayne (Editor), Stephen A. Mahin (Editor), Collin Anderson, Dustin Cook, Michael Erceg, Carlos Esparza, Jose Jimenez, Dorian Krausz, Andrew Lo, Stephanie Lopez, Nicole McCurdy, Paul Shipman, Alexander Strum, Eduardo Vega. December 2012.

PEER 2012/06 *Fragilities for Precarious Rocks at Yucca Mountain.* Matthew D. Purvance, Rasool Anooshehpoor, and James N. Brune. December 2012.

PEER 2012/05 *Development of Simplified Analysis Procedure for Piles in Laterally Spreading Layered Soils.* Christopher R. McGann, Pedro Arduino, and Peter Mackenzie–Helnwein. December 2012.

PEER 2012/04 *Unbonded Pre-Tensioned Columns for Bridges in Seismic Regions.* Phillip M. Davis, Todd M. Janes, Marc O. Eberhard, and John F. Stanton. December 2012.

PEER 2012/03 *Experimental and Analytical Studies on Reinforced Concrete Buildings with Seismically Vulnerable Beam-Column Joints.* Sangjoon Park and Khalid M. Mosalam. October 2012.

PEER 2012/02 *Seismic Performance of Reinforced Concrete Bridges Allowed to Uplift during Multi-Directional Excitation.* Andres Oscar Espinoza and Stephen A. Mahin. July 2012.

PEER 2012/01 *Spectral Damping Scaling Factors for Shallow Crustal Earthquakes in Active Tectonic Regions.* Sanaz Rezaeian, Yousef Bozorgnia, I. M. Idriss, Kenneth Campbell, Norman Abrahamson, and Walter Silva. July 2012.

PEER 2011/10 *Earthquake Engineering for Resilient Communities: 2011 PEER Internship Program Research Report Collection.* Eds. Heidi Faison and Stephen A. Mahin. December 2011.

PEER 2011/09 *Calibration of Semi-Stochastic Procedure for Simulating High-Frequency Ground Motions.* Jonathan P. Stewart, Emel Seyhan, and Robert W. Graves. December 2011.

PEER 2011/08 *Water Supply in regard to Fire Following Earthquake.* Charles Scawthorn. November 2011.

PEER 2011/07 *Seismic Risk Management in Urban Areas. Proceedings of a U.S.-Iran-Turkey Seismic Workshop.* September 2011.

PEER 2011/06 *The Use of Base Isolation Systems to Achieve Complex Seismic Performance Objectives.* Troy A. Morgan and Stephen A. Mahin. July 2011.

PEER 2011/05 *Case Studies of the Seismic Performance of Tall Buildings Designed by Alternative Means.* Task 12 Report for the Tall Buildings Initiative. Jack Moehle, Yousef Bozorgnia, Nirmal Jayaram, Pierson Jones, Mohsen Rahnama, Nilesh Shome, Zeynep Tuna, John Wallace, Tony Yang, and Farzin Zareian. July 2011.

PEER 2011/04 *Recommended Design Practice for Pile Foundations in Laterally Spreading Ground.* Scott A. Ashford, Ross W. Boulanger, and Scott J. Brandenberg. June 2011.

PEER 2011/03 *New Ground Motion Selection Procedures and Selected Motions for the PEER Transportation Research Program.* Jack W. Baker, Ting Lin, Shrey K. Shahi, and Nirmal Jayaram. March 2011.

PEER 2011/02 *A Bayesian Network Methodology for Infrastructure Seismic Risk Assessment and Decision Support.* Michelle T. Bensi, Armen Der Kiureghian, and Daniel Straub. March 2011.

PEER 2011/01 *Demand Fragility Surfaces for Bridges in Liquefied and Laterally Spreading Ground.* Scott J. Brandenberg, Jian Zhang, Pirooz Kashighandi, Yili Huo, and Minxing Zhao. March 2011.

PEER 2010/05 *Guidelines for Performance-Based Seismic Design of Tall Buildings.* Developed by the Tall Buildings Initiative. November 2010.

PEER 2010/04 *Application Guide for the Design of Flexible and Rigid Bus Connections between Substation Equipment Subjected to Earthquakes.* Jean-Bernard Dastous and Armen Der Kiureghian. September 2010.

PEER 2010/03 *Shear Wave Velocity as a Statistical Function of Standard Penetration Test Resistance and Vertical Effective Stress at Caltrans Bridge Sites.* Scott J. Brandenberg, Naresh Bellana, and Thomas Shantz. June 2010.

PEER 2010/02 *Stochastic Modeling and Simulation of Ground Motions for Performance-Based Earthquake Engineering.* Sanaz Rezaeian and Armen Der Kiureghian. June 2010.

PEER 2010/01 *Structural Response and Cost Characterization of Bridge Construction Using Seismic Performance Enhancement Strategies.* Ady Aviram, Božidar Stojadinović, Gustavo J. Parra-Montesinos, and Kevin R. Mackie. March 2010.

PEER 2009/03 *The Integration of Experimental and Simulation Data in the Study of Reinforced Concrete Bridge Systems Including Soil-Foundation-Structure Interaction.* Matthew Dryden and Gregory L. Fenves. November 2009.

PEER 2009/02 *Improving Earthquake Mitigation through Innovations and Applications in Seismic Science, Engineering, Communication, and Response. Proceedings of a U.S.-Iran Seismic Workshop.* October 2009.

PEER 2009/01 *Evaluation of Ground Motion Selection and Modification Methods: Predicting Median Interstory Drift Response of Buildings.* Curt B. Haselton, Ed. June 2009.

PEER 2008/10 *Technical Manual for Strata.* Albert R. Kottke and Ellen M. Rathje. February 2009.

PEER 2008/09 *NGA Model for Average Horizontal Component of Peak Ground Motion and Response Spectra.* Brian S.-J. Chiou and Robert R. Youngs. November 2008.

PEER 2008/08 *Toward Earthquake-Resistant Design of Concentrically Braced Steel Structures.* Patxi Uriz and Stephen A. Mahin. November 2008.

PEER 2008/07 *Using OpenSees for Performance-Based Evaluation of Bridges on Liquefiable Soils.* Stephen L. Kramer, Pedro Arduino, and HyungSuk Shin. November 2008.

PEER 2008/06 *Shaking Table Tests and Numerical Investigation of Self-Centering Reinforced Concrete Bridge Columns.* Hyung IL Jeong, Junichi Sakai, and Stephen A. Mahin. September 2008.

PEER 2008/05 *Performance-Based Earthquake Engineering Design Evaluation Procedure for Bridge Foundations Undergoing Liquefaction-Induced Lateral Ground Displacement.* Christian A. Ledezma and Jonathan D. Bray. August 2008.

PEER 2008/04 *Benchmarking of Nonlinear Geotechnical Ground Response Analysis Procedures.* Jonathan P. Stewart, Annie On-Lei Kwok, Yousseff M. A. Hashash, Neven Matasovic, Robert Pyke, Zhiliang Wang, and Zhaohui Yang. August 2008.

PEER 2008/03 *Guidelines for Nonlinear Analysis of Bridge Structures in California.* Ady Aviram, Kevin R. Mackie, and Božidar Stojadinović. August 2008.

PEER 2008/02 *Treatment of Uncertainties in Seismic-Risk Analysis of Transportation Systems.* Evangelos Stergiou and Anne S. Kiremidjian. July 2008.

PEER 2008/01 *Seismic Performance Objectives for Tall Buildings.* William T. Holmes, Charles Kircher, William Petak, and Nabih Youssef. August 2008.

PEER 2007/12 *An Assessment to Benchmark the Seismic Performance of a Code-Conforming Reinforced Concrete Moment-Frame Building.* Curt Haselton, Christine A. Goulet, Judith Mitrani-Reiser, James L. Beck, Gregory G. Deierlein, Keith A. Porter, Jonathan P. Stewart, and Ertugrul Taciroglu. August 2008.

PEER 2007/11 *Bar Buckling in Reinforced Concrete Bridge Columns.* Wayne A. Brown, Dawn E. Lehman, and John F. Stanton. February 2008.

PEER 2007/10 *Computational Modeling of Progressive Collapse in Reinforced Concrete Frame Structures.* Mohamed M. Talaat and Khalid M. Mosalam. May 2008.

PEER 2007/09 *Integrated Probabilistic Performance-Based Evaluation of Benchmark Reinforced Concrete Bridges.* Kevin R. Mackie, John-Michael Wong, and Božidar Stojadinović. January 2008.

PEER 2007/08 *Assessing Seismic Collapse Safety of Modern Reinforced Concrete Moment-Frame Buildings.* Curt B. Haselton and Gregory G. Deierlein. February 2008.

PEER 2007/07 *Performance Modeling Strategies for Modern Reinforced Concrete Bridge Columns.* Michael P. Berry and Marc O. Eberhard. April 2008.

PEER 2007/06 *Development of Improved Procedures for Seismic Design of Buried and Partially Buried Structures.* Linda Al Atik and Nicholas Sitar. June 2007.

PEER 2007/05 *Uncertainty and Correlation in Seismic Risk Assessment of Transportation Systems.* Renee G. Lee and Anne S. Kiremidjian. July 2007.

PEER 2007/04 *Numerical Models for Analysis and Performance-Based Design of Shallow Foundations Subjected to Seismic Loading.* Sivapalan Gajan, Tara C. Hutchinson, Bruce L. Kutter, Prishati Raychowdhury, José A. Ugalde, and Jonathan P. Stewart. May 2008.

PEER 2007/03 *Beam-Column Element Model Calibrated for Predicting Flexural Response Leading to Global Collapse of RC Frame Buildings.* Curt B. Haselton, Abbie B. Liel, Sarah Taylor Lange, and Gregory G. Deierlein. May 2008.

PEER 2007/02 *Campbell-Bozorgnia NGA Ground Motion Relations for the Geometric Mean Horizontal Component of Peak and Spectral Ground Motion Parameters.* Kenneth W. Campbell and Yousef Bozorgnia. May 2007.

PEER 2007/01 *Boore-Atkinson NGA Ground Motion Relations for the Geometric Mean Horizontal Component of Peak and Spectral Ground Motion Parameters.* David M. Boore and Gail M. Atkinson. May. May 2007.

PEER 2006/12 *Societal Implications of Performance-Based Earthquake Engineering.* Peter J. May. May 2007.

PEER 2006/11 *Probabilistic Seismic Demand Analysis Using Advanced Ground Motion Intensity Measures, Attenuation Relationships, and Near-Fault Effects.* Polsak Tothong and C. Allin Cornell. March 2007.

PEER 2006/10 *Application of the PEER PBEE Methodology to the I-880 Viaduct.* Sashi Kunnath. February 2007.

PEER 2006/09 *Quantifying Economic Losses from Travel Forgone Following a Large Metropolitan Earthquake.* James Moore, Sungbin Cho, Yue Yue Fan, and Stuart Werner. November 2006.

PEER 2006/08 *Vector-Valued Ground Motion Intensity Measures for Probabilistic Seismic Demand Analysis.* Jack W. Baker and C. Allin Cornell. October 2006.

PEER 2006/07 *Analytical Modeling of Reinforced Concrete Walls for Predicting Flexural and Coupled–Shear-Flexural Responses.* Kutay Orakcal, Leonardo M. Massone, and John W. Wallace. October 2006.

PEER 2006/06 *Nonlinear Analysis of a Soil-Drilled Pier System under Static and Dynamic Axial Loading.* Gang Wang and Nicholas Sitar. November 2006.

PEER 2006/05 *Advanced Seismic Assessment Guidelines.* Paolo Bazzurro, C. Allin Cornell, Charles Menun, Maziar Motahari, and Nicolas Luco. September 2006.

PEER 2006/04 *Probabilistic Seismic Evaluation of Reinforced Concrete Structural Components and Systems.* Tae Hyung Lee and Khalid M. Mosalam. August 2006.

PEER 2006/03 *Performance of Lifelines Subjected to Lateral Spreading.* Scott A. Ashford and Teerawut Juirnarongrit. July 2006.

PEER 2006/02 *Pacific Earthquake Engineering Research Center Highway Demonstration Project.* Anne Kiremidjian, James Moore, Yue Yue Fan, Nesrin Basoz, Ozgur Yazali, and Meredith Williams. April 2006.

PEER 2006/01 *Bracing Berkeley. A Guide to Seismic Safety on the UC Berkeley Campus.* Mary C. Comerio, Stephen Tobriner, and Ariane Fehrenkamp. January 2006.

PEER 2005/16 *Seismic Response and Reliability of Electrical Substation Equipment and Systems.* Junho Song, Armen Der Kiureghian, and Jerome L. Sackman. April 2006.

PEER 2005/15   *CPT-Based Probabilistic Assessment of Seismic Soil Liquefaction Initiation.* R. E. S. Moss, R. B. Seed, R. E. Kayen, J. P. Stewart, and A. Der Kiureghian. April 2006.

PEER 2005/14   *Workshop on Modeling of Nonlinear Cyclic Load-Deformation Behavior of Shallow Foundations.* Bruce L. Kutter, Geoffrey Martin, Tara Hutchinson, Chad Harden, Sivapalan Gajan, and Justin Phalen. March 2006.

PEER 2005/13   *Stochastic Characterization and Decision Bases under Time-Dependent Aftershock Risk in Performance-Based Earthquake Engineering.* Gee Liek Yeo and C. Allin Cornell. July 2005.

PEER 2005/12   *PEER Testbed Study on a Laboratory Building: Exercising Seismic Performance Assessment.* Mary C. Comerio, editor. November 2005.

PEER 2005/11   *Van Nuys Hotel Building Testbed Report: Exercising Seismic Performance Assessment.* Helmut Krawinkler, editor. October 2005.

PEER 2005/10   *First NEES/E-Defense Workshop on Collapse Simulation of Reinforced Concrete Building Structures.* September 2005.

PEER 2005/09   *Test Applications of Advanced Seismic Assessment Guidelines.* Joe Maffei, Karl Telleen, Danya Mohr, William Holmes, and Yuki Nakayama. August 2006.

PEER 2005/08   *Damage Accumulation in Lightly Confined Reinforced Concrete Bridge Columns.* R. Tyler Ranf, Jared M. Nelson, Zach Price, Marc O. Eberhard, and John F. Stanton. April 2006.

PEER 2005/07   *Experimental and Analytical Studies on the Seismic Response of Freestanding and Anchored Laboratory Equipment.* Dimitrios Konstantinidis and Nicos Makris. January 2005.

PEER 2005/06   *Global Collapse of Frame Structures under Seismic Excitations.* Luis F. Ibarra and Helmut Krawinkler. September 2005.

PEER 2005//05   *Performance Characterization of Bench- and Shelf-Mounted Equipment.* Samit Ray Chaudhuri and Tara C. Hutchinson. May 2006.

PEER 2005/04   *Numerical Modeling of the Nonlinear Cyclic Response of Shallow Foundations.* Chad Harden, Tara Hutchinson, Geoffrey R. Martin, and Bruce L. Kutter. August 2005.

PEER 2005/03   *A Taxonomy of Building Components for Performance-Based Earthquake Engineering.* Keith A. Porter. September 2005.

PEER 2005/02   *Fragility Basis for California Highway Overpass Bridge Seismic Decision Making.* Kevin R. Mackie and Božidar Stojadinović. June 2005.

PEER 2005/01   *Empirical Characterization of Site Conditions on Strong Ground Motion.* Jonathan P. Stewart, Yoojoong Choi, and Robert W. Graves. June 2005.

PEER 2004/09   *Electrical Substation Equipment Interaction: Experimental Rigid Conductor Studies.* Christopher Stearns and André Filiatrault. February 2005.

PEER 2004/08   *Seismic Qualification and Fragility Testing of Line Break 550-kV Disconnect Switches.* Shakhzod M. Takhirov, Gregory L. Fenves, and Eric Fujisaki. January 2005.

PEER 2004/07   *Ground Motions for Earthquake Simulator Qualification of Electrical Substation Equipment.* Shakhzod M. Takhirov, Gregory L. Fenves, Eric Fujisaki, and Don Clyde. January 2005.

PEER 2004/06   *Performance-Based Regulation and Regulatory Regimes.* Peter J. May and Chris Koski. September 2004.

PEER 2004/05   *Performance-Based Seismic Design Concepts and Implementation: Proceedings of an International Workshop.* Peter Fajfar and Helmut Krawinkler, editors. September 2004.

PEER 2004/04   *Seismic Performance of an Instrumented Tilt-up Wall Building.* James C. Anderson and Vitelmo V. Bertero. July 2004.

PEER 2004/03   *Evaluation and Application of Concrete Tilt-up Assessment Methodologies.* Timothy Graf and James O. Malley. October 2004.

PEER 2004/02   *Analytical Investigations of New Methods for Reducing Residual Displacements of Reinforced Concrete Bridge Columns.* Junichi Sakai and Stephen A. Mahin. August 2004.

PEER 2004/01   *Seismic Performance of Masonry Buildings and Design Implications.* Kerri Anne Taeko Tokoro, James C. Anderson, and Vitelmo V. Bertero. February 2004.

PEER 2003/18   *Performance Models for Flexural Damage in Reinforced Concrete Columns.* Michael Berry and Marc Eberhard. August 2003.

PEER 2003/17   *Predicting Earthquake Damage in Older Reinforced Concrete Beam-Column Joints.* Catherine Pagni and Laura Lowes. October 2004.

PEER 2003/16   *Seismic Demands for Performance-Based Design of Bridges.* Kevin Mackie and Božidar Stojadinović.   August 2003.

PEER 2003/15   *Seismic Demands for Nondeteriorating Frame Structures and Their Dependence on Ground Motions.* Ricardo Antonio Medina and Helmut Krawinkler. May 2004.

PEER 2003/14   *Finite Element Reliability and Sensitivity Methods for Performance-Based Earthquake Engineering.* Terje Haukaas and Armen Der Kiureghian. April 2004.

PEER 2003/13   *Effects of Connection Hysteretic Degradation on the Seismic Behavior of Steel Moment-Resisting Frames.* Janise E. Rodgers and Stephen A. Mahin. March 2004.

PEER 2003/12   *Implementation Manual for the Seismic Protection of Laboratory Contents: Format and Case Studies.* William T. Holmes and Mary C. Comerio. October 2003.

PEER 2003/11   *Fifth U.S.-Japan Workshop on Performance-Based Earthquake Engineering Methodology for Reinforced Concrete Building Structures.* February 2004.

PEER 2003/10   *A Beam-Column Joint Model for Simulating the Earthquake Response of Reinforced Concrete Frames.* Laura N. Lowes, Nilanjan Mitra, and Arash Altoontash. February 2004.

PEER 2003/09   *Sequencing Repairs after an Earthquake: An Economic Approach.* Marco Casari and Simon J. Wilkie. April 2004.

PEER 2003/08   *A Technical Framework for Probability-Based Demand and Capacity Factor Design (DCFD) Seismic Formats.* Fatemeh Jalayer and C. Allin Cornell. November 2003.

PEER 2003/07   *Uncertainty Specification and Propagation for Loss Estimation Using FOSM Methods.* Jack W. Baker and C. Allin Cornell. September 2003.

PEER 2003/06   *Performance of Circular Reinforced Concrete Bridge Columns under Bidirectional Earthquake Loading.* Mahmoud M. Hachem, Stephen A. Mahin, and Jack P. Moehle. February 2003.

PEER 2003/05   *Response Assessment for Building-Specific Loss Estimation.* Eduardo Miranda and Shahram Taghavi. September 2003.

PEER 2003/04   *Experimental Assessment of Columns with Short Lap Splices Subjected to Cyclic Loads.* Murat Melek, John W. Wallace, and Joel Conte. April 2003.

PEER 2003/03   *Probabilistic Response Assessment for Building-Specific Loss Estimation.* Eduardo Miranda and Hesameddin Aslani. September 2003.

PEER 2003/02   *Software Framework for Collaborative Development of Nonlinear Dynamic Analysis Program.* Jun Peng and Kincho H. Law. September 2003.

PEER 2003/01   *Shake Table Tests and Analytical Studies on the Gravity Load Collapse of Reinforced Concrete Frames.* Kenneth John Elwood and Jack P. Moehle. November 2003.

PEER 2002/24   *Performance of Beam to Column Bridge Joints Subjected to a Large Velocity Pulse.* Natalie Gibson, André Filiatrault, and Scott A. Ashford. April 2002.

PEER 2002/23   *Effects of Large Velocity Pulses on Reinforced Concrete Bridge Columns.* Greg L. Orozco and Scott A. Ashford. April 2002.

PEER 2002/22   *Characterization of Large Velocity Pulses for Laboratory Testing.* Kenneth E. Cox and Scott A. Ashford. April 2002.

PEER 2002/21   *Fourth U.S.-Japan Workshop on Performance-Based Earthquake Engineering Methodology for Reinforced Concrete Building Structures.* December 2002.

PEER 2002/20   *Barriers to Adoption and Implementation of PBEE Innovations.* Peter J. May. August 2002.

PEER 2002/19   *Economic-Engineered Integrated Models for Earthquakes: Socioeconomic Impacts.* Peter Gordon, James E. Moore II, and Harry W. Richardson. July 2002.

PEER 2002/18   *Assessment of Reinforced Concrete Building Exterior Joints with Substandard Details.* Chris P. Pantelides, Jon Hansen, Justin Nadauld, and Lawrence D. Reaveley. May 2002.

PEER 2002/17   *Structural Characterization and Seismic Response Analysis of a Highway Overcrossing Equipped with Elastomeric Bearings and Fluid Dampers: A Case Study.* Nicos Makris and Jian Zhang. November 2002.

PEER 2002/16   *Estimation of Uncertainty in Geotechnical Properties for Performance-Based Earthquake Engineering.* Allen L. Jones, Steven L. Kramer, and Pedro Arduino. December 2002.

PEER 2002/15   *Seismic Behavior of Bridge Columns Subjected to Various Loading Patterns.* Asadollah Esmaeily-Gh. and Yan Xiao. December 2002.

PEER 2002/14   *Inelastic Seismic Response of Extended Pile Shaft Supported Bridge Structures.* T.C. Hutchinson, R.W. Boulanger, Y.H. Chai, and I.M. Idriss. December 2002.

PEER 2002/13   *Probabilistic Models and Fragility Estimates for Bridge Components and Systems.* Paolo Gardoni, Armen Der Kiureghian, and Khalid M. Mosalam. June 2002.

PEER 2002/12   *Effects of Fault Dip and Slip Rake on Near-Source Ground Motions: Why Chi-Chi Was a Relatively Mild M7.6 Earthquake.* Brad T. Aagaard, John F. Hall, and Thomas H. Heaton. December 2002.

PEER 2002/11   *Analytical and Experimental Study of Fiber-Reinforced Strip Isolators.* James M. Kelly and Shakhzod M. Takhirov. September 2002.

PEER 2002/10   *Centrifuge Modeling of Settlement and Lateral Spreading with Comparisons to Numerical Analyses.* Sivapalan Gajan and Bruce L. Kutter. January 2003.

PEER 2002/09   *Documentation and Analysis of Field Case Histories of Seismic Compression during the 1994 Northridge, California, Earthquake.* Jonathan P. Stewart, Patrick M. Smith, Daniel H. Whang, and Jonathan D. Bray. October 2002.

PEER 2002/08   *Component Testing, Stability Analysis and Characterization of Buckling-Restrained Unbonded Braces^{TM}.* Cameron Black, Nicos Makris, and Ian Aiken. September 2002.

PEER 2002/07   *Seismic Performance of Pile-Wharf Connections.* Charles W. Roeder, Robert Graff, Jennifer Soderstrom, and Jun Han Yoo. December 2001.

PEER 2002/06   *The Use of Benefit-Cost Analysis for Evaluation of Performance-Based Earthquake Engineering Decisions.* Richard O. Zerbe and Anthony Falit-Baiamonte. September 2001.

PEER 2002/05   *Guidelines, Specifications, and Seismic Performance Characterization of Nonstructural Building Components and Equipment.* André Filiatrault, Constantin Christopoulos, and Christopher Stearns. September 2001.

PEER 2002/04   *Consortium of Organizations for Strong-Motion Observation Systems and the Pacific Earthquake Engineering Research Center Lifelines Program: Invited Workshop on Archiving and Web Dissemination of Geotechnical Data, 4–5 October 2001.* September 2002.

PEER 2002/03   *Investigation of Sensitivity of Building Loss Estimates to Major Uncertain Variables for the Van Nuys Testbed.* Keith A. Porter, James L. Beck, and Rustem V. Shaikhutdinov. August 2002.

PEER 2002/02   *The Third U.S.-Japan Workshop on Performance-Based Earthquake Engineering Methodology for Reinforced Concrete Building Structures.* July 2002.

PEER 2002/01   *Nonstructural Loss Estimation: The UC Berkeley Case Study.* Mary C. Comerio and John C. Stallmeyer. December 2001.

PEER 2001/16   *Statistics of SDF-System Estimate of Roof Displacement for Pushover Analysis of Buildings.* Anil K. Chopra, Rakesh K. Goel, and Chatpan Chintanapakdee. December 2001.

PEER 2001/15   *Damage to Bridges during the 2001 Nisqually Earthquake.* R. Tyler Ranf, Marc O. Eberhard, and Michael P. Berry. November 2001.

PEER 2001/14   *Rocking Response of Equipment Anchored to a Base Foundation.* Nicos Makris and Cameron J. Black. September 2001.

PEER 2001/13   *Modeling Soil Liquefaction Hazards for Performance-Based Earthquake Engineering.* Steven L. Kramer and Ahmed-W. Elgamal. February 2001.

PEER 2001/12   *Development of Geotechnical Capabilities in OpenSees.* Boris Jeremić. September 2001.

PEER 2001/11   *Analytical and Experimental Study of Fiber-Reinforced Elastomeric Isolators.* James M. Kelly and Shakhzod M. Takhirov. September 2001.

PEER 2001/10   *Amplification Factors for Spectral Acceleration in Active Regions.* Jonathan P. Stewart, Andrew H. Liu, Yoojoong Choi, and Mehmet B. Baturay. December 2001.

PEER 2001/09   *Ground Motion Evaluation Procedures for Performance-Based Design.* Jonathan P. Stewart, Shyh-Jeng Chiou, Jonathan D. Bray, Robert W. Graves, Paul G. Somerville, and Norman A. Abrahamson. September 2001.

PEER 2001/08   *Experimental and Computational Evaluation of Reinforced Concrete Bridge Beam-Column Connections for Seismic Performance.* Clay J. Naito, Jack P. Moehle, and Khalid M. Mosalam. November 2001.

PEER 2001/07   *The Rocking Spectrum and the Shortcomings of Design Guidelines.* Nicos Makris and Dimitrios Konstantinidis. August 2001.

PEER 2001/06   *Development of an Electrical Substation Equipment Performance Database for Evaluation of Equipment Fragilities.* Thalia Agnanos. April 1999.

PEER 2001/05   *Stiffness Analysis of Fiber-Reinforced Elastomeric Isolators.* Hsiang-Chuan Tsai and James M. Kelly. May 2001.

PEER 2001/04   *Organizational and Societal Considerations for Performance-Based Earthquake Engineering.* Peter J. May. April 2001.

PEER 2001/03   *A Modal Pushover Analysis Procedure to Estimate Seismic Demands for Buildings: Theory and Preliminary Evaluation.* Anil K. Chopra and Rakesh K. Goel. January 2001.

PEER 2001/02   *Seismic Response Analysis of Highway Overcrossings Including Soil-Structure Interaction.* Jian Zhang and Nicos Makris. March 2001.

PEER 2001/01   *Experimental Study of Large Seismic Steel Beam-to-Column Connections.* Egor P. Popov and Shakhzod M. Takhirov. November 2000.

PEER 2000/10   *The Second U.S.-Japan Workshop on Performance-Based Earthquake Engineering Methodology for Reinforced Concrete Building Structures.* March 2000.

PEER 2000/09   *Structural Engineering Reconnaissance of the August 17, 1999 Earthquake: Kocaeli (Izmit), Turkey.* Halil Sezen, Kenneth J. Elwood, Andrew S. Whittaker, Khalid Mosalam, John J. Wallace, and John F. Stanton. December 2000.

PEER 2000/08   *Behavior of Reinforced Concrete Bridge Columns Having Varying Aspect Ratios and Varying Lengths of Confinement.* Anthony J. Calderone, Dawn E. Lehman, and Jack P. Moehle. January 2001.

PEER 2000/07   *Cover-Plate and Flange-Plate Reinforced Steel Moment-Resisting Connections.* Taejin Kim, Andrew S. Whittaker, Amir S. Gilani, Vitelmo V. Bertero, and Shakhzod M. Takhirov. September 2000.

PEER 2000/06   *Seismic Evaluation and Analysis of 230-kV Disconnect Switches.* Amir S. J. Gilani, Andrew S. Whittaker, Gregory L. Fenves, Chun-Hao Chen, Henry Ho, and Eric Fujisaki. July 2000.

PEER 2000/05   *Performance-Based Evaluation of Exterior Reinforced Concrete Building Joints for Seismic Excitation.* Chandra Clyde, Chris P. Pantelides, and Lawrence D. Reaveley. July 2000.

PEER 2000/04   *An Evaluation of Seismic Energy Demand: An Attenuation Approach.* Chung-Che Chou and Chia-Ming Uang. July 1999.

PEER 2000/03   *Framing Earthquake Retrofitting Decisions: The Case of Hillside Homes in Los Angeles.* Detlof von Winterfeldt, Nels Roselund, and Alicia Kitsuse. March 2000.

PEER 2000/02   *U.S.-Japan Workshop on the Effects of Near-Field Earthquake Shaking.* Andrew Whittaker, ed. July 2000.

PEER 2000/01   *Further Studies on Seismic Interaction in Interconnected Electrical Substation Equipment.* Armen Der Kiureghian, Kee-Jeung Hong, and Jerome L. Sackman. November 1999.

PEER 1999/14   *Seismic Evaluation and Retrofit of 230-kV Porcelain Transformer Bushings.* Amir S. Gilani, Andrew S. Whittaker, Gregory L. Fenves, and Eric Fujisaki. December 1999.

PEER 1999/13   *Building Vulnerability Studies: Modeling and Evaluation of Tilt-up and Steel Reinforced Concrete Buildings.* John W. Wallace, Jonathan P. Stewart, and Andrew S. Whittaker, editors. December 1999.

PEER 1999/12   *Rehabilitation of Nonductile RC Frame Building Using Encasement Plates and Energy-Dissipating Devices.* Mehrdad Sasani, Vitelmo V. Bertero, James C. Anderson. December 1999.

PEER 1999/11   *Performance Evaluation Database for Concrete Bridge Components and Systems under Simulated Seismic Loads.* Yael D. Hose and Frieder Seible. November 1999.

PEER 1999/10   *U.S.-Japan Workshop on Performance-Based Earthquake Engineering Methodology for Reinforced Concrete Building Structures.* December 1999.

PEER 1999/09   *Performance Improvement of Long Period Building Structures Subjected to Severe Pulse-Type Ground Motions.* James C. Anderson, Vitelmo V. Bertero, and Raul Bertero. October 1999.

PEER 1999/08   *Envelopes for Seismic Response Vectors.* Charles Menun and Armen Der Kiureghian. July 1999.

PEER 1999/07   *Documentation of Strengths and Weaknesses of Current Computer Analysis Methods for Seismic Performance of Reinforced Concrete Members.* William F. Cofer. November 1999.

PEER 1999/06   *Rocking Response and Overturning of Anchored Equipment under Seismic Excitations.* Nicos Makris and Jian Zhang. November 1999.

PEER 1999/05   *Seismic Evaluation of 550 kV Porcelain Transformer Bushings.* Amir S. Gilani, Andrew S. Whittaker, Gregory L. Fenves, and Eric Fujisaki. October 1999.

PEER 1999/04   *Adoption and Enforcement of Earthquake Risk-Reduction Measures.* Peter J. May, Raymond J. Burby, T. Jens Feeley, and Robert Wood.

PEER 1999/03   *Task 3 Characterization of Site Response General Site Categories.* Adrian Rodriguez-Marek, Jonathan D. Bray, and Norman Abrahamson. February 1999.

PEER 1999/02   *Capacity-Demand-Diagram Methods for Estimating Seismic Deformation of Inelastic Structures: SDF Systems.* Anil K. Chopra and Rakesh Goel. April 1999.

PEER 1999/01   *Interaction in Interconnected Electrical Substation Equipment Subjected to Earthquake Ground Motions.* Armen Der Kiureghian, Jerome L. Sackman, and Kee-Jeung Hong. February 1999.

PEER 1998/08   *Behavior and Failure Analysis of a Multiple-Frame Highway Bridge in the 1994 Northridge Earthquake.* Gregory L. Fenves and Michael Ellery. December 1998.

PEER 1998/07   *Empirical Evaluation of Inertial Soil-Structure Interaction Effects.* Jonathan P. Stewart, Raymond B. Seed, and Gregory L. Fenves. November 1998.

PEER 1998/06   *Effect of Damping Mechanisms on the Response of Seismic Isolated Structures.* Nicos Makris and Shih-Po Chang. November 1998.

PEER 1998/05   *Rocking Response and Overturning of Equipment under Horizontal Pulse-Type Motions.* Nicos Makris and Yiannis Roussos. October 1998.

PEER 1998/04   *Pacific Earthquake Engineering Research Invitational Workshop Proceedings, May 14–15, 1998: Defining the Links between Planning, Policy Analysis, Economics and Earthquake Engineering.* Mary Comerio and Peter Gordon. September 1998.

PEER 1998/03   *Repair/Upgrade Procedures for Welded Beam to Column Connections.* James C. Anderson and Xiaojing Duan. May 1998.

PEER 1998/02   *Seismic Evaluation of 196 kV Porcelain Transformer Bushings.* Amir S. Gilani, Juan W. Chavez, Gregory L. Fenves, and Andrew S. Whittaker. May 1998.

PEER 1998/01   *Seismic Performance of Well-Confined Concrete Bridge Columns.* Dawn E. Lehman and Jack P. Moehle. December 2000.

ONLINE PEER REPORTS

The following PEER reports are available by Internet only at http://peer.berkeley.edu/publications/peer_reports_complete.html.

PEER 2012/103   *Performance-Based Seismic Demand Assessment of Concentrically Braced Steel Frame Buildings.* Chui-Hsin Chen and Stephen A. Mahin. December 2012.

PEER 2012/102   *Procedure to Restart an Interrupted Hybrid Simulation: Addendum to PEER Report 2010/103.* Vesna Terzic and Bozidar Stojadinovic. October 2012.

PEER 2012/101   *Mechanics of Fiber Reinforced Bearings.* James M. Kelly and Andrea Calabrese. February 2012.

PEER 2011/107   *Nonlinear Site Response and Seismic Compression at Vertical Array Strongly Shaken by 2007 Niigata-ken Chuetsu-oki Earthquake.* Eric Yee, Jonathan P. Stewart, and Kohji Tokimatsu. December 2011.

PEER 2011/106   *Self Compacting Hybrid Fiber Reinforced Concrete Composites for Bridge Columns.* Pardeep Kumar, Gabriel Jen, William Trono, Marios Panagiotou, and Claudia Ostertag. September 2011.

PEER 2011/105   *Stochastic Dynamic Analysis of Bridges Subjected to Spacially Varying Ground Motions.* Katerina Konakli and Armen Der Kiureghian. August 2011.

PEER 2011/104   *Design and Instrumentation of the 2010 E-Defense Four-Story Reinforced Concrete and Post-Tensioned Concrete Buildings.* Takuya Nagae, Kenichi Tahara, Taizo Matsumori, Hitoshi Shiohara, Toshimi Kabeyasawa, Susumu Kono, Minehiro Nishiyama (Japanese Research Team) and John Wallace, Wassim Ghannoum, Jack Moehle, Richard Sause, Wesley Keller, Zeynep Tuna (U.S. Research Team). June 2011.

PEER 2011/103   *In-Situ Monitoring of the Force Output of Fluid Dampers: Experimental Investigation.* Dimitrios Konstantinidis, James M. Kelly, and Nicos Makris. April 2011.

PEER 2011/102   *Ground-motion prediction equations 1964 - 2010.* John Douglas. April 2011.

PEER 2011/101   *Report of the Eighth Planning Meeting of NEES/E-Defense Collaborative Research on Earthquake Engineering.* Convened by the Hyogo Earthquake Engineering Research Center (NIED), NEES Consortium, Inc. February 2011.

PEER 2010/111   *Modeling and Acceptance Criteria for Seismic Design and Analysis of Tall Buildings.* Task 7 Report for the Tall Buildings Initiative - Published jointly by the Applied Technology Council. October 2010.

PEER 2010/110   *Seismic Performance Assessment and Probabilistic Repair Cost Analysis of Precast Concrete Cladding Systems for Multistory Buildlings.* Jeffrey P. Hunt and Božidar Stojadinovic. November 2010.

PEER 2010/109   *Report of the Seventh Joint Planning Meeting of NEES/E-Defense Collaboration on Earthquake Engineering. Held at the E-Defense, Miki, and Shin-Kobe, Japan, September 18–19, 2009.* August 2010.

PEER 2010/108   *Probabilistic Tsunami Hazard in California.* Hong Kie Thio, Paul Somerville, and Jascha Polet, preparers. October 2010.

PEER 2010/107   *Performance and Reliability of Exposed Column Base Plate Connections for Steel Moment-Resisting Frames.* Ady Aviram, Božidar Stojadinovic, and Armen Der Kiureghian. August 2010.

PEER 2010/106   *Verification of Probabilistic Seismic Hazard Analysis Computer Programs.* Patricia Thomas, Ivan Wong, and Norman Abrahamson. May 2010.

PEER 2010/105   *Structural Engineering Reconnaissance of the April 6, 2009, Abruzzo, Italy, Earthquake, and Lessons Learned.* M. Selim Günay and Khalid M. Mosalam. April 2010.

PEER 2010/104   *Simulating the Inelastic Seismic Behavior of Steel Braced Frames, Including the Effects of Low-Cycle Fatigue.* Yuli Huang and Stephen A. Mahin. April 2010.

PEER 2010/103   *Post-Earthquake Traffic Capacity of Modern Bridges in California.* Vesna Terzic and Božidar Stojadinović. March 2010.

PEER 2010/102   *Analysis of Cumulative Absolute Velocity (CAV) and JMA Instrumental Seismic Intensity (I_{JMA}) Using the PEER–NGA Strong Motion Database.* Kenneth W. Campbell and Yousef Bozorgnia. February 2010.

PEER 2010/101   *Rocking Response of Bridges on Shallow Foundations.* Jose A. Ugalde, Bruce L. Kutter, and Boris Jeremic. April 2010.

PEER 2009/109   *Simulation and Performance-Based Earthquake Engineering Assessment of Self-Centering Post-Tensioned Concrete Bridge Systems.* Won K. Lee and Sarah L. Billington. December 2009.

PEER 2009/108   *PEER Lifelines Geotechnical Virtual Data Center.* J. Carl Stepp, Daniel J. Ponti, Loren L. Turner, Jennifer N. Swift, Sean Devlin, Yang Zhu, Jean Benoit, and John Bobbitt. September 2009.

PEER 2009/107   *Experimental and Computational Evaluation of Current and Innovative In-Span Hinge Details in Reinforced Concrete Box-Girder Bridges: Part 2: Post-Test Analysis and Design Recommendations.* Matias A. Hube and Khalid M. Mosalam. December 2009.

PEER 2009/106   *Shear Strength Models of Exterior Beam-Column Joints without Transverse Reinforcement.* Sangjoon Park and Khalid M. Mosalam. November 2009.

PEER 2009/105   *Reduced Uncertainty of Ground Motion Prediction Equations through Bayesian Variance Analysis.* Robb Eric S. Moss. November 2009.

PEER 2009/104   *Advanced Implementation of Hybrid Simulation.* Andreas H. Schellenberg, Stephen A. Mahin, Gregory L. Fenves. November 2009.

PEER 2009/103   *Performance Evaluation of Innovative Steel Braced Frames.* T. Y. Yang, Jack P. Moehle, and Božidar Stojadinovic. August 2009.

PEER 2009/102   *Reinvestigation of Liquefaction and Nonliquefaction Case Histories from the 1976 Tangshan Earthquake.* Robb Eric Moss, Robert E. Kayen, Liyuan Tong, Songyu Liu, Guojun Cai, and Jiaer Wu. August 2009.

PEER 2009/101   *Report of the First Joint Planning Meeting for the Second Phase of NEES/E-Defense Collaborative Research on Earthquake Engineering.* Stephen A. Mahin et al. July 2009.

PEER 2008/104   *Experimental and Analytical Study of the Seismic Performance of Retaining Structures.* Linda Al Atik and Nicholas Sitar. January 2009.

PEER 2008/103   *Experimental and Computational Evaluation of Current and Innovative In-Span Hinge Details in Reinforced Concrete Box-Girder Bridges. Part 1: Experimental Findings and Pre-Test Analysis.* Matias A. Hube and Khalid M. Mosalam. January 2009.

PEER 2008/102   *Modeling of Unreinforced Masonry Infill Walls Considering In-Plane and Out-of-Plane Interaction.* Stephen Kadysiewski and Khalid M. Mosalam. January 2009.

PEER 2008/101   *Seismic Performance Objectives for Tall Buildings.* William T. Holmes, Charles Kircher, William Petak, and Nabih Youssef. August 2008.

PEER 2007/101   *Generalized Hybrid Simulation Framework for Structural Systems Subjected to Seismic Loading.* Tarek Elkhoraibi and Khalid M. Mosalam. July 2007.

PEER 2007/100   *Seismic Evaluation of Reinforced Concrete Buildings Including Effects of Masonry Infill Walls.* Alidad Hashemi and Khalid M. Mosalam. July 2007.

PEER Core Institutions:
University of California, Berkeley (Lead Institution)
California Institute of Technology
Oregon State University
Stanford University
University of California, Davis
University of California, Irvine
University of California, Los Angeles
University of California, San Diego
University of Southern California
University of Washington

PEER reports can be ordered at http://peer.berkeley.edu/publications/peer_reports.html or by contacting

Pacific Earthquake Engineering Research Center
University of California, Berkeley
325 Davis Hall, mail code 1792
Berkeley, CA 94720-1792
Tel: 510-642-3437
Fax: 510-642-1655
Email: peer_editor@berkeley.edu

ISSN 1547-0587X